ABSTRACT

Title of dissertation: THEORY OF SUPERCONDUCTING PHASE QUBITS

Frederick W. Strauch
Doctor of Philosophy, 2004

Dissertation directed by: Professor Alex J. Dragt
Department of Physics

The theory of superconducting phase qubits—also known as current-biased Josephson junctions—is presented. In the first part of this thesis, I introduce quantum computation, quantum simulation, and their deep connection with symplectic integration. I then consider the fundamental many-body theory of superconductivity and Josephson junctions and show how the quantum dynamics of a single macroscopic degree of freedom, the gauge invariant phase difference, emerges. A complete study of the Hilbert space structure of such a variable is performed for the current-biased junction. The resulting resonance structure is studied in detail, using various formalisms including the WKB approximation, instanton methods, the complex scaling transformation, basis set stabilization, numerical integration, and dynamical simulation using Lie algebraic wave-packet propagation.

The second part of this thesis explores how the current-biased junction can

be used as an element of a quantum computer—a quantum bit (qubit). Single qubit operations are studied, followed by the presentation of the theory of coupled qubit devices. My key result is the design and optimization of quantum logic gates with high fidelity ($F \sim 0.9999$) for capacitively coupled phase qubits with short gate times ($\sim$ 10 ns). Finally, I examine an advanced qubit-coupling scheme, a resonant coupling method utilizing a harmonic oscillator as the auxiliary degree of freedom. The models and methods presented here have been developed in direct collaboration with an experimental program. These experiments are the first to show spectroscopic evidence for entanglement between two and three macroscopic degrees of freedom in a superconducting circuit.

THEORY OF SUPERCONDUCTING PHASE QUBITS

by

Frederick W. Strauch

Dissertation submitted to the Faculty of the Graduate School of the
University of Maryland, College Park in partial fulfillment
of the requirements for the degree of
Doctor of Philosophy
2004

Advisory Commmittee:

Professor Alex J. Dragt, Chair/Advisor
Professor James R. Anderson
Professor Stephen Kudla
Professor Christopher J. Lobb
Professor Frederick C. Wellstood

ACKNOWLEDGEMENTS

I wish to gratefully acknowledge all who are responsible for the success of this research and this dissertation.

First and foremost, I thank my advisor Alex Dragt. His is the model of a scientist—one with a neverending desire to figure things out. From him this work takes a clear, unwavering desire to understand.

The remaining advisors and primary members of the Superconducting Quantum Computing Group have equal share in this work: Bob Anderson, who has always had wonderful questions and jokes; Chris Lobb, whose insightful advice and cheerful criticism have always been appreciated; Fred Wellstood, whose strong motivation and determined good sense is without peer. From each, my work has benefited, and I am grateful.

Fellow researchers and travelers also deserve thanks, especially Phil Johnson, Andrew Berkley, Huizhong Xu, Roberto Ramos, Hanhee Paik, Sudeep Dutta, Mark Gubrud, and Bill Parsons. Their interest, assistance, and guidance cannot be replaced. Belta Pollard in the Center for Superconducitivty Research, and Jane Hessing of the Physics Department are invaluable for truly getting things done, in spite of us physicists. I also acknowledge those who have financially supported this

work: LPS, NSF, DoD, and the Center for Superconductivity Research.

Finally, I thank my parents, extended family, and most of all my wife Laura, whose loving patience cannot be adequately rewarded. Thank you all and God bless.

TABLE OF CONTENTS

LIST OF FIGURES

LIST OF TABLES

Chapter 1

Introduction

This thesis focuses on particular physical systems which, through significant hard work, may one day be elements of a quantum computer. We start in this Chapter by considering the important questions: What is a quantum computer? Why is it interesting? and For what can it be used? Along the way we deal with issues of entanglement, universal quantum logic gates, and quantum simulation protocols. Finally, we point out the significant overlap between these issues and the study of symplectic maps, and particularly symplectic integration. These theoretical considerations will then be used in the remaining Chapters of this thesis to simulate and characterize the fundamental dynamics of the phase qubit.

Recent work has shown that quantum computation can be more powerful than classical models of computation. This follows from the fact, observed by Feynman [1], that the simulation of an arbitrary state of a quantum system with n qubits

requires resources exponential (2^n) in the number of elements (n). This exponential overhead is due to the existence of quantum entanglement [2]. Conversely, the presence of entangled states is a necessary (although not sufficient) condition for a quantum computer to be exponentially faster than a classical computer [3]. A prime example is Shor's algorithm [4] for factoring an n-bit number. This algorithm runs exponentially faster (n^3) than the known classical factoring algorithms ($\exp(n^{1/3}(\log_2 n)^{2/3})$) [5].

These developments have inspired a significant effort, spanning many theoretical and experimental disciplines, to find suitable systems that can implement quantum information processing. Many reviews on this new field exist [5, 6, 7, 8]. Most theoretical work on physical realizations of a quantum computer attempt to reduce the system to some ideal set of simple Hamiltonians which are known to be sufficient for implementing quantum algorithms. The Hamiltonians of most systems, however, are certainly not simple. The reduction of the system to some ideal typically requires the neglect of higher energy levels as well as the dynamics of coupling elements. Including these effects is necessary because ultimately one must show that the implementation of quantum logic succeeds with high probability. One of the central topics of this thesis is to show how one can approximate the ideal qubit dynamics while taking into account all of the nuances of the real system.

Finally, we note that there are deep connections between unitary methods for quantum systems and symplectic methods for classical systems. This connection is due to the central role of Lie algebras in dynamical systems. Solving both Hamilton's and Schrödinger's equations can be seen as the exponentiating of the Lie algebra.

This is most clearly seen in quantum mechanics. The evolution of observables with the Hamiltonian operator $\hat{H}$ is given by the wave-function $|\Psi(t)\rangle$, which for time-independent Hamiltonians evolves as

$$|\Psi(t)\rangle = \exp(-i\hat{H}t/\hbar)|\Psi(0)\rangle. \tag{1.1}$$

A similar expression can be given for classical systems. The time-evolution of any observable $f(q,p)$, a function of the phase-space coordinates (q,p), is given by the Hamiltonian $H(q,p)$ through the *symplectic* map

$$f(q,p,t) = \exp(-t : H(q,p) :) f(q,p). \tag{1.2}$$

This map is called symplectic [9] since it generalizes the definition of a $2N \times 2N$ symplectic matrix M, which satisfies

$$M^\dagger J M = J \tag{1.3}$$

where J the antisymmetric $2N \times 2N$ matrix, with the block diagonal form

$$J = \begin{pmatrix} 0 & -I_N \\ I_N & 0 \end{pmatrix}, \tag{1.4}$$

and I_N is the $N \times N$ identity matrix. The full exponential in (1.2) is defined by its power series. In the exponent, $: H :$ is a Lie operator, whose action is defined by

$$: H(q,p) : f(q,p) = \{H, f\}(q,p) = \frac{\partial H}{\partial q}\frac{\partial f}{\partial p} - \frac{\partial H}{\partial p}\frac{\partial f}{\partial q}. \tag{1.5}$$

Note that this is the Poisson bracket of H and f. The commutator of two Lie operators is also a Lie operator, by the fundamental homomorphism

$$[: H_1 :, : H_2 :] =: H_1 :: H_2 : - : H_2 :: H_1 :=: \{H_1, H_2\} :, \tag{1.6}$$

which can be proved using the fundamental definition and the Jacobi property of the Poisson bracket

$$\{A,\{B,C\}\}+\{B,\{C,A\}\}+\{C,\{A,B\}\}=0. \tag{1.7}$$

These instances of Lie algebraic and group properties are both governed by the Baker-Campbell-Haussdorf (BCH) theorem [10]. This theorem states that the product of two exponentials e^A and e^B is also the exponential of an element in the free Lie algebra generated by A and B. That is

$$\exp(A)\exp(B)=\exp(C) \tag{1.8}$$

where

$$\begin{aligned} C = \;& A+B+\tfrac{1}{2}[AB]+\tfrac{1}{12}([AAB]+[BBA])+\tfrac{1}{24}([ABBA]) \\ & -\tfrac{1}{720}([BBBBA]+[AAAAB])+\tfrac{1}{360}([BAAAB]+[ABBBA]) \\ & +\tfrac{1}{120}([AABBA]+[BBAAB])+\cdots, \end{aligned} \tag{1.9}$$

and we have introduced an abbreviated commutator notation such that $[XYZ]=[X,[Y,Z]]$, $[WXYZ]=[W,[XYZ]]=[W,[X,[Y,Z]]]$ and so on. In general, the series for C is infinite, with all higher order terms formed only from commutators of A and B—there are no terms like A^n or $[AB]^n$. This deep property of the exponential function is essential for our understanding of quantum logic, quantum simulation, and symplectic integration.

The brief introduction of this Chapter cannot fully describe the interest and usefulness of quantum computation. As a relatively new field of research, it is certain that much remains to be discovered. Taking recent history as our guide, we may only begin to know what is possible when working quantum computers have actually been built.

The remaining Chapters of this dissertation are devoted to a particular solid-state device, the current-biased Josephson junction—called a phase qubit. In Chapter 2 we explore the fundamental physics of the Josephson effect. We show how the many-body dynamics reduces to the quantum mechanics of a single macroscopic degree of freedom: γ, the phase difference across the junction. A critical examination is made of various subtle issues regarding number-phase commutation relations, and the periodicity of the phase in current-biased devices.

We fully explore the quantum mechanics of the simplest model of a junction in Chapter 3. The resonances of the "washboard" potential are the focus of this Chapter. We first introduce three methods of characterizing resonances: the stabilization method for constructing a discrete density of states, the Gamow-Siegert method to find poles of the Green's function, and finally the continuum wavefunctions. To illustrate and justify these methods we examine two exactly solvable models. We then show how stabilization, complex scaling, and a continuum normalization method can be used to find and characterize the resonances of the washboard.

In Chapter 4 we extend this analysis by looking at a typical approximation used in the literature, that of a quadratic plus cubic potential. Many analytical results are derived in this Chapter: high-order perturbation theory for the energy levels, tunneling rates from WKB, and instanton methods. We compare these results with the exact numerical methods derived in Chapter 3.

In Chapter 5, we analyze how a junction can be used for quantum computation. We study two types of single qubit operations: Rabi oscillations to drive logic transitions and adiabatic bias current ramps to shift the qubit operating point.

In particular, we develop simple theoretical models of these operations. We then compare these with numerical simulations that fully model the ideal dynamics of the circuit and show how simple control pulses can optimize the fidelity.

Chapter 6 introduces a simple capacitive coupling scheme for two phase qubits. We analyze the energy levels and entanglement structure of this device. We also construct two model two-qubit operations: controlled phase and swap gates. We then compare simple theoretical models of these operations with numerical simulations that fully model the ideal dynamics of the circuit. We then show how to optimize the fidelity.

In Chapter 7, we study the quantum mechanical behavior of a macroscopic, three-body, superconducting circuit, based on recent experimental work by Dr. Huizhong Xu [11]. Here, we provide theoretical analysis of the microwave spectroscopy of a resonator coupling two large Josephson junctions. By tuning each junction separately into resonance with the resonator, strong coupling is observed between each junction and the resonator. Bringing both junctions together into resonance with the resonator, we find spectroscopic evidence for entanglement between all three degrees of freedom, and demonstrate a new method for controllable coupling of distant qubits.

Finally, we conclude this dissertation in Chapter 8 by outlining some of the remaining issues for quantum computation with phase qubits.

1.1 Quantum Computation

Historically, Feynman was the first to truly explore quantum computation. He was inspired by the difficulty of simulating quantum systems using classical computers [1]. This led him to consider a quantum mechanical model of computation, by constructing a Hamiltonian whose dynamics would produce logic gates on simple two-state elements [12], now called quantum bits, or qubits [13]. The next key theoretical development was Deutsch's observation [14] that the existence of quantum superpositions ("quantum parallelism") may allow quantum computers to sample a larger space than that of classical computers. In this Section we review the basic theory of quantum computation. We begin with the classical notion of a bit and the fundamental reversible logic operations on one and two bits, and then extend these to the quantum case. We conclude by discussing the concept of a universal set of quantum logic gates.

1.1.1 Classical Reversible Computation

A general model for computation includes: (i) a memory storage medium, (ii) procedures that manipulate the memory, and (iii) a set of instructions for manipulation. The essence of all computational tasks can be represented by the dynamical manipulation of information-storage elements. We shall first consider reversible computation because quantum computation, being a unitary operation, must be reversible. While most existing classical computers use irreversible gates, the same algorithms can always be implemented using reversible logic gates [7].

The most fundamental element of information is the bit. A bit has only two states, which we designate as $|0\rangle$ and $|1\rangle$, or in general by $|x\rangle$, where x can be 0 or 1. The fundamental importance of the bit is due to Shannon's coding theorem [7]. The theorem states: given *any* information source with an alphabet of N symbols where the relative frequency of the k-th symbol is given by p_k (such that $\sum_{k=1}^{N} p_k = 1$), for that information source there exists a binary coding procedure for which the average number of bits needed to encode each symbol of the information source is the Shannon entropy:

$$H(\{p_k\}) = -\sum_{k=1}^{N} p_k \log_2 p_k. \tag{1.10}$$

Based on this theorem there is no loss of generality to consider the bit as our abstract general information storage element.

Dynamical manipulations of bits are called logic gates. A classical computer can perform only two operations on a single bit: leave the bit alone, or flip it. In matrix form we represent the two states of our bit by

$$|0\rangle = \begin{pmatrix} 1 \\ 0 \end{pmatrix}, \quad |1\rangle = \begin{pmatrix} 0 \\ 1 \end{pmatrix}. \tag{1.11}$$

Then the fundamental bit-flip operation would be the NOT gate X

$$X = \begin{pmatrix} 0 & 1 \\ 1 & 0 \end{pmatrix}. \tag{1.12}$$

This gate has the property that $X|x\rangle = |x \oplus 1\rangle$, where x can be 0 or 1 (the addition is modulo base 2 with $0 \oplus 0 = 0$, $0 \oplus 1 = 1 \oplus 0 = 1$, and $1 \oplus 1 = 0$). Note that X is unitary and therefore invertible. The operation that leaves the bit alone is the identity

$$I = \begin{pmatrix} 1 & 0 \\ 0 & 1 \end{pmatrix} \tag{1.13}$$

which has the correct property $I|x\rangle = |x\rangle$.

For two bits, the four possible states are $|xy\rangle$ with both x and y independently equal to 0 or 1. In matrix form we can set

$$|00\rangle = \begin{pmatrix} 1 \\ 0 \\ 0 \\ 0 \end{pmatrix}, \quad |01\rangle = \begin{pmatrix} 0 \\ 1 \\ 0 \\ 0 \end{pmatrix}, \quad |10\rangle = \begin{pmatrix} 0 \\ 0 \\ 1 \\ 0 \end{pmatrix}, \quad |11\rangle = \begin{pmatrix} 0 \\ 0 \\ 0 \\ 1 \end{pmatrix}. \tag{1.14}$$

A simple set of logical operations on these states is

$$\begin{aligned} I \otimes I &= \begin{pmatrix} 1 & 0 & 0 & 0 \\ 0 & 1 & 0 & 0 \\ 0 & 0 & 1 & 0 \\ 0 & 0 & 0 & 1 \end{pmatrix}, \quad I \otimes X = \begin{pmatrix} 0 & 1 & 0 & 0 \\ 1 & 0 & 0 & 0 \\ 0 & 0 & 0 & 1 \\ 0 & 0 & 1 & 0 \end{pmatrix}, \\ U_{\text{SWAP}} &= \begin{pmatrix} 1 & 0 & 0 & 0 \\ 0 & 0 & 1 & 0 \\ 0 & 1 & 0 & 0 \\ 0 & 0 & 0 & 1 \end{pmatrix}, \quad U_{\text{CNOT}} = \begin{pmatrix} 1 & 0 & 0 & 0 \\ 0 & 1 & 0 & 0 \\ 0 & 0 & 0 & 1 \\ 0 & 0 & 1 & 0 \end{pmatrix}. \end{aligned} \tag{1.15}$$

These gates have the following effects on a two-bit state $|x\,y\rangle$:

$$\begin{aligned} I \otimes I|x\,y\rangle &= |x\,y\rangle, \\ I \otimes X|x\,y\rangle &= |x\,y \oplus 1\rangle, \\ U_{\text{SWAP}}|x\,y\rangle &= |y\,x\rangle, \\ U_{CNOT}|x\,y\rangle &= |x\,y \oplus x\rangle. \end{aligned} \tag{1.16}$$

They are also all unitary. The controlled-NOT gate U_{CNOT} is particularly important for computation, for it has the structure of a conditional operation: bit two is flipped if and only if bit one is set to 1. In this way, bit one controls the state of bit two. By combining these gates appropriately, all permutations of the states $|x\,y\rangle$ can be generated. One useful identity for these gates is

$$U_{\text{CNOT}} U_{\text{SWAP}} U_{\text{CNOT}} = U_{\text{SWAP}} U_{\text{CNOT}} U_{\text{SWAP}}. \tag{1.17}$$

Note that we have used the tensor product notation for the two bits and the logic gates (e.g. $I \otimes X$). The tensor product in vector space induces a tensor product in matrix space given by

$$\begin{pmatrix} a_{00} & a_{01} \\ a_{10} & a_{11} \end{pmatrix} \otimes \begin{pmatrix} b_{00} & b_{01} \\ b_{10} & b_{11} \end{pmatrix} = \begin{pmatrix} a_{00}b_{00} & a_{00}b_{01} & a_{01}b_{00} & a_{01}b_{01} \\ a_{00}b_{10} & a_{00}b_{11} & a_{01}b_{10} & a_{01}b_{11} \\ a_{10}b_{00} & a_{10}b_{01} & a_{11}b_{00} & a_{11}b_{01} \\ a_{10}b_{10} & a_{10}b_{11} & a_{11}b_{10} & a_{11}b_{11} \end{pmatrix}. \tag{1.18}$$

It is perhaps surprising that the gates described above are not capable of *universal* classical computation. For universal classical reversible computation, it is necessary to include an appropriate *three-bit* gate. The matrix form for three bits is

$$\begin{aligned} |000\rangle &= \begin{pmatrix} 1 \\ 0 \\ 0 \\ 0 \\ 0 \\ 0 \\ 0 \\ 0 \end{pmatrix}, \quad |001\rangle = \begin{pmatrix} 0 \\ 1 \\ 0 \\ 0 \\ 0 \\ 0 \\ 0 \\ 0 \end{pmatrix}, \quad |010\rangle = \begin{pmatrix} 0 \\ 0 \\ 1 \\ 0 \\ 0 \\ 0 \\ 0 \\ 0 \end{pmatrix}, \quad |011\rangle = \begin{pmatrix} 0 \\ 0 \\ 0 \\ 1 \\ 0 \\ 0 \\ 0 \\ 0 \end{pmatrix}, \\ |100\rangle &= \begin{pmatrix} 0 \\ 0 \\ 0 \\ 0 \\ 1 \\ 0 \\ 0 \\ 0 \end{pmatrix}, \quad |101\rangle = \begin{pmatrix} 0 \\ 0 \\ 0 \\ 0 \\ 0 \\ 1 \\ 0 \\ 0 \end{pmatrix}, \quad |110\rangle = \begin{pmatrix} 0 \\ 0 \\ 0 \\ 0 \\ 0 \\ 0 \\ 1 \\ 0 \end{pmatrix}, \quad |111\rangle = \begin{pmatrix} 0 \\ 0 \\ 0 \\ 0 \\ 0 \\ 0 \\ 0 \\ 1 \end{pmatrix}. \end{aligned} \tag{1.19}$$

One such three-bit gate is the Toffoli gate T. This gate has the matrix form

$$T = \begin{pmatrix} 1 & 0 & 0 & 0 & 0 & 0 & 0 & 0 \\ 0 & 1 & 0 & 0 & 0 & 0 & 0 & 0 \\ 0 & 0 & 1 & 0 & 0 & 0 & 0 & 0 \\ 0 & 0 & 0 & 1 & 0 & 0 & 0 & 0 \\ 0 & 0 & 0 & 0 & 1 & 0 & 0 & 0 \\ 0 & 0 & 0 & 0 & 0 & 1 & 0 & 0 \\ 0 & 0 & 0 & 0 & 0 & 0 & 0 & 1 \\ 0 & 0 & 0 & 0 & 0 & 0 & 1 & 0 \end{pmatrix}. \tag{1.20}$$

The action of T on bit states can be summarized by $T|x\,y\,z\rangle = |x\,y\,(z \oplus x \cdot y)\rangle$, where $x \cdot y$ denotes bitwise multiplication. The matrix T is also unitary. Bit three is

flipped if and only if $x = y = 1$, a nice generalization of the controlled-not. Another universal gate is the Fredkin gate F, which has the matrix form

$$F = \begin{pmatrix} 1 & 0 & 0 & 0 & 0 & 0 & 0 & 0 \\ 0 & 1 & 0 & 0 & 0 & 0 & 0 & 0 \\ 0 & 0 & 1 & 0 & 0 & 0 & 0 & 0 \\ 0 & 0 & 0 & 0 & 0 & 1 & 0 & 0 \\ 0 & 0 & 0 & 0 & 1 & 0 & 0 & 0 \\ 0 & 0 & 0 & 1 & 0 & 0 & 0 & 0 \\ 0 & 0 & 0 & 0 & 0 & 0 & 1 & 0 \\ 0 & 0 & 0 & 0 & 0 & 0 & 0 & 1 \end{pmatrix}. \tag{1.21}$$

This gate acts on three-bit states as $F|x\,y\,z\rangle = |x'\,y'\,z\rangle$, with $x' = x \oplus z \cdot (x \oplus y)$ and $y' = y \oplus z \cdot (x \oplus y)$. The matrix F is unitary. This gate swaps x and y if and only if $z = 1$. This gate is sometimes called a controlled-swap gate. All classical computations can be implemented using networks of reversible two-bit gates and either of these three-bit gates.

1.1.2 Quantum Logic Gates

For quantum computation, we must generalize our classical model. The *qubit* is the quantum generalization of the bit. The key quantum feature we add to the bit is the principle of superposition. That is, the state of each qubit of our quantum computer can not only be $|0\rangle$ and $|1\rangle$, but also any linear combination

$$|\Psi\rangle = c_0|0\rangle + c_1|1\rangle. \tag{1.22}$$

The amplitudes c_x can be complex, and must satisfy $|c_0|^2 + |c_1|^2 = 1$. Note that the overall phase of $|\Psi\rangle$ is generally irrelevant; we can therefore let $c_0 = \cos\theta$ be real and by the normalization we have $c_1 = e^{i\phi}\sin\theta$. Thus there are two real parameters (θ, ϕ) that specify $|\Psi\rangle$. The two logic operations introduced above, the identity I

and the NOT gate X, can now act on our quantum state $|\Psi\rangle$. Their quantum action is just their classical action on each basis state $|x\rangle$, extended by linearity:

$$I|\Psi\rangle = c_0 I|0\rangle + c_1 I|1\rangle = c_0|0\rangle + c_1|1\rangle \tag{1.23}$$

$$X|\Psi\rangle = c_0 X|0\rangle + c_1 X|1\rangle = c_0|1\rangle + c_1|0\rangle. \tag{1.24}$$

These logic gates are unitary operators on the qubit Hilbert space.

There are many more unitary operators which can act on qubits and have no classical analogue. A convenient basis for these operators is the Pauli basis: $\{I, X, Y, Z\}$, where I and X are defined above, and Y and Z are:

$$Y = \begin{pmatrix} 0 & -i \\ i & 0 \end{pmatrix}, \quad Z = \begin{pmatrix} 1 & 0 \\ 0 & -1 \end{pmatrix}. \tag{1.25}$$

Letting $\vec{\sigma} = \{X, Y, Z\}$, we can write an arbitrary unitary operator U by

$$U = e^{i\phi} \exp\left(-i\theta \vec{n} \cdot \vec{\sigma}\right) = e^{i\phi} \cos(\theta) I - i e^{i\phi} \sin(\theta) \vec{n} \cdot \vec{\sigma}, \tag{1.26}$$

where U has been parametrized by two angles ϕ and θ, and a three-dimensional unit vector $\vec{n}$—a total of four real parameters.

A fundamental result, discussed below, is that *every* unitary operator (up to the overall phase ϕ) can be constructed from repeated composition of only two fundamental operators. Thus, while there are a continuum of values for θ and $\vec{n}$, only two such values are needed. The overall phase ϕ has no physical effect on a qubit and can therefore be neglected.

Two important gates in quantum algorithms are the Hadamard gate U_H and the controlled-Z gate U_{CZ}, also called the controlled-phase gate. These have the

matrix form

$$U_H = \frac{1}{\sqrt{2}} \begin{pmatrix} 1 & 1 \\ 1 & -1 \end{pmatrix}, \tag{1.27}$$

$$U_{\mathrm{CZ}} = \begin{pmatrix} 1 & 0 & 0 & 0 \\ 0 & 1 & 0 & 0 \\ 0 & 0 & 1 & 0 \\ 0 & 0 & 0 & -1 \end{pmatrix}. \tag{1.28}$$

The controlled-Z and the controlled-NOT gates are simply related

$$(I \otimes U_H) U_{\mathrm{CZ}} (I \otimes U_H) = U_{\mathrm{CNOT}}. \tag{1.29}$$

The combination of the non-classical features of U_H (superposition) and U_{CZ} (controlled-phase) have "interfered" to yield the "classical" controlled-NOT gate.

So far we have seen that the elements of quantum computing are significantly different from the classical elements. While classical bits can be in only one of two states ($|0\rangle$ or $|1\rangle$), and can only be manipulated in two ways (I or X), qubits can be in an arbitrary superposition of $|0\rangle$ and $|1\rangle$, and can be manipulated in many ways (recall the continuum of parameters for U above). This divide becomes even greater when superposition is extended to multiple qubits. For example, the quantum state of two independent qubits (A and B) is

$$\begin{aligned} |\Psi_A\rangle \otimes |\Psi_B\rangle &= (a_0|0\rangle + a_1|1\rangle) \otimes (b_0|0\rangle + b_1|1\rangle) \\ &= a_0 b_0 |00\rangle + a_0 b_1 |01\rangle + a_1 b_0 |10\rangle + a_1 b_1 |11\rangle. \end{aligned} \tag{1.30}$$

This, however, is not the most general quantum state of two qubits, which is

$$|\Psi_{AB}\rangle = c_{00}|00\rangle + c_{01}|01\rangle + c_{10}|10\rangle + c_{11}|11\rangle, \tag{1.31}$$

with $|c_{00}|^2 + |c_{01}|^2 + |c_{10}|^2 + |c_{11}|^2 = 1$. States of the form (1.31) cannot be written as (1.30) unless the coefficients satisfy $|c_{00}c_{11} - c_{01}c_{10}| = 0$. States that can be written

in the the form given by (1.30) are called *product* states; states that cannot be so written are called *entangled* states. Note that the number of real parameters needed to specify the product states (1.30) are 4, i.e. 2 parameters for each qubit. For an n-qubit product state we would need $2n$ real parameters. This is in contrast to the generally entangled state (1.31), which requires $8 - 2 = 6$ real parameters (two can be removed since the phase is arbitrary and the amplitudes are normalized). For an n-qubit entangled state, we would need $2^{n+1} - 2$ real parameters. This exponential difference, first noted by Feynman [1], suggests that the use of quantum systems may generate great computational power.

The potential of quantum computation would be a curiosity if the relevant dynamics could not be generated by simple, physically realizable operations. The first progress in formulating a realizable model of quantum computation was Deutsch's study of quantum networks (or circuits) [15], and the observation that certain fundamental operations on qubits could be universal. Universality means that an arbitary operation on n-qubits can be achieved by repeated applications of elements of the gate set G. Deutsch showed that a certain 3-qubit gate of the form

$$D = \begin{pmatrix} 1 & 0 & 0 & 0 & 0 & 0 & 0 & 0 \\ 0 & 1 & 0 & 0 & 0 & 0 & 0 & 0 \\ 0 & 0 & 1 & 0 & 0 & 0 & 0 & 0 \\ 0 & 0 & 0 & 1 & 0 & 0 & 0 & 0 \\ 0 & 0 & 0 & 0 & 1 & 0 & 0 & 0 \\ 0 & 0 & 0 & 0 & 0 & 1 & 0 & 0 \\ 0 & 0 & 0 & 0 & 0 & 0 & i\cos\theta & \sin\theta \\ 0 & 0 & 0 & 0 & 0 & 1 & \sin\theta & i\cos\theta \end{pmatrix}, \tag{1.32}$$

and the set of simple permutations of the qubits, together form a universal gate set. This seems natural, as universal classical computation required the three-bit Toffoli or Fredkin gate.

Deutsch's work initiated a study of the complexity of constructing unitary operations, and the discovery of simpler sets of universal gates. In particular, DiVincenzo showed, using aspects of Lie group theory, that only two-qubit gates are necessary to create D [16]. A particular two-qubit gate which (with qubit permutation) is universal was given by Barenco [17]. Using Lie methods, Lloyd [18] and independently Deutsch, Barenco, and Ekert [19] showed that almost any two-qubit gate was universal. Finally, Barenco *et al.* [20] showed that the set of single-qubit gates and the two-qubit controlled-NOT gate U_{CNOT} formed a universal gate set.

The Lie theory needed to understand the universality of almost any gate [18, 19] is a simple application of the Baker-Campbell-Haussdorf relation (1.8)-(1.9). Suppose we have two gates $U_A(\tau) = e^{i\tau A}$ and $U_B(\tau) = e^{i\tau B}$, where A and B are two Hermitian operators and the time τ is under our control. If we then form the product

$$W = U_A(\tau_N)U_B(\tau_{N-1})U_A(\tau_{N-2})\cdots U_A(\tau_3)U_B(\tau_2)U_A(\tau_1) \tag{1.33}$$

we know that the C in $W = e^{iC}$ will be a sum of elements of the free Lie algebra over A and B. If A and B are finite dimensional and sufficiently general, then we can choose the τ_k in (1.33) such that any particular C in the algebra is realized. A constructive argument that this is possible can be seen from the fundamental Trotter-type formulae

$$e^{i(A+B)\tau} = \lim_{n\to\infty}\left(e^{iA\tau/n}e^{iB\tau/n}\right)^n, \tag{1.34}$$

$$e^{[A,B]\tau} = \lim_{n\to\infty}\left(e^{-iB\sqrt{\tau/n}}e^{-iA\sqrt{\tau/n}}e^{iB\sqrt{\tau/n}}e^{iA\sqrt{\tau/n}}\right)^n. \tag{1.35}$$

(The $n \to \infty$ limit is unnecessary for approximate work; see below). By using

(1.34)-(1.35) and their generalizations, one can construct any element of the unitary group by repeated applications of $U_A(\tau)$ and $U_B(\tau)$.

There is an important feature in the commutator formula (1.35): negative values of τ_k seem to be needed. Most interactions, however, cannot be easily reversed in the laboratory. This problem can be avoided for A and B of sufficiently small dimension [21]. In this case $e^{i\tau A}$ is nearly a periodic function of τ with the period depending on the distribution of the eigenvalues of A. In particular, there will be a recurrence time τ_A such that $e^{i\tau_A A} \simeq I$. Then, negative values of τ can be simulated by $e^{i(\tau_A - \tau)A} \simeq e^{-i\tau A}$.

The proven universality of the product (1.33) does not seem to be useful in practice. The simple constructive formulae (1.34) and (1.35) will require a large number of fundamental steps to achieve a given level of accuracy. In general, for A and B d-by-d matrices the number of terms in the product (1.33) needed to specify an arbitrary C is $2d^2$. For N qubits, $d = 2^N$, and thus this construction is exponential in the number of qubits. There are, however, many algorithms which can be constructed by a number of gates polynomial in N. These issues will be explored later when we consider quantum simulation.

There is, however, a particular decomposition of two-qubit gates which allows us to understand even better the structure of universality. This canonical decomposition theorem was first discovered by Kraus and Cirac [22], and independently discussed using Lie group theory by Khaneja, Brockett, and Glaser [23]. That such a decomposition exists can also be seen in the work of Makhlin [24]. A complete discussion is given by Zhang *et al.* [25]. The central result is that any two-qubit

unitary operator (acting on qubits A and B) can be written in the form:

$$U = (U_A \otimes U_B)\, U_d\, (V_A \otimes V_B) \tag{1.36}$$

where U_A and V_A are operators on qubit A, U_B and V_B are operators on qubit B, and U_d has the form

$$U_d = \exp(i(\alpha_x X \otimes X + \alpha_y Y \otimes Y + \alpha_z Z \otimes Z)). \tag{1.37}$$

This form was discovered by Kraus and Cirac in the context of determining how to generate as much entanglement as possible between two initially unentangled systems. It is therefore useful, before deriving their result, to discuss how to quantify the entanglement present in a given quantum state.

1.1.3 Entanglement

There are many measures of entanglement. We will define three related measures below: the entropy of entanglement $\mathcal{E}$ (1.41), the entanglement of formation $\mathcal{E}_F$ (1.46), and the two-qubit concurrence C (1.47). Fortunately, one finds that in many instances all measures are roughly equivalent. The basic principle is that entanglement is a resource shared between parties that can be used for the transfer or manipulation of quantum information such as quantum teleportation [26]. Therefore, any entanglement measure should be able to say something about how a given quantum state can be used for these processes. For pure states, the entropy of entanglement is the fundamental measure. This is related to the Schmidt decomposition,

which for a quantum state $|\Psi_{AB}\rangle$ shared between parties A and B has the form

$$|\Psi_{AB}\rangle = \sum_{k=1}^{d} c_k |a_k\rangle \otimes |b_k\rangle. \tag{1.38}$$

The coefficients c_k can be chosen real and are called the Schmidt coefficients, while $|a_k\rangle$ and $|b_k\rangle$ are called the Schmidt bases for systems A and B, respectively. For simplicity we have assumed that the dimensions of A and B are both equal to d. This special form of $|\Psi_{AB}\rangle$ follows from a singular-value decomposition of the matrix $c_{ij} = \langle i_A\, j_B|\Psi_{AB}\rangle$, where $|i_A\rangle$ and $|j_B\rangle$ are arbitrary bases for systems A and B. Now, all statistical properties of state $|\Psi_{AB}\rangle$ for system A are determined by the reduced density matrix:

$$\rho_A = \mathrm{tr}_B(|\Psi_{AB}\rangle\langle\Psi_{AB}|) = \sum_{k=1}^{d} c_k^2 |a_k\rangle\langle a_k|. \tag{1.39}$$

Similarly, all statistical properties for system B are determined by its reduced density matrix:

$$\rho_B = \mathrm{tr}_A(|\Psi_{AB}\rangle\langle\Psi_{AB}|) = \sum_{k=1}^{d} c_k^2 |b_k\rangle\langle b_k|. \tag{1.40}$$

Thus, the Schmidt decomposition of the state $|\Psi_{AB}\rangle$ directly yields the eigenvalues (c_k^2) and eigenvectors of both of the reduced density matrices ρ_A and ρ_B. Any entanglement measure should only be a function of the Schmidt coefficients, as these are the only properties of the state shared equally between systems A and B. Furthermore, any entanglement measure should be equal to zero for product states $|\Psi_{AB}\rangle = |\Phi_A\rangle \otimes |\Phi_B\rangle$. These states are already in Schmidt form (1.38), with $c_1 = 1$ and $c_{k\neq 1} = 0$. The *entropy of entanglement* is one such measure. For a

d-dimensional quantum system, it is defined by the rule

$$\mathcal{E}(\Psi_{AB}) = -\mathrm{tr}_A(\rho_A \log_2 \rho_A) = -\mathrm{tr}_B(\rho_B \log_2 \rho_B) = -\sum_{k=1}^{d} c_k^2 \log_2(c_k^2). \tag{1.41}$$

For two qubits, a maximally entangled state has $c_1 = c_2 = 2^{-1/2}$ with a quantum state of the form

$$|\Psi\rangle = \frac{1}{\sqrt{2}} \left(|00\rangle + |11\rangle\right). \tag{1.42}$$

Using these Schmidt coefficients in (1.41) we find $\mathcal{E} = 1$. For a general d-dimensional state (qudit) we have $c_1 = c_2 = \cdots = c_d = d^{-1/2}$, that is

$$|\Psi\rangle = \frac{1}{\sqrt{d}} \left(|00\rangle + |11\rangle + \cdots |dd\rangle\right) \tag{1.43}$$

with $\mathcal{E} = \log_2(d)$.

Both the unit of the entanglement measure (1.41), and states of the form (1.42) have been called ebits [27], since maximally entangled two-qubit states such as (1.42) have $\mathcal{E} = 1$. Furthermore, there is a very physical motivation for this measure [27]. By local operations (unitary transformations and measurements) and classical communication between A and B, n copies of $|\Psi_{AB}\rangle$ can be converted into N standard ebits with the asymptotic ($n \to \infty$) relation $N = n\mathcal{E}(\Psi)$. Conversely, local operations and classical communication can convert N standard ebits into n copies of $|\Psi_{AB}\rangle$ with the same asymptotic ratio. These two procedures define the entanglement of distillation (making ebits from Ψ) and the entanglement of formation (making Ψ from ebits).

The above discussion is for *pure* states, defined as quantum system which are described by a state vector such as (1.42) with certainty. A *mixed* state is a

description for a quantum system which can be in one of several states $|\psi_j\rangle$, each with probability p_j. A mixed state is described by a *density matrix* ρ, of the form

$$\rho = \sum_j p_j |\psi_j\rangle\langle\psi_j|. \tag{1.44}$$

Note that the states $|\psi_j\rangle$ are not necessarily mutually orthogonal, nor are the weights p_j necessarily the eigenvalues of ρ. The form of (1.44) suggests that we compute the entanglement of each pure state $|\psi_j\rangle$ using (1.41), and then perform the average

$$\bar{\mathcal{E}}(p_j, \psi_j) = \sum_j p_j \mathcal{E}(\psi_j). \tag{1.45}$$

For a general density matrix ρ, there are in fact many different decompositions of the form (1.44). For each we can calculate the average entanglement. The *entanglement of formation* for ρ is then defined as the minimal average entanglement, minimizing over all decompositions:

$$\mathcal{E}_F(\rho) = \min_{p_j, \psi_j} \sum_j p_j \mathcal{E}(\psi_j). \tag{1.46}$$

If there is a decomposition of the density matrix such that it can be written as a mixture of product states ($\mathcal{E}(\psi_j) = 0$), then the mixed state has a vanishing entanglement of formation ($\mathcal{E}_F(\rho) = 0$).

Finding the minimal decomposition in (1.46) is difficult, since there is no bound on the number of pure states $|\psi_j\rangle$, which need not be orthogonal or linearly independent. Nevertheless, Wootters [28] derived the exact entanglement of formation for an arbitary two-qubit state. To this end he introduced the *concurrence* C, defined for normalized pure states by

$$C(\psi) = |\langle\psi|Y \otimes Y|\psi^*\rangle|, \tag{1.47}$$

where $|\psi^*\rangle$ is the complex-conjugate of $|\psi\rangle$ in the two-qubit computation basis (in which Y takes its standard Pauli form). Using the Schmidt decomposition (1.38) for two-qubits ($d = 2$), one finds $C(\Psi) = 2c_1\sqrt{1-c_1^2}$. This definition satisfies the two properties required of an entanglement measure: on a product state ($c_1 = 1$) $C(\Psi) = 0$, while on a standard ebit ($c_1 = 1/\sqrt{2}$) $C(\Psi) = 1$. For a general density matrix one defines

$$C(\rho) = \max\{0, \lambda_1 - \lambda_2 - \lambda_3 - \lambda_4\} \tag{1.48}$$

where the λ_k are the square roots of the eigenvalues of the matrix

$$\rho(Y \otimes Y)\rho^*(Y \otimes Y), \tag{1.49}$$

and the entanglement is

$$\mathcal{E}_F(\rho) = -x \log_2 x - (1-x)\log_2(1-x) \tag{1.50}$$

with

$$x = \frac{1}{2}\left(1 + \sqrt{1 - C(\rho)^2}\right). \tag{1.51}$$

Two essential properties regarding the pure state concurrence (1.47) are needed below, and these motivate the introduction of the "magic basis" for two-qubit states. These basis states $|\Phi_k\rangle$ are defined by the rules

$$\begin{array}{rl} |\Phi_1\rangle = & 2^{-1/2}(|00\rangle + |11\rangle), \\ |\Phi_2\rangle = & -i2^{-1/2}(|00\rangle - |11\rangle), \\ |\Phi_3\rangle = & 2^{-1/2}(|01\rangle - |10\rangle), \\ |\Phi_4\rangle = & -i2^{-1/2}(|01\rangle + |10\rangle). \end{array} \tag{1.52}$$

This basis is magic for the following reasons. First, each state is maximally entangled (with $\mathcal{E}(\Phi_k) = C(\Phi_k) = 1$ for all k. Second, each state is a simultaneous eigenstate of $X \otimes X$, $Y \otimes Y$, and $Z \otimes Z$. Furthermore, $Y \otimes Y|\Phi_k^*\rangle = -|\Phi_k\rangle$ for all k. This last

property allows an easy calculation of the concurrence for an arbitrary state when written in the magic basis: for $|\Psi\rangle = \sum_k \mu_k |\Phi_k\rangle$, the concurrence is

$$C(\Psi) = |\sum_k \mu_k^2|. \tag{1.53}$$

Since $|\Psi\rangle$ is normalized, $\sum_k |\mu_k^2| = 1$. Therefore, if $|\Psi\rangle$ is to be maximally entangled with $C(\Psi) = 1$, each coefficient in the sum for the concurrence must add in phase, or $\mu_k^2 = e^{i\alpha}|\mu_k|^2$ for all k. Thus, up to an overall phase, all maximally entangled states, when expressed in the magic basis, have real coefficients. Finally, the magic basis coefficients of a product state satisfy $\sum_k \mu_k^2 = 0$.

1.2 Canonical Decomposition

Having defined the magic basis and the concurrence, we now state the logic of the canonical decomposition theorem. First, in the magic basis one can show that an arbitary unitary operator U has the form:

$$U = \sum_k e^{i\epsilon_k} |\tilde{\Psi}_k\rangle\langle\Psi_k| \tag{1.54}$$

where $|\Psi_k\rangle$ and $|\tilde{\Psi}_k\rangle$ are two (possibly distinct) bases, in which each basis vector is maximally entangled. Second, any maximally entangled basis can be constructed from the standard magic basis by using local unitary operations and phases; that is we can find U_A, U_B, V_A, V_B and phases ζ_k and η_k such that:

$$\begin{array}{ll} |\Psi_k\rangle & = e^{-i\zeta_k} V_A^\dagger \otimes V_B^\dagger |\Phi_k\rangle \\ |\tilde{\Psi}_k\rangle & = e^{i\eta_k} U_A \otimes U_B |\Phi_k\rangle. \end{array} \tag{1.55}$$

Finally, using (1.54) and (1.55), one can write an arbitrary unitary operator as

$$U = (U_A \otimes U_B) U_d (V_A \otimes V_B) \tag{1.56}$$

with

$$U_d = \sum_k e^{i\lambda_k} |\Phi_k\rangle\langle\Phi_k|, \tag{1.57}$$

and $\lambda_k = \epsilon_k + \zeta_k + \eta_k$. Since the $|\Phi_k\rangle$ are simultaneous eigenvectors of $X \otimes X$, $Y \otimes Y$, and $Z \otimes Z$, U_d can be written

$$U_d = e^{i(\alpha_0 I\otimes I + \alpha_x X\otimes X + \alpha_y Y\otimes Y + \alpha_z Z\otimes Z)}, \tag{1.58}$$

with

$$\begin{array}{ll} \alpha_0 & = \lambda_1 + \lambda_2 + \lambda_3 + \lambda_4 \\ \alpha_x & = \frac{1}{4}(\lambda_1 - \lambda_2 - \lambda_3 + \lambda_4) \\ \alpha_y & = \frac{1}{4}(-\lambda_1 + \lambda_2 - \lambda_3 + \lambda_4) \\ \alpha_z & = \frac{1}{4}(\lambda_1 + \lambda_2 - \lambda_3 - \lambda_4). \end{array} \tag{1.59}$$

By absorbing the global phase α_0 into the local unitary operators, we have completed the decomposition (1.36).

We first consider (1.55). Each $|\Psi_k\rangle$ is a maximally entangled state, and as a basis there is the orthogonality condition $\langle\Psi_j|\Psi_k\rangle = \delta_{jk}$. Using these, and the properties of the concurrence one can show [22] that the Schmidt decomposition of each state must be

$$\begin{array}{ll} |\Psi_1\rangle & = e^{i\phi_1} 2^{-1/2}(|a_1\rangle \otimes |b_1\rangle + |a_2\rangle \otimes |b_2\rangle), \\ |\Psi_2\rangle & = e^{i\phi_2} 2^{-1/2}(|a_1\rangle \otimes |b_1\rangle - |a_2\rangle \otimes |b_2\rangle), \\ |\Psi_3\rangle & = e^{i\phi_3} 2^{-1/2}(|a_1\rangle \otimes |b_2\rangle + |a_2\rangle \otimes |b_1\rangle), \\ |\Psi_4\rangle & = e^{i\phi_4} 2^{-1/2}(|a_1\rangle \otimes |b_2\rangle - |a_2\rangle \otimes |b_1\rangle). \end{array} \tag{1.60}$$

In (1.60), the Schmidt basis vectors $|a_j\rangle$ and $|b_j\rangle$ are arbitrary, but normalized such that $\langle a_j|a_k\rangle = \langle b_j|b_k\rangle = \delta_{jk}$. We present a simple argument why this must be the case. Up to global phases, to specify a two-qubit basis one must use 14 real numbers. These consist of 6 parameters for each state (see (1.31)), minus 6 for orthogonality and 4 for the entanglement relations, or $4 \times 6 - 6 - 4 = 14$. Similarly, if we remove the global phases in (1.60) there are 3 parameters for each Schmidt vector, plus 2

for the relative phases in the superpositions (in $|\Psi_1\rangle$ and $|\Psi_3\rangle$, for example); thus $4 \times 3 + 2 = 14$. Up to a simple relabelling of the states, the set given in (1.60) is the only solution. Now, forming the unitary operators

$$\begin{array}{ll} V_A & = |0\rangle\langle a_1| + |1\rangle\langle a_2| \\ V_B & = |0\rangle\langle b_1| + |1\rangle\langle b_2| \end{array} \tag{1.61}$$

and using (1.60), we see that (1.55) is indeed correct.

We now prove (1.54). Let the symbol T denote the operation of taking the transpose (of matrix elements) with respect to the magic basis. Then define the symmetric unitary operators $W_1 = U^T U$ and $W_2 = U U^T$. Since these operators are symmetric, their eigenvectors are orthogonal and can be chosen to have real coefficients. Let the eigenvectors of W_1 be $|\Psi_k\rangle$ and those of W_2 be $|\tilde{\Psi}_k\rangle$. By the first property of the concurrence, these vectors both form a maximally entangled basis. In terms of these, we have:

$$\begin{array}{ll} W_1 & = \sum_k e^{-i2\epsilon_k} |\Psi_k\rangle\langle\Psi_k|, \\ W_2 & = \sum_k e^{-i2\epsilon_k} |\tilde{\Psi}_k\rangle\langle\tilde{\Psi}_k|. \end{array} \tag{1.62}$$

Note that the eigenvalues of W_1 and W_2 are both $e^{-i2\epsilon_k}$ since they are related by the unitary transformation $W_2 = U W_1 U^\dagger$. Their eigenvectors must also be related: $|\tilde{\Psi}_k\rangle = e^{-i\delta_k} U |\Psi_k\rangle$, where the phase is as yet undetermined. Altogether, we can write U in the form:

$$U = \sum_k e^{-i\delta_k} |\tilde{\Psi}_k\rangle\langle\Psi_k|. \tag{1.63}$$

Since the coefficients of both $|\Psi_k\rangle$ and $|\tilde{\Psi}_k\rangle$ are real in the magic basis we have $(|\tilde{\Psi}_k\rangle\langle\Psi_k|)^T = |\Psi_k\rangle\langle\tilde{\Psi}_k|)$. Then, by forming W_1, we find that $\delta_k = \epsilon_k$, proving (1.54).

Using the canonical decomposition, there is a large body of work showing how to simplify quantum logic gate construction. The controlled-NOT gate U_{CNOT} can be exactly generated by repeated application of an arbitrary entangling two-qubit gate U and single-qubit gates [29]. Similar constructions exist to construct an arbitrary gate using single-qubit gates and U [30, 31], or a two-qubit Hamiltonian [25] in optimal time [32, 33, 34, 35]. Finally, it has recently been shown that it takes at most 3 applications of U_{CNOT}, with single-qubit gates, to generate an arbitrary two-qubit gate U [36].

These simplifications arise due to the assumption that single-qubit operations are easy. The key aspect is therefore the nonlocal part of U, namely U_d in

$$U = (U_A \otimes U_B)\, U_d\, (V_A \otimes V_B) \tag{1.64}$$

which has the form

$$U_d = \exp\left(i(\alpha_x X \otimes X + \alpha_y Y \otimes Y + \alpha_z Z \otimes Z)\right). \tag{1.65}$$

Since each of the terms in the exponent of U_d commute with each other, repeated applications of the gate will evolve $\alpha_x, \alpha_y, \alpha_z$. Similarly, by simple single-qubit logical gates one can permute these parameters, or reverse their sign. Using these elements one can ensure that $\alpha_x, \alpha_y, \alpha_z$ approach the appropriate target parameters. Finally, the gate construction can be completed by applying any additional single-qubit gates.

Some examples of the decomposition are the following. For U_{CNOT} we have

$$U_{\mathrm{CNOT}} = e^{i\pi/4}(I \otimes U_H) \exp\left(i\frac{\pi}{4} Z \otimes Z\right) (R_z(\pi/2) \otimes R_z(\pi/2) U_H) \tag{1.66}$$

where we have defined $R_z(\phi) = \exp(-i\phi Z/2)$. We also have

$$U_{\text{SWAP}} = e^{-i\pi/4} \exp\left(i\frac{\pi}{4}(X \otimes X + Y \otimes Y + Z \otimes Z)\right). \tag{1.67}$$

Finally, we will construct the following two quantum logic gates that are relevant for coupled superconducting phase qubits described in Chapter 6 [37]: a controlled-phase gate

$$U_1(\phi) = \begin{pmatrix} 1 & 0 & 0 & 0 \\ 0 & 1 & 0 & 0 \\ 0 & 0 & 1 & 0 \\ 0 & 0 & 0 & e^{-i\phi} \end{pmatrix}, \tag{1.68}$$

and a swap-like gate

$$U_2(\theta_1, \theta_2) = \begin{pmatrix} 1 & 0 & 0 & 0 \\ 0 & \cos\theta_1 & -i\sin\theta_1 & 0 \\ 0 & -i\sin\theta_1 & \cos\theta_1 & 0 \\ 0 & 0 & 0 & e^{-i\theta_2} \end{pmatrix}. \tag{1.69}$$

Their decompositions are

$$U_1(\phi) = e^{-i\phi/4}(R_z(-\phi/2) \otimes R_z(-\phi/2)) \exp\left(-i\frac{\phi}{4} Z \otimes Z\right), \tag{1.70}$$

and

$$\begin{aligned} U_2(\theta_1, \theta_2) = \; & e^{-i\theta_2/4}(R_z(-\theta_2/2) \otimes R_z(-\theta_2/2)) \\ & \times \exp\left(-i\tfrac{1}{4}(2\theta_1 X \otimes X + 2\theta_1 Y \otimes Y + \theta_2 Z \otimes Z)\right). \end{aligned} \tag{1.71}$$

1.3 Quantum Simulation

Feynman's original work [1] on quantum computers was titled "Simulating Physics with Computers". From a physics perspective, quantum computers, if built, will be perhaps most useful for simulating other quantum mechanical systems. Therefore, much theoretical effort has been focused on precisely how one quantum system can simulate the dynamics of another.

The concept of *simulation* often has the unfortunate connotation of being inferior to some real physical experiment. It is, of course, tempting to argue that any physical quantum computer is actually a quantum simulator, simulating the dynamics of an ideal quantum computer. In this view, there are only quantum simulators.

The true goal of this section (and thesis) is not to merely simulate some particular system, but to understand how to *control* the dynamics of some system such that it can simulate the dynamics of another arbitrary system. This concept of control is very important. In fact, many of the considerations of this section have been studied as control techniques in nuclear magnetic resonance (NMR) spectroscopy [38]. Quantum control theory is at the heart of quantum computation and quantum simulation [39].

A key result of quantum simulation, given by Lloyd [40], is remarkably similar to the quantum logic gate universality proof given above (1.33)-(1.35). Suppose we are given the task of simulating an arbitrary N-body Hamiltonian H with two-body interactions, using a quantum computer. We can write H in either of the forms

$$H = \sum_k H_k + \sum_{j<k} H_{jk} = \sum_K \tilde{H}_K \tag{1.72}$$

where H_k acts on system k, and H_{jk} is the interaction between systems j and k; the final sum is over all one and two-body interactions $\tilde{H}_K$. Can such a general H be simulated on our quantum computer efficiently?

The affirmative answer can be found by using a generalization of (1.34):

$$e^{-iH\tau} = \prod_K e^{-i\tilde{H}_K\tau} + \sum_{K>J} [H_K, H_J]\tau^2/2 + O(\tau^3). \tag{1.73}$$

This splitting formula shows that, if we have the ability to simulate each interaction H_K, by simulating each one in sequence, we can build up the full simulation of the many-body Hamiltonian H. While such simulation is not exact, the error terms can be made sufficiently small for small enough τ. If each term in the product can be simulated efficiently, then the entire Hamiltonian can be simulated efficiently.

We now recount Lloyd's analysis [40]. Each individual system can be described by a discrete d-dimensional system, which can be encoded by $n_q = \log_2 d$ qubits. For each such system the simulation of its internal Hamiltonian H_k requires using approximately d^2 fundamental operations, while the interaction terms H_{jk} may require d^4 operations. The accuracy of the algorithm is determined by the number of systems and size of the chosen time-step τ. For a total time $T = n\tau$, the total error is of order $E \sim L^2T^2/n$, and the total number of operations is $N_{op} \sim nLd^2$ for the single-system terms H_k, or at most $N_{op} \sim nLd^4$ for the interaction terms H_{jk}. For each, n is the number of timesteps and L is the number of terms in the Hamiltonian. Note that for long-range interactions, $L \sim N^2$, while for local interactions (such as nearest-neighbor), $L \sim N$. Observe that all of these simulation parameters are polynomial in the number of elements N. By encoding the system in a set of qubits, we can efficiently simulate the evolution of any wavefunction using H.

In contrast, on a classical computer, the wavefunction alone requires the storage of d^N numbers, which is exponential in N. Even the simple multiplication of one term of H runs exponentially slower on a classical computer [41].

Lloyd's analysis shows that we can simulate H by breaking it into the simpler terms H_K, each of which can be efficiently implemented using quantum logic gates.

Other studies have followed this pattern [42, 43]. A more challenging question is to assume that we have access to some many-body Hamiltonian H itself, plus some restricted local operators (such as single-qubit gates). What types of Hamiltonians can this set of interactions simulate, and can these simulations be done efficiently?

The solution to this inverse problem is much more difficult. While building up H from simple elements was possible using the splitting formula, it is not so clear how to start from H and end up with simpler elements. This problem has been studied in many interesting cases, and is a topic of continuing research. We will summarize the work of Nielsen and co-workers [44, 45, 46, 47]; a complete set of references can be found therein.

The key result of [45] for qudits (d-level quantum systems) is this: "Let H be a given two-body entangling Hamiltonian on N qudits, and let K be a desired two-body Hamiltonian on N qudits. Then we have an efficient algorithm to simulate evolution due to K using only (a) the ability to evolve according to H, and (b) the ability to perform local unitaries (that is, single-qudit unitaries) on the individual qudits."

The simulation algorithm begins with the fundamental interactions, and uses a series of *composition laws* to enlarge the group of accessible Hamiltonians, which will ultimately include all possible two-body Hamiltonians, including the desired Hamiltonian K. The composition rules are the following.

I. Scaling. If we can simulate Hamiltonian A, then by proper timing we can simulate $B = \lambda A$ for any λ. This follows by setting $t_A = \lambda t_B$ such that $e^{-it_A A} = e^{-it_B B}$.

II. Splitting. If we can simulate A and B, then by using a splitting formula we can simulate $A+B$. This approximate simulation uses the second order splitting

$$e^{-i\tau A/2}e^{-i\tau B}e^{-i\tau A/2} \simeq e^{-i\tau(A+B)-i\tau^3 C}, \tag{1.74}$$

where the correction term C can be calculated using the Baker-Campbell-Haussdorf theorem (1.8)-(1.9). Later in this Chapter we will prove that for higher-order schemes we must include $-A$ and $-B$.

III. Commutating. If we can simulate A, $-A$, B, $-B$, then we can simulate $C = -i[A, B]$. This is due to the formula

$$e^{-i\tau A}e^{-i\tau B}e^{i\tau A}e^{i\tau B} \simeq e^{-\tau^2[A,B]}. \tag{1.75}$$

IV. Conjugating. If we can simulate A, and implement the gates U and $U^\dagger$, then we can simulate the conjugated Hamiltonian $UAU^\dagger$, which follows from the exact relation

$$U\exp(-i\tau A)U^\dagger = \exp(-i\tau UAU^\dagger). \tag{1.76}$$

V. Symmetrizing. If we can implement a group of unitaries $\mathcal{G} = \{g_1, \ldots, g_N\}$ and simulate A, then we can simulate the symmetrized Hamiltonian

$$\bar{A} = \frac{1}{N}\sum_{j=1}^{N} g_j^\dagger A g_j, \tag{1.77}$$

where N is the order of the group $N = |\mathcal{G}|$. This follows by from the (simple) splitting property (II)

$$e^{-i\tau\bar{A}} \simeq \prod_{j=1}^{N} g_j^\dagger e^{-i\tau A} g_j \tag{1.78}$$

and conjugation (IV). This important operation, introduced independently by Viola, Knill and Lloyd [48, 49] and Zanardi [50] allows one to decouple all terms in A which do not commute with the group $\mathcal{G}$: after symmetrizing we have $[\bar{A}, g_k] = 0$ for all k.

As a particular example, consider the two-qubit Hamilonian

$$H = Z \otimes I + 2X \otimes Z + Z \otimes Z. \tag{1.79}$$

We can eliminate the coupling terms by averaging over the Pauli group of the second qubit, with

$$\mathcal{G}_1 = \{g_1 = I \otimes I, g_2 = I \otimes X, g_3 = I \otimes Y, g_4 = I \otimes Z\}. \tag{1.80}$$

We find

$$\frac{1}{4}\left(g_1^\dagger H g_1 + g_2^\dagger H g_2 + g_2^\dagger H g_2 + g_2^\dagger H g_2\right) = Z \otimes I, \tag{1.81}$$

where we have used $XZX = YZY = -Z$. If instead, we use the full Pauli group

$$\begin{aligned} \mathcal{G}_2 = \; & \{g_1 = I \otimes I, g_2 = I \otimes X, g_3 = I \otimes Y, g_4 = I \otimes Z \\ & g_5 = X \otimes I, g_6 = X \otimes X, g_7 = X \otimes Y, g_8 = X \otimes Z \\ & g_9 = Y \otimes I, g_{10} = Y \otimes X, g_{11} = Y \otimes Y, g_{12} = Y \otimes Z \\ & g_{13} = Z \otimes I, g_{14} = Z \otimes X, g_{15} = Z \otimes Y, g_{16} = Z \otimes Z\} \end{aligned} \tag{1.82}$$

in (1.77) we find

$$\bar{H} = \frac{1}{16}\sum_{j=1}^{16} g_j^\dagger H g_j = 0. \tag{1.83}$$

Finally, by extracting the $j = 1$ term in (1.83), we have the decomposition

$$\frac{1}{16}\sum_{j=2}^{16} g_j^\dagger H g_j = -H. \tag{1.84}$$

Thus, by symmetrization over the local unitary operators in $\mathcal{G}_2$, we can exactly eliminate all of the dynamics of H, or even simulate $-H$. Note that while we have explored a particular example, these constructions can be readily extended to arbitrary n-qudit Hamiltonians [45].

By application of the composition laws I-V, any Hamiltonian can be simulated. The algorithm presented in [45] systematically isolates a particular term in the two-qudit Hamiltonian H. This term can then be used, by the same composition laws, to construct the desired two-qudit K. Thus, it is the simple ability of H to entangle qudits, and not the particular form of H, that allows universal quantum simulation.

Note that composition law V allows us to simulate $-A$ and $-B$, which are needed for commutation (law III), from A, B and local unitaries. This simulation uses the second-order splitting formula (1.74). We will explore higher-order algorithms later in this Chapter, and find that the need to simulate $-A$ reappears. We will show that *higher-order* quantum simulation will generally require additional resources.

1.4 Symplectic Integration

Symplectic integration was introduced by Ruth in 1983 [51], initially in the guise of sequential canonical transformations. That the underlying technique was quite general for all Lie algebras was first observed by Neri [52]. In this section we describe symplectic integration. We will see how its results are in fact closely related to universal quantum simulation.

The central goal of symplectic integration is to approximate the symplectic map

$$\exp(-\epsilon : H_0 :) = \exp(-\epsilon : (T + V) :) \tag{1.85}$$

by the factorized from

$$\prod_{i=1}^{N} \exp(-t_i \epsilon : T :) \exp(-v_i \epsilon : V :), \tag{1.86}$$

where the coefficients t_i and v_i are chosen to make the resulting symplectic map approximate $\exp(-\epsilon : H_0 :)$ as closely as possible. We have assumed that H_0 can be written as the sum of kinetic energy $T(p)$ which is a function of the momentum, and the potential energy $V(q)$ which is a function of the position. If this is true, the product form of (1.86) is desirable since each term is both a symplectic map and easy to evaluate:

$$\begin{array}{lll} \exp(-\epsilon : T :)q & = (1 - \epsilon : T : + \cdots)q & = q + \epsilon \frac{dT}{dp}, \\ \exp(-\epsilon : T :)p & = (1 - \epsilon : T : + \cdots)p & = p, \\ \exp(-\epsilon : V :)q & = (1 - \epsilon : V : + \cdots)q & = q, \\ \exp(-\epsilon : V :)p & = (1 - \epsilon : V : + \cdots)p & = p - \epsilon \frac{dV}{dq}. \end{array} \tag{1.87}$$

That the product (1.86) can be used to approximate (1.85) follows from the Baker-Campbell-Haussdorf theorem, which implies

$$\prod_{i=1}^{N} \exp(-t_i \epsilon T) \exp(-v_i \epsilon V) = \exp(-\epsilon H(\epsilon)) \tag{1.88}$$

where we have simplified the notation by replacing $: T :$ by T, $: V :$ by V, and where $H(\epsilon)$ is defined by

$$H(\epsilon) = h_T T + h_V V + \epsilon \left(h_{TV}[TV]\right) + \epsilon^2 \left(h_{TTV}[TTV] + h_{VVT}[VVT]\right) + \cdots \tag{1.89}$$

and the higher-order terms are all repeated commutators of T and V. By choosing the coefficients t_i and v_i appropriately, one arranges to have $h_T = h_V = 1$, and the remaining error terms equal to 0, up to some order in ϵ. We call a factorization an n-th order scheme if the the first error term in $H(\epsilon)$ occurs at ϵ^n. A classic example

is the second-order factorization

$$S_2(\epsilon) = e^{-\epsilon V/2} e^{-\epsilon T} e^{-\epsilon V/2} = e^{-\epsilon H_2(\epsilon)} \tag{1.90}$$

where $H_2(\epsilon)$ is

$$H_2(\epsilon) = T + V + \epsilon^2 \left(\frac{1}{12}[TTV] - \frac{1}{24}[VVT] \right) + \cdots \tag{1.91}$$

1.4.1 Higher-Order Symplectic Integration

There are general methods to generate higher-order factorizations. The most direct method [52] is to derive and hopefully solve the order conditions that arise from the BCH expansion (1.89). In this method, the algebraic difficulties quickly grow as the order n of the integrator increases [53]. Another, more subtle, method is to symmetrize a lower-order integrator, as proposed by Yoshida [54] and Suzuki [55]. Suppose we have an n-th order factorization

$$S_n(\epsilon) = \exp(-\epsilon H_0 - \epsilon^{n+1} H_n). \tag{1.92}$$

Then consider the symmetrized factorization

$$\bar{S}(\epsilon) = S_n(a\epsilon) S_n((1-2a)\epsilon) S_n(a\epsilon). \tag{1.93}$$

Using the Baker-Campbell-Haussdorf formula, we find

$$\bar{S}(\epsilon) = \exp\left(-\epsilon H_0 - \epsilon^{n+1} \left(2a^{n+1} + (1-2a)^{n+1} \right) H_n + O(\epsilon^{n+3}) \right). \tag{1.94}$$

If a satisifies

$$2a^{n+1} + (1-2a)^{n+1} = 0 \tag{1.95}$$

then $\bar{S}$ will be an integrator of order $n+2$. Equation (1.95) can be satisfied if n is an even integer, in which case

$$a = a_n = \frac{1}{2 - 2^{1/(n+1)}}, \tag{1.96}$$

a result first found by Creutz and Gocksch [56]. A somewhat more complicated construction was proposed by Suzuki

$$S_{n+2}(\epsilon) = S_n(b\epsilon)S_n(b\epsilon)S_n((1-4b)\epsilon)S_n(b\epsilon)S_n(b\epsilon), \tag{1.97}$$

with

$$b = b_n = \frac{1}{4 - 4^{1/(n+1)}}. \tag{1.98}$$

Applying (1.95) and (1.96) to the second-order integrator (1.90) leads to the fourth-order integrator found by Forest and Ruth [57]

$$S_{\mathrm{FR}}(\epsilon) = e^{-a\epsilon V/2}e^{-a\epsilon T}e^{-(1-a)\epsilon V/2}e^{-(1-2a)\epsilon T}e^{-(1-a)\epsilon V/2}e^{-a\epsilon T}e^{-a\epsilon V/2} \tag{1.99}$$

with $a = (2 - 2^{1/3})^{-1}$.

1.4.2 Sheng-Suzuki Theorem

Both of the symmetrized constructions (1.93) and (1.97) require *negative* timesteps, since we have $1 - 2a_n < 1 - 4b_n < 0$. This is a general consequence of the form

$$\prod_{i=1}^{N} \exp(-t_i\epsilon T)\exp(-v_i\epsilon V). \tag{1.100}$$

Sheng [58] and Suzuki [59] proved the important result that there is no integrator above second order which is of this form with purely positive coefficients: $t_i > 0$

and $v_i > 0$ for all i. To prove this, we follow the method of Chin [60], which is more direct than Suzuki's geometric arguments. The Taylor expansion of (1.100) is

$$\begin{array}{l} 1 + c_T\epsilon T + c_V\epsilon V + c_{TT}\epsilon^2 T^2 + c_{TV}\epsilon^2 TV + c_{VT}\epsilon^2 VT + c_{VV}\epsilon^2 V^2 \\ +c_{TTT}\epsilon^3 T^3 + c_{TTV}\epsilon^3 T^2 V + c_{TVT}\epsilon^3 TVT + c_{TVV}\epsilon^3 TV^2 + c_{VTT}\epsilon^3 VT^2 \\ +c_{VTV}\epsilon^3 VTV + c_{VVT}\epsilon^3 V^2 T + c_{VVV}\epsilon^3 V^3 + \cdots \end{array} \tag{1.101}$$

where the coefficients, polynomials in t_i and v_i, can be found by direct expansion. A few of these are

$$\begin{array}{r} c_T = \sum_{i=1}^N t_i \\ c_V = \sum_{i=1}^N v_i \\ c_{TV} = \sum_{i=1,j=i}^N t_i v_j \\ c_{TTV} = \sum_{i=1,j=i,k=j}^N (1-\delta_{ij}/2) t_i t_j v_k \\ c_{TVV} = \sum_{i=1,j=i,k=j}^N (1-\delta_{jk}/2) t_i v_j v_k. \end{array} \tag{1.102}$$

These coefficients are related to the error coefficents of the symplectic map $\exp(-\epsilon H(\epsilon))$. Performing a Taylor expansion of the exponential, using (1.89) and comparing with (1.101) we find that

$$\begin{array}{l} c_T = h_T, \\ c_V = h_V, \\ c_{TV} = h_{TV} + \frac{1}{2} h_T h_V, \\ c_{TTV} = h_{TTV} + \frac{1}{2} h_T h_{TV} + \frac{1}{6} h_T^2 h_V, \\ c_{TVV} = h_{VVT} + \frac{1}{2} h_V h_{TV} + \frac{1}{6} h_T h_V^2. \end{array} \tag{1.103}$$

If the integrator of (1.100) is third-order or higher, we must have

$$h_T = h_V = 1,\ h_{TV} = h_{TTV} = h_{VVT} = 0. \tag{1.104}$$

We first observe that the expression for c_{TTV} can be rewritten by reordering the sums, yielding

$$c_{TTV} = \frac{1}{2} \sum_{k=1}^N v_k \left(\sum_{j=1}^k t_j \right)^2 \tag{1.105}$$

and similarly for c_{TVV}

$$c_{TVV} = \frac{1}{2} \sum_{i=1}^N t_i \left(\sum_{j=i}^N v_j \right)^2 . \tag{1.106}$$

Defining the variables

$$s_i = \sum_{j=1}^{i} t_j, \quad u_i = \sum_{j=i}^{N} v_j, \tag{1.107}$$

we observe that $t_i = s_i - s_{i-1}$, $s_0 = 0$, $s_N = e_T = 1$ and $v_i = u_i - u_{i+1}$, $u_1 = e_V = 1$, $u_{N+1} = 0$. Using definitions (1.107) in (1.102), (1.105), (1.106) and subsitituting these and (1.104) into (1.103), we find that

$$\sum_{i=1}^{N} (s_i - s_{i-1}) u_i = \frac{1}{2}, \tag{1.108}$$

$$\frac{1}{2} \sum_{i=1}^{N} u_i (s_i^2 - s_{i-1}^2) = \frac{1}{6}, \tag{1.109}$$

$$\frac{1}{2} \sum_{i-1}^{N} (s_i - s_{i-1}) u_i^2 = \frac{1}{6}. \tag{1.110}$$

If all $t_i = s_i - s_{i-1} > 0$, then (1.110) is a positive-definite quadratic form in the variables u_i. If we minimize this subject to (1.108)-(1.109) as constraints, and it is greater than 1/6, then we will have proven that (1.104) cannot hold with $t_i > 0$.

To do so we form the functional

$$F(u_i, s_i, \lambda_1, \lambda_2) = \frac{1}{2} \sum_{i=1}^{N} (s_i - s_{i-1}) u_i^2 - \lambda_1 \left(\sum_{i=1}^{N} (s_i - s_{i-1}) u_i - \frac{1}{2} \right) - \lambda_2 \left(\sum_{i=1}^{N} u_i (s_i^2 - s_{i-1}^2) - \frac{1}{3} \right), \tag{1.111}$$

where λ_1 and λ_2 are Lagrange multipliers used to ensure the constraints (1.108)-(1.109), through $\partial F / \partial \lambda_1 = 0$ and $\partial F / \partial \lambda_2 = 0$. Taking the variation of F with respect to u_k yields

$$\frac{\partial F}{\partial u_k} = (s_k - s_{k-1}) \left(u_k - \lambda_1 - \lambda_2 (s_k + s_{k-1}) \right) = 0 \tag{1.112}$$

with the solution

$$u_k = \lambda_1 + \lambda_2 (s_k + s_{k-1}). \tag{1.113}$$

Substituting (1.113) into the first constraint (1.108) yields

$$\lambda_1 + \lambda_2 \sum_{i=1}^{N} (s_i^2 - s_{i-1}^2) = \lambda_1 + \lambda_2 = \frac{1}{2}, \tag{1.114}$$

where we have used the relation $\sum_{i=1}^{N}(s_i^2 - s_{i-1}^2) = s_N^2 = 1$. The second constraint (1.109) yields

$$\lambda_1 + \lambda_2 \sum_{i=1}^{N} (s_i^2 - s_{i-1}^2)(s_i + s_{i-1}) = \frac{1}{3} \tag{1.115}$$

which we simplify by defining

$$g = \sum_{i=1}^{N} (s_i^2 s_{i-1} - s_i s_{i-1}^2) \tag{1.116}$$

in terms of which (1.115) becomes

$$\lambda_1 + \lambda_2 + g\lambda_2 = \frac{1}{3}. \tag{1.117}$$

Substituting (1.114) in (1.117) we find $g\lambda_2 = -1/6$. Finally, if we substitute (1.113) in (1.111), with both constraints set to zero we find

$$\begin{aligned} F = \frac{1}{2} \sum_{i=1}^{N} (s_i - s_{i-1})(\lambda_1 + \lambda_2(s_i + s_{i-1}))^2 &= \frac{1}{2}(\lambda_1^2 + 2\lambda_1\lambda_2 + \lambda_2^2(1+g)) \\ = \frac{1}{2}((\lambda_1 + \lambda_2)^2 + g\lambda_2^2) = \frac{1}{2}\left(\frac{1}{4} + \frac{1}{36}g^{-1}\right) &= \frac{1}{8} + \frac{1}{72}g^{-1}. \end{aligned} \tag{1.118}$$

Thus, the minimum of F is the maximum of g. To find this maximum we use (1.116) to calculate

$$\frac{\partial g}{\partial s_k} = (s_{k+1} - s_{k-1})(s_{k+1} + s_{k-1} - 2s_k) = 0 \tag{1.119}$$

which yields

$$s_k = (s_{k+1} + s_{k-1})/2 = k/N \tag{1.120}$$

where we have used the normalization $s_N = 1$.

Finally, substituting (1.120) into g (1.116) we find

$$g = \frac{1}{N^3}\sum_{i=1}^{N} k(k-1) = \frac{1}{3}(1 - N^{-2}), \tag{1.121}$$

with $\sum_{k=0}^{N} k = N(N+1)/2$ and $\sum_{k=0}^{N} k^2 = N(N+1)(2N+1)/6$. That (1.121) is a maximum can be shown by using (1.120) in the second derivatives

$$\frac{\partial^2 g}{\partial s_j \partial s_k} = \frac{2}{N}(\delta_{j,k+1} + \delta_{j,k-1} - 2\delta_{j,k}). \tag{1.122}$$

The eigenvalues of $G = \partial^2 g/\partial s_j \partial s_k$, as a matrix operator (using periodic boundary conditions), are

$$G_n = -\frac{8}{N}\sin^2(\pi n/N) \tag{1.123}$$

$(1 \leq n \leq N)$, and always negative. Thus, (1.121) truly is the maximum of g, and by (1.118) the minimum of F is

$$F_{min} = \frac{1}{8} + \frac{1}{72}g^{-1} = \frac{1}{6} + \frac{1}{24}\frac{N^{-2}}{1 - N^{-2}} > \frac{1}{6}. \tag{1.124}$$

This proves that for any finite N there is no factorization of the form (1.100) that satisfies (1.104) and has $t_i > 0$. This is the Sheng-Suzuki theorem.

1.4.3 Extended Symplectic Integration

Recently, Suzuki [61] and Chin [62] have proposed a new factorization scheme

$$\prod_{i=1}^{N} \exp(-t_i \epsilon T) \exp(-v_i \epsilon \tilde{V}) \tag{1.125}$$

where $\tilde{V}$ is the modified potential

$$\tilde{V} = V + c\epsilon^2 [VVT]. \tag{1.126}$$

For quadratic kinetic energies with the matrix form $T = \frac{1}{2}p^T M^{-1} p$ this next (classical) commutator is solely a function of q

$$[VVT] = \{V, \{V, T\}\} = \left(\frac{\partial V}{\partial q}\right)^T M^{-1} \left(\frac{\partial V}{\partial q}\right). \tag{1.127}$$

This extension of the original symplectic integration scheme is not restricted by the Sheng-Suzuki theorem. Namely, there exist fourth-order factorizations of the form (1.125) with coefficients $t_i > 0$. One example [63] is

$$S_{4\mathrm{A}}(\epsilon) = e^{-\epsilon V/6} e^{-\epsilon T/2} e^{-2\epsilon \tilde{V}/3} e^{-\epsilon T/2} e^{-\epsilon V/6} \tag{1.128}$$

with $\tilde{V}$ given by (1.126) with $c = -1/48$. Surprisingly, when this scheme is iterated to higher orders [64, 65] negative time-steps reappear; this seems to be unavoidable [66]. Thus, above fourth-order there is no known symplectic algorithm with purely positive coefficients.

1.4.4 Wave-packet Propagation

The symplectic integrators given above can be directly applied to quantum mechanical problems by letting $\epsilon = i\tau$. The kinetic energy operator is then diagonal in momentum space and the potential energy operator is diagonal in position space. Implementing these operators between alternating Fast Fourier Transforms (FFTs) constitutes a convenient "split-operator" scheme for propagating wavepackets [67]. A clear discussion of this method can be found in [68]. While there are many other propagation schemes of similar accuracy [69] the split-operator scheme is particularly useful with time-dependent potentials [68, 70]. Associating a time-shift operator $p_t = -i\partial/\partial t$ with each kinetic energy term takes care of the correct sequencing

of the potential energy operators. For the second-order method this yields

$$S_2(t+\tau,t) = e^{-i\tau V(t+\tau)/2} e^{-i\tau T} e^{-i\tau V(t)/2}, \tag{1.129}$$

while for the Forest-Ruth propagator we have

$$\begin{aligned} S_{\mathrm{FR}}(t+\tau,t) = {} & e^{-ia\tau V(t+\tau)/2} e^{-ia\epsilon T} e^{-i(1-a)\tau V(t+\tau-a\tau)/2} e^{-i(1-2a)\tau T} \\ & \times e^{-i(1-a)\tau V(t+a\tau)/2} e^{-a\epsilon T} e^{-ia\tau V(t)/2} \end{aligned} \tag{1.130}$$

with $a = (2-2^{1/3})^{-1}$. Finally, Chin's algorithm 4A gives

$$S_{4\mathrm{A}}(t+\tau,t) = e^{-i\tau V(t+\tau)/6} e^{-i\tau T/2} e^{-i2\tau \tilde{V}(t+\tau/2)/3} e^{-i\tau T/2} e^{-i\tau V(t)/6}. \tag{1.131}$$

1.5 Higher-Order Quantum Simulation

Recall that the general two-qudit simulation used the second-order splitting formula (1.74). We now consider higher-order versions, the Forest-Ruth propagator

$$\begin{aligned} e^{-i\tau(H_1+H_2)} \simeq {} & e^{-ia\tau H_1/2} e^{-ia\tau H_2} e^{-i\tau(1-a)H_1} \\ & \times e^{-i\tau(1-2a)H_2} e^{-i\tau(1-a)H_1} e^{-ia\tau H_2} e^{-ia\tau H_1/2} \end{aligned} \tag{1.132}$$

with $a = (2-2^{1/3})^{-1}$, and Chin's propagator 4A

$$e^{-i\tau(H_1+H_2)} \simeq e^{-i\tau H_1/6} e^{-i\tau H_2/2} e^{-i\tau 2\tilde{H}_1/3} e^{-i\tau H_2/2} e^{-i\tau H_1/6} \tag{1.133}$$

with

$$\tilde{H}_1 = H_1 + \frac{1}{48}\tau^2 [H_1,[H_1,H_2]]. \tag{1.134}$$

The use of the Forest-Ruth propagator requires us to be able to simulate *both* H_1 and $-H_1$, since $(1-2a) < 0$. One might be tempted to recall that symmetrization (composition law V) allowed us to simulate $-H_1$. However, the symmetrization

procedure itself *assumed* a splitting formula. Thus, by the Sheng-Suzuki theorem there is no general uniform higher-order quantum simulation algorithm when $-H_1$ is not directly available. For certain interactions, however, the dynamics can be reversed without using the full symmetrization procedure. The Ising interaction $Z \otimes Z$ is an example, since

$$(I \otimes X)(Z \otimes Z)(I \otimes X) = -Z \otimes Z. \tag{1.135}$$

Thus, while there is no general algorithm, interesting higher-order implementations exist.

To use Chin's propagator requires we must be able to simulate the commutator

$$[H_1, [H_1, H_2]]. \tag{1.136}$$

This simulation need only be to low order in τ, since the commutator is multiplied by τ^2 in (1.134). Note that a direct use of the generalized commutator formula requires negative timesteps, and thus the ability to simulate $-H_1$. As this cannot be done in general, we must look more carefully at the structure of H_1. For certain interactions we may be able to simulate the commutator directly.

We consider the example studied by Dodd *et al.* [44], where the given two-qubit Hamiltonian is

$$H_1 = Z \otimes I + 2X \otimes Z + Z \otimes Z, \tag{1.137}$$

and we wish to simulate

$$K = X \otimes Z. \tag{1.138}$$

Simulating K for time $t_K = \pi/4$ will generate a gate equivalent to U_{CNOT}. Note

that by conjugating H_1 with $X \otimes I$, we get

$$H_2 = -Z \otimes I + 2X \otimes Z - Z \otimes Z \tag{1.139}$$

and thus

$$K = \frac{1}{4}(H_1 + H_2). \tag{1.140}$$

We can directly simulate H_1 and H_2, and thus we can use the second-order algorithm to simulate K. Calculating the commutator we find

$$\begin{aligned}[H_1, [H_1, H_2]] &= -32Z \otimes I - 32Z \otimes Z + 32X \otimes Z + 32X \otimes I \\ &= 8(H_1 + H_2) + 8(R \otimes I)(H_1 + H_2)(R^\dagger \otimes I) - 32Z \otimes I + 32X \otimes I,\end{aligned} \tag{1.141}$$

where $R = 2^{-1/2}(I + iY)$. As this is a sum of accessible Hamiltonians, we can simulate the commutator using the first-order splitting $e^{-i\tau^3 A}e^{-i\tau^3 B}$. The resulting error will be of order τ^6, which can be neglected.

Using the Baker-Campbell-Haussdorf formula (1.8)-(1.9), and symbolic calculations using Mathematica, we can calculate the error terms of the second and fourth-order factorizations. We define the total propagators by

$$e^{-i\tau(H_1+H_2)-i\tau^{n+1}C_n}. \tag{1.142}$$

For the second-order factorization we find

$$C_2 = \frac{1}{24}[H_1H_1H_2] - \frac{1}{12}[H_2H_2H_1]. \tag{1.143}$$

For the Forest-Ruth propagator (with $n = 4$) we find

$$\begin{aligned}C_{\mathrm{FR}} = \; & a_1[H_1H_1H_1H_1H_2] + a_2[H_2H_2H_2H_2H_1] + a_3[H_1H_2H_2H_2H_1] \\ & + a_4[H_2H_1H_1H_1H_2] + a_5[H_1H_1H_2H_2H_1] + a_6[H_2H_2H_1H_1H_2]\end{aligned} \tag{1.144}$$

where the coefficients are

$$\begin{aligned} a_1 &= \tfrac{1}{960}(21 - 42^{1/3} - 92^{2/3})(-2 + 2^{1/3})^{-5}, \\ a_2 &= \tfrac{1}{120}(7 - 172^{1/3} + 102^{1/3})(-2 + 2^{1/3})^{-5}, \\ a_3 &= \tfrac{1}{120}(4 - 52^{1/3} + 2^{1/3})(-2 + 2^{1/3})^{-5}, \\ a_4 &= \tfrac{1}{240}(-2 + 52^{1/3} - 32^{2/3})(-2 + 2^{1/3})^{-5}, \\ a_5 &= \tfrac{1}{80}(3 - 52^{1/3} + 22^{2/3})(-2 + 2^{1/3})^{-5}, \\ a_6 &= \tfrac{1}{80}(-2 + 52^{1/3} - 32^{2/3})(-2 + 2^{1/3})^{-5}. \end{aligned} \tag{1.145}$$

From Chin's algorithm we have

$$\begin{aligned} C_{4A} = \; & b_1[H_1H_1H_1H_1H_2] + b_2[H_2H_2H_2H_2H_1] + b_3[H_1H_2H_2H_2H_1] \\ & + b_4[H_2H_1H_1H_1H_2] + b_5[H_1H_1H_2H_2H_1] + b_6[H_2H_2H_1H_1H_2] \end{aligned} \tag{1.146}$$

with

$$\begin{aligned} b_1 &= -79/155520, \quad b_2 = -73/25920 \\ b_3 &= -1/2160, \quad\;\; b_4 = 1/3240 \\ b_5 &= -1/4320, \quad\;\; b_6 = 1/2880. \end{aligned} \tag{1.147}$$

We let each algorithm simulate the dynamics of K for a total time $t = N\tau$ of order unity. As a measure of the error we consider the norm $E = |U - V|$, where U is the exact evolution and V the simulated evolution. Using the error terms calculated above, we can approximate the total error by $E \simeq N\tau^{n+1}\|C_n\|$. We can also calculate the total number $n(H)$ of applications of H. Using $\tau \sim N^{-1}$, and the worst case for the norms of C_n for each factorization, we can show that

$$\begin{aligned} E_2 &\simeq \tfrac{1}{2}N^{-2}, \quad\;\; n_2(H) = 3N, \\ E_{\mathrm{FR}} &\simeq \tfrac{16}{7}N^{-4}, \quad n_{\mathrm{FR}}(H) = 7N, \\ E_{4A} &\simeq \tfrac{8}{105}N^{-4}, \quad n_{4A}(H) = 10N. \end{aligned} \tag{1.148}$$

We see the expected scaling of each factorization with N. To illustrate how the number of applications compare, consider $E \sim 10^{-6}$. We find that $n(H) \simeq 2100$ for the second-order propagator, $n(H) \simeq 270$ for the Forest-Ruth propagator, and $n(H) \simeq 170$ for the Chin-4A propagator. While the higher-order factorizations do not reach the optimal value of $n(H) = 3$ [25], these methods are general and can be extended to systems of higher dimension, and even higher accuracy.

Chapter 2

The Josephson Effect

The phase qubit considered in this thesis relies on the Josephson effect. This remarkable discovery by Brian Josephson [71] is that supercurrent can coherently tunnel from one superconductor through an insulating barrier to another superconductor. There are in fact two Josephson effects: there can be constant current at zero voltage (the dc Josephson effect), alternating current at constant voltage (the ac Josephson effect), all without dissipation of energy. This effect was so startling that John Bardeen, of the Bardeen-Cooper-Schrieffer theory of superconductivity [72], initially denied such a possibility [73, 74]. The Josephson effect was quickly measured and is now both the foundation of the voltage standard and the fundamental physics of superconducting qubit devices [6]. A tunnel junction from from three layers, superconductor-insulator-superconductor is now called a Josephson junction. The effect is actually more general than superconductivity, and has also been measured

in superfluid helium [75, 76].

We first recount Feynman's classic presentation [77]. Assume that there are two macroscopic wavefunctions for two adjacent superconductors separated by an insulating barrier, of the form $\Psi_1 = \rho_1^{1/2} e^{i\phi_1}$ and $\Psi_2 = \rho_2^{1/2} e^{i\phi_2}$, where ρ_k is the Cooper pair density of each superconductor ($k = 1, 2$). Further assume that these two wavefunctions are weakly coupled (with some coupling strength K), and that there is a voltage difference V across the two superconductors. For this system, Feynman proposed that we write an effective Schrödinger equation:

$$\begin{aligned} i\hbar \frac{d\Psi_1}{dt} &= eV\Psi_1 + K\Psi_2, \\ i\hbar \frac{d\Psi_2}{dt} &= -eV\Psi_2 + K\Psi_1. \end{aligned} \tag{2.1}$$

Here e is the electric charge. Substituting our wavefunctions, we find Josephson's current relation

$$I = \frac{d\rho_1}{dt} = -\frac{d\rho_2}{dt} = \frac{2K}{\hbar}\sqrt{\rho_1\rho_2}\sin(\phi_2 - \phi_1), \tag{2.2}$$

and Josephson's voltage relation

$$\frac{d(\phi_2 - \phi_1)}{dt} = \frac{2eV}{\hbar} + \frac{K}{\hbar}\sqrt{\frac{\rho_1}{\rho_2}}\left(1 - \frac{\rho_2}{\rho_1}\right)\cos(\phi_2 - \phi_1). \tag{2.3}$$

If the two superconductors are similar and the net current is small, then $\rho_1 \simeq \rho_2 = \rho_0$ and we can simplify the voltage relation (2.3) to

$$V = \frac{\hbar}{2e}\frac{d}{dt}(\dot{\phi} - \dot{\phi}). \tag{2.4}$$

Defining the critical current $I_c = 2K\rho_0/\hbar$ we can rewrite the current relation (2.2) as

$$I = I_c \sin(\phi_2 - \phi_1). \tag{2.5}$$

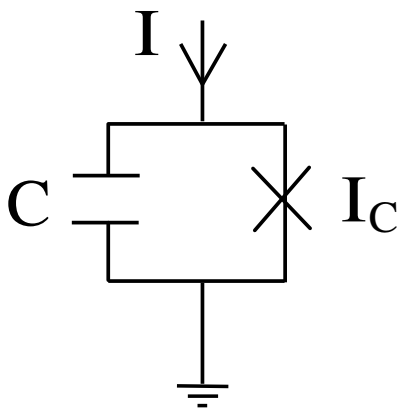

Figure 2.1: Circuit diagram of the current-biased Josephson junction.

Note that the coherence of the superconductors is essential, since both (2.4) and (2.5) involve the phase difference $\gamma = \phi_2 - \phi_1$.

From the Josephson relations (2.4)-(2.5) we can derive the classical dynamics of the current-biased Josephson junction, whose circuit diagram is shown in Fig. 2.1. In addition to the two superconductors, there is a capacitor formed across the insulating barrier. The bias current can either charge the capacitor C or tunnel through the junction, and these two channels add

$$I = I_c \sin\gamma + C\dot{V}. \tag{2.6}$$

where we have used $\gamma = \phi_2 - \phi_1$ and (2.5). Using (2.4) for the voltage, we find that we have the following equation of motion for the phase difference γ

$$C(\Phi_0/2\pi)\ddot{\gamma} + I_c \sin\gamma - I = 0 \tag{2.7}$$

where we have used the flux quantum $\Phi_0 = h/2e$.

The dynamics of (2.7) can also be derived from the Lagrangian

$$\mathcal{L} = \frac{1}{2}C(\Phi_0/2\pi)^2\dot{\gamma}^2 + \frac{\Phi_0}{2\pi}\left(I_c\cos\gamma + I\gamma\right), \tag{2.8}$$

and we have introduced a factor of $\Phi_0/2\pi$ to give $\mathcal{L}$ the units of energy. The canonical momentum conjugate to γ is

$$p = \frac{\partial \mathcal{L}}{\partial \dot{\gamma}} = C(\Phi_0/2\pi)^2 \dot{\gamma} = m\dot{\gamma}, \tag{2.9}$$

where the effective mass is $m = C(\Phi_0/2\pi)^2$. The Hamiltonian corresponding to $\mathcal{L}$ is

$$H = p\dot{\gamma} - \mathcal{L}. \tag{2.10}$$

Using (2.9) and (2.8) in (2.10) we have

$$H = \frac{1}{2m}p^2 - \frac{\Phi_0}{2\pi}\left(I_c \cos\gamma + I\gamma\right). \tag{2.11}$$

We have applied standard Hamiltonian dynamics to the superconducting circuit of Fig. 2.1, with the phase γ as a classical variable. An entirely similar treatment can be given to an inductor-capacitor (LC) harmonic oscillator. The main novelty of (2.11) is the nonlinear current-voltage relations (2.4)-(2.5) of the Josephson junction. We now take the rather unfamiliar step to use the Hamiltonian of (2.11) as the basis of a *quantum* dynamics for the phase. That is, we postulate that the phase is governed by a wavefunction $\Psi(\gamma, t)$ which satisfies the Schrödinger equation given with the Hamiltonian (2.11) and the canoncial momentum operator $p = -i\hbar\partial/\partial\gamma$,

$$i\hbar\frac{\partial \Psi}{\partial t}(\gamma, t) = -\frac{\hbar^2}{2m}\frac{\partial^2 \Psi}{\partial \gamma^2}(\gamma, t) - \frac{\Phi_0}{2\pi}\left(I_c \cos\gamma + I\gamma\right)\Psi(\gamma, t). \tag{2.12}$$

This crucial step was first argued by Philip Anderson in 1964 [78], and is the basis for the study of macroscopic quantum phenomena initiated by Anthony Leggett in 1980 [79, 80]. Indeed, the quantum dynamics of the phase is the basis

of all superconducting qubits [6]. Quantum phenomena associated with (2.12) have been observed experimentally. These include macroscopic quantum tunneling [81, 82, 83, 84], energy level quantization [85, 86, 87, 88] and pulsed [89, 90, 91] and driven (Rabi) coherent oscillations [92, 93, 94].

Conceptually, there are several questions that arise. First, we have already used the quantum mechanics of the system to find the Josephson relations (2.4)-(2.5). In passing from (2.11) to (2.12), it seems that we are *re-quantizing* the system. How can such a procedure be understood? Second, the meaning of the phase as a fundamental quantum variable may seem somewhat mysterious. For example, it is well-known that, for a harmonic oscillator, there is no uniquely defined phase operator ϕ that is conjugate to the number operator N such that $[\phi, N] = i$ [95]. What then does the superconducting phase γ represent, and what are the true conjugate variables of the Josephson junction? Finally, a phase is normally defined as a periodic variable which is only defined up to 2π. The Hamiltonian in (2.12), however, breaks this periodicity by the term linear in the phase. How can such a term arise? Does this truly model a current-biased Josephson junction?

In this Chapter, we critically examine these questions, and review the various solutions that have been proposed in the literature. We will find that the first two questions can be answered definitively. It is our opinion that the third question is not completely resolved, although there are several intriguing possibilities. We note that many (though not all) of these issues have been previously addressed by Leggett ([96, 97, 98, 99, 100]). See also the review by Schön and Zaikin [101].

In the remainder of this thesis we take the view that the Hamiltonian of (2.12)

is correct, taking the phase as an extended coordinate ($-\infty < \gamma < \infty$). The justification for this is the following: The unresolved conceptual issues can only be settled by a combination of theory and experiment. By choosing a definite model we can generate theoretical results and predictions. Many of these predictions have been tested in experiments, and the agreement is quite compelling. Thus, while much remains to be learned aboutfor our the quantum dynamics of the phase, much can been gained by using the simplest model.

2.1 Josephson Effect in the BCS model

We first review how the phase degree of freedom γ emerges from the microscopic theory of superconductivity and the the Josephson effect. This many-body theory is the Bardeen-Cooper-Schrieffer (BCS) theory of superconductivity [72]. In brief, the BCS theory is based on the fact that the Fermi surface of a metal is unstable in the presence of an attractive interaction [102]. The electrons become Cooper pairs whose dynamics yields superconductivity.

The standard BCS model Hamiltonian can be written [103]

$$H = \sum_k \epsilon_k (n_k + n_{-k}) - \sum_{k,k'} V_{k,k'} b_k^\dagger b_{k'} \tag{2.13}$$

where we have used the operators

$$\begin{array}{ll} n_k & = C_k^\dagger C_k, \\ n_{-k} & = C_{-k}^\dagger C_{-k}, \\ b_k^\dagger & = C_k^\dagger C_{-k}^\dagger, \\ b_k & = C_{-k} C_k, \end{array} \tag{2.14}$$

and $C_k^\dagger$ is the (fermionic) creation operator for an electron in momentum state k with spin up and energy ϵ_k, $C_{-k}^\dagger$ the creation operator for an electron in momentum state

$-k$ with spin down. The operator $b_k^\dagger$ creates paired electrons, one with momentum k and spin up, the other with momentum $-k$ and spin down. The matrix $V_{k,k'} > 0$ represents an effective attractive interaction between these paired electrons. For simplicity (following [72]) this can be taken as constant V in a region of momentum space such that $\epsilon_F - \hbar\omega_D < \epsilon_k < \epsilon_F + \hbar\omega_D$ and zero otherwise, where $\hbar\omega_D$ is the characteristic phonon energy. This phonon-mediated interaction is physically due to the scattering of an electron off the crystal lattice. The lattice is then deformed in such a way to attract another electron.

Of central importance to (2.13) is the ground state, which is approximately given by

$$|\phi\rangle = \prod_k \left(u_k + v_k e^{i\phi} b_k^\dagger\right) |0\rangle \tag{2.15}$$

where $|0\rangle$ representes the vacuum state. The real amplitudes u_k and v_k satisfy $u_k^2 + v_k^2 = 1$, and are found by the variational method of BCS [72] or the mean-field approximation of Anderson [103]. Their explicit form is not needed here.

What is important about (2.15) is the uniform phase ϕ of the pair states, and that the ground state energy is independent of ϕ. For an isolated superconductor it is convenient to neglect it entirely, and set $\phi = 0$. Josephson saw that this cannot be done for coupled superconductors.

The tunneling Hamiltonian used by Josephson was first used by Cohen, Falicov, and Phillips [104] to study tunneling between a superconducting and a normal metal and subsequently studied thereafter [74, 105, 106]. It reads

$$H = H_R + H_L + H_T \tag{2.16}$$

where H_R and H_L are BCS Hamiltonians of the form (2.13), and the tunneling term is

$$H_T = \sum_{k,q,\alpha} \left(T_{kq\alpha} C^\dagger_{Lk\alpha} C_{Rq\alpha} + T^*_{kq\alpha} C^\dagger_{Rq\alpha} C_{Lk\alpha} \right). \tag{2.17}$$

This interaction represents the tunneling of *electrons* between the left and right superconductors. The first term in the sum destroys a particle on the right in momentum state q and spin state α, creates a particle on the left in momentum state k and spin state α, with the tunneling amplitude $T_{kq\alpha}$. Josephson showed that tunneling of actual electron *pairs* can be found by working to second-order in H_T in perturbation theory. Pair tunneling occurs with only virtual excitation of the quasi-particles—a superposition of an electron and a hole (see also [78]).

We follow work of Wallace and Stavn [107], who use the quasi-spin formalism of Anderson [103]. They showed how these virtual excitations could be formally eliminated by a canonical transformation to an effective pair-tunneling term. Taking $T_2 \sim |T_{k,q,\alpha}|^2$ as a constant they obtained the new tunneling Hamiltonian

$$H_{T_2} = -T_2 \sum_{k,q} \left(b^\dagger_{Lk} b_{Rq} + b^\dagger_{Rq} b_{Lk} \right). \tag{2.18}$$

The appropriate BCS state for the coupled superconductors is

$$|\phi_1, \phi_2\rangle = \prod_k \left(u_{Lk} + v_{Lk} e^{i\phi_1} b^\dagger_{Lk} \right) \otimes \left(u_{Rk} + v_{Rk} e^{i\phi_2} b^\dagger_{Rk} \right) |0\rangle. \tag{2.19}$$

We see that there are now two phases, and global transformations of the electron operators will not change the phase difference $\gamma = \phi_2 - \phi_1$. Furthermore, the energy of the state with the tunneling Hamiltonian now depends on γ. In fact, the coupling energy is given by taking the expectation value of (2.18) with (2.19), which yields

$$\Delta E = -E_J \cos\gamma \tag{2.20}$$

with

$$E_J = 2T_2 \frac{\Delta^2}{V^2}. \tag{2.21}$$

Here Δ is the superconducting gap energy for each superconductor (assumed equal), and V is the coupling energy of (2.13). This is of course the potential energy obtained in (2.12). The current can also be directly calculated and is

$$J = \frac{4eT_2}{\hbar} \frac{\Delta^2}{V^2} \sin\gamma. \tag{2.22}$$

By adding a voltage term to the Hamiltonian, Wallace and Stavn also derive (2.5).

This brief summary of the Josephson effect shows that the phase difference γ is the relevant new degree of freedom for coupled superconductors. As long as the coupling energy of (2.21) is smaller than that of quasi-particle excitations, we can restrict the dynamics to the BCS ground state (2.19). We can also, however, form a superposition of such states [100], via

$$|\Psi\rangle = \int d\gamma \Psi(\gamma) |\phi, \phi + \gamma)\rangle. \tag{2.23}$$

The states $|\phi, \phi+\gamma\rangle$ are essentially orthogonal, and the expansion coefficient $\Psi(\gamma)$ is precisely the wavefunction of the junction which appears in the Schrödinger equation of (2.11), with (2.20) as a "potential energy." Missing is the "kinetic energy", which is the electrostatic interaction

$$\frac{Q^2}{2C} = \frac{e^2}{2C} \left(\frac{1}{2} \sum_k (n_{Rk} + n_{R-k} - n_{Lk} - n_{L-k}) \right)^2. \tag{2.24}$$

It remains to show that (2.24), when acting on (2.23), will yield the kinetic term of (2.11). The difficulty is that states such as (2.19) are not states of definite number

for either superconductor. Thus we must consider number states, and the possibilty that the phase is conjugate to the number operator.

2.2 Number-Phase Operators

In the space of pair states, the number of electron pairs for the right superconductor is

$$N_R = \frac{1}{2}\sum_k (n_{Rk} + n_{R-k})$$
$$N_L = \frac{1}{2}\sum_k (n_{Lk} + n_{L-k}) \tag{2.25}$$

and the charge difference across the capacitor is $2Q = 2e(N_R - N_L)$ and thus

$$\frac{Q^2}{2C} = \frac{(2e)^2}{2C}\left(\frac{N_R - N_L}{2}\right)^2. \tag{2.26}$$

If we define the relative number operator $n = (N_R - N_L)/2$, and assume the commumation relation

$$[n, \gamma] = i \tag{2.27}$$

then in the representation of γ we can let $n = id/d\gamma$, and we will have reproduced two terms in (2.11):

$$\frac{Q^2}{2C}\Psi(\gamma) = -\frac{(2e)^2}{2C}\frac{\partial^2\Psi}{\partial\gamma^2}(\gamma). \tag{2.28}$$

We wish to examine this solution, namely the possibility of (2.27), in this section. Note that there is no essential difference between (2.27) and the alternative form $[\gamma, n] = i$, which is often found in the literature—the choice of sign is a conventional choice that varies in the literature.

First we consider the following formal manipulation by Anderson [78]. We again consider the BCS state

$$|\phi\rangle = \prod_k \left(u_k + v_k e^{i\phi} b_k^\dagger\right)|0\rangle, \tag{2.29}$$

and consider the following superposition of these states

$$|N\rangle = \int_0^{2\pi} d\phi e^{-iN\phi}|\phi\rangle. \tag{2.30}$$

To understand this state (and the notation), we see that each term in (2.29) with N pairs is accompanied by a factor of $e^{iN\phi}$. Only these terms will survive the integration in (2.30), which thus projects out fixed particle states. As an operator we have $\hat{N}|N\rangle = N|N\rangle$. Equivalently, we see that in the ϕ-representation there is the relation

$$\langle\phi|\hat{N}|\Psi\rangle = i\frac{\partial}{\partial\phi}\langle\phi|\Psi\rangle \tag{2.31}$$

and thus it would seem that we have the commutation relation

$$[N, \phi] = i. \tag{2.32}$$

Unfortunately, there are two well-known problems with (2.32) [95], if N and ϕ are both taken as Hermitian operators. The first problem is associated with the matrix element

$$\langle n|[N,\phi]|n'\rangle = \langle n|(N\phi - \phi N)|n'\rangle \stackrel{?}{=} (n-n')\langle n|\phi|n'\rangle. \tag{2.33}$$

Since the phase is a bounded operator we have $\langle\phi\rangle < 2\pi$, and thus (2.33) with $n = n'$ yields

$$\langle n|[N,\phi]|n\rangle \stackrel{?}{=} 0 \neq i \tag{2.34}$$

contradicting (2.32). As indicated by the question marks, this argument is *incorrect*. The mistake lies in letting N act to the left in $\langle n|N\phi|n'\rangle$. Assuming that (2.32) is correct, with ϕ a periodic variable, N is Hermitian operator only on periodic functions of ϕ, with eigenfunctions

$$\langle\phi|n\rangle = (2\pi)^{1/2}e^{-in\phi}. \tag{2.35}$$

N is *not* Hermitian on $\phi|n'\rangle$, which is not a periodic function of ϕ. Thus $\langle n|N\phi|n'\rangle \neq n\langle n|\phi|n'\rangle$. Indeed, by using the full inner product we have

$$\begin{aligned}\langle n|N\phi|n'\rangle = \tfrac{1}{2\pi}\int_0^{2\pi} d\phi e^{in\phi} i\tfrac{d}{d\phi}\left(\phi e^{-in'\phi}\right) &= i - \tfrac{1}{2\pi}\int_0^{2\pi} i\left(\tfrac{de^{in\phi}}{d\phi}\right)\phi e^{-in'\phi} \\ &= i + n\langle n|\phi|n'\rangle\end{aligned} \tag{2.36}$$

Using this correct evaluation of the commutator we find that that the commuation relation (2.32) is not ruled out [108].

The second problem [95] is typical number operators such as N_L and N_R in (2.25) are bounded from below. In this case we can show that ϕ is not a Hermitian operator, or equivalently the periodic exponential operator

$$E = e^{i\phi} \tag{2.37}$$

is not unitary. Observe that if (2.32) is correct, we have the commutation relations

$$[N, E] = -E, \quad [N, E^\dagger] = E^\dagger. \tag{2.38}$$

and thus

$$NE = E(N-1), \quad NE^\dagger = E^\dagger(N+1) \tag{2.39}$$

If we apply (2.39) to a state $|n\rangle$ we find

$$E|n\rangle = |n-1\rangle, \quad E^\dagger|n\rangle = |n+1\rangle. \tag{2.40}$$

If we let $n = 0$ we have $E|0\rangle = 0$ while $E^\dagger|0\rangle = |1\rangle$. This implies that

$$EE^\dagger = I, \quad E^\dagger E = I - |0\rangle\langle 0|. \tag{2.41}$$

The lower bound to N ($N|0\rangle = 0$) prevents E from being a unitary operator.

These difficulties were initially ignored in Anderson's original work [78], although subsequent discussion [109] (regarding superfluids) and a similar treatment by Leggett [110] (for two-band superconductors) suggested that the number-phase commutator exists only as a matrix element for states with large $\langle N\rangle$. In this case the lack of unitarity of E presumably does not arise, and thus ϕ is effectively Hermitian.

For the Josephson junction, these difficulties can be resolved in the following way. If the total number $N_L + N_R$ is fixed and tends to ∞, the number *difference* operator $n = (N_R - N_L)/2$ has an *unbounded* spectrum from $-\infty$ to $+\infty$, and therefore a conjugate phase variable exists: the *relative* phase $\gamma = \phi_R - \phi_L$. For the relative variables the commutation relation (2.27) is correct, and thus we have nearly derived (2.11) from the microscopic BCS model.

2.3 Exact Quantum Phase Model

An exact resolution of the number-phase problem of the previous section can be studied using a somewhat simpler model of a Josephson junction. This is the two-mode boson Hamiltonian

$$H = \frac{E_c}{8}(n_2 - n_1)^2 - \frac{E_J}{N}(a_1^\dagger a_2 + a_2^\dagger a_1). \tag{2.42}$$

where $a_1^\dagger$ and $a_2^\dagger$ are creation operators for the bosonic modes 1 and 2, and the number operators are $n_1 = a_1^\dagger a_1$, $n_2 = a_2^\dagger a_2$. This model is perhaps more relevant for Bose-Einstein condensates [111] where the total number $N = n_1 + n_2$ and the parameters E_c and E_J can all be controlled by laser intensity, trap geometry, or magnetic fields.

We consider the exact quantum phase model proposed by Anglin, Drummond, and Smerzi [112, 113]. They derive an exact Schrödinger equation from (2.42) that reads

$$i\hbar\frac{\partial\Psi}{\partial t}(\phi,t) = -\frac{E_c}{2}\frac{\partial^2\Psi}{\partial\phi^2}(\phi,t) - E_J\left(1+\frac{2}{N}\right)\cos\phi\Psi(\phi,t) - 2\frac{E_J}{N}\sin\phi\frac{\partial\Psi}{\partial\phi}(\phi,t). \tag{2.43}$$

In the limit $N \to \infty$ we see that the surviving terms of (2.43) reproduce the terms in (2.11). Thus, the Schrödinger equation for the relative phase variable can be derived exactly. Similar results can be found in [114]) using somewhat different phase representations. We follow the presentation in [113], with minor changes in notation.

The Hamiltonian (2.42) conserves the total particle number $N = n_1 + n_2$, which can therefore be considered constant. The appropriate states are then the two-mode relative number states of the form

$$|n_1, n_2\rangle = |N/2 + n, N/2 - n\rangle = |n\rangle_N \tag{2.44}$$

where we have introduced the *relative* number $n = (n_1 - n_2)/2$. We can define (relative) phase states by

$$|\phi\rangle_N = \frac{1}{\sqrt{2^N N!}}\left(a_1^\dagger e^{i\phi/2} + a_2^\dagger e^{-i\phi/2}\right)^N |0,0\rangle \tag{2.45}$$

which has the explicit form (using the binomial expansion)

$$|\phi\rangle_N = \sum_{n=-N/2}^{N/2} c_{N,n} e^{in\phi} |N/2+n, N/2-n\rangle \tag{2.46}$$

with

$$c_{N,n} = \left(\frac{N!}{2^N (N/2+n)!(N/2-n)!} \right)^{1/2}. \tag{2.47}$$

The phase states $|\phi\rangle_N$ are an overcomplete basis, related to coherent states. We can expand any state (with N particles) as

$$|\Psi\rangle_N = \frac{1}{2\pi} \int_0^{2\pi} d\phi \Psi(\phi) |\phi\rangle_N \tag{2.48}$$

where $\Psi(\phi)$ is the wavefunction. Now, it is straightforward to calculate the action of of the number operators n_1 and n_2 on (2.46),

$$\begin{array}{ll} n_1|\phi\rangle_N = a_1^\dagger a_1 |\phi\rangle_N & = (N/2)|\phi\rangle_N - i(d/d\phi)|\phi\rangle_N, \\ n_2|\phi\rangle_N = a_2^\dagger a_2 |\phi\rangle_N & = (N/2)|\phi\rangle_N + i(d/d\phi)|\phi\rangle_N, \end{array} \tag{2.49}$$

and thus we have found the result

$$n|\phi\rangle_N = -i \frac{d}{d\phi} |\phi\rangle_N. \tag{2.50}$$

We can also show that

$$\begin{array}{ll} a_1^\dagger a_2 |\phi\rangle_N & = (N/2) e^{-i\phi} |\phi\rangle_N - i e^{-i\phi} (d/d\phi)|\phi\rangle_N, \\ a_2^\dagger a_1 |\phi\rangle_N & = (N/2) e^{i\phi} |\phi\rangle_N + i e^{i\phi} (d/d\phi)|\phi\rangle_N. \end{array} \tag{2.51}$$

In deriving (2.51) we have used the following property of $c_{N,n}$ in (2.47):

$$\frac{c_{N,n\pm1}}{c_{N,n}} = \frac{(N/2 \mp n)^{1/2}}{(N/2 \mp n + 1)^{1/2}}. \tag{2.52}$$

Now, define the differential operator H_ϕ by

$$H|\Psi\rangle_N = \frac{1}{2\pi} \int_0^{2\pi} d\phi \left(H_\phi \Psi(\phi) \right) |\phi\rangle_N. \tag{2.53}$$

H_ϕ is the phase representation of the Hamiltonian (2.42). Using (2.50) and (2.51) and integrating each derivative $d|\phi\rangle_N/d\phi$ by parts, we find

$$H_\phi\Psi(\phi) = -\frac{E_c}{2}\frac{\partial^2\Psi}{\partial\phi^2}(\phi) - E_J\left(1+\frac{2}{N}\right)\cos\phi\Psi(\phi) - 2\frac{E_J}{N}\sin\phi\frac{\partial\Psi}{\partial\phi}(\phi). \tag{2.54}$$

Using the phase representation (2.54) for the Hamiltonian (2.42) we have found that the Schrödinger equation

$$i\frac{\partial}{\partial t}|\Psi\rangle_N = H|\Psi\rangle_N \tag{2.55}$$

takes the promised form

$$i\hbar\frac{\partial\Psi}{\partial t}(\phi,t) = -\frac{E_c}{2}\frac{\partial^2\Psi}{\partial\phi^2}(\phi,t) - E_J\left(1+\frac{2}{N}\right)\cos\phi\Psi(\phi,t) - 2\frac{E_J}{N}\sin\phi\frac{\partial\Psi}{\partial\phi}(\phi,t). \tag{2.56}$$

The inner product between two states $|\Psi\rangle_N$ and $|\Phi\rangle_N$ takes the form

$$\langle\Phi|\Psi\rangle_N = \frac{1}{(2\pi)^2}\int_0^{2\pi} d\phi_1 d\phi_2 \Phi^*(\phi_2)\langle\phi_2|\phi_1\rangle_N\Psi(\phi_1). \tag{2.57}$$

This differs from a usual inner product by the appearance of $\langle\phi_2|\phi_1\rangle_N$, an indication of the overcomplete basis. Using (2.46) and (2.47), we have

$$\langle\phi_2|\phi_1\rangle_N = \sum_{n=-N/2}^{N/2}\frac{N!e^{in(\phi_1-\phi_2)}}{2^N(N/2+n)!(N/2-n)!} = \left[\cos\left(\frac{\phi_1-\phi_2}{2}\right)\right]^N. \tag{2.58}$$

Here we have again used the binomial theorem. In the limit that $N\to\infty$, however, the inner product (2.58) becomes proportional (as a distribution) to a δ-function

$$\lim_{N\to\infty}\langle\phi_2|\phi_1\rangle_N = 2\pi\delta(\phi_2-\phi_1). \tag{2.59}$$

In this limit, we can use Stirling's approximation to simplify (2.47):

$$c_{N,n} \simeq \exp(-2n^2/N) \to 1, \tag{2.60}$$

and thus we find

$$|\phi\rangle_N \simeq \sum_{n=-N/2}^{N/2} e^{in\phi}|n\rangle_N, \tag{2.61}$$

a result strikingly similar to (2.30).

The two-mode model shows how, in a controlled way, the phase-variable can be introduced and an exact Schrödinger equation can be derived. In the limit $N \to \infty$ this equation reproduces all the terms of (2.12) except the current-bias. Note that there are no difficulties with a number-phase commutation relation, since in this limit the relative number operator n has a discrete unbounded spectrum from $-\infty$ to $+\infty$. The relative phase ϕ is its conjugate variable, and is periodic.

2.4 Other Models

The relative number-phase model of a Josephson has actually been used long before the analysis of Anglin, Drummond, and Smerzi. It appeared first in the very clever derivation of the Josephson effect by Ferrell and Prange [115] (see also [116]). There are actually a few subtleties that remain to be discussed. First, the transition from the fermionic BCS states such as (2.19) to the bosonic model is not exact. When a pair tunnels from one superconductor to the next, the final state must be unoccupied, and there is no extra bosonic enhancment of the coupling energy. The factor of $1/N$ in the tunneling term of (2.42) is needed to model this.

A more accurate fermionic model could be that based on quasi-spin operators [103, 107]. Unfortunately, there seems to be some disagreement regarding the proper formulation of the theory [117, 118, 119, 120, 121], and the validity of predicted

corrections to the classical Josephson equations (2.4)-(2.5) [122, 123, 124, 125]. A pedagogical introduction to the quasi-spin model of the Josephson effect can be found in [126]. The quasi-spin method does contain the number-phase model as a special case.

An entirely different modification of the theory is to include the charging energy of the superconductors *before* considering the Josephson coupling [127, 128]. This modifies the perturbation theory, and yields a phase-dependent correction to the capacitance $\Delta C(\phi)$ which is proportional to E_c/Δ, where E_c is the charging energy $e^2/2C$ and Δ is the gap energy. This correction $\Delta C(\phi)$ is typically small for the junctions we will consider.

Finally, the path-integral treatment of Ambegaokar, Eckern, and Schön is perhaps the most elegant derivation of the dynamics of the phase [129, 130, 131]. They begin with the full tunneling Hamiltonian (2.16) and the electrostatic interaction (2.24), and by a sequence of auxiliary field definitions and semi-classical approximations to the path integral they first derive superconductivity in the BCS approximation. Subsequent integrations reduce the dynamics to an effective Lagrangian such as (2.8), including a capacitance renormalization and coupling terms to quasiparticles. This capacitance renormalization is apparently different from that found in [127]. A complete reconciliation of these different models has not been performed. Most importantly, none of the above models addresses the periodicity of the phase, which we now consider.

2.5 Periodicity of the Phase

Anderson's [78] model of the "tilted" washboard potential cannot be correct if the phase is a periodic variable (defined on the range $0 \leq \gamma < 2\pi$). There are two possibilities: (a) the phase is not a periodic variable but is an extended coordinate ($-\infty < \gamma < \infty$), or (b) the washboard potential is incorrect. For physical Josephson junctions, experiments show that the washboard potential is a very good model: thus the evidence suggests possibility (a). Alternatively, if position (b) is correct, the true model must somehow reproduce the experimental observations. The theoretical challenge is to show how either solution comes about. We now discuss the main proposals. Surprisingly, all of these start from position (b).

2.5.1 Time-Dependent Hamiltonian

The simplest approach is to note that the Lagrangian of (2.8)

$$\mathcal{L} = \frac{1}{2}C(\Phi_0/2\pi)^2\dot{\gamma}^2 + \frac{\Phi_0}{2\pi}\left(I_c\cos\gamma + I\gamma\right), \tag{2.62}$$

can be modified by adding a total time derivative

$$\Delta\mathcal{L} = -\frac{\Phi_0}{2\pi}\frac{d}{dt}(\gamma Q(t)) \tag{2.63}$$

with $dQ/dt = I$; the equations of motion (2.7) remain the same under this transformation. The new Lagrangian is

$$\mathcal{L}_2 = \frac{1}{2}C(\Phi_0/2\pi)^2\dot{\gamma}^2 + \frac{\Phi_0}{2\pi}\left(I_c\cos\gamma\right) - \frac{\Phi_0}{2\pi}\dot{\gamma}Q(t), \tag{2.64}$$

with the new canonical momentum

$$p_2 = \frac{\partial\mathcal{L}_2}{\partial\dot{\gamma}} = C(\Phi_0/2\pi)^2\dot{\gamma} - (\Phi_0/2\pi)Q = m\dot{\gamma} - p_Q \tag{2.65}$$

where the mass is $m = C(\Phi_0/2\pi)^2$ and the momentum $p_Q = (\Phi_0/2\pi)Q$. The Hamiltonian is

$$H = \frac{1}{2m}(p_2 + p_Q)^2 - \frac{I_c\Phi_0}{2\pi}\cos\gamma. \tag{2.66}$$

Using $n = \hbar^{-1}p_2$ we can rewrite this as

$$H = \frac{1}{2C}(2en + Q)^2 - \frac{I_c\Phi_0}{2\pi}I_c\cos\gamma. \tag{2.67}$$

In this Hamiltonian the phase can be either extended or periodic. For a constant current, the charge is $Q = It$, and thus H is explicity time-dependent. This model was introduced [132] to study small capacitance current-biased junctions, where the periodicity of ϕ and the fact that n has discrete spectrum are essential.

There is actually a hidden relation of (2.67) to the washboard when $Q = It$. Note that there is the natural time-scale $\tau = 2e/I$ (called the Bloch period [133]). This is the time-scale for one pair to tunnel through the junction. The Hamiltonian (2.67) has a hidden symmetry, which can be written as

$$H(t + \tau) = e^{i\phi}H(t)e^{-i\phi}. \tag{2.68}$$

This symmetry is quite similar to periodic Hamiltonians $H(t+\tau) = H(t)$, often studied using Floquet theory [134]. By exploiting this symmetry it was shown [135] that the time-dependent Floquet eigenfunctions are in fact precisely the eigenstates of the washboard, with a new extended coordinate. We can therefore extract the essential dynamics (Floquet eigenvalues and eigenstates) of the time-dependent Hamiltonian (2.67) by studying the washboard. Note that the junctions we will consider have bias currents of $I \sim 20\mu$A., and thus $\tau \sim 10^{-5}$ ns, while the frequency scale is $f \sim 6$

GHz, and thus $f\tau \sim 10^{-5}$. The system transfers roughly 10^5 electron pairs over the relevant timescale for the circuit. This is also the effective number of charge states we would need to fully capture the dynamics. This large number suggests that the distinction between the Floquet and washboard solutions may be irrelevant, and we then recover the washboard dynamics. A quantitative numerical analysis has confirmed some of these issues [136].

2.5.2 Stochastic Current-Bias

Note that both the washboard and time-dependent models treat the bias current as an arbitrary classical quantity. In actuality, the current must come from somewhere, and thus the true Hamiltonian must include extra degrees of freedom associated with the current source. One possible model is that the current bias is a weakly coupled system which, every so often, puts particles into superconductor L and takes them from superconductor R. On average, it generates the bias current I. A theoretical analysis of this model has been given by Rogovin, Nagel and Scully [137, 116, 138], and also by Unnerstall [139]. The net effect of the current bias is to generate the following master equation for the density matrix,

$$i\hbar\frac{d\rho}{dt} = [H,\rho] - i\frac{\hbar I}{2e}\left(JJ^\dagger\rho + \rho JJ^\dagger - 2J^\dagger\rho J\right) \tag{2.69}$$

where J is an operator which transfers Cooper pairs from L to R. On the relative number states we have

$$J|n\rangle = |n+1\rangle. \tag{2.70}$$

Taking the matrix elements of (2.69) in the phase basis we find

$$i\hbar\frac{\partial\rho}{\partial t}(\phi,\phi') = [H,\rho] - i\frac{\hbar I}{2e}\left(1 - e^{i(\phi-\phi')}\right)\rho(\phi,\phi'). \tag{2.71}$$

Note that for small $(\phi - \phi')$ we can expand the exponential in (2.71) to get an approximate washboard term

$$i\hbar\frac{\partial\rho}{\partial t}(\phi,\phi') \simeq [H,\rho] - \frac{\hbar I}{2e}\left(\phi\rho(\phi,\phi') + \rho(\phi,\phi')\phi'\right) = [H_{\rm WB},\rho] \tag{2.72}$$

with the standard washboard Hamiltonian

$$H_{\rm WB}\Psi(\phi) = -\frac{\hbar^2}{2m}\frac{\partial^2\Psi}{\partial\phi^2} - \frac{\Phi_0}{2\pi}\left(I_c\cos\phi + I\phi\right)\Psi(\phi). \tag{2.73}$$

There are a number of deficiencies in this approach. First, the current is essentially a noisy current, which is only equal to I on average. Second, the master equation (2.71) is arbitrary. The same physics can be achieved by a current source which produces not one pair at a time, but many. In fact, we could consider multiple current bias channels and get

$$i\hbar\frac{\partial\rho}{\partial t}(\phi,\phi') = [H,\rho] - i\frac{\hbar}{2e}\sum_{n=1}^{N} I_n\left(1 - e^{in(\phi-\phi')}\right)\rho(\phi,\phi') \tag{2.74}$$

with a total bias current of

$$I = \sum_{n=1}^{N} nI_n. \tag{2.75}$$

Finally, there is a basic prediction that distinguishes this model from the washboard. If we include the higher-order terms in the expansion of the exponential in (2.64), we find

$$i\hbar\frac{\partial\rho}{\partial t}(\phi,\phi') = [H_{\rm WB},\rho] - i\frac{\hbar I}{4e}(\phi-\phi')^2\rho(\phi,\phi'). \tag{2.76}$$

This last term is a well-known decoherence term [140], which will cause superpositions of the first two resonant-state wavefunctions (to be discussed in the next Chapter) to decay at a rate greater than ω_0, where ω_0 is the frequency of small oscillations in the well of the washboard. This is significantly faster than the decoherence rates seen in Rabi oscillation experiments [93, 92]. We conclude that this model is not a viable generalization of the washboard.

2.5.3 Environment-Induced Decompactification

The final argument for the "decompactification" of the phase also explicitly introduces additional degrees of freedom for the circuit. However, instead of assuming weak coupling, we now assume adiabatic coupling whereby the environment essentially measures the motion of the phase in such a way that displacements greater than 2π become orthogonal. In other words, the environment makes ϕ and $\phi + 2\pi$ distinguishable. There are actually several models with this property, all based on an effective Hamiltonian similar to (2.67):

$$H = \frac{1}{2C}(2en + Q)^2 - \frac{I_c\Phi_0}{2\pi}\cos\gamma. \tag{2.77}$$

where now the charge Q is itself an operator. In this case, when the phase evolves, the charge is displaced in such a way that ϕ and $\phi + 2\pi$ lead to orthogonal states of Q.

Note that if the phase is an extended coordinate, the conjugate variable n should have a continuous spectrum. That the charge should be a continuous variable makes sense for many models of the circuit [141, 142]; consider, for example, an LC-

oscillator. If the charges can move in a continuous fashion, the effective charge across the junction need not be discrete.

The model studied by Zwerger, Dorsey and Fisher [143] uses a modification of the Caldeira-Leggett analysis [97] where the environment is directly coupled to n instead of ϕ. They found that for matrix elements of the system with Ohmic dissipation, the dynamics of the periodic and extended coordinates coincide. Interaction with the environment suppresses the possibility of interference of states with ϕ and $\phi+2\pi$. Note, however, that their analysis is quite involved and their choice of initial conditions has come under criticism [144].

A clear analysis of a related model has been given by Apenko [145] and reviewed in [101]. By including an inductance for the external charge, he considers the basic Hamiltonian

$$H = \frac{1}{2C}(2en + Q)^2 + \frac{P^2}{2L} - E_J \cos\gamma \tag{2.78}$$

with $E_J = I_c(\Phi_0/2\pi)$. The energy states of H can be written, with $x = (\Phi_0/2\pi)\gamma$

$$\Psi_\xi(x, Q) = A \sum_{n=-\infty}^{\infty} e^{-i\hbar^{-1}Q(x+n\Phi_0-\xi)}\chi(x + n\Phi_0; \xi) \tag{2.79}$$

where $P\Psi_\xi(x, Q) = \xi\Psi_\xi(x, Q)$ and $\chi(x; \xi)$ satisfies

$$-\frac{\hbar^2}{2C}\frac{\partial^2\chi}{\partial x^2}(x) + \frac{1}{2L}(x - \xi)^2\chi(x) - E_J \cos(2\pi x/\Phi_0)\chi(x) = E\chi(x). \tag{2.80}$$

This last equation is the Schrödinger equation for the rf-SQUID, whose circuit is shown in Fig. 2.2, where ξ plays the role of an external flux. The wavefunctions $\chi(x)$ are defined on an extended coordinate x. These wavefunctions are combined in such a way that the total wavefunction $\Psi_\chi(x, Q)$ is periodic in x. However,

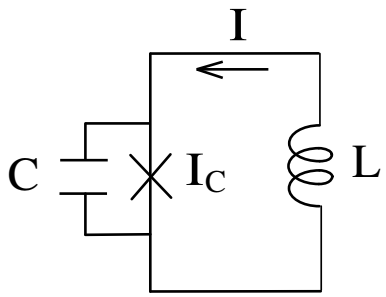

Figure 2.2: Circuit diagram of the rf-SQUID (Superconducting Quantum Inteference Device), a Josephson junction in an inductive loop.

the form of the wavefunction ensures that when only the properties of the phase are considered, there is no interference between x and $x+2\pi$. The phase is now locked to another degree of freedom (the charge Q), and has become an extended coordinate. Note, however, that the circuit dynamics of (2.78) do not seem to correspond to the physical circuit [144], nor is (2.80) the washboard.

This brings us to our final model, which is the most uncomplicated way to derive the washboard. We directly consider the SQUID dynamics of Fig. 2.2, which yields a Hamiltonian of the form

$$H = \frac{1}{2C}p_\Phi^2 + \frac{1}{2L}(\Phi - \Phi_x)^2 - E_J \cos(2\pi\Phi/\Phi_0). \tag{2.81}$$

The coupling of the current to the electromagnetic field through the inductor yields the extended coordinate Φ of the flux. This flux is essentially the same coordinate that would appear in a Hamiltonian for an LC-oscillator, without the junction. Leggett has carefully analyzed [100] the many-body wavefunction for Fig. 2.2. The charge p_Φ is then a continous variable related to the electronic coordinates around the loop, and furthermore we can make the replacement $p_\Phi \rightarrow -i\hbar d/d\Phi$. The

inductor now plays the role of a current bias, and if we take the limit $L \to \infty$, $\Phi_x/L \to I$, and write the flux as $\Phi = (\Phi_0/2\pi)\gamma$, the Hamiltonian (2.81) reduces to that of a particle in the washboard potential:

$$H = \frac{1}{2m}p^2 - \frac{\Phi_0}{2\pi}\left(I_c \cos\gamma + I\gamma\right). \tag{2.82}$$

Chapter 3

Resonances of the Washboard

As discussed in Chapter 2, the dynamics of a single current-biased Josephson junction can be described using the Hamiltonian

$$H = 4E_c\hbar^{-2}p_\gamma^2 - E_J(\cos\gamma + J\gamma), \tag{3.1}$$

where γ is an extended coordinate $-\infty < \gamma < \infty$, $J = I/I_c$, and $p_\gamma = -i\hbar d/d\gamma$. This Hamiltonian is equivalent to a particle in a washboard potential. To explore the dynamics near a minimum of the washboard we define a scale factor α by

$$\alpha = \left(\frac{8E_c}{E_J}\right)^{1/4}(1-J^2)^{-1/8}, \tag{3.2}$$

the plasma frequency ω_0

$$\omega_0 = \hbar^{-1}\sqrt{8E_cE_J}(1-J^2)^{1/4}, \tag{3.3}$$

and perform the canonical transformation

$$\begin{aligned} x &= \alpha^{-1}(\gamma - \arcsin J) \\ p &= \alpha p_\gamma. \end{aligned} \tag{3.4}$$

Neglecting an arbitary constant of energy we find

$$H/\hbar\omega_0 = \frac{1}{2}\hbar^{-2}p^2 + \alpha^{-2}\left(1 - \cos(\alpha x) + J(1-J^2)^{-1/2}(\sin(\alpha x) - \alpha x)\right). \qquad (3.5)$$

This transformation sets the potential minimum at $x = 0$, and for small displacements about the minimum the particle will oscillate with the plasma frequency ω_0. There is a potential barrier that separates the bound motion in the well from free running motion down the washboard. If we measure the barrier height in units of $\hbar\omega_0$, we find that the number of harmonic oscillator states that can be supported in the well is

$$N_s = \frac{\Delta U}{\hbar\omega} = 2^{-1/2}\left(\frac{E_J}{E_c}\right)^{1/2}\left((1-J^2)^{1/4} - J(1-J^2)^{-1/4}\arccos J\right). \qquad (3.6)$$

The relevant region of this potential is shown in Fig. 3.1, for realistic junction parameters and N_s near 3.

Josephson's equations show that the voltage across the junction is

$$V = (\Phi_0/2\pi)d\gamma/dt. \qquad (3.7)$$

If the particle is bound in one of the wells of the washboard, its average velocity is zero, and thus the junction exhibits zero average voltage ($V_{\rm dc}$). However, if the junction is unbound, the particle freely runs down the washboard with $V \neq 0$, until any dissipation from the environment becomes non-negligible. Quantum mechanically, if the system has $V_{\rm dc} = 0$ for $t < 0$, then it can be associated with a state that is localized in a well of the washboard. Through time evolution, this state will tunnel to the unbound region, eventually yielding a nonzero voltage. The escape rate has a characteristic dependence on bias current and temperature, and is dominated by

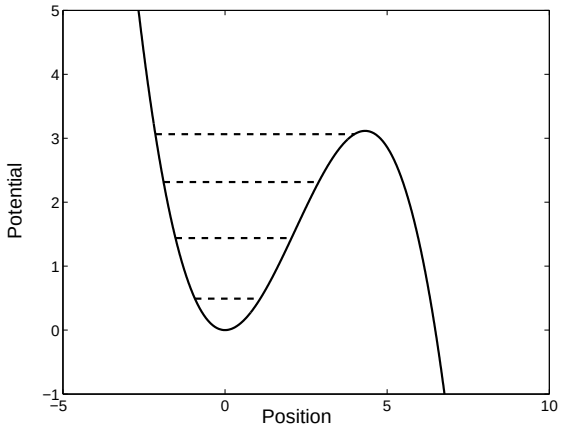

Figure 3.1: Washboard potential with typical Josephson junction parameters ($C_J =$ 6pF, $I_c = 20\mu$A, $I = 0.99I_c = 19.8\mu$A) and a reduced barrier height $N_s \sim 3$. The relevant energy levels in a metastable well are indicated by the dashed lines. The length and energy scale have been scaled by α and $\hbar\omega_0$ (see text).

quantum tunneling at low temperatures. This phenomenon of macroscopic quantum tunneling has been seen experimentally by several groups [81, 84]. Furthermore, if microwaves are applied to the junction, then for certain frequencies there is a clear enhancement of the tunneling rate [85, 146]. This enhancement occurs in a way that is consistent with a set of energy levels associated with the metastable well.

Strictly speaking, these energy levels are not true energy levels at all, but the equivalent of scattering resonances. That is, the initially localized state of the system is actually a superposition of the true eigenstates. These eigenstates are the continuum eigenstates of the Hamiltonian with the natural Hilbert space $L^2(-\infty, \infty)$. This metastable state eventually evolves into a state with appreciable amplitude to be found outside the well, and does so with approximate exponential

decay. Microwaves can drive transitions predominantly to localized states near a resonance in the continuum. If these states are sufficiently long-lived, the lowest two can be used as the two states of a qubit.

In this Chapter we introduce a set of analytical tools that can be used to characterize the resonances of the washboard. The washboard is in fact an example of the more general Wannier-Stark problem, originally studied in the context of an electron in a crystal and a homogeneous static electric field. This problem is in fact quite old and sometimes controversial. In 1960, Wannier proposed to analyze this problem in terms of states localized about the minima of the potential [147]. In a periodic potential with zero field, the energy eigenvalues are in fact energy bands, labelled by the band index n and the quasimomentum k. Wannier functions are the localized states formed by superpositions over the quasimomentum. However, the band index is no longer a good quantum number in the presence of an electric field, and because of this Wannier's use of localized functions labelled by n came under strong criticism from Zak [148], with subsequent discussion in [149, 150]. A concise review of the literature on this subject can be found in the paper by Krieger and Iafrate [133] (for a longer review see [151]).

There has been a revival of interest in Wannier-Stark systems due to recent experiments with electrons in superlattices and with cold neutral atoms in accelerated optical lattices. A number of theoretical studies have used the Wannier-Stark picture of a ladder of localized states in each metastable well [152, 153, 154, 155, 156, 157]. The experiments have included the observation of Bloch oscillations [158], the Wannier-Stark ladder [159, 160, 161], and various tunneling experiments with

non-exponential decay [162, 163, 164]. The theoretical work is reviewed in [165].

While much can be learned by studying the atomic Wannier-Stark literature, there are several issues that require special attention. First we must emphasize that for a truly infinite system with an applied field there are no discrete eigenstates and the Wannier-Stark states are actually resonances. This point is often glossed over in the theoretical formalisms, which emphasize a discrete set of states in each well of the periodic potential. Second, if we set the tilt to zero, then in the electronic and atomic experiments the number of metastable states in each well is generally small, while for the Josephson junction case there may be thousands of states. In the Josephson junction, this is determined by the ratio E_J/E_c, which for current-biased devices is of order 10^6. In the atomic physics case, the energy scale analogous to the charging energy E_c is the recoil energy $E_R = \hbar^2 k_L^2/2M$, where $k_L = 2\pi/\lambda$, λ is the wavelength of the laser used to create the optical potential, and M is the mass of the atom. The analog of the Josephson energy E_J is the light shift V_0 (also known as the optical dipole moment), and is under experimental control, but is typically of the same order of magnitude as the recoil energy (in the experiments in [158] we find $1 < V_0/E_R < 7$). Third, the tilt achieved in the Josephson junction is such that there is virtually no overlap in energy of one well's metastable states and those of its neigboring wells, indicated in Fig. 3.2. Thus, one can approximate the single well by a quadratic-plus-cubic potential (to be described in the next chapter), and the physics is dominated by the first few levels localized in such a well. This approximation is generally not possible for the atomic systems (see, however [166]), where most of the interesting physics comes from interference between neighboring

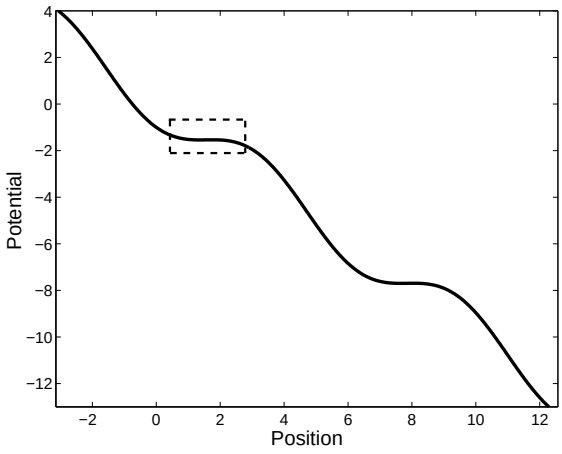

Figure 3.2: Washboard potential with typical Josephson junction parameters. The relevant energy levels are in a metastable well in the dashed box. The length scale is the true phase difference, the energy scale is E_J.

wells, such as the resonant tunneling case shown in Fig. 3.3, when the ground state in one well coincides with the excited state of the next. This regime may also be of interest for small current-biased junctions [167]. Note that the methods used in this chapter, however, are equally applicable to both the Josephson junction and Wannier-Stark situations.

We first illustrate how the resonances of a continuous spectrum can be identified by studying two simple models. The first is a simple model of alpha decay introduced by Winter in 1961 [168]. The second is a one-dimensional model of an atom in an electric field, as in the Stark effect in hydrogen. While this model was studied before, its connection to the current literature was first made by Ludviksson [169]. Each of these models is analytically soluble in terms of simple functions, which makes them ideal for the presentation of our general methods. There are four

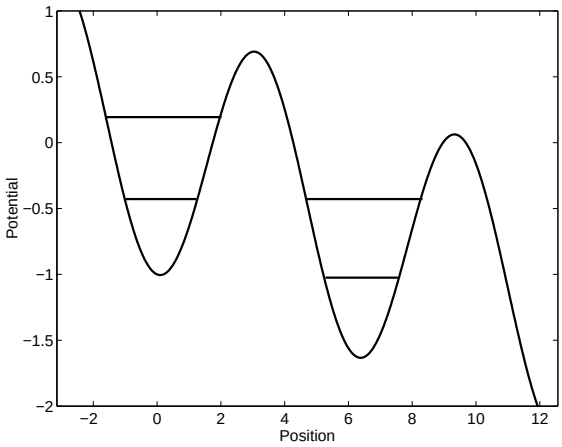

Figure 3.3: Wannier-Stark potential with atomic physics parameters. The levels in each well interact strongly with each other, here via resonant tunneling.

main methods.

The first method is to put the system in a box of length L. This bounded system has a discrete spectrum whose eigenvalues depend on L. The resonance energies, however, are only weakly dependent on L. Thus, by studying the eigenvalues as L is varied, the resonances are those that are most stable. The stabilization method we use is due to Mandelshtam, Ravuri and Taylor [170]. The virtue of this method is that it is relatively easy to implement and quickly yields a graphical interpretation of the spectrum. In the exactly solvable models the eigenvalues are determined by the zeros of simple functions, while we use numerical basis set diagonalization for the washboard.

The second method is to solve the Schrödinger equation subject to an outgoing wave boundary condition. This boundary condition, originally due to Gamow [171] and later refined by Siegert [172], yields a discrete spectrum of complex eigenvalues.

This seems contradictory, since they are complex eigenvalues of an otherwise Hermitian Hamiltonian, whose eigenvalues must be real. However, the Gamow-Siegert states are not normalizable and thus are not truly elements of the Hilbert space. The Hamiltonian need not be Hermitian when applied outside the Hilbert space, and thus its eigenvalues need not be real. The Gamow-Siegert states are sometimes incorporated into the quantum formalism through the rigged Hilbert space [173]. Nevertheless, these eigenvalues are the poles of the Green's function (also called the resolvent operator) when considered as a function on the complex energy plane. Since bound states are also poles of the Green's function (on the negative real axis), the Gamow-Siegert eigenvalues are the natural generalization of bound states. Again, the eigenvalues for our simple models can be expressed as the complex roots of simple functions. To solve the washboard, however, we show how the Gamow-Siegert boundary conditions can be achieved through the method of complex scaling, and find the eigenvalues through numerical basis set diagonalization.

The third method is to study the actual continuum eigenfunctions, which are truly eigenstates, with delta-function normalization. This method, using semiclassical WKB arguments was first used by Gurney and Condon [174] (see [175] for the early history of quantum tunneling). Near a resonance these wavefunctions exhibit a large variation in both amplitude and phase as the energy is varied. The normalization of continuum states is generally difficult in practice, although it can be done for the exactly solvable models we consider. For the washboard, we can easily use numerical integration to find energy states. To fix the normalization, we develop a normalization algorithm using asymptotic matching of the numerical solutions.

Scattering phase shifts can also be found from the numerical solutions.

The final method to consider is the time-evolution of states. For our simple models this can be done exactly in terms of an integral at each time of interest, which can be done numerically. These integrals can be deformed into the complex plane and separated into pole contributions (which are precisely the Gamow-Siegert eigenvalues) and a background term. For the washboard we use the split-operator FFT algorithm with absorbing boundaries to remove the effects of periodic boundary conditions. We defer the numerical calculations of the washboard until Chapter 5, when we discuss the current-biased junction as a single qubit.

These methods are applied to each model in the following sections, with detailed comparisons for each. Doing so illustrates how resonances can be identified from multiple points of view. While these methods are well-known, there is still some confusion that can arise when discussing resonances. This is likely due to the fact there is not one unique model of a resonance—thus we have considered several and subjected them to detailed comparison. While there has been some discussion in the past of the resonances of the washboard for Josephson junctions [176, 177, 178]), at a technical level each used a combination of the cubic approximation and further semi-classical approximations. Since their main focus was to model the first spectroscopy experiments [85] including the effects of dissipation from the outset, the achieved accuracy was sufficient. The physical picture of the resonances, however, remained lacking. To use these quantum states as elements in a quantum computer a more sophisticated approach is necessary. Thus the present chapter goes far beyond these early studies of the fundamental quantum mechanics to clearly elucidate

the resonances of the washboard.

3.1 Winter's Model

Winter analyzed a simplified model of alpha decay in 1961 [168]. This model exhibits all of the complexity of quasi-stationary resonance states, exponential decay, and both the short and long time deviations, and can be exactly solved up to an integration. Winter's model is that of a particle on the half-line with a δ-function barrier at some distance a:

$$H = \frac{p^2}{2m} + V(x), \tag{3.8}$$

$$V(x) = \left\{ \begin{array}{cc} \infty & x < 0 \\ V_0\delta(x-a) & x > 0 \end{array} \right\}. \tag{3.9}$$

In the following, we let the energy $\mathcal{E}$ be given by $\mathcal{E} = \hbar^2 E/2m$, and the coupling constant $V_0 = \hbar^2 g/2m$ (alternatively, we use units with $\hbar = 2m = 1$). The parameters E and g represent the energy and coupling constant of the δ-function.

3.1.1 Stabilization Method

The stabilization method looks at the properties of the discrete spectrum that results when the system is confined to a box. Thus, we modify the potential and look at the eigenfunctions of the differential equation

$$-\frac{d^2\Psi}{dx^2}(x) + v(x)\Psi(x) = E\Psi(x) \tag{3.10}$$

with the potential $v(x) = 2m\hbar^{-2}V(x)$:

$$v(x) = \left\{ \begin{array}{cc} \infty & x < 0 \\ g\delta(x-a) & 0 < x < L \\ \infty & L < x \end{array} \right\}. \tag{3.11}$$

Due to the hard walls of the potential, the boundary conditions are $\Psi(0) = \Psi(L) = 0$. Since we have a free particle in the absence of the δ-function, we can write

$$\Psi(x) = A_k \left\{ \begin{array}{ll} \sin(kx)\sin(kL-ka) & 0 < x < a \\ \sin(ka)\sin(kL-kx) & a < x < L \end{array} \right\}. \tag{3.12}$$

This form satisfies the boundary conditions, and has energy $E = k^2$. The normalization constant has the explicit form

$$A_k = 2k^{1/2} \left(\begin{array}{l} (2ka - \sin(2ka))\sin^2(kL-ka) \\ +(2kL - 2ka - \sin(2kL-2ka))\sin^2(ka) \end{array} \right)^{-1/2}. \tag{3.13}$$

To handle the presence of the δ-function, we integrate the Schrödinger equation (3.10) with $v(x)$ in (3.11) from $a-\epsilon$ to $a+\epsilon$. We find that there is a discontinuity in the derivative of $\Psi(x)$ at $x = a$:

$$-\lim_{\epsilon \to 0} \left(\frac{d\Psi}{dx}(a+\epsilon) - \frac{d\Psi}{dx}(a-\epsilon) \right) + g\Psi(a) = 0. \tag{3.14}$$

Substituting our form for the wavefunction, (3.12), into (3.14), we find that not every value of k is allowed, but rather k must satisfy the quantization condition

$$F(k) = k\sin(kL) + g\sin(ka)\sin(kL-ka) = 0. \tag{3.15}$$

$F(k)$ is plotted in Fig. 3.4. There are two parts to $F(k)$. The first term is independent of g, and corresponds to the full square well with walls at $x = 0$ and $x = L$, whose eigenvalues would be given by $\sin(kL) = 0$. For large g this term can usually be ignored. The second term in (3.15), however, incorporates the δ-function, and has the interesting physics. It is a product of $\sin(ka)$, whose roots ($k_n = n\pi/a$) give the eigenvalues in the smaller left square well, and $\sin(kL-ka)$, whose roots are the eigenvalues in the large right square well ($k_n = n\pi/(L-a)$) (see Fig.3.5).

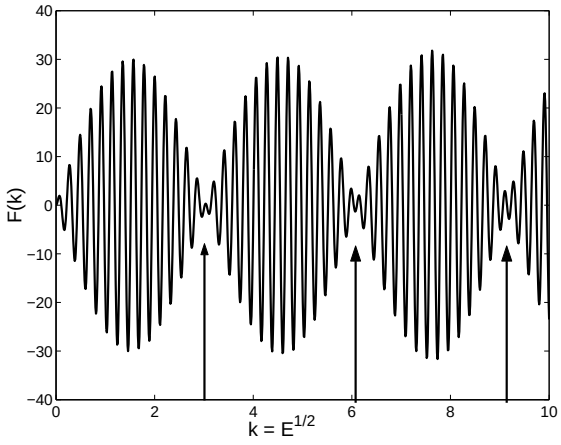

Figure 3.4: Quantization condition $F(k)$, plotted with $g = L = 30$ and $a = 1$. The roots k_* of F yield the allowed energies $E = k_*^2$. The discrete resonance levels appear near the minima of the overall modulation, here indicated by the arrows near $\pi, 2\pi$ and 3π.

Their multiplication yields the characteristic modulation pattern shown in the figure, where the slow oscillations are due to the small well and the fast oscillations are from the large well. Note that near either of these sets of roots the probability to be in the other well is necessarily small due to the form of the wavefunction, i.e. if $\sin(ka) = 0$, then $\Psi(x > a) = 0$. Thus, the picture we see is that, in general, there are two sets of eigenvalues, the first corresponding to states localized in the left well with

$$k_n^{(1)} \simeq \frac{n\pi}{a}\left(1 - \frac{1}{ga}\right) \tag{3.16}$$

where we have included the first order effect of g^{-1}; the second set of states are localized in the right well with

$$k_m^{(2)} \simeq \frac{m\pi}{L-a}\left(1 - \frac{1}{g(L-a)}\right). \tag{3.17}$$

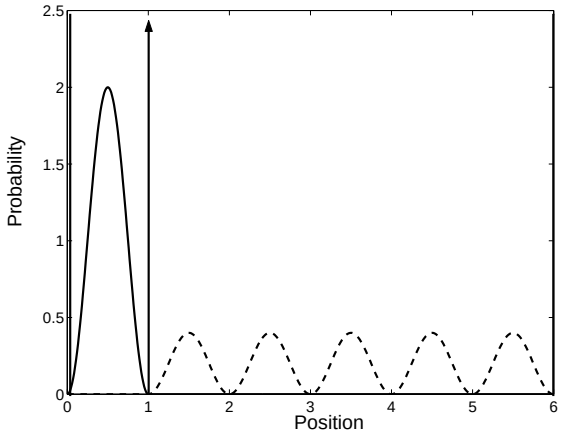

Figure 3.5: Schematic illustration of left and right well eigenfunctions, valid for $g \to \infty$, $L = 6$ and $a = 1$. The solid curve denotes the probability density of the ground state of the left well (from $x = 0$ to $x = 1$). The dashed curve denotes an excited state of the right well (from $x = 1$ to $x = 6$). The arrow indicates the δ-function barrier. For this particular choice of L, the two states are degenerate. For finite g, the true eigenstates are even and odd superpositions of these states.

For certain values of L, an eigenvalue of the right well would become degenerate with one in the left. This is schematically illustrated in Fig. 3.5. From (3.16) and (3.17), states will be degenerate if we set

$$L/a \simeq 1 + m/n - \frac{1}{ga}(1 - m/n). \tag{3.18}$$

In this case we find that there is no degeneracy, but rather an avoided level crossing. That is, if we substitute (3.18) for L and $k = k_n^{(1)} + \Delta k = k_m^{(2)} + \Delta k$ into our eigenvalue equation (3.15), then to lowest order we find (after some algebra)

$$\Delta k^2 = \frac{n^2\pi^2}{g^2a^2}\frac{1}{a^2(L/a - 1)}. \tag{3.19}$$

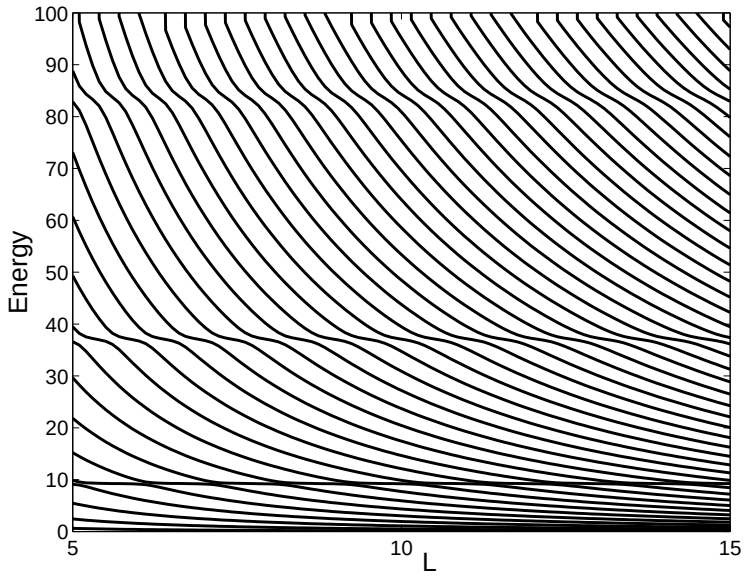

Figure 3.6: Energy eigenvalues of discrete δ-well with $g = 30$ and $a = 1$. Each curve represents the corresponding eigenvalue $E_n(L)$ as the length L is increased. The plateaus near π^2, $4\pi^2$ and $9\pi^2$ indicate the energies of discrete resonance states which are localized in the left well.

This shows that for large g the eigenvalues have split into $k_n^{(1)} \pm \Delta k$. Note that our expressions are simply given to lowest order in g^{-1}. These can be systematically improved and are an excellent guide to understanding the exact results given by the numerical roots of the eigenvalue equation. An example of this discrete spectrum is shown in Fig. 3.6, as L is increased. The states in the left well are nearly stable, independent of L, except near each avoided level crossing. These states are the resonances of the δ-well, and this figure is called the stablization diagram.

Now, one can imagine that in the limit that $L \to \infty$ the discrete states of the right well have disappeared, leaving only the resonances. The stabilization method

reveals this limit from the finite L eigenvalue curves, such as Fig. 3.6. First, we consider the discrete density of states

$$\rho(E) = \mathrm{tr}[\delta(E - H)] = \sum_n \delta(E - E_n). \tag{3.20}$$

By a suitable averaging of $\rho(E)$, one can extract out the continuum and the resonance. That is, near a resonance one expects the density of states $\rho(E) = \rho_R(E) + \rho_0(E)$ to have a background term $\rho_0(E)$ and resonance contribution $\rho_R(E)$, often taken to have the simple Lorentzian form

$$\rho_R(E) = \frac{1}{\pi} \frac{\Gamma/2}{(E - E_0)^2 + (\Gamma/2)^2} \tag{3.21}$$

where E_0 is the position of the resonance and Γ the full width. The background contribution $\rho_0(E)$ can often be identified with the continuum when the perturbating potential is zero. In our particular case $\rho_0(E)$ can be written as an explicit function of E and L:

$$\rho_0(E) = L \left(\frac{m}{2\pi^2\hbar^2}\right)^{1/2} E^{-1/2} \to L \frac{1}{2\pi E^{1/2}}, \tag{3.22}$$

where we have used dimensionless units by the replacement $\hbar = 1$ and $m = 1/2$. We remove this background level density and define the continuum level density

$$\Delta(E) = \rho(E) - \rho_0(E). \tag{3.23}$$

Mandelshtam, Ravuri and Taylor [170] proposed a simple averaging procedure to extract $\Delta(E)$. That is, if we calculate the eigenvalues in a box, both the eigenstates and the density of states are functions of the box size L. Averaging $\rho(E)$ in (3.20) over L we find that

$$\rho(E) = \frac{1}{L_2 - L_1} \int_{L_1}^{L_2} dL \rho_L(E) = \frac{1}{L_2 - L_1} \sum_n \int_{L_1}^{L_2} dL \delta(E - E_n(L)). \tag{3.24}$$

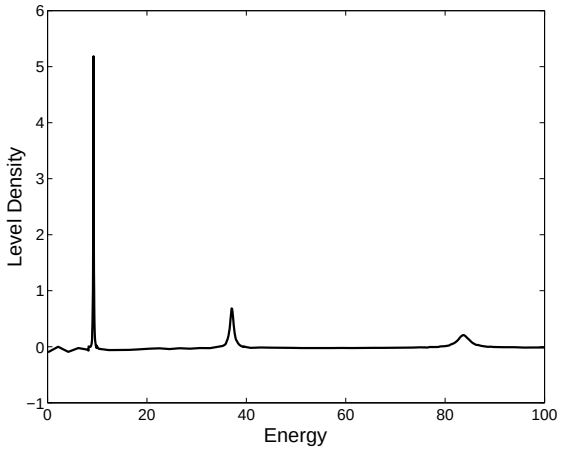

Figure 3.7: Continuum level density numerically constructed by the stabilization method, with $g = 30$ and $a = 1$.

To perform this integral we must sum over all values of L such that $E_n(L) = E$. Using $\delta(f(x)) = |f'(0)|^{-1}\delta(x)$ we find the result

$$\rho(E) = \frac{1}{L_2 - L_1} \sum_{E_n(L)=E} \left| \frac{dE_n}{dL} \right|^{-1} . \tag{3.25}$$

This equation has an obvious graphical meaning: sum the inverse slopes of the eigenvalue curves that cross energy E. At energies near the stable eigenvalues dE/dL is near zero, and thus there is a peak in the level density. Subtracting off the averaged density of states of a free particle, we show the continuum level density $\Delta(E)$ in Fig. 3.7.

3.1.2 Green's Function and Complex Eigenvalue

We now consider the complex eigenvalues of the Hamiltonian. As discussed in the introduction, the Gamow-Siegert states are not in the Hilbert space. However, in certain expansions of the resolvent or the time-evolution operator the complex poles

of the Green's function $G^+(E) = (E + i\epsilon - H)^{-1}$ can be used. This is due to the following alternative definition

$$G^+(E) = -i \int_0^\infty dt \exp[i(E + i\epsilon - H)t]. \tag{3.26}$$

The Green's function is proportional to the Fourier transform of the retarded propagator (time evolution operator), and will arise when one considers energy-conserving transitions. The introduction of $i\epsilon$ ensures convergence of the integral, and this operator plays a fundamental role in formal scattering theory [179], aspects of which we will use below.

Of particular interest are the poles of the Green's function. We have in fact, implicitly encountered these, in the form of the Lorentzian density of states formula (3.21), which is the simplest formula giving a pole in the complex energy plane:

$$\rho_R(E) = \frac{1}{\pi} \frac{\Gamma/2}{(E - E_0)^2 + (\Gamma/2)^2} = \frac{\Gamma}{2\pi} \frac{1}{(E - E_0 - i\Gamma/2)(E - E_0 + i\Gamma/2)}. \tag{3.27}$$

In this section we first show how the exact Green's function can be constructed, and then how the complex poles are precisely those associated with the Gamow-Siegert states.

The Green's function satisfies the differential equation

$$\left(E + \frac{d^2}{dx^2} - V(x)\right) G^+(x, x'; E) = \delta(x - x'). \tag{3.28}$$

Note that the + (which we now drop) implies a particular choice of boundary condition, namely we solve this equation subject to the condition that $G(x, x'; E)$ remain bounded as $x, x' \to \infty$ if E has a positive imaginary part ($i\epsilon$). First we consider the

free Green's function. A solution satisfying the boundary conditions, with $E = k^2$, is

$$G_0(x, x') = A_k \left\{ \begin{array}{ll} \sin(kx)e^{ikx'} & 0 < x < x' \\ \sin(kx')e^{ikx} & 0 < x' < x \end{array} \right\}. \tag{3.29}$$

To fix A_k, we must treat the δ-function. Integrating (3.28) from $x = x' - \epsilon$ to $x = x' + \epsilon$ we find

$$\left(\frac{dG_0}{dx}(x' + \epsilon, x') - \frac{dG_0}{dx}(x' - \epsilon, x') \right) = 1. \tag{3.30}$$

Substituting (3.29) into (3.30) yields $A_k = -1/k$. Now we consider the full Green's function of $H = H_0 + V$. In operator terms we have

$$(E - H_0)G - VG = I \tag{3.31}$$

Multiplying by $G_0 = (E - H_0)^{-1}$ and using $G_0(E - H_0) = I$ and rearranging yields

$$G = G_0 + G_0 V G, \tag{3.32}$$

which in coordinate-space is the integral equation

$$G(x, x'; E) = G_0(x, x'; E) + \int dy G_0(x, y; E) V(y) G(y, x'; E). \tag{3.33}$$

Since $V(y) = g\delta(y - a)$ this integration is trivial

$$G(x, x'; E) = G_0(x, x'; E) + g G_0(x, a; E) G(a, x'; E) \tag{3.34}$$

If we set $x = a$ we can solve (3.34) for $G(a, x'; E)$

$$G(a, x'; E) = \frac{G_0(a, x'; E)}{1 - g G_0(a, a; E)}. \tag{3.35}$$

Altogether we have

$$G(x, x'; E) = G_0(x, x'; E) + \frac{G_0(x, a; E) G_0(a, x'; E)}{g^{-1} - G_0(a, a; E)}. \tag{3.36}$$

This is the full Green's function for the problem, and has been solved by the simple properties of the δ-function. This is an example of what is sometimes called a separable potential, since V has the simple operator form $V_0|v\rangle\langle v|$, with $\langle x|v\rangle = \delta(x-a)$. Now, the poles of the Green's function can only come from the denominator of the second term in (3.36)

$$g^{-1} - G_0(a,a;E) = g^{-1} + k^{-1}\sin kae^{ika} = 0. \tag{3.37}$$

We now wish to show that this is a complex eigenvalue of the Schrödinger equation.

A complex eigenvalue is found by imposing outgoing wave boundary conditions, thus we consider the wavefunction

$$\Psi(x) = \left\{ \begin{array}{ll} \sin(kx)e^{ika} & 0 < x < a \\ \sin(ka)e^{ikx} & a < x \end{array} \right\}. \tag{3.38}$$

Now, we must integrate over the δ-function as in (3.14), where we found

$$-\lim_{\epsilon\to 0}\left(\frac{d\Psi}{dx}(a+\epsilon) - \frac{d\Psi}{dx}(a-\epsilon)\right) + g\Psi(a) = 0. \tag{3.39}$$

For our outgoing wave ansatz (3.38) we find that k must satisfy the complex eigenvalue equation

$$-\left(ike^{ika}\sin(ka) - ke^{ika}\cos(ka)\right) + ge^{ika}\sin ka = 0 \tag{3.40}$$

which can be simplified to

$$g^{-1} + k^{-1}e^{ika}\sin ka = 0. \tag{3.41}$$

Thus, the complex poles of the Green's function (3.37) are precisely the eigenvalues of the Gamow-Siegert states. As bound states are also poles of the Green's function, this is a traditional method of identifying metastable states, i.e. resonances.

In the limit of large g, we can solve the eigenvalue equation (3.41) perturbatively, to find

$$k_n \approx \frac{n\pi}{a}\left(1-(ga)^{-1}+(ga)^{-2}-in\pi(ga)^{-2}\right) \tag{3.42}$$

and thus

$$E_n \approx \frac{n^2\pi^2}{a^2}\left(1-2(ga)^{-1}\right)-i\frac{2n^3\pi^3}{a^2}(ga)^{-2}. \tag{3.43}$$

The real part is the resonance energy E_0, the imaginary part the half-width $\Gamma/2$.

Finally, we note that having computed the Green's function we can compute the exact continuum level density. By Cauchy's formula for the pinciple value

$$G(E)=\frac{1}{E-H+i\epsilon}=P\left(\frac{1}{E-H}\right)+i\pi\delta(E-H), \tag{3.44}$$

we can write the continuum level density in the form [180]

$$\begin{aligned}\Delta(E) &= \mathrm{tr}[\delta(E-H)-\delta(E-H_0)]\\ &= -\pi^{-1}\mathrm{Im}\left(\mathrm{tr}[G(E)-G_0(E)]\right).\end{aligned} \tag{3.45}$$

Note that for a continuous spectrum each individual trace in (3.45) is divergent, although their difference is not. For Winter's model the trace can be computed exactly. Using the operator form of (3.36)

$$G=G_0+\frac{G_0|a\rangle\langle a|G_0}{g^{-1}-\langle a|G_0|a\rangle}, \tag{3.46}$$

and the cyclic property of the trace ($\mathrm{tr}(AB)=\mathrm{tr}(BA)$) we find

$$\mathrm{tr}[G-G_0]=\frac{\langle a|G_0^2|a\rangle}{g^{-1}-\langle a|G_0|a\rangle}. \tag{3.47}$$

Finally we note that

$$G_0^2=\frac{1}{(E-H_0)^2}=-\frac{\partial G_0}{\partial E} \tag{3.48}$$

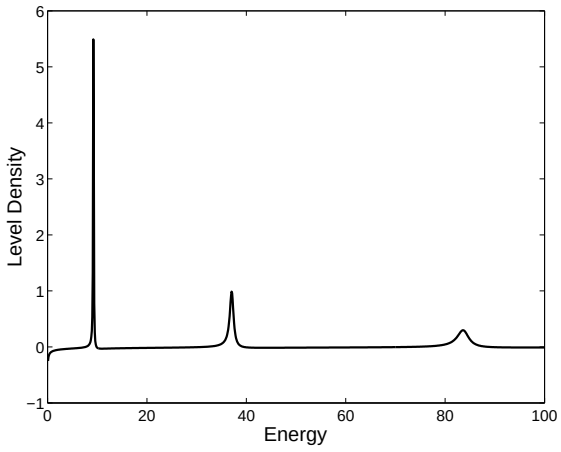

Figure 3.8: Exact continuum level density for the δ-well, constructed from the Green's function, with $g = 30$ and $a = 1$.

and thus

$$\Delta(E) = \frac{1}{\pi}\mathrm{Im}\left(\frac{\langle a|\partial G_0/\partial E|a\rangle}{g^{-1} - \langle a|G_0|a\rangle}\right). \tag{3.49}$$

The derivatives of (3.29) (with $A_k = -1/k$) are straightforward using $d/dE = (2k)^{-1}d/dk$, and the final result is

$$\Delta(E) = \frac{1}{\pi k^3}\frac{\sin^2(ka)(1 - ga/2) - ka\sin(2ka)}{2g^{-1} + 2k^{-1}\sin(2ka) + 2gk^{-2}\sin^2(ka)}. \tag{3.50}$$

Naturally, the poles of $\Delta(E)$ are the same as the Green's function. This continuum level density is plotted in Fig. 3.8. Note its resemblance to Fig. 3.7, the level density constructed from the stabilization diagram.

3.1.3 Continuum Solutions

While the discrete and complex approaches to resonances are useful, the most complete method is to consider the full continuous spectrum of the Hamiltonian. The

continuum solutions of this model are not too hard to find. Writing the wavefunction as

$$\Psi(x) = \left\{ \begin{array}{cc} A\sin(kx) & 0 < x < a \\ B\sin(kx) + C\cos(kx) & a < x \end{array} \right\}, \tag{3.51}$$

continuity at $x = a$ requires

$$A\sin(ka) = B\sin(ka) + C\cos(ka) \tag{3.52}$$

and the derivative discontinuity (3.14) requires

$$kB\cos(ka) - kC\sin(ka) - kA\cos(ka) - 2gA\sin(ka) = 0 \tag{3.53}$$

which can be solved

$$\begin{array}{ll} B & = A(1 + gk^{-1}\sin(ka)\cos(ka)) \\ C & = A(-gk^{-1}\cos^2(ka)). \end{array} \tag{3.54}$$

It remains to compute the continuum normalization integral

$$\int_0^\infty dx \Psi_E(x)\Psi'_E(x) = \delta(E - E'). \tag{3.55}$$

Before doing so, we compute the following integral

$$\begin{array}{ll} \int_0^\infty dz \cos(kz)\cos(k'z)dz & = \frac{1}{2}\int_{-\infty}^\infty dz \cos(kz)\cos(k'z) \\ & = \frac{1}{8}\int_{-\infty}^\infty dz \left(e^{i(k+k')z} + e^{-i(k+k')z} + e^{i(k-k')z} + e^{i(k'-k)z}\right) \\ & = \frac{\pi}{2}\left(\delta(k+k') + \delta(k-k')\right), \end{array} \tag{3.56}$$

and similarly

$$\int_0^\infty dz \sin(kz)\sin(k'z) = \frac{\pi}{2}\left(\delta(k-k') - \delta(k+k')\right). \tag{3.57}$$

We also compute

$$I(k,k') = \int_0^\infty dz \left(k^{-1}\sin(kz)\cos(k'z) + k'^{-1}\sin(k'z)\cos(kz)\right). \tag{3.58}$$

Note that this can be written

$$I(k,k') = \int_0^\infty dz \int_0^z dy \left(\cos(ky)\cos(k'z) + \cos(k'y)\cos(kz)\right) \tag{3.59}$$

By the symmetries of the integrand, we can extend the integration from its original wedge in the $y-z$ plane to the whole space

$$I(k,k') = \frac{1}{8}\int_{-\infty}^\infty dz \int_{-\infty}^\infty dy \left(\cos(ky)\cos(k'z) + \cos(k'y)\cos(kz)\right), \tag{3.60}$$

as these integrals factorize we can use (3.56) to show

$$I(k,k') = \pi^2\delta(k)\delta(k'). \tag{3.61}$$

Note however, that for the normalization we only need the $\delta(k-k')$ term. Substituting our wavefunction (3.51) and using (3.56) and (3.57) we find (after some algebra)

$$\int_0^\infty dx \Psi_k(x)\Psi'_k(x) = A^2\frac{\pi}{2}\delta(k-k')\left(1 + gk^{-1}\sin(ka)\cos(ka) + g^2k^{-2}\sin^2(ka)\right). \tag{3.62}$$

For continuum normalization this should be $\delta(E-E') = (2k)^{-1}\delta(k-k')$, thus

$$A^2 = \frac{1}{\pi k}\frac{1}{1 + gk^{-1}\sin(2ka) + g^2k^{-2}\sin^2(ka)}. \tag{3.63}$$

These continuum solutions have an intuitive interpretation when considering the scattering of a particle off of the potential. The nature of the scattering is found by looking at the form of the wavefunctions. Thus, a final rewrite of these continuum states is useful [181]

$$\Psi(x) = \left(\frac{1}{\pi k}\right)^{1/2}\left\{\begin{array}{ll} X(k)\sin(kx) & 0 < x < a \\ \sin(kx+\phi(k)) & a < x \end{array}\right\}, \tag{3.64}$$

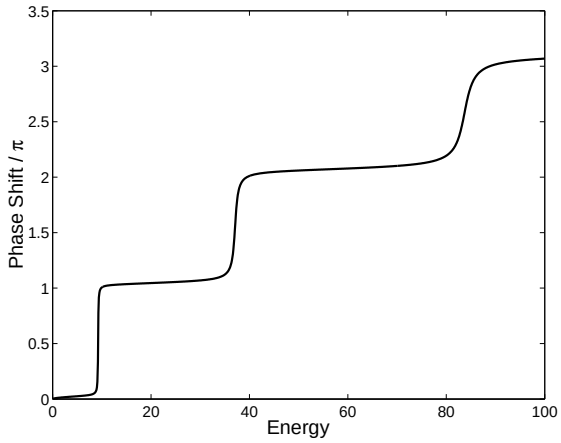

Figure 3.9: Resonant part of the scattering phase shift $\phi_R(E)$ (divided by π), with $g = 30$ and $a = 1$. At each resonance energy, the phase shift increases by π. This rapid variation allows a superposition of nearby energies to effectively cancel outside the well.

where $X(k)$ is the internal amplitude

$$X^2(k) = \frac{1}{1 + gk^{-1}\sin(2ka) + g^2k^{-2}\sin^2(ka)}, \tag{3.65}$$

and $\phi(k)$ is the scattering phase shift

$$\phi(k) = -ka + \arctan\left(\frac{ka}{ga + ka\cot(ka)}\right). \tag{3.66}$$

The phase shift has two contributions, the first is the phase shift associated with scattering off a hard wall at $x = a$, the second corresponding to scattering into (and subsequently out of) the metastable square well, thus we define $\phi_R = \phi + ka$. These functions are plotted in Figs. 3.9 and 3.10. Near the resonance energies the internal amplitude of the wavefunction goes through a maximum, and the resonant part of the phase shift quickly rises by π. In terms of a quasi-stationary state, these two

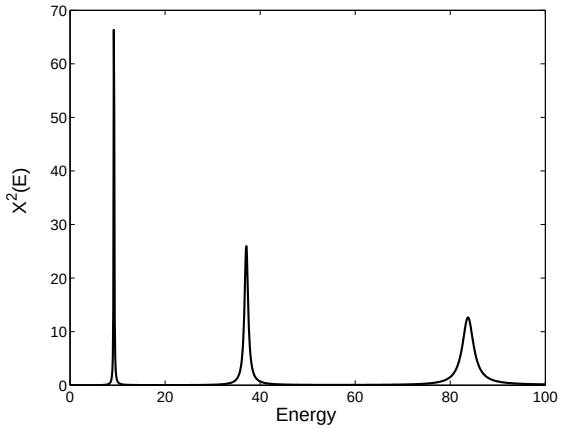

Figure 3.10: Internal amplitude (squared) $X^2(E)$, for $g = 30$. At each resonance energy, the internal amplitude is very large. This large amplitude allows the superposition of nearby energies to be highly localized in the well.

functions serve two complementary purposes. The large internal amplitude shows that a state localized in the well will have most of its overlap with the continuum states near resonance. The rapid variation of the phase shift shows that such a state will have very little amplitude outside the well, since the varying phase shift allows the external wavefunctions to cancel efficiently. Finally, by taking the derivative of the phase shift with respect to energy we find an exact relation between the continuum level density (3.50) and the phase shift (3.66)

$$\Delta(E) = \frac{1}{\pi}\frac{d\phi}{dE}. \tag{3.67}$$

3.1.4 Time Evolution

The motivation for studying the continuum states is that they can directly describe the decay of a metastable state. To understand this approach, consider a wave packet

analysis of scattering. The scattering wavefunctions (3.64) in this one-dimensional example can be written as

$$\Psi(x) \sim e^{-ikx} - Se^{ikx}, \tag{3.68}$$

where the scattering S-matrix relates the ingoing and outgoing waves, and is simply related to the phase shift

$$S(E) = \exp(i2\phi(E)). \tag{3.69}$$

The poles of the Green's function are also the poles of both the internal amplitude $X(k)$ and the S-matrix.

The scattering states have the simple time evolution

$$\Psi(x,t) \sim e^{-ikx-iEt/\hbar} - e^{ikx-iEt/\hbar+2i\phi}. \tag{3.70}$$

If we prepare an ingoing wavepacket centered at k_0, the peak of the outgoing wave will be found at the location of stationary phase, which is (with $E = \hbar^2k^2/2m$, $v = \hbar k_0/m$)

$$x = v\left(t - 2\hbar\frac{d\phi}{dE}\right). \tag{3.71}$$

Thus we find that the outgoing wave emerges after the so-called Wigner time delay [182]

$$\tau = 2\hbar\frac{d\phi}{dE}. \tag{3.72}$$

The connection between the phase shift and $\Delta(E)$ given by (3.67) shows that this delay will be longest for the resonance energies near maxima of $\Delta(E)$. For the characteristic Lorentzian (3.21), this maxima is $\Delta(E_0) = 2/\pi\Gamma$ and we find

$$\tau = 4\hbar/\Gamma. \tag{3.73}$$

Thus the width of the resonance and the time-delay of the wave-packet are directly connected, the latter associated with the preparation and subsequent decay of the metastable state.

An alternative connection can be made by constructing not an ingoing wave-packet (from ∞) which scatters off of the potential, but a state Ψ that is initially localized in the well. Since the continuum wavefunctions have large internal amplitude for energies near the resonance, the energy distribution for the localized state can be approximated by the Lorentzian form

$$|c(E)|^2 = |\langle \Psi | E \rangle|^2 \simeq \frac{1}{\pi} \frac{\Gamma/2}{(E - E_0)^2 + \Gamma^2/4}. \tag{3.74}$$

This quantity is key to the survival amplitude $A(t)$, which is

$$A(t) = \langle \Psi | e^{-iHt/\hbar} | \Psi \rangle = \int_{-\infty}^{\infty} dE |c(E)|^2 e^{-iEt/\hbar}. \tag{3.75}$$

Note that we have let the integration run from $-\infty$ to ∞, while for our particular example the energy is bounded from below—thus $c(E) = 0$ for $E < 0$. Taking the Lorentzian distribution (3.74) literally, we can perform integral in (3.75) by contour integration, picking up the pole in $|c(E)|^2$ at $E = E_0 - i\Gamma/2$, to find

$$A(t) \simeq e^{-iE_0 t/\hbar} e^{-\Gamma t/2\hbar}. \tag{3.76}$$

Since the Lorentzian distribution is not literally true (especially for $E < 0$), this expression is neither correct for short times (when energies greater the resonance are important) nor for long times (when the energies near 0 are important) [183]. Nevertheless, it is this connection that shows how a resonance yields metastable states with characteristic exponential decay.

More careful study of Winter's model reveals the deviations from exponential decay. First, if we choose the initial state to be

$$\Psi(x) = \left\{ \begin{array}{cc} (2/a)^{1/2}\sin(n\pi x/a) & 0 < x < a \\ 0 & a < x \end{array} \right\}, \tag{3.77}$$

then the energy coefficent is

$$c(E) = \frac{2^{1/2} n\pi^{1/2} a^{1/2} (-1)^n \sin(ka)}{k^{1/2}((ka)^2 - (n\pi)^2)} X(k) \tag{3.78}$$

where $X(k)$ is the internal amplitude of (3.65), and $c(E) = 0$ for $E < 0$. Inserting (3.78) for $c(E)$ into (3.75) for the survival amplitude $A(t)$ solves the problem. By deforming the contour of integration into the complex plane one can show that

$$A(t) = \sum_n C_n e^{-iE_n t} + A_0(t) \tag{3.79}$$

where the sum is over the poles E_n of $|c(E)|^2$ in the complex plane, and $A_0(t)$ is a remaining integral that extends from $E = 0$ to $E = -i\infty$. The dominant term in the sum yields exponential decay, while the remainder yields a power law. These features are shown in Fig. 3.11, where the survival probability $P(t) = |A(t)|^2$ is shown , where we consider the weak barrier $g = 6$. The lowest complex eigenvalue for this g is $k = 2.75794 - i0.140433$. Performing the energy integral numerically, we find that $P(t)$ exhibits some initial oscillations (shown in Fig. 3.12), then settles into a period of exponential decay, and finally the late stage is governed by a power law of the form $P(t) \approx Ct^{-3}$, and is determined by the density of states at low energy. This long-time deviation is expected for any system with a lower bound to the energy [183, 184].

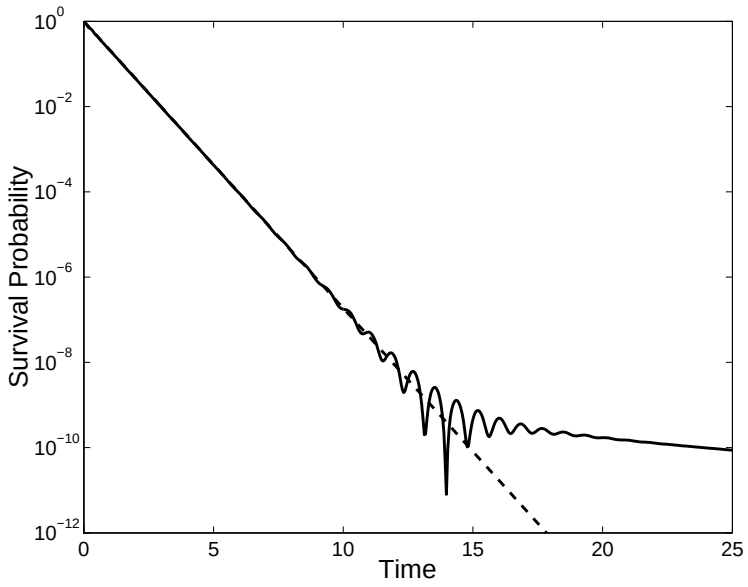

Figure 3.11: Time evolution of a quasi-stationary state in Winter's model, with $g = 6$ and $a = 1$. The localized state decays nearly exponentially (indicated by the dashed line) until $t \approx 14$, when the decay crosses over into a power law.

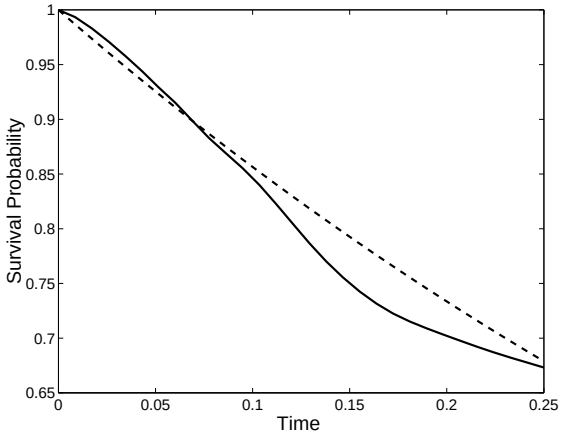

Figure 3.12: Very short time evolution of a quasi-stationary state in Winter's model, with $g = 6$. For short times, the decay of the localized state exhibits oscillations over the expected exponential decay (indicated by the dashed line).

All of these features were found in Winter's initial study, and reexamined in [185], which inspired our figure. More recent work has focused on the asymptotic form of the decaying wavepacket [186, 187], with improved expressions beyond the non-normalizable Gamow-Siegert wavefunction. Note that using pole expansions to describe the wavefunction can be quite tricky and can lead to incorrect results unless carefully analyzed (see the controversy in [188, 189, 190]). However, all of this work shows that for intermediate times the complex poles of the Green's function dominate the time evolution, and thus there is approximate exponential decay with a wavefunction that can be locally approximated by the Gamow-Siegert state.

There have been attempts to use rigged-Hilbert-space ideas to promote exponential decay from an approximate to an exact law [191, 192]. This is probably irrelevant now that the short time deviations from exponential decay have been observed experimentally [162]. Long time deviation have not been observed, probably due to the effects of continuous measurement [184]. That is, unless one can turn the measuring device on and off, the effects of continuous weak measurement will confine one's observations to the intermediate regime where the decay is predominantly exponential; this is a type of Zeno effect. Another Zeno effect is due to continuous strong measurement which forces the system into either short time decay, or no decay whatsoever [193]. These and so-called anti-Zeno effects [194] might be observable in current-biased Josephson junctions [195].

3.2 Ludviksson's Model

In this section, we consider a simple model of the Stark effect. This problem is interesting in its own right, but especially since the asymptotic properties of the potential are signficantly different from the α-decay models. In particular, the energy is not bounded from below, and the wavefunctions are suitably modified. These properties are shared with the Wannier-Stark system and the Josephson junction washboard. While this model attracted a great deal of prior attention [196, 197, 198, 199, 200], it was Ludviksson's reference to the work of Leggett and Schmid that caught our attention. It is for this reason that we, perhaps unfairly, attribute the model to him. As with Winter's model, we consider the stabilization, Gamow-Siegert, and scattering state methods. Note that the last method involves the construction of the phase shifts and S-matrix for a tilted potential, concepts necessary for the washboard.

Finally, we note that this particular model and its variations have been studied by many others since Ludviksson [201, 202, 203, 204]. The studies by Reichl and co-workers are particularly clear [205, 206, 207]. In addition, this model has recently been extended to the molecular Stark effect [208, 209]. In spite of this long history, our work is the first to introduce the continuum level density $\Delta(E)$ and its relation to the Green's function, the scattering phase shifts, and the stabilization method.

The Hamiltonian for this model is

$$H = \frac{p_z^2}{2m} - V_0\delta(z) - Fz, \tag{3.80}$$

with $p_z = -i\hbar d/dz$ and F is the force on the particle. The units can be scaled out

by letting $z = \alpha x$, with α a length scale given by

$$\alpha = \left(\frac{\hbar^2}{2mF}\right)^{1/3} \tag{3.81}$$

from which we can also define an energy scale

$$E_0 = F\alpha = \left(\frac{\hbar^2 F^2}{2m}\right)^{1/3}, \tag{3.82}$$

and a dimensionless coupling constant

$$g = \frac{V_0}{E_0\alpha} = V_0\left(\frac{4m^2}{\hbar^4 F}\right)^{1/3}. \tag{3.83}$$

Using these quantities, we can rewrite the Hamiltonian (3.80) as

$$h = H/E_0 = -\frac{d^2}{dx^2} - g\delta(x) - x. \tag{3.84}$$

We will use this h in the remainder of this section. Note that we have chosen to put the coupling constant in front of the δ-function. Alternatively, we can define $x' = gx$, and $E_0' = g^2 E_0$, in which case we have $h' = g^{-2}h$

$$h' = H/E_0' = -\frac{d^2}{dx'^2} - \delta(x') - g^{-3}x' \tag{3.85}$$

This convention is sometimes found in the literature. For any particular expression the constants F, m and $\hbar$ can be reintroduced using the scaling transformations above.

3.2.1 Stabilization Method

We place the "tilt plus δ-function" into a box of length L, and thus consider

$$-\frac{d^2\Psi}{dx^2} + v(x)\Psi(x) = E\Psi(x) \tag{3.86}$$

with

$$v(x) = \left\{ \begin{array}{cc} -g\delta(x) - x & x < L \\ \infty & x > L \end{array} \right\}. \tag{3.87}$$

The appropriate solutions to this equation are the Airy functions $\mathrm{Ai}(-x-E)$ and $\mathrm{Bi}(-x-E)$, whose properties are summarized in the Appendix. Since we require $\Psi(x \to -\infty) \to 0$, we have

$$\Psi(x) = N_E \left\{ \begin{array}{cc} \mathrm{Ai}(-x-E) & x < 0 \\ c_A \mathrm{Ai}(-x-E) + c_B \mathrm{Bi}(-x-E) & 0 < x < L \end{array} \right\}. \tag{3.88}$$

Continuity of the wavefunction at $x = 0$ requires

$$c_A \mathrm{Ai}(-E) + c_B \mathrm{Bi}(-E) = \mathrm{Ai}(-E), \tag{3.89}$$

while the presence of the δ-function is handled as in (3.14) (with $g \to -g$) to find

$$c_A \mathrm{Ai}'(-E) + c_B \mathrm{Bi}'(-E) - \mathrm{Ai}'(-E) - g\mathrm{Ai}(-E) = 0. \tag{3.90}$$

We solve (3.89) and (3.90) for c_A and c_B, and using (A.4) from the Appendix we find

$$\begin{array}{ll} c_A & = 1 - \pi g \mathrm{Ai}(-E)\mathrm{Bi}(-E), \\ c_B & = \pi g \mathrm{Ai}^2(-E). \end{array} \tag{3.91}$$

Finally, the wavefunction (3.88) must vanish at $x = L$, thus we have a quantization condition

$$F(E) = c_A \mathrm{Ai}(-E-L) + c_B \mathrm{Bi}(-E-L) = 0. \tag{3.92}$$

The normalization constant is found using (A.4), (A.18) from the Appendix, and (3.92):

$$N_E = \left(\begin{array}{l} (c_A \mathrm{Ai}'(-E-L) + c_B \mathrm{Bi}'(-E-L))^2 \\ -2g\mathrm{Ai}(-E)\mathrm{Ai}'(-E) - g^2 \mathrm{Ai}^2(-E) \end{array} \right)^{-1/2}. \tag{3.93}$$

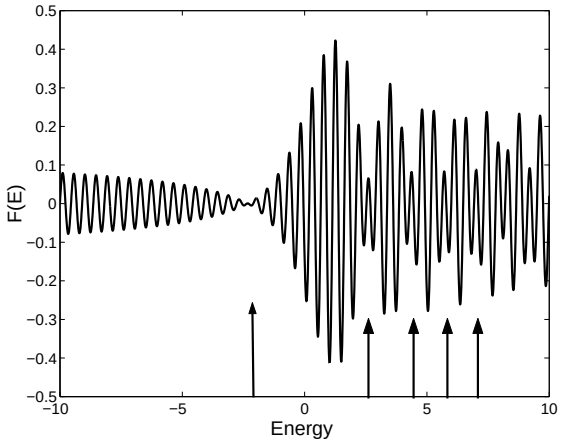

Figure 3.13: Quantization condition $F(E)$, plotted with $g = 3$, $L = 200$. The arrows discrete resonance levels appear near the minima of the overall modulation, here indicated by the arrows.

The quantization condition (3.92) can be rewritten in the following form

$$\begin{aligned} F(E) \quad &= \mathrm{Ai}(-E-L) + \pi g \mathrm{Ai}(-E) \\ &\times \{\mathrm{Ai}(-E)\mathrm{Bi}(-E-L) - \mathrm{Bi}(-E)\mathrm{Ai}(-E-L)\} = 0, \end{aligned} \tag{3.94}$$

and is shown in Fig. 3.13. Just as in the square-well potential, this function has two parts. The first term, independent of g, is zero for eigenvalues of the "wedge" potential formed by the tilt and the wall at $x = L$. For large g this can usually be neglected. The second term is the product of two eigenvalue conditions. The first ($\mathrm{Ai}(-E)$) is zero for the wedge potential with a wall at $x = 0$. The eigenvalues for these states are

$$E_n^{(1)} \simeq a_n + g^{-1} \tag{3.95}$$

with

$$\mathrm{Ai}(-a_n) = 0 \tag{3.96}$$

and the corresponding states are highly localized in the left well with c_A and c_B both proportional to g^{-1}:

$$\begin{array}{ll} c_A & \simeq -\pi g^{-1}\mathrm{Ai}'(-a_n)\mathrm{Bi}'(-a_n), \\ c_B & \simeq \pi g^{-1}(\mathrm{Ai}'(-a_n))^2. \end{array} \tag{3.97}$$

The second eigenvalue condition has zeros for the eigenvalues of the "trapezoid" potential with walls at $x = 0$ and $x = L$, and the states predominantly in the region $0 < x < L$. The energies are approximately

$$E_m^{(2)} \simeq b_m - g^{-1}\left(1 - \mathrm{Ai}(-b_m)^2(\mathrm{Ai}(-b_m - L))^{-2}\right) \tag{3.98}$$

with

$$\mathrm{Ai}(-b_m)\mathrm{Bi}(-b_m - L) - \mathrm{Bi}(-b_m)\mathrm{Ai}(-b_m - L) = 0, \tag{3.99}$$

and states localized in the right well.

Thus, for large g we find that there are two sets of eigenvalues. By tuning L one can bring these two sets of levels into near degeneracy, which becomes an avoided crossing. However, for $g > 0$, there is an additional eigenvalue that is associated with the bound state of the delta function with zero tilt. This has the wavefunction

$$\Psi_b(x) = e^{-g|x|/2} \tag{3.100}$$

and eigenvalue

$$E_b = -\frac{1}{4}g^2. \tag{3.101}$$

This energy can be found by consider the eigenvalue equation (3.94) in the limit that $E < 0$, $|E| \gg 1$, and $L \gg |E|$. Under these conditions we have $\mathrm{Bi}(-E) \gg \mathrm{Ai}(-E)$, and our eigenvalue equation reduces to

$$F(E) \simeq \mathrm{Ai}(-E - L)\left(1 - g\pi\mathrm{Ai}(-E)\mathrm{Bi}(-E)\right) = 0. \tag{3.102}$$

Using the asymptotic properties of the Airy functions we have

$$\mathrm{Ai}(-E)\mathrm{Bi}(-E) \simeq \frac{1}{2\pi}(-E)^{-1/2}. \tag{3.103}$$

Substituting (3.103) into (3.102) we can solve for E:

$$E = -\frac{1}{4}g^2. \tag{3.104}$$

Note that this approximate eigenvalue equation yields $c_A = 0$, and the asymptotic forms of the Airy functions with $|x| \ll |E_b|$ yields the untilted ground state wavefunction (3.100). These states are illustrated in Fig. 3.14.

The stabilization diagram Fig. 3.15 illustrates all of these properties of the spectrum. The density of states for the tilted well with $g = 0$ can be found using the WKB method, or equivalently, from the asymptotic zeros of the Airy function. That is, with no δ-function, the roots of the Airy function $\mathrm{Ai}(-E-L)$ are approximately given by (with $n \geq 1$).

$$E_n = -L + \left(\frac{3\pi(n-1/4)}{2}\right)^{2/3}. \tag{3.105}$$

We can solve this for large n to yield the number of levels less than E:

$$N(E) = \frac{2}{3\pi}(E+L)^{3/2}. \tag{3.106}$$

The background density of states is then

$$\rho_0(E) = \frac{dN}{dE} = \frac{1}{\pi}(E+L)^{1/2} \tag{3.107}$$

Subtracting this, we plot the continuum level density in Fig. 3.16. Clearly seen is the bound state resonance, and the resonances associated with the wedge potential for $x < 0$. Suprisingly, these are not the only resonances in the system; a resonance which is always under the barrier will be found in the next section.

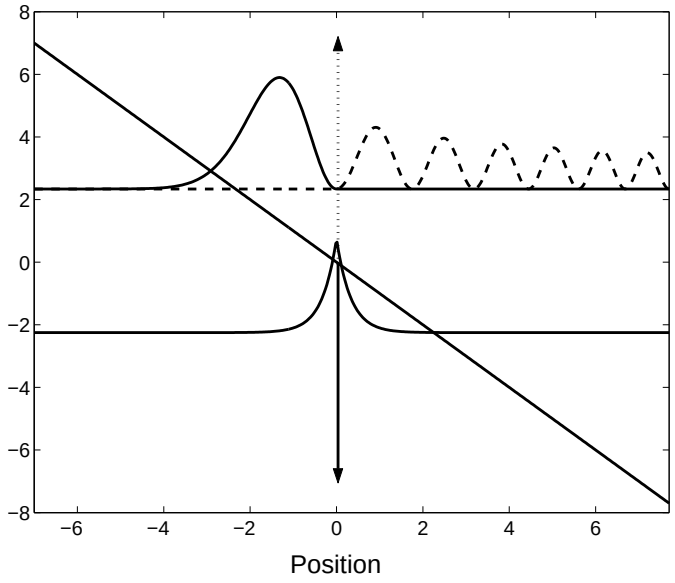

Figure 3.14: Schematic illustration of left and right well eigenfunctions, valid for $g \to \infty$ and $L \approx 7.7027$. The upper solid curve denotes the probability density of the ground state of the left well. The dashed curve denotes an excited state of the right well. The solid and dotted arrows indicate the attractive and repulsive δ-function barriers. For the former, the probability density of the bound state is shown in the lower solid curve.

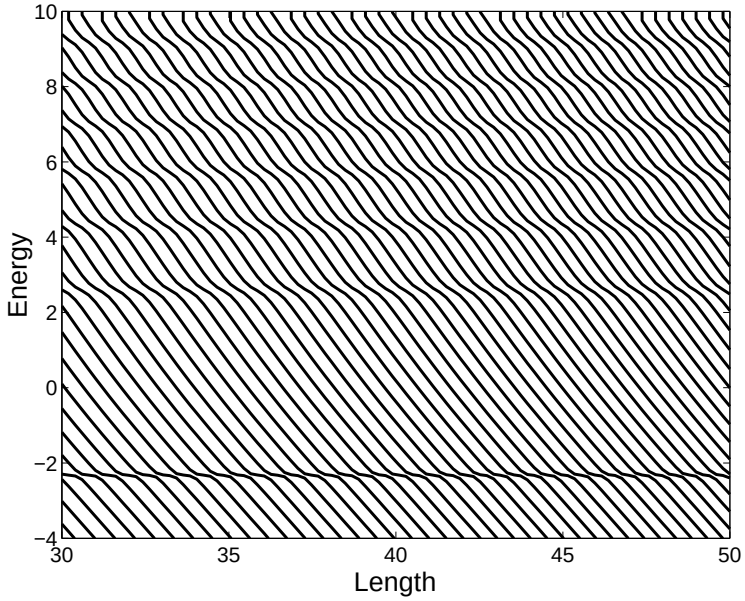

Figure 3.15: Energy eigenvalues of the tilted δ-function with $g = 3$. Each curve represents the corresponding eigenvalue $E_n(L)$ as the length L is increased. The plateaus indicate the discrete resonance levels of the left well.

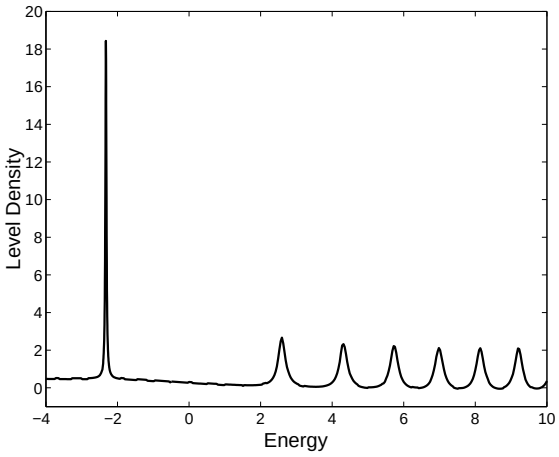

Figure 3.16: Continuum level density numerically constructed by the stabilization method, with $g = 3$.

3.2.2 Green's Function and Complex Eigenvalue

The Hamiltonian is sufficiently simple that exact results can be obtained for the Green's function. Without the δ-function potential term, the Green's function satisfies

$$\left(E + \frac{d^2}{dx^2} + x\right) G(x, x'; E) = \delta(x - x'). \tag{3.108}$$

For $x > x'$, the Green's function should represent an outgoing wave formed by the linear combination $\mathrm{Bi}(-x - E) + i\mathrm{Ai}(-x - E)$, thus we have

$$G_0(x, x'; E) = -\pi \left\{ \begin{array}{ll} \mathrm{Ai}(-x - E)[\mathrm{Bi}(-x' - E) + i\mathrm{Ai}(-x' - E)] & x < x' \\ \mathrm{Ai}(-x' - E)[\mathrm{Bi}(-x - E) + i\mathrm{Ai}(-x - E)] & x > x' \end{array} \right\}, \tag{3.109}$$

where the normalization $(-\pi)$ has been fixed by integrating over $\delta(x - x')$ in (3.108). The presence of the δ-function in H can be treated by solving the operator equation

$$G = G_0 + G_0 V G \tag{3.110}$$

with $V = -g|v\rangle\langle v|$ and $\langle x|v\rangle = \delta(x)$. Acting on (3.110) with $\langle v|$, we can solve for $\langle v|G_0$, and substituting back yields

$$G = G_0 - \frac{G_0|v\rangle\langle v|G_0}{g^{-1} + \langle v|G_0|v\rangle} \tag{3.111}$$

which is

$$G(x, x'; E) = G_0(x, x'; E) - \frac{G_0(x, 0; E) G_0(0, x'; E)}{g^{-1} + G_0(0, 0; E)}. \tag{3.112}$$

The poles of this Green's function are the poles of the denominator of (3.112)

$$g^{-1} + G_0(0, 0; E) = g^{-1} - \pi \mathrm{Ai}(-E)[\mathrm{Bi}(-E) + i\mathrm{Ai}(-E)]. \tag{3.113}$$

These poles correspond to Gamow-Siegert states, which are wavefunctions of the form

$$\Psi(x) = \left\{ \begin{array}{cc} \mathrm{Ai}(-x-E)[\mathrm{Bi}(-E)+i\mathrm{Ai}(-E)] & x<0 \\ \mathrm{Ai}(-E)[\mathrm{Bi}(-x-E)+i\mathrm{Ai}(-x-E)] & x>0 \end{array} \right\}. \tag{3.114}$$

Inserting (3.114) into the Schrödinger equation (3.86), and integrating over the δ-function yields the complex eigenvalue equation

$$\begin{array}{r} \mathrm{Ai}(-E)[\mathrm{Bi}'(-E)+i\mathrm{Ai}'(-E)] - \mathrm{Ai}'(-E)[\mathrm{Bi}(-E)+i\mathrm{Ai}(-E)] \\ -g\mathrm{Ai}(-E)[\mathrm{Bi}(-E)+i\mathrm{Ai}(-E)] \end{array} = 0, \tag{3.115}$$

which can be simplified using (A.4) to yield

$$\pi^{-1} - g\mathrm{Ai}(-E)[\mathrm{Bi}(-E)+i\mathrm{Ai}(-E)] = 0. \tag{3.116}$$

Comparison shows that the roots of (3.116) are indeed the poles of the Green's function in (3.113).

There are three classes of poles. Inspection of (3.116) for large g shows that one class corresponds to the zeros of $\mathrm{Ai}(-E)$, i.e. states bound in the wedge potential. These poles have the approximate energies:

$$E_n \simeq a_n + g^{-1} - ig^{-2}a_n^{1/2}, \tag{3.117}$$

$n = 1, 2, \cdots$, with

$$a_n \simeq \left(\frac{3\pi(n-1/4)}{2}\right)^{2/3}. \tag{3.118}$$

Another pole corresponds to the bound state of the δ-function as in (3.104) with energy

$$E_0 \simeq -\frac{g^2}{4} - i\frac{g^2}{4}e^{-g^3/6}. \tag{3.119}$$

Finally, there are poles at the zeros of $\mathrm{Bi}(-E) + i\mathrm{Ai}(-E)$. Note that we have the relation (Eq. 10.4.9 in [210])

$$\mathrm{Bi}(z) + i\mathrm{Ai}(z) = \frac{i}{2} e^{i\pi/3} \mathrm{Ai}(z e^{i2\pi/3}). \tag{3.120}$$

The zeros of (3.120) are simply those of the first class (3.117) but rotated by an angle in the complex plane. The physical origin of these poles is quite curious. They correspond to under-barrier resonances of the tilted potential with a hard wall at $x = 0$. That is, they persist in the classically forbidden region, bouncing back and forth off $x = 0$ and the turning point at $x = E$. The resonances are quite broad, with the real and imaginary parts of similar magnitudes.

Finally, we note that we can compute the continuum level density directly from the Green's function. Using the simple form of (3.112) we find (as in (3.49) with $g \to -g$)

$$\Delta(E) = -\frac{1}{\pi} \mathrm{Im} \left(\frac{\langle 0 | \partial G_0 / \partial E | 0 \rangle}{g^{-1} + \langle 0 | G_0 | 0 \rangle} \right). \tag{3.121}$$

Taking the derivative of the free Green's function (3.109) and using (A.4) we find

$$\Delta(E) = -\frac{\mathrm{Ai}^2(-E) + 2g^{-1}\mathrm{Ai}(-E)\mathrm{Ai}'(-E)}{\pi^2 \mathrm{Ai}^4(-E) + (g^{-1} - \pi \mathrm{Ai}(-E)\mathrm{Bi}(-E))^2}, \tag{3.122}$$

which we show in Fig. 3.17. The continuum level density $\Delta(E)$ is almost indistinguishable from the stabilization method results in Fig. 3.16.

3.2.3 Continuum Solutions

The continuum solutions are

$$\Psi_E(x) = N_E \left\{ \begin{array}{cc} \mathrm{Ai}(-x - E) & x < 0 \\ c_A \mathrm{Ai}(-x - E) + c_B \mathrm{Bi}(-x - E) & x > 0 \end{array} \right\}, \tag{3.123}$$

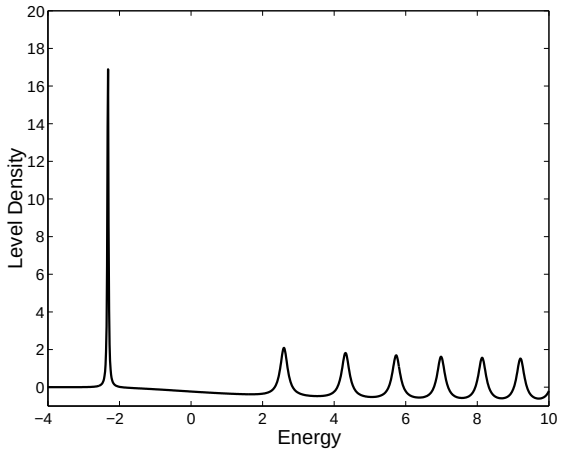

Figure 3.17: Exact continuum level density for the tilted δ-function, constructed from the Green's function

where the coefficients have been found already in (3.92):

$$\begin{aligned} c_A &= 1 - \pi g \mathrm{Ai}(-E)\mathrm{Bi}(-E) \\ c_B &= \pi g \mathrm{Ai}^2(-E). \end{aligned} \tag{3.124}$$

The normalization constant is found using the continuum normalization

$$\int_{-\infty}^{\infty} dx \Psi_E(x)\Psi_{E'}(x) = \delta(E - E'). \tag{3.125}$$

Using (3.123) and the integrals in the Appendix, (A.33)-(A.37), we find after some remarkable cancellations

$$\int_{-\infty}^{\infty} dx \Psi_E(x)\Psi_{E'}(x) = N_E^2(c_A^2 + c_B^2)\delta(E - E') \tag{3.126}$$

and thus

$$N_E = (c_A^2 + c_B^2)^{-1/2} = \left(\pi^2 g^2 \mathrm{Ai}^2(-E) + (1 - \pi g \mathrm{Ai}(-E)\mathrm{Bi}(-E))^2\right)^{-1/2}. \tag{3.127}$$

By the same normalization, we also have the completeness relation

$$\int_{-\infty}^{\infty} dE \Psi_E(x)\Psi_E(x') = \delta(x - x'). \tag{3.128}$$

The continuum states can be written in a way that illustrates their scattering character. That is, just as for Winter's model, we can define an internal amplitude and a scattering phase shift that characterizes the wavefunctions. Here we focus on the phase shift. Note that the scattering theory for Stark systems is not usually developed in standard texts, and as such there is no definite convention for the phase shifts. We choose to define the phase shift such that it closely parallels the scattering theory for asymptotically free particles (other conventions are introduced in [207, 211]).

As in the previous section, there is a linear combination of Airy functions that represent propagating waves. We call these $\Psi_{\pm}(x) = \mathrm{Bi}(-x-E) \pm i\mathrm{Ai}(-x-E)$. In terms of these the continuum states given by (3.123) are, for $x > 0$

$$\Psi_E(x) = N_E \left(\frac{1}{2}(c_B + ic_A)\Psi_-(x) + \frac{1}{2}(c_B - ic_A)\Psi_+(x) \right). \tag{3.129}$$

We define the scattering phase shift by

$$e^{i\phi} = \frac{c_A + ic_B}{\sqrt{c_A^2 + c_B^2}} \tag{3.130}$$

or equivalently

$$\tan\phi = \frac{c_B}{c_A} = \frac{g\pi \mathrm{Ai}^2(-E)}{1 - g\pi \mathrm{Ai}(-E)\mathrm{Bi}(-E)}. \tag{3.131}$$

With this phase shift the continuum states (3.123) are

$$\Psi_E(x) = ie^{-i\phi}\left(\Psi_-(x) - e^{i2\phi}\Psi_+(x)\right). \tag{3.132}$$

This expression is exactly analogous to Winter's model, (3.68), and has the same interpretation. An incoming wave ($\Psi_-(x)$) scatters off of the δ-function, and

the outgoing wave emerges with a shift in phase. Finally, we note that direct calculation shows that the derivative of the phase shift in (3.131) is directly connected to the continuum level density (3.122)

$$\Delta(E) = \frac{1}{\pi}\frac{d\phi}{dE}. \tag{3.133}$$

This relation is a general relation in scattering theory [212].

In the limit $g \to \infty$ we see from (3.131) that the phase shift does not go to zero, but rather

$$\tan\phi_\infty = -\frac{\mathrm{Ai}(-E)}{\mathrm{Bi}(-E)}. \tag{3.134}$$

In analogy with Winter's model, we define the resonance phase shift $\phi_R = \phi - \phi_\infty$, which can be written as

$$\tan\phi_R = \frac{\tan\phi - \tan\phi_\infty}{1 + \tan\phi\tan\phi_\infty}. \tag{3.135}$$

This resonance phase shift is shown in Fig. 3.18. An internal amplitude can also be defined, and has similar structure to the level density (Fig. 3.17).

3.2.4 Time Evolution

By sending a wavepacket from large x and observing its return, the time delay can be determined just as for Winter's model. Here we explain the time delay in a slightly different way [213]. In particular, using the asymptotic behavior of the Airy functions, we find that the propagating solutions have the form

$$\Psi_\pm(x) \simeq \pi^{-1/2}(x+E)^{-1/4}\exp\left\{\pm i\frac{2}{3}(x+E)^{3/2} \pm i\frac{\pi}{4}\right\}. \tag{3.136}$$

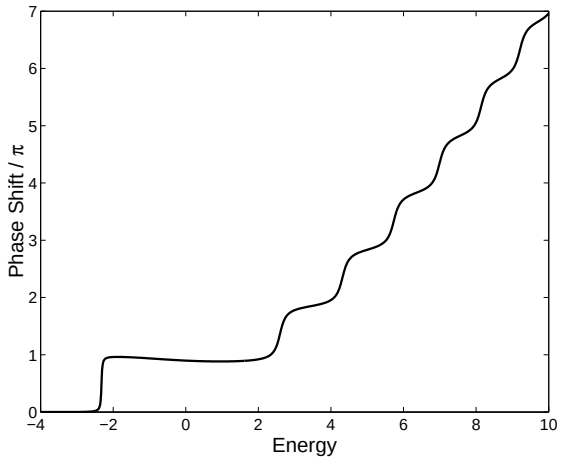

Figure 3.18: Resonance part of the scattering phase shift $\phi_R(E)$ (divided by π), with $g = 3$. At each resonance energy, the phase shift increases by π. This rapid variation allows a superposition of nearby energies to cancel outside the well.

Except for the factor of $\pi/4$ in the exponential, this is precisely the form of a WKB solution with $k(x) = (E + x)^{1/2}$:

$$\Psi_{\pm}(x) \simeq \pi^{-1/2} k(x)^{-1/2} \exp\left\{ i \int^x k(s) ds \right\}. \tag{3.137}$$

Then the outgoing wave components are of the form

$$\Psi_{out}(x,t) = S e^{-iEt} \Psi_+(x) \approx \pi^{-1/2} k(x)^{-1/2} \exp\left\{ i \int^x k(s) ds - iEt + i2\phi(E) \right\}. \tag{3.138}$$

If we form a wavepacket, its outgoing component will be

$$\Psi_{out}(x,t) \approx \int dE c(E) \pi^{-1/2} k(x)^{-1/2} \exp\left\{ i \int^x k(s) ds - iEt + i2\phi(E) \right\}. \tag{3.139}$$

We want to find the time t when the center of the outgoing wave packet is at a given position x. This is found by the method of stationary phase, that is we find t

such that the variation of the phase is zero. At this time and position the outgoing waves are in phase and constructively interfere, yielding a large amplitude. Taking the derivative of the exponent we have

$$\int^x \frac{dk}{dE} ds - t + 2\frac{d\phi}{dE} = 0 \tag{3.140}$$

or, using $dk/dE = 1/v$, where v is the velocity

$$t = \int^x \frac{ds}{v(s)} + 2\frac{d\phi}{dE} \tag{3.141}$$

This shows that wave packet emerges at x after the classical transit time (the first term) plus the time delay (the second):

$$\tau = 2\frac{d\phi}{dE}, \tag{3.142}$$

precisely as in (3.10), with $\hbar = 1$.

Note that the time delay is proportional to the continuum level density, and is sometimes negative. This is not an error, but represents real physics. These negative values occurred in Winter's model as well. Our choice of the free Hamiltonian (in G_0) assumes that the particle scatters off of the *interior* of the δ-function well. If, however, the particle scatters off of the δ-function before it enters the interior, it will emerge before its free counterparts, leading to a negative time delay. Thus, for certain energies there is little amplitude transmitted to the interior and a lack of energy level density.

The study of the exponential decay of an initially localized state follows the same procedure as before: one looks at the survival amplitude

$$A(t) = \int_{-\infty}^{\infty} |c(E)|^2 e^{-iEt}. \tag{3.143}$$

For the tilted potential, there is no lower bound to the energy. Thus, it is possible that there is no long-time deviation from exponential decay [214]. Short-time deviations persist, and can be seen in the time-dependent studies found in [199, 201, 205, 206].

3.3 Washboard

Having illustrated general methods, and their mutual agreement, for resonances in two model potentials, we now turn to the resonances of the washboard. We use a typical set of junction parameters: $C_J = 6$ pF and $I_c = 20\mu$A. These correspond to the well in Fig. 3.1. In Fig. 3.19 we show the results of our general method, the wavefunctions corresponding to the resonance energies of the washboard.

These wavefunctions are continuum states, and not directly normalizable. Indeed, the last resonance shown is clearly oscillatory outside the well. However, for deep wells the resonances are particularly sharp, and thus localized states prepared near the resonance energies will be very long-lived, and almost discrete. This is seen in the lower states, whose amplitude outside the well is very small, but still non-zero. In this section we show how the continuum states can be constructed. First, however, we look at the results from stabilization and complex scaling.

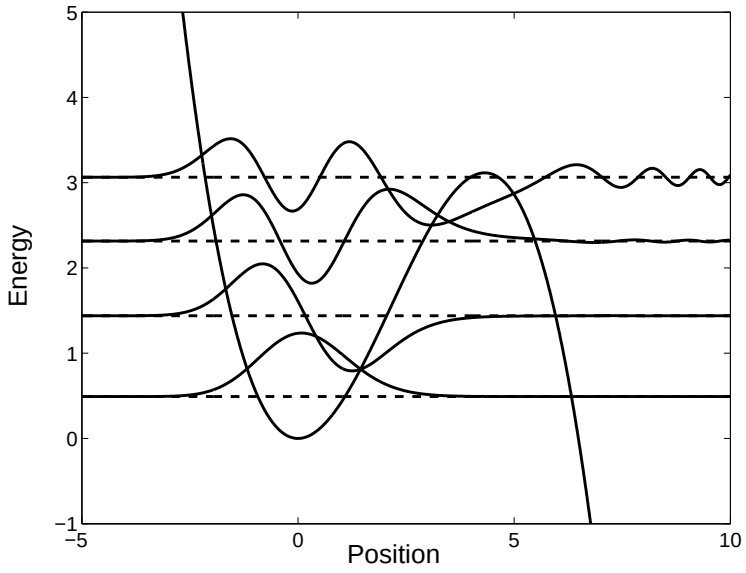

Figure 3.19: Washboard potential with Josephson junction parameters $C_J = 6\text{pF}$, $I_c = 20\mu\text{A}$, and $I = 0.99I_c = 19.8\mu\text{A}$. The relevant energy levels in a metastable well are indicated by the dashed lines. About each energy level, the corresponding continuum wavefunctions (with arbitrary normalization) are shown as solid curves. The position and energy scale have been scaled [see text and (3.5)].

3.3.1 Stabilization Method

As before, we place the system into a finite box of size L. We then explore the discrete spectrum as L varies. We use the scaled Hamiltonian (3.5)

$$h = \frac{1}{2}p^2 + \alpha^{-2}\left(1 - \cos(\alpha x) + J(1-J^2)^{-1/2}(\sin(\alpha x) - \alpha x)\right), \tag{3.144}$$

where for our junction parameters $\alpha \simeq 0.0655$ and $J = 0.99$. As a basis set we choose the square well states subject to the boundary condition that $\Psi_n(x = -L/2) = \Psi_n(x = +L/2) = 0$. These discrete states, labelled by n, can be written as

$$\Psi_n(x) = \sqrt{2/L}\sin(n\pi(x/L + 1/2)). \tag{3.145}$$

The matrix elements needed for the Hamiltonian $h_{n,m}$ are given in the Appendix. By truncating the matrix at some large value of N_{max}, and using a standard numerical matrix diagonalization routine, we calculate the eigenvalues of the discretized washboard. The stabilization diagram is shown in Fig. 3.20.

At each apparent intersection of energy curves, there is in fact a small avoided crossing. The energies that correspond to the resonances of the washboard appear as the L independent horizontal curves. The non-resonance energy levels decrease with L. This is due to the tilt, since for large L the system explores the negative portions of the potential. The overall ground state is then very similar to the ground state of the wedge potential explored in Ludviksson's model. Its energy goes as $E_1 \approx c_0 - c_1 L$, where c_0 and c_1 are constants from the appropriately scaled wedge potential.

To summarize the energy level density, we use a simple histogram of the energy levels in each energy range, shown in Fig. 3.21. A direct use of the stabilization

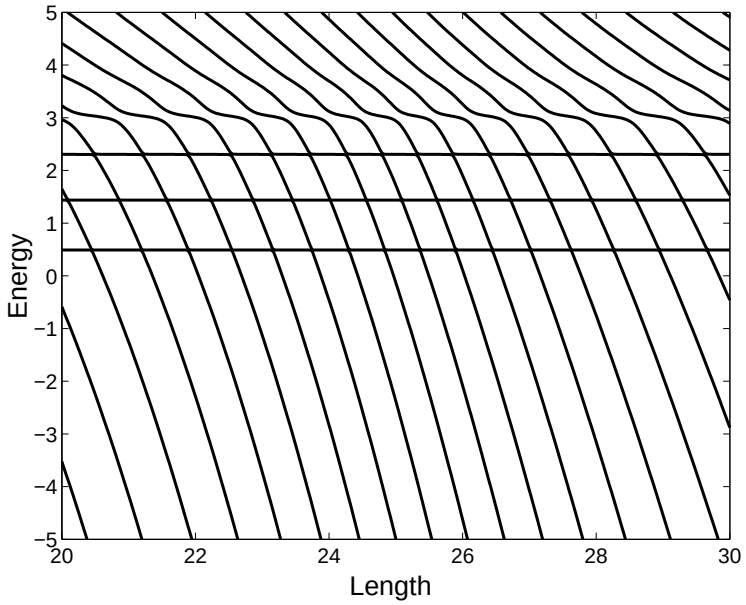

Figure 3.20: Stabilization diagram for washboard with Josephson junction parameters $C_J = 6\text{pF}$, $I_c = 20\mu\text{A}$, and $I = 0.99I_c = 19.8\mu\text{A}$. Each curve represents the corresponding eigenvalue $E_n(L)$ as the length L is increased. Each apparent intersection is actually an avoided crossing. The plateaus near 1/2, 3/2, 5/2 and 7/2 indicate discrete resonance states which are localized in the metastable well.

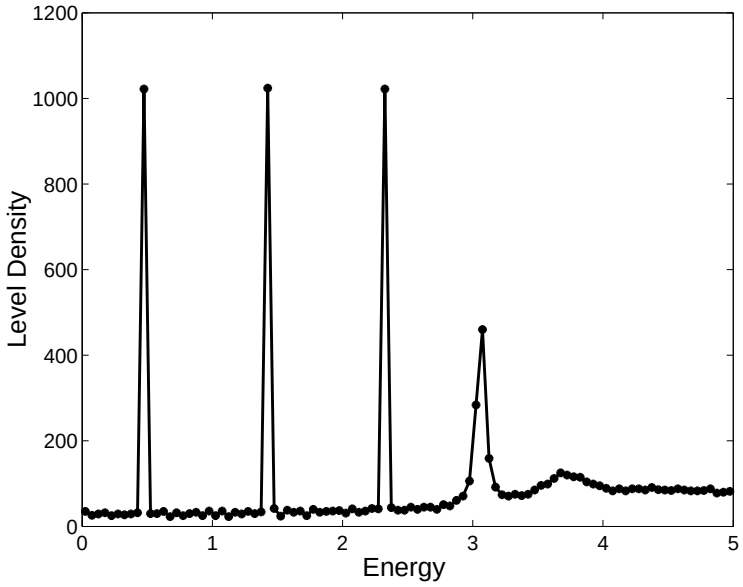

Figure 3.21: Continuum level density for washboard with Josephson junction parameters $C_J = 6\text{pF}$, $I_c = 20\mu\text{A}$, and $I = 0.99I_c = 19.8\mu\text{A}$. The curve is a histogram of the energy levels in the stabilization diagram. The peaks correspond to the discrete resonances.

formula (3.25) for the level density is possible, but is no more accurate than the histogram, due to numerical approximations to dE_n/dL.

3.3.2 Complex Scaling

As shown in Winter's and Ludviksson's models, and true in general, the complex poles of the Green's function can be found by solving Schrödinger's equation subject to an outgoing wave boundary condition, as proposed by Gamow and Siegert. Note that this boundary condition is intimately related to the boundary condition on the Green's function, and ultimately due to the choice of the retarded propagator (which

vanishes for $t < 0$). However, the Gamow-Siegert states are not normalizable and not elements of the Hilbert space. The complex scaling transformation was introduced to rigorously define these states in autoionizing multi-electron atoms [215, 216], and a later variation was used in the hydrogen Stark effect [217]. In fact, the complex scaling method can do much more (see the review by Moiseyev [218]). Here we consider it as merely a numerical method to find Gamow-Siegert states.

First, we recall that Winter's model had outgoing wave states with energy $E = k^2$ where k was complex: $k = k_R - ik_I$. The Gamow-Siegert wavefunction (3.38) for $x > a$ has the form

$$\Psi_{GS}(x) = e^{ikx} = e^{ik_R x} e^{k_I x}. \tag{3.146}$$

The imaginary part of k leads to the exponential growth of $\Psi_{GS}(x)$. This is actually not terribly surprising. The outgoing wave boundary condition is time-independent, and hence the Gamow-Siegert wavefunction describes an *eternally* decaying state. This is more obviously seen by noting that $\Gamma = 4k_R k_I$, $v = 2k_R$ and thus

$$|\Psi_{GS}(x,t)|^2 = e^{-\Gamma t} e^{2k_I x} = e^{-\Gamma(t-x/v)}. \tag{3.147}$$

Surfaces of constant probability correspond to $x = vt = v(t_f - t_i)$. Thus, the exponential growth with x at a fixed time $t_f = 0$ corresponds to the buildup of probability from decay that occurred *in the past* starting at $t_i = -x/v$. One can remove this peculiarity by defining a *time-dependent* Gamow-Siegert state which is zero for $x > vt$ [175]. This state is not a solution of the Schrödinger equation, but is a reasonable approximation that can be systematically improved [186].

The complex scaling transformation tames the exponential divergence of $\Psi_{GS}(x)$. This involves the new coordinate $\tilde{x}$, defined by

$$x = \tilde{x}e^{i\theta}, \tag{3.148}$$

where $\tilde{x}$ is *real*, and thus x is complex. Using this transformation, the wavefunction in (3.146) becomes

$$\Psi_{GS}(x = \tilde{x}e^{i\theta}) = \exp[i(k_R\cos\theta + k_I\sin\theta)\tilde{x}]\exp[-(k_R\sin\theta - k_I\cos\theta)\tilde{x}]. \tag{3.149}$$

Thus, if $\tan\theta > k_I/k_R$ (which for small k_I implies a small θ), we have constructed a normalizable state. A completely equivalent statement is that if we integrate Schrödinger's equation in the complex plane, the Gamow-Siegert state is an eigenfunction subject to the boundary condition $\Psi_{GS}(x) \to 0$ with $x \to Re^{i\theta}$, $R \to \infty$.

The complex scaling transformation also works for Stark systems [219]. Recall that the outgoing wave (for $x > 0$) in Ludviksson's model, (3.114) was

$$\Psi(x) = \mathrm{Bi}(-x - E) + i\mathrm{Ai}(-x - E). \tag{3.150}$$

Using the asymptotic forms of the Airy functions we have

$$\Psi(x) \sim \exp\left\{i\frac{2}{3}(x + E)^{3/2}\right\}, \tag{3.151}$$

where we have ignored all terms in the prefactor to the exponential. If the energy has a negative imaginary part $E = E_R - i\Gamma/2$, this state will diverge as

$$\Psi(x) \sim \exp\left\{i\frac{2}{3}(x + E_R)^{3/2} + \frac{3}{4}\Gamma(x + E_R)^{1/2}\right\}. \tag{3.152}$$

However, performing the same complex scaling transformation as above, we find that

$$\Psi(x = \tilde{x}e^{i\theta}) \sim \exp\left\{ i\frac{2}{3}(\tilde{x}\cos\theta + E_R)^{3/2} - \frac{3}{2}(\tilde{x}\cos\theta + E_R)^{1/2}(\tilde{x}\sin\theta - \Gamma/2) \right\}. \tag{3.153}$$

Thus, for any nonzero θ, the complex scaling transformation will make the Gamow-Siegert state normalizable (a more careful analysis shows $0 < \theta < 2\pi/3$ [219]).

The complex scaling method is particularly useful in numerical work. Since the Gamow-Siegert state is bounded as a function of $\tilde{x}$, it can be well approximated by a finite-dimensional basis set. Thus, the calculation reduces to a standard basis set calculation but now with respect to the non-Hermitian hamiltonian

$$H = \frac{1}{2m}e^{-i2\theta}\tilde{p}^2 + V(\tilde{x}e^{i\theta}). \tag{3.154}$$

Using the harmonic oscillator basis we can readily calculate the complex eigenvalues of the washboard, using matrix elements derived in the Appendix. As an example Fig. 3.22 shows the calculated the transition frequencies between the first few states. Since the calculated energies are complex, we can also consider the spectral widths due to tunneling from the final state (contributions from the initial state are generally much smaller). These are shown in Fig. 3.22 as the dashed curves.

3.3.3 Continuum Solutions

The most complete method to study the spectrum of the washboard is to construct the continuum scattering states. Unlike the simple models considered in the beginning of this chapter, however, there are no general solutions to use as our standard

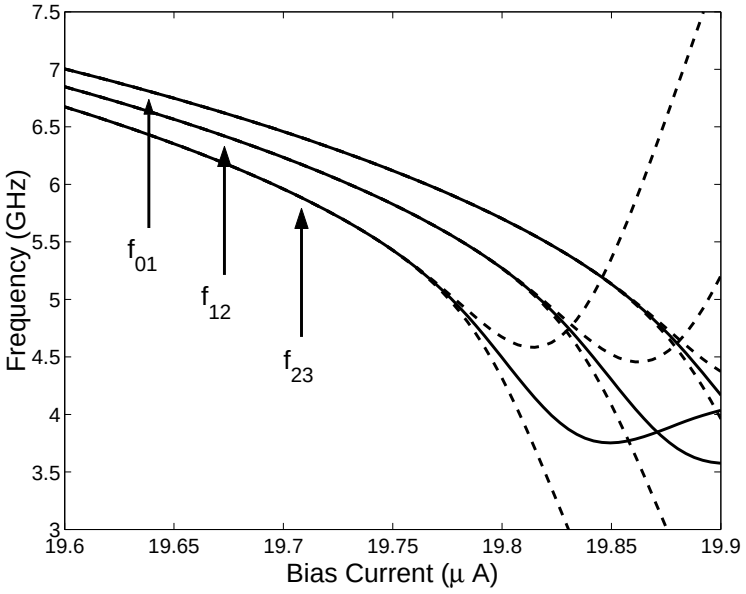

Figure 3.22: Transition frequencies $f_{n,n+1}$ from states $n \to n+1$ for $n = 0, 1$, and 2 for the Gamow-Siegert states of the washboard with Josephson junction parameters $C_J = 6\text{pF}$ and $I_c = 20\mu\text{A}$. The dashed curves are $f_{n,n+1} \pm \Gamma_{n+1}/2h$, indicating the widths of the final states.

basis, and no exact continuum normalization methods. Our proposed solution is an asymptotic WKB normalization, which we show is appropriate for the washboard parameters used here. In fact, it should be possible to use it for the more general Wannier-Stark problem. We note that a similar method was used to study the spectrum of the hydrogen Stark problem [220, 221].

One might expect that the Airy functions would be the appropriate basis, since for sufficiently large energy the contributions of the cosine potential should become negligible. It turns out, however, that for the washboard parameters the WKB wavefunctions become good approximations before the Airy functions. This can be seen by the following simple argument.

The effects of the cosine might be neglected once the distance (from the turning point) has spanned at least two minima of the washboard. Thus, if we count the approximate number of nodes N of the relevant Airy function over this distance, and $N \gg 1$, then the WKB approximation will be appropriate—with or without the cosine. Without the cosine, the asymptotics of the Airy functions are precisely the WKB approximation. Starting from the tilted Hamiltonian (3.1) without the cosine and $J = 1$

$$H = -4E_c \frac{d^2}{d\gamma^2} - E_J \gamma, \tag{3.155}$$

we perform the scale transformation $\gamma = \alpha x$ with $\alpha^3 = 4E_c/E_J$, which yields

$$H = (4E_c E_J^2)^{1/3} \left(-\frac{d^2}{dx^2} - x \right) \tag{3.156}$$

The tilted eigenfunctions are thus

$$\Psi(\gamma) = -\mathrm{Ai}(-\alpha^{-1}\gamma) \tag{3.157}$$

and the relevant distance is $\alpha^{-1}2\pi$. To count the number of nodes we can assume the WKB form for Ai with little error, and we find that the number of nodes is

$$N \approx \frac{2}{3\pi}(\alpha^{-1}2\pi)^{3/2} = \frac{2^{3/2}\pi^{1/2}}{3}\left(\frac{E_J}{E_c}\right)^{1/2}. \tag{3.158}$$

For typical junction parameters $E_J/E_c \sim 10^6$, and thus

$$N \sim 1700. \tag{3.159}$$

Since $N \gg 1$, the WKB approximation will be valid before the effects of the cosine can be neglected.

Numerical integration can yield an un-normalized wavefunction. That is, for any energy E we can rewrite the general Schrödinger equation as the first order system

$$\begin{array}{ll} d\Psi/dx(x) & = \Pi(x) \\ d\Pi/dx(x) & = -G(x)\Psi(x) \end{array} \tag{3.160}$$

with

$$G(x) = \frac{2m}{\hbar^2}(E - V(x)). \tag{3.161}$$

By choosing an initial condition $\{\Psi(x_i), \Pi(x_i)\}$, it is numerically straightforward to integrate this system for both $x > x_i$ and $x < x_i$. The initial condition should be chosen such that $\Psi(x) \to 0$ for $x \to -\infty$. Since this system is linear, one can set $\Pi(x_i) = p$ with p arbitrary, and find the appropriate $q = \Psi(x_i)$. For large negative x, $\Psi(x)$ is of WKB type

$$\Psi(x) \sim c_0(q)e^{S(x)} + c_1(q)e^{-S(x)} \tag{3.162}$$

where S is positive, and goes to ∞ for $x \to -\infty$. In principle, we must find the root q_* where $c_0(q_*) = 0$, for example by a simple iterative root search.

In practice, round-off error in the integration routine will cause any $\Psi(x)$ to eventually diverge for some negative $x = x_D$. This divergence introduces an error in our root q_*. We can avoid the root search entirely by setting $\Psi(x_D) = 0$, $\Pi(x_D)$ arbitrary, and only integrating to the right. The intrinsic error in this wavefunction will be exponentially small by (3.162), of order $e^{-2S(x_D)}$. For the following calculations we use a fourth order Runge-Kutta integrator.

After generating a state by this method, we must extract the resonance features such as an internal amplitude $X(E)$ and the phase shift $\phi(E)$. For the former we must normalize the wavefunction to a continuum, for the latter we must match the wavefunction to a set of in and out-going standard wavefunctions. We use the WKB approximation for both, and assume that for large x we have

$$\Psi_E(x) = \tilde{A}_E(2m(E - V(x))/\hbar^2)^{-1/4} \sin(S_E(x)/\hbar + \phi_E) \tag{3.163}$$

with

$$S_E(x) = \int_a^x ds(2m(E - V(s))^{1/2}, \tag{3.164}$$

and a is the appropriate classical turning point.

We first consider the normalization. The constant $\tilde{A}_E$ that arises from numerical integration is somewhat arbitrary. In order that the wavefunctions be normalized to a continuum, however, it must take a particular form, which we now calculate. We wish to normalize Ψ_E such that

$$g(E, E') = \int_0^\infty \Psi_E(x)\Psi_{E'}(x)dx = \delta(E - E'). \tag{3.165}$$

We let $E' = E + \Delta E$, and insert the WKB form (3.163) into (3.165) for each

wavefunction. Their product reduces to

$$\Psi_E(x)\Psi_{E'}(x) \approx A_E^2(2m(E-V(x))/\hbar^2)^{-1/2}(1/4)\left(e^{i\partial_E S_E(x)\Delta E/\hbar} + e^{-i\partial_E S_E(x)\Delta E/\hbar}\right) \tag{3.166}$$

where we have neglected higher order terms in ΔE and also the rapidly oscillating terms $e^{\pm i2S_E(x)/\hbar}$. If we define z by

$$z(x) = \partial_E S_E(x)/\hbar = \int_a^x \frac{m/\hbar^2}{(2m(E-V(s))/\hbar^2)^{1/2}} ds. \tag{3.167}$$

and substitute (3.166) into (4.13), we find

$$g(E,E') \approx A_E^2(\hbar^2/4m)\int_0^\infty dz(e^{iz\Delta E} + e^{-iz\Delta E}). \tag{3.168}$$

Setting $z \to -z$ in the second integral in (3.168) yields

$$g(E,E') \approx A_E^2(\hbar^2/4m)\int_{-\infty}^\infty dz e^{iz\Delta E} = A_E^2(\hbar^2/4m)2\pi\delta(E-E'), \tag{3.169}$$

and thus $A_E = (2m/\pi\hbar^2)^{1/2}$. We have shown that the appropriately continuum normalized WKB function is

$$\Psi_E(x) = (2m/\pi\hbar^2)^{1/2}(2m(E-V(x))/\hbar^2)^{-1/4}\sin(S_E(x)/\hbar + \phi_E) \tag{3.170}$$

with $S_E(x)$ given by (3.164). Thus, we can normalize an arbitrary state by matching it to one of this form.

In summary, our procedure, with $\hbar = m = 1$, is to numerically construct a wavefunction Φ_E with the asymptotic form

$$\Phi_E(x) \sim A_0 k(x)^{1/2}\sin\left\{\int_a^x k(s)ds + \phi\right\} \tag{3.171}$$

with $k = (2(E - V(x)))^{1/2}$. We use the WKB identity

$$\left(k^{1/2}\Phi_E\right)^2 + \left(k^{-1}\frac{d}{dx}(k^{1/2}\Phi_E)\right)^2 = A_0^2, \tag{3.172}$$

to both ensure that (3.171) is correct and to find the initial normalization A_0. Then, we construct the normalized wavefunction $\Psi_E(x) = A_N\Phi_E(x)/A_0$, where $A_N = (2/\pi)^{1/2}$ is the appropriate continuum normalization factor.

Using this procedure, we first show the normalized wavefunctions near the third resonance at $E_R = 2.3151$ in Fig. 3.23. The top and bottom wavefunctions have been offset for clarity. Clearly seen in this figure is the enhancment in amplitude at the resonance. Also noticeable is the shift in a node of the wavefunction outside the well ($x > 5$) as the energy increases. This is the scattering phase shift.

Repeating this procedure for multiple energies, we can construct an internal amplitude function from each wavefunction

$$X^2(E) = \int_{x_0}^{x_1} dx \Psi_E^2(x), \tag{3.173}$$

where x_0 and x_1 are the turning points in the potential well. The internal amplitude function is shown in Fig. 3.24. We can also construct a phase shift from (3.171):

$$\tan\phi_R(E) = \left(\frac{k^{3/2}\Psi_E}{d(k^{1/2}\Psi_E)/dx}\right)_{x=R}. \tag{3.174}$$

Note that this phase shift will weakly depend on the position $x = R$. To determine resonances, however, this dependence is irrelevant. The phase shift is shown in Fig. 3.25.

Finally, we can repeat this procedure for various bias currents. A contour plot of $X^2(E)$ is shown in Fig. 3.26. Also shown is the results of the complex scaling

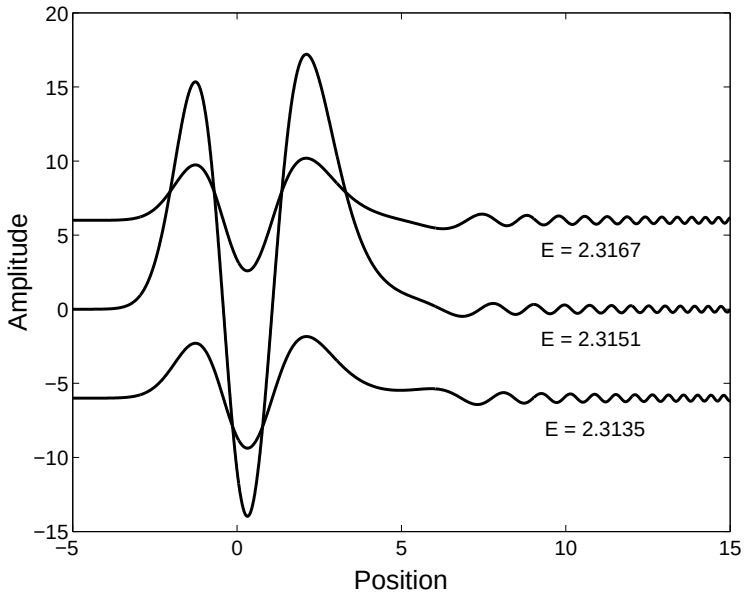

Figure 3.23: Normalized continuum wavefunctions for the washboard with Josephson junction parameters $C_J = 6\text{pF}$, $I_c = 20\mu\text{A}$, and $I = 0.99I_c = 19.8\mu\text{A}$. The wavefunction amplitude is shown for energies near the third resonance at $E_R = 2.3151$. The energies and position have been scaled [see text and (3.5)].

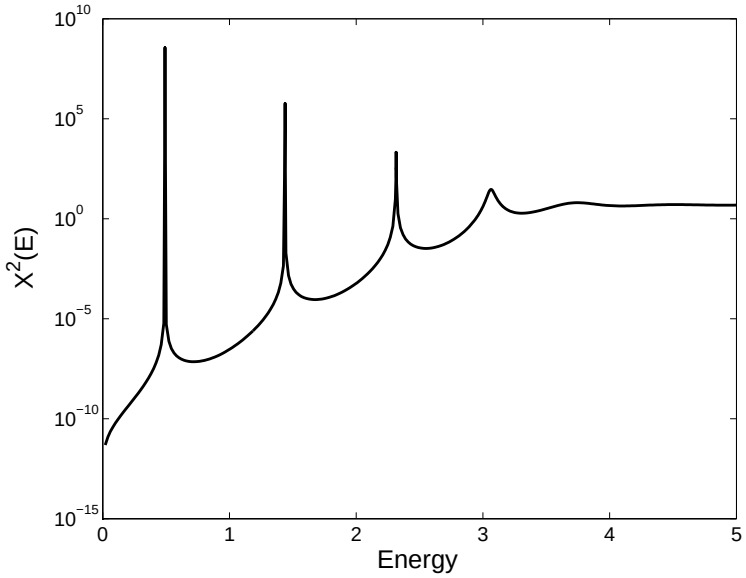

Figure 3.24: Internal amplitude (squared) $X^2(E)$ for the washboard with Josephson junction parameters $C_J = 6\text{pF}$, $I_c = 20\mu\text{A}$, and $I = 0.99I_c = 19.8\mu\text{A}$. The scaled energy is plotted on the horizontal axis. Note that the vertical scale is logarithmic. The resonances are highly localized in energy and have very large amplitudes. These large amplitudes allow the superposition of nearby energies to be highly localized in the well.

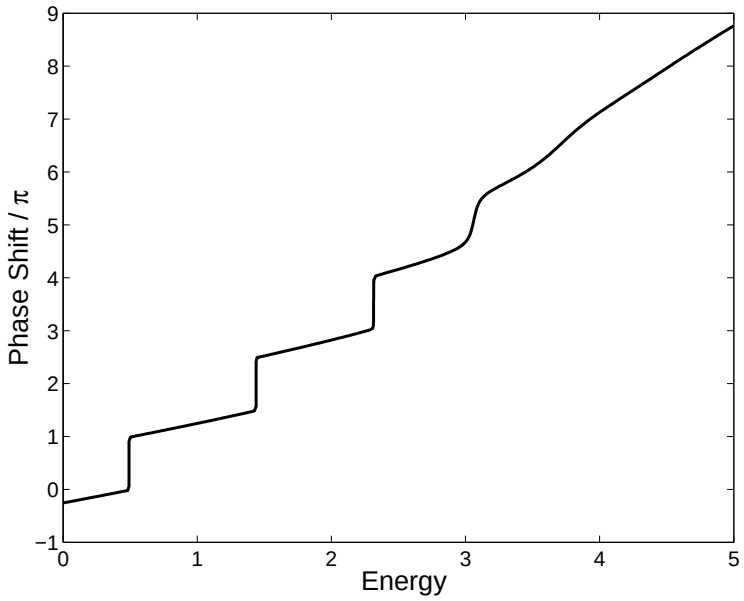

Figure 3.25: Scattering phase shift $\phi(E)$ (divided by π) for the washboard with Josephson junction parameters $C_J = 6\text{pF}$, $I_c = 20\mu\text{A}$, and $I = 0.99I_c = 19.8\mu\text{A}$. At each resonance energy, the phase shift increases by π. This rapid variation allows a superposition of nearby energies to cancel outside the well.

Table 3.1: The resonance energies E and widths $\Gamma/2$ from complex scaling (CS) and phase shift (PS) analysis.

State	E_{CS}	E_{PS}	$\Gamma_{CS}/2$	$\Gamma_{PS}/2$
0	0.4911958	0.4911958	1.2409×10^{-9}	1.2408×10^{-9}
1	1.4389926	1.4389926	1.2194×10^{-6}	1.2194×10^{-6}
2	2.3150917	2.3150917	3.9784×10^{-4}	3.9781×10^{-4}
3	3.0620256	3.0621948	2.9638×10^{-2}	2.9672×10^{-2}

calculation. While the visual agreement between the two is very pleasing, we can study this at higher accuracy. By taking the derivative of the phase shift, and fitting to a Lorentzian, we have parametrized the first four resonances. In Table 3.1 we compare these with the complex eigenvalues of the complex scaling calculation. We find excellent agreement for both the energies and widths, the most significant deviation occurring in the last resonance. As this resonance is quite broad and somewhat asymmetric (near the top of the barrier, see Fig. 3.19), this deviation is to be expected. For the resonances deeper in the well, the agreement is nearly exact. Thus, we have accurately found the resonances of the washboard.

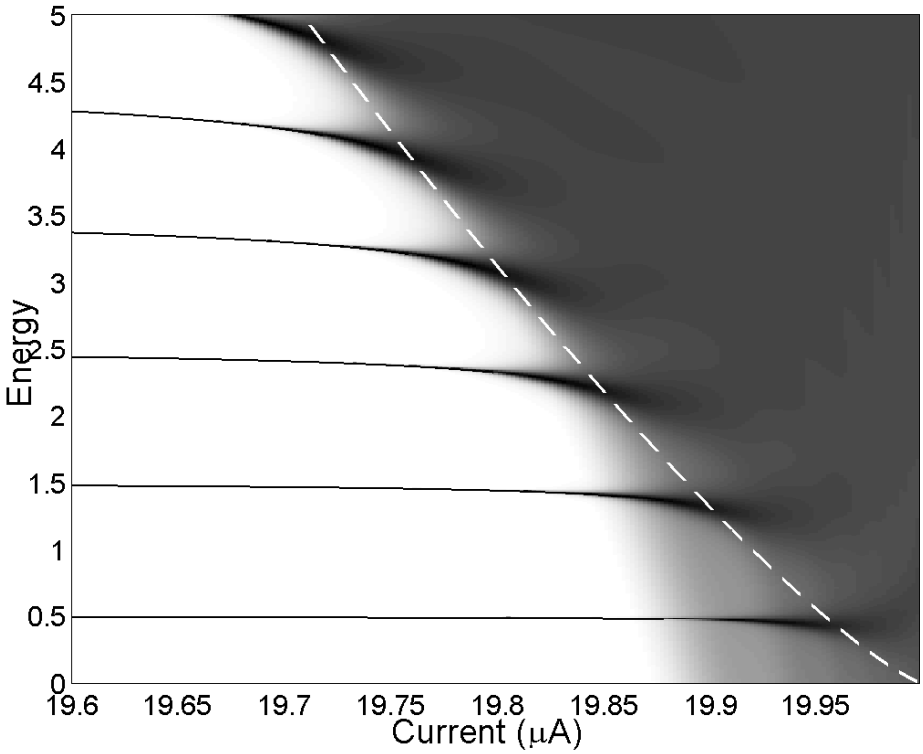

Figure 3.26: Internal amplitude (squared) $X^2(E)$ for Josephson junction parameters $C_J = 6\text{pF}$ and $I_c = 20\mu\text{A}$. The vertical scale is the scaled energy, the horizontal is the bias current in μA. The dark regions correspond to large amplitude, the light to zero amplitude. The thin solid lines are the results of the complex scaling calculation. The white dashed line is the barrier height.

Chapter 4

The Cubic Approximation

In this Chapter we present results for the cubic approximation of the washboard potential. Near each well of the washboard, the potential can be locally described by a simple cubic polynomial. For the whole potential, however, the cubic is clearly inadequate. It is actually more than inadequate. As shown below, the quantum mechanics of the cubic potential is not uniquely defined because the Hamiltonian is not essentially self-adjoint. This raises the natural question, if accurate numerical methods exist for the washboard, such as those described in Chapter 3, why bother with the cubic?

There are two main motivations. The first is that this polynomial approximation can be applied to junctions with a wide range of parameters. Conversely, one can map junctions of different parameters to an equivalent cubic. This is useful in that no fine-tuning of junction parameters is necessary to design its quantum

dynamics. Furthermore, numerical calculations for quantum logic operations using the cubic potential will be valid for all junctions satisfying some natural condition. As will be shown, this condition is $E_J \gg E_c$, which applies to nearly all phase qubits. Without these methods, calculations must be performed for each possible set of junction parameters.

The second motivation is that many analytical results can be formally derived for the cubic due to its relative simplicity. These results demonstrate how the tunneling rates and energy level spacings change with the potential barrier. These results are necessary for constructing simple pictures of the physics.

While much of this material has been studied before (such as [176, 177, 178]), these results are necessary for the subsequent work on coupled junctions. In particular, many useful formulae, such as the variation of the position of the minimum, are not to be found in the literature. Neglecting this variation can lead to wildly inaccurate results. Accurate formulae are derived in Section 2. The curious ambiguity of the spectrum of the cubic, and possible resolutions, are discussed in Section 3. This is followed by the perturbative calculation of the energy eigenvalues and wavefunctions in Section 4, while a WKB calculation for the tunneling rate is performed in Section 5. We consider another method to calculate the tunneling rate in Section 6, the instanton approach. Finally, Section 7 completes this Chapter by presenting the first (to our knowledge) numerical verification of the cubic approximation to the washboard potential.

4.1 Washboard to Cubic

While the methods discussed in Chapter 3 are sufficiently developed for treating the washboard potential directly, much can be gained by simplifying the dynamics to a cubic potential. In particular, we will show that up to an energy scale the cubic approximation parametrizes the washboard by a single parameter, the approximate number of energy levels in the well.

We recall that the Hamiltonian of a current-biased Josephson junction is

$$H = \frac{p_\gamma^2}{2m} - E_J(\cos\gamma + J\gamma). \tag{4.1}$$

Here γ is the junction's coordinate (the phase difference), p_γ its conjugate momentum, $1/m = 8E_c\hbar^{-2}$ where $E_c = e^2/(2C_J)$ is the charging energy of the junction, $E_J = \hbar I_c/(2e)$ is the Josephson energy with I_c the junction critical current and $J = I/I_c$ is the dimensionless bias current. As will be discussed below, typical experiments have $J \simeq 0.99$, i.e. the washboard is strongly tilted. The three fundamental properties of the washboard that are important for quantum computing are the position of the minimum, the curvature at the minimum, and the overall barrier height. To understand the dynamics in this regime, we first explore these as a function of the bias current J. The minimum and its curvature are

$$dU/d\gamma|_{min} = E_J(\sin\gamma_{min} - J) = 0 \Rightarrow \gamma_{min} = \arcsin J, \tag{4.2}$$

$$d^2U/d\gamma^2|_{min} = E_J\cos\gamma_{min} = E_J\sqrt{1-J^2}, \tag{4.3}$$

while the position of the maximum and its curvature are

$$\gamma_{max} = \pi - \arcsin J \tag{4.4}$$

$$d^2U/d\gamma^2|_{max} = -d^2U/d\gamma^2|_{min} = -E_J\sqrt{1-J^2}. \tag{4.5}$$

From (4.3) we can compute the frequency of small oscillations about the minimum

$$\begin{aligned} \omega &= \sqrt{(d^2U/d\gamma^2|_{min})/m} \\ &= \hbar^{-1}\sqrt{8E_cE_J}(1-J^2)^{1/4}. \end{aligned} \tag{4.6}$$

The barrier height can also be calculated

$$\begin{aligned} \Delta U &= U(\gamma_{max}) - U(\gamma_{min}) \\ &= 2E_J(\sqrt{1-J^2} + J(\arcsin J - \pi/2)) \\ &= 2E_J(\sqrt{1-J^2} - J\arccos J), \end{aligned} \tag{4.7}$$

and finally the number N_s of harmonic oscillator states whose energies lie beneath the barrier is

$$\begin{aligned} N_s &= \Delta U/\hbar\omega \\ &= 2^{-1/2}\left(E_J/E_c\right)^{1/2}\left((1-J^2)^{1/4} - J(1-J^2)^{-1/4}\arccos J\right). \end{aligned} \tag{4.8}$$

The above equations are exact. We now consider the case when J is near unity, and perform expansions of the above quantities in terms of $\Delta J = 1 - J$. First, we let $\gamma_{min} = \pi/2 - \Delta\gamma$, and attempt to solve $dU/d\gamma = 0$:

$$\begin{aligned} dU/d\gamma = 0 \Rightarrow \sin(\pi/2 - \Delta\gamma) - 1 + \Delta J &= 0, \\ \cos\Delta\gamma - 1 + \Delta J &= 0, \\ \Delta J - \frac{1}{2}\Delta\gamma^2 + \frac{1}{24}\Delta\gamma^4 - \frac{1}{720}\Delta\gamma^6 + \cdots &= 0. \end{aligned} \tag{4.9}$$

Eq. (4.9) shows that, to lowest order, $\Delta\gamma = \sqrt{2\Delta J}$. Proceeding to higher orders we find

$$\Delta\gamma = \sqrt{2\Delta J}\left(1 + \frac{1}{12}\Delta J + \frac{3}{160}\Delta J^2 + \cdots\right), \tag{4.10}$$

in terms of which $\gamma_{min} = \pi/2 - \Delta\gamma$ and $\gamma_{max} = \pi/2 + \Delta\gamma$. For the curvature we find

$$d^2U/d\gamma^2|_{min} = E_J\sqrt{2\Delta J}\left(1 - \frac{1}{4}\Delta J - \frac{1}{32}\Delta J^2 + \cdots\right). \tag{4.11}$$

and $d^2U/d\gamma^2|_{max} = -d^2U/d\gamma^2|_{min}$. The barrier height is

$$\Delta U = E_J \frac{4\sqrt{2}}{3} \Delta J^{3/2} \left(1 + \frac{3}{16}\Delta J + \cdots\right). \tag{4.12}$$

Finally, the number N_s of harmonic oscillator states has the expansion

$$N_s \simeq (2^{3/4}/3)\,(E_J/E_c)^{1/2}\,\Delta J^{5/4} + O(\Delta J^{9/4}). \tag{4.13}$$

These preliminary results are completely independent of the cubic approximation.

To proceed to a cubic approximation of the potential, we follow a simple stepwise approach. For quantum computing applications we need to keep track of the bias current J at all times. It is the primary experimental knob through which we manipulate the quantum system. Thus, and for future convenience, we choose a reference bias current J_0, which will be the physical starting point of our quantum algorithm. We define α by

$$\alpha = \left(\frac{8E_c}{E_J}\right)^{1/4} (1 - J_0^2)^{-1/8} \tag{4.14}$$

and consider the transformation

$$\begin{aligned} x &= \alpha^{-1}(\gamma - \arcsin J_0) \\ p &= \alpha p_\gamma. \end{aligned} \tag{4.15}$$

Using (4.14) and (4.15) in (4.1), we find

$$H = U_0 + \frac{1}{2m\alpha^2}p^2 + E_J\left(\sqrt{1 - J_0^2}(1 - \cos(\alpha x)) + J_0 \sin(\alpha x) - J\alpha x\right), \tag{4.16}$$

where U_0 is a constant (independent of x and p), which we will subsequently ignore. Now, if we define the reference frequency ω_0 by $\hbar\omega_0 = m^{-1}\alpha^{-2}$, that is

$$\hbar\omega_0 = \sqrt{8E_cE_J}(1 - J_0^2)^{1/4} \tag{4.17}$$

then (4.16) can be written as

$$H/\hbar\omega_0 = \frac{1}{2}\hbar^{-2}p^2 + \alpha^{-2}\left(1 - \cos(\alpha x) + (1 - J_0^2)^{-1/2}(J_0 \sin(\alpha x) - J\alpha x)\right). \quad (4.18)$$

So far, all of this is exact, and parallel to the transformations used in Chapter 3. We show below that for typical parameters α is small, and thus we expand the potential in (4.18) in α to find

$$H/\hbar\omega_0 \simeq \frac{1}{2}p^2 + \frac{1}{2}x^2 + sx - \lambda x^3, \quad (4.19)$$

with

$$s = \alpha^{-1}(1 - J_0^2)^{-1/2}(J_0 - J) \quad (4.20)$$

and

$$\lambda = \frac{1}{3!}J_0\alpha(1 - J_0^2)^{-1/2}. \quad (4.21)$$

The next correction to H occurs at order α^2. Now, the cubic potential

$$V(x) = \frac{1}{2}x^2 + sx - \lambda x^3 \quad (4.22)$$

has for a minimum

$$x_* = \frac{1}{6\lambda}(1 - \sqrt{1 + 12s\lambda}), \quad (4.23)$$

and its curvature there is

$$d^2V/dx^2|_* = \omega^2 = \sqrt{1 + 12s\lambda}. \quad (4.24)$$

Using (4.23) and (4.24), we can rewrite (4.22) as

$$V(x) = V_* + \frac{1}{2}\omega^2(x - x_*)^2 - \lambda(x - x_*)^3, \quad (4.25)$$

and as before, we drop the constant V_*. Substituting (4.20) and (4.21) into (4.24) we find ω in terms of $J, J_0 \sim 1$

$$\omega^4 = 1 + 2J_0(1 - J_0^2)^{-1}(J_0 - J) \simeq \frac{1 - J}{1 - J_0}. \tag{4.26}$$

We also note that the number of harmonic oscillator states N_s whose energies lie below the barrier of the cubic potential with $\omega = 1$ is given by

$$\begin{aligned} N_s = (54\lambda^2)^{-1} &= \frac{2}{3} J_0^{-2} \alpha^{-2} (1 - J_0^2) \\ &\simeq \frac{2^{3/4}}{3} \left(\frac{E_J}{E_c} \right)^{1/2} (1 - J_0)^{5/4}, \end{aligned} \tag{4.27}$$

in agreement with the expansion (4.13). With this identification, we write (4.23) as

$$x_* = (3N_s/2)^{1/2}(1 - \omega^2). \tag{4.28}$$

Recall that in moving from the washboard to the cubic we have considered two expansions, one in $1 - J_0$ and one in α. We now show that both quantities are small for typical junction operations if $E_J \gg E_c$. First, during typical operations we generally expect that $1 < N_s < 10$. Our expansions are therefore consistent since N_s involves the product of $(E_J/E_c)^{1/2}$, which we have assumed is large, and $(1 - J_0)^{5/4}$, which must therefore be small. We can invert (4.13) for N_s to find J_0

$$J_0 \simeq 1 - \left(\frac{3N_s}{2^{3/4}} \right)^{4/5} \left(\frac{E_c}{E_J} \right)^{2/5}. \tag{4.29}$$

Substituting (4.29) for J_0 in (4.14), the scaling parameter α becomes

$$\alpha \simeq \left(\frac{2^{13/4}}{3N_s} \right)^{1/10} \left(\frac{E_c}{E_J} \right)^{1/5}. \tag{4.30}$$

Thus, for a reasonable N_s, both $1 - J_0$ and α are proportional to powers of E_c/E_J. The qubits considered in this thesis have large Josephson junctions such that $I_c \simeq$

20μA and $C_J \simeq 6$pF. These values yield $E_c/E_J \sim 10^{-6}$, and for $N_s \simeq 3$ we have $J_0 \simeq 0.99$ and $\alpha \simeq 0.065$. We conclude that the formal expansions from the washboard to the cubic approximation are reasonable.

In summary, we find that a cubic approximation to the washboard is

$$H_{cubic} = \hbar\omega_0 \left(\frac{1}{2}p^2 + \frac{1}{2}\omega^2(x - x_*)^2 - \lambda(x - x_*)^3 \right). \tag{4.31}$$

In (4.31), the momentum is the differential operator $p = -id/dx$, and the energy scale is

$$\hbar\omega_0 = \sqrt{8E_cE_J}(1 - J_0^2)^{1/4}. \tag{4.32}$$

The approximate number of harmonic oscillator states for this cubic is

$$N_s = \frac{2^{3/4}}{3}\left(\frac{E_J}{E_c}\right)^{1/2}(1 - J_0)^{5/4}, \tag{4.33}$$

in terms of which the cubic parameter in (4.31) can be written as

$$\lambda = \frac{1}{\sqrt{54N_s}}. \tag{4.34}$$

Finally, the relative frequency is

$$\omega^2 = \left(\frac{1 - J}{1 - J_0}\right)^{1/2}, \tag{4.35}$$

and the position of the minimum is

$$x_* = (3N_s/2)^{1/2}(1 - \omega^2). \tag{4.36}$$

4.2 Spectral properties of the Cubic Oscillator

In the remainder of this Chapter we measure all energies in units of $\hbar\omega_0$ and use $J = J_0$ so that $\omega = 1$ and $x_* = 0$ in (4.31). Thus we consider

$$H = \frac{1}{2}p^2 + \frac{1}{2}x^2 - \lambda x^3. \tag{4.37}$$

As touched upon in the Introduction, there is no unique mathematical definition of the spectrum for the cubic oscillator. This is due to the fact that the asymptotic solutions of the Schrödinger equation $H\Psi = E\Psi$ are in fact square-integrable for *any energy*. To show this, we consider the WKB, outgoing wave function

$$\Psi_+(x) \simeq (2E - x^2 + 2\lambda x^3)^{-1/4} \exp iS(x) \tag{4.38}$$

For large x and S real, we find

$$|\Psi_+(x)|^2 \simeq (2E - x^2 + 2\lambda x^3)^{-1/2} \sim Ax^{-3/2}. \tag{4.39}$$

Since $|\Psi_+(x)|^2$ is falling off faster than x^{-1} at large x, its integral is convergent, and therefore it is square-integrable. Now, the WKB exponent has the form

$$\begin{array}{ll} S & = \int^x ds(2E - s^2 + 2\lambda s^3)^{1/2} \\ & \simeq (2\lambda)^{1/2}\left(\frac{2}{5}x^{5/2} - \frac{1}{6\lambda}x^{3/2} - \frac{1}{64\lambda^2}x^{1/2} + \frac{1}{256\lambda^3}(1 - 64\lambda^2 E)x^{-1/2}\right). \end{array} \tag{4.40}$$

Since S is asymptotically independent of E (its contribution goes as $x^{-1/2}$), any value of the energy is allowed, real or complex!

This situation is quite different from the washboard, whose asymptotic wave-functions are Airy-type, which for complex energy diverge for $x \to \infty$ [see 3.152]. For real energy they form a continuum, which while not square-integrable, can be

normalized to form a delta function in energy. The cubic wavefunctions cannot be so normalized, and thus the spectrum is discrete rather than continuous, and admits any energy as a true eigenvalue. The technical statement is that the point spectrum of the maximal differential operator for H fills the entire complex plane [222]. Thus, there is no mathematically unique way to make physical sense of H.

Square-integrability (or its continuum extension) is not the only boundary condition that can be used to determine the spectrum. The relevant alternative for resonances is to choose the Gamow-Siegert outgoing wave boundary condition [171, 172]. An equivalent condition is to use complex scaling, that is to find wavefuctions such that $|\Psi(x)| \to 0$ along the complex contour $x \to \infty e^{i\theta}$ (for general analysis, boundary conditions must specify particular paths in the complex plane [223]). In principle, use of this boundary condition could yield a unique meaning to the spectrum. In practice, this has only been shown through the use of some regularization of the cubic potential [224].

When the Gamow-Siegert boundary condition is used for a regularized potential, the real parts of the eigenvalues match to the oscillator energies found through perturbation theory, with imaginary parts that can be found via WKB methods. Thus, a meaningful perturbation series exists for the Gamow-Siegert boundary condition on this modified potential. Note however, that the standard boundary conditions on this new problem yield a continuous spectrum, and the connection between the complex resonances and scattering theory hold as for the washboard in Chapter 3.

The above considerations apply for λ real. For complex λ, a great deal more

can be said about the cubic. In this case, the spectrum of H is unique, discrete, and, for $|\lambda|$ sufficiently small, in one to one correspondence with the spectrum of the harmonic oscillator [225]. Furthermore, these eigenvalues remain pseudoeigenvalues when λ is continued to the real axis. Thus the spectrum of the complex cubic seems to uniquely yield some of the spectrum of (any self-adjoint extension of) the real cubic. Finally, these eigenvalues can be put into correspondence with the resonances of the regularized potential [224].

A great deal of recent interest has focused on purely imaginary $\lambda = ig$. In this case, the Hamiltonian is invariant under the combined action of parity $\mathcal{P}(x) = -x$ and time-reversal $\mathcal{T}(\lambda) = (\lambda)^* = -\lambda$, i.e. $\mathcal{PT}(H) = H$. There is strong numerical evidence [226, 227] and recent theoretical work [228, 229] that for certain λ the spectrum of the imaginary cubic oscillator is real and discrete. While a complete physical interpretation of these results is missing, the creation of a $\mathcal{PT}$-symmetric theory of quantum mechanics holds promise for both mathematical physics and for applications in field theory and condensed matter systems [226, 230].

This brief discussion of the status of the cubic oscillator serves mainly to show that the simple formalism derived below can be made mathematically meaningful only through somewhat complicated arguments. For our purposes, however, the problem is quite clearcut. Using the Gamow-Siegert picture of resonances, we can construct wavefunctions and energies of the washboard by applying a combination of perturbation theory and WKB methods on its cubic approximation. These constructions are unique since the they follow from a well-defined limit of the well-behaved tilted washboard Hamiltonian. Thus, while there is no unique quantum mechanics

of the cubic oscillator, there is a unique cubic approximation to the tilted washboard model.

4.3 Perturbation Theory

4.3.1 Direct Method

Here we collect perturbation theory results for the energy of the cubic oscillator

$$H = \frac{1}{2}p^2 + \frac{1}{2}x^2 - \lambda x^3. \tag{4.41}$$

First, we derive the Rayleigh-Schrödinger perturbation theory (RSPT) series for $H = H_0 + \lambda H_1$, with

$$H_0 = \frac{1}{2}p^2 + \frac{1}{2}x^2 \tag{4.42}$$

and

$$H_1 = -x^3. \tag{4.43}$$

We begin by expanding the n-th energy eigenstate, $|\Psi_n\rangle$, in powers of λ

$$|\Psi_n\rangle = \sum_{k=0}^{\infty} \lambda^k |n,k\rangle. \tag{4.44}$$

In this expansion, $|n,0\rangle$ is the n-th energy eigenstate of H_0, and $|n,k\rangle$ are the k-th order perturbative corrections. We also expand the energy eigenvalue in powers of λ,

$$E_n = \sum_{k=0}^{\infty} \lambda^k E_{n,k}, \tag{4.45}$$

where $H_0|n,0\rangle = E_{n,0}|n,0\rangle$. Substituting (4.44) and (4.45) into the eigenvalue equation

$$(H_0 + \lambda H_1)|\Psi_n\rangle = E_n|\Psi_n\rangle \tag{4.46}$$

and grouping terms of order λ^k we find

$$H_0|n,k\rangle + H_1|n,k-1\rangle = \sum_{j=0}^{k} E_{n,j}|n,k-j\rangle. \tag{4.47}$$

Assuming that both $E_{n,j}$ and $|n,j\rangle$ are known for $0 \leq j \leq k-1$, we can pull the unknown terms out of the sum on the right hand side of (4.47)

$$H_0|n,k\rangle + H_1|n,k-1\rangle = E_{n,k}|n,0\rangle + E_{n,0}|n,k\rangle + \sum_{j=1}^{k-1} E_{n,j}|n,k-j\rangle. \tag{4.48}$$

Multiplying (4.48) by $\langle m,0|$ we get

$$\begin{aligned} E_{m,0}\langle m,0|n,k\rangle + \langle m,0|H_1|n,k-1\rangle = E_{n,k}\delta_{n,m} + E_{n,0}\langle m,0|n,k\rangle \\ + \textstyle\sum_{j=1}^{k} E_{n,j}\langle m,0|n,k-j\rangle. \end{aligned} \tag{4.49}$$

If $m \neq n$, we can solve (4.49) for $\langle m,0|n,k\rangle$

$$\langle m,0|n,k\rangle = \frac{\langle m,0|H_1|n,k-1\rangle - \sum_{j=1}^{k-1} E_{n,j}\langle m,0|n,k-j\rangle}{E_{n,0} - E_{m,0}} \tag{4.50}$$

which we can rewrite as

$$|n,k\rangle = \sum_{m\neq n} \frac{\langle m,0|H_1|n,k-1\rangle - \sum_{j=1}^{k-1} E_{n,j}\langle m,0|n,k-j\rangle}{E_{n,0} - E_{m,0}}|m,0\rangle. \tag{4.51}$$

If $m = n$, however, we solve (4.49) for $E_{n,k}$:

$$E_{n,k} = \langle n,0|H_1|n,k-1\rangle \tag{4.52}$$

Equations (4.51) and (4.52) determine the perturbation theory, yielding $E_{n,k}$ and $|n,k\rangle$ in terms of lower order expressions. We now exhibit a few of the explicit formulae.

Letting $V_{n,m} = \langle n,0|H_1|m,0\rangle$, and using (4.51) and (4.52), we find the usual first order results

$$E_{n,1} = V_{n,n} \tag{4.53}$$

and

$$|n,1\rangle = \sum_{m\neq n} \frac{V_{n,m}}{E_{n,0}-E_{m,0}}|m,0\rangle. \tag{4.54}$$

In second order we find

$$E_{n,2} = \sum_{m\neq n} \frac{V_{n,m}V_{m,n}}{E_{n,0}-E_{m,0}} \tag{4.55}$$

and

$$|n,2\rangle = \sum_{m_1,m_2\neq n} \frac{(V_{m_1,m_2}V_{m_2,n} - V_{n,n}\delta_{m_1,m_2}V_{m_1,n})}{(E_{n,0}-E_{m_1,0})(E_{n,0}-E_{m_2,0})}|m_1,0\rangle. \tag{4.56}$$

For the following we consider the simplification $V_{n,n} = 0$, appropriate for our current problem with $H_1 = -x^3$. Proceeding to third order we have

$$E_{n,3} = \sum_{m_1,m_2\neq n} \frac{V_{n,m_1}V_{m_1,m_2}V_{m_2,n}}{(E_{n,0}-E_{m_1,0})(E_{n,0}-E_{m_2,0})} \tag{4.57}$$

and

$$|n,3\rangle = \sum_{m_1,m_2,m_3\neq n} \frac{(V_{m_1,m_2}V_{m_2,m_3}V_{m_3,n} - \delta_{m_1,m_3}V_{n,m_2}V_{m_2,n}V_{m_3,n})}{(E_{n,0}-E_{m_1,0})(E_{n,0}-E_{m_2,0})(E_{n,0}-E_{m_3,0})}|m_1,0\rangle. \tag{4.58}$$

In fourth order we find

$$E_{n,4} = \sum_{m_1,m_2,m_3\neq n} \frac{V_{n,m_1}V_{m_3,n}(V_{m_1,m_2}V_{m_2,m_3} - \delta_{m_1,m_3}V_{m_2,n}V_{n,m_2})}{(E_{n,0}-E_{m_1,0})(E_{n,0}-E_{m_2,0})(E_{n,0}-E_{m_3,0})} \tag{4.59}$$

and

$$|n,4\rangle = \sum_{m_1,m_2,m_3,m_4\neq n} \frac{G^{(4)}_{n,m_1,m_2,m_3,m_4}}{\prod_{i=1}^{4}(E_{n,0}-E_{m_i,0})}|m_1,0\rangle \tag{4.60}$$

with

$$\begin{aligned} G^{(4)}_{n,m_1,m_2,m_3,m_4} = \; & V_{m_1,m_2}V_{m_2,m_3}V_{m_3,m_4}V_{m_4,n} \\ & -\delta_{m_2,m_4}V_{m_1,m_2}V_{m_2,n}V_{n,m_3}V_{m_3,n} \\ & -\delta_{m_1,m_2}V_{m_1,m_3}V_{m_3,n}V_{n,m_4}V_{m_4,n}. \end{aligned} \tag{4.61}$$

In fifth order we have

$$E_{n,5} = \sum_{m_1,m_2,m_3,m_4 \neq n} \frac{V_{n,m_1} G^{(4)}_{n,m_1,m_2,m_3,m_4}}{\prod_{i=1}^{4}(E_{n,0} - E_{m_i,0})} \tag{4.62}$$

and

$$|n,5\rangle = \sum_{m_1,m_2,m_3,m_4,m_5 \neq n} \frac{G^{(5)}_{n,m_1,m_2,m_3,m_4,m_5}}{\prod_{i=1}^{5}(E_{n,0} - E_{m_i,0})} |m_1,0\rangle \tag{4.63}$$

with

$$\begin{aligned} G^{(5)}_{n,m_1,m_2,m_3,m_4,m_5} = \; & V_{m_1,m_2}V_{m_2,m_3}V_{m_3,m_4}V_{m_4,m_5}V_{m_5,n} \\ & -\delta_{m_3,m_5}V_{m_1,m_2}V_{m_2,m_3}V_{m_3,n}V_{n,m_4}V_{m_4,n} \\ & -\delta_{m_2,m_3}V_{m_1,m_3}V_{m_3,m_4}V_{m_4,n}V_{n,m_5}V_{m_5,n} \\ & -\delta_{m_1,m_2}V_{m_1,m_3}V_{m_3,m_4}V_{m_4,n}V_{n,m_5}V_{m_5,n} \\ & +\delta_{m_1,m_2}\delta_{m_2,m_4}V_{m_1,n}V_{n,m_3}V_{m_3,n}V_{n,m_4}V_{m_5,n} \\ & -\delta_{m_1,m_2}V_{m_1,n}V_{n,m_3}V_{m_3,m_4}V_{m_4,m_5}V_{m_5,n} \\ & +\delta_{m_1,m_2}\delta_{m_3,m_5}V_{m_1,n}V_{n,m_3}V_{m_3,n}V_{n,m_4}V_{m_4,n}. \end{aligned} \tag{4.64}$$

Finally the sixth order energy is

$$E_{n,6} = \sum_{m_1,m_2,m_3,m_4,m_5 \neq n} \frac{V_{n,m_1} G^{(5)}_{n,m_1,m_2,m_3,m_4,m_5}}{\prod_{i=1}^{5}(E_{n,0} - E_{m_i,0})}. \tag{4.65}$$

Clearly, this series can be extended to ever higher orders, but more efficient procedures exist for the cubic oscillator, to be shown in the next section.

The harmonic oscillator matrix elements for the cubic are

$$\begin{aligned} V_{n,m} = -\langle n|x^3|m\rangle = \; & -8^{-1/2}(\sqrt{m(m-1)(m-2)}\delta_{n,m-3} \\ & +3m^{3/2}\delta_{n,m-1} + 3(m+1)^{3/2}\delta_{n,m+1} \\ & +\sqrt{(m+1)(m+2)(m+3)}\delta_{n,m+3}). \end{aligned} \tag{4.66}$$

Using this, we can perform each of the above sums. Actually, we only need to do half, since by symmetry all energy coefficients $E_{n,k}$ with k odd vanish. This is due to the fact that the parity operator

$$\mathcal{P} = \int_{-\infty}^{+\infty} dx |x\rangle\langle -x| \tag{4.67}$$

is unitary and the Hamiltonian satisfies $H(-\lambda) = \mathcal{P}H(\lambda)\mathcal{P}^\dagger$. Since the spectrum is invariant under unitary transformations ($UHU^\dagger$ has the same spectrum as H), we

find that $E_n(-\lambda) = E_n(\lambda)$. This implies $E_{n,k} = (-1)^k E_{n,k}$, which therefore vanishes for k odd.

Thus, we focus on the even terms. $E_{n,2}$ in (4.55) is a sum of only four terms ($m = n \pm 1, n \pm 3$) and is easy to evaluate:

$$E_{n,2} = -\frac{15}{4}(n^2 + n + 11/30). \tag{4.68}$$

The sum $E_{n,4}$ in (4.59) is composed of two sets of terms, the second having sixteen terms: $m_1 = n \pm 1, n \pm 3$, $m_2 = n \pm 1, n \pm 3$ and $m_3 = m_1$. The first set has $m_1 = n \pm 1, n \pm 3$, $m_3 = n \pm 1, n \pm 3$, and m_2 the union of $m_1 \pm 1, m_1 \pm 3$ and $m_3 \pm 1, m_3 \pm 3$, a grand total of 84 terms, many of which are zero. Performing this sum via Mathematica, we find

$$E_{n,4} = -\frac{15}{32}(94n^3 + 141n^2 + 109n + 31). \tag{4.69}$$

The sum $E_{n,6}$ in Eq. (4.65) is even longer, with the final result

$$E_{n,6} = -\frac{1}{128}(115755n^4 + 231510n^3 + 278160n^2 + 162405n + 39709). \tag{4.70}$$

We show the (un-normalized) wavefunctions for only $k = 1$ and $k = 2$:

$$\begin{aligned} |n,1\rangle = \; & \tfrac{1}{6\sqrt{2}}\sqrt{(n+1)(n+2)(n+3)}|n+3,0\rangle \\ & \tfrac{3}{2\sqrt{2}}(n+1)^{3/2}|n+1,0\rangle + \tfrac{3}{2\sqrt{2}}n^{3/2}|n-1,0\rangle \\ & -\tfrac{1}{6\sqrt{2}}\sqrt{n(n-1)(n-2)}|n-3,0\rangle, \end{aligned} \tag{4.71}$$

and

$$\begin{aligned} |n,2\rangle = \; & \tfrac{1}{144}\sqrt{(n+1)(n+2)(n+3)(n+4)(n+5)(n+6)}|n+6,0\rangle \\ & +\tfrac{1}{8}(n+\tfrac{7}{4})\sqrt{(n+1)(n+2)(n+3)(n+4)}|n+4,0\rangle \\ & +\tfrac{1}{16}(7n^2+33n+27)\sqrt{(n+1)(n+2)}|n+2,0\rangle \\ & +\tfrac{1}{16}(7n^2-19n+1)\sqrt{n(n-1)}|n-2,0\rangle \\ & +\tfrac{1}{8}(n-\tfrac{3}{4})\sqrt{n(n-1)(n-2)(n-3)}|n-4,0\rangle \\ & +\tfrac{1}{144}\sqrt{n(n-1)(n-2)(n-3)(n-4)(n-5)}|n-6,0\rangle. \end{aligned} \tag{4.72}$$

Thus, the first few states are, to second order,

$$|\Psi_0\rangle = |0\rangle + \lambda\left(+\frac{3}{2\sqrt{2}}|1\rangle + \frac{1}{2\sqrt{3}}|3\rangle\right) + \lambda^2\left(\frac{27\sqrt{2}}{16}|2\rangle + \frac{7\sqrt{6}}{16}|4\rangle + \frac{2\sqrt{5}}{24}|6\rangle\right), \quad (4.73)$$

$$|\Psi_1\rangle = |1\rangle + \lambda\left(-\frac{3}{2\sqrt{2}}|0\rangle + 3|2\rangle + \frac{\sqrt{3}}{3}|4\rangle\right) + \lambda^2\left(\frac{67\sqrt{6}}{16}|3\rangle + \frac{11\sqrt{30}}{16}|5\rangle + \frac{\sqrt{35}}{12}|7\rangle\right), \quad (4.74)$$

and

$$|\Psi_2\rangle = |2\rangle + \lambda\left(-3|1\rangle + \frac{9\sqrt{3}}{2\sqrt{2}}|3\rangle + \frac{\sqrt{15}}{3\sqrt{2}}|5\rangle\right) + \lambda^2\left(-\frac{9\sqrt{2}}{16}|0\rangle + \frac{121\sqrt{3}}{8}|4\rangle + \frac{45\sqrt{10}}{16}|6\rangle + \frac{\sqrt{35}}{6}|7\rangle\right). \quad (4.75)$$

Finally, for future reference we compute matrix elements using these second order expressions and the definition

$$x_{n,m} = \frac{\langle\Psi_n|x|\Psi_m\rangle}{|\Psi_n||\Psi_m|} \quad (4.76)$$

with $|\Psi|^2 = \langle\Psi|\Psi\rangle$:

$$x_{0,0} = \frac{3}{2}\lambda + O(\lambda^3), \quad (4.77)$$

$$x_{0,1} = \frac{1}{\sqrt{2}}\left(1 + \frac{11}{4}\lambda^2\right) + O(\lambda^3), \quad (4.78)$$

$$x_{0,2} = -\frac{1}{\sqrt{2}}\lambda + O(\lambda^3), \quad (4.79)$$

$$x_{1,1} = \frac{9}{2}\lambda + O(\lambda^3), \quad (4.80)$$

$$x_{1,2} = 1 + \frac{11}{2}\lambda^2 + O(\lambda^3), \quad (4.81)$$

and

$$x_{2,2} = \frac{15}{2}\lambda + O(\lambda^3). \quad (4.82)$$

4.3.2 Recursion Method

The perturbation theory results of the previous section become quite tedious at high order. This is due to formulas such as (4.65), which apply to general perturbations $V_{n,m}$ with $V_{n,n} = 0$. The matrix elements of the cubic, however have a banded structure, only connecting state n to terms $n \pm 1$ and $n \pm 3$, with the maximum level encountered at order k being $n + 3k$. This observation suggests that there may be a more efficient way to group and proceed at each order. Indeed there is, and it was first explored by Bender and Wu for the quartic oscillator [231]. The cubic was later studied by Drummond [232], and more recently (with imaginary λ) by Bender and Dunne [227]. Here we explain the recursion method and show how explicit results can be generated for all of the energy states.

The first step is to write the wavefunction for level n as

$$\Psi_n(x) = e^{-x^2/2} \sum_{k=0}^{\infty} \lambda^k B_k^{(n)}(x). \tag{4.83}$$

Taking two derivatives of (4.83) we have

$$\frac{d^2\Psi_n}{dx^2}(x) = -\Psi_n(x) + x^2\Psi_n(x) - e^{-x^2} \sum_{k=0}^{\infty} \lambda^k \left(\frac{d^2 B_k^{(n)}}{dx^2}(x) - 2x \frac{dB_k^{(n)}}{dx}(x) \right). \tag{4.84}$$

Substituting (4.84) into the Schrödinger equation

$$-\frac{1}{2}\frac{d^2\Psi_n}{dx^2}(x) + \frac{1}{2}x^2\Psi_n(x) - \lambda x^3 \Psi_n(x) = E_n \Psi_n(x) \tag{4.85}$$

we find the result

$$(E_n - \frac{1}{2})\Psi_n(x) = -\frac{1}{2}e^{-x^2} \sum_{k=0}^{\infty} \lambda^k \left(\frac{d^2 B_k^{(n)}}{dx^2}(x) - 2x \frac{dB_k^{(n)}}{dx}(x) + 2\lambda x^3 B_k^{(n)}(x) \right). \tag{4.86}$$

This can be simplified by cancelling the exponential, which yields

$$(E_n - \frac{1}{2})\sum_{k=0}^{\infty} \lambda^k B_k^{(n)}(x) = -\frac{1}{2}\sum_{k=0}^{\infty} \lambda^k \left(\frac{d^2 B_k^{(n)}}{dx^2}(x) - 2x\frac{dB_k^{(n)}}{dx} + 2\lambda x^3 B_k^{(n)}(x) \right). \tag{4.87}$$

At lowest order ($O(\lambda^0)$), using (4.45) in (4.87) we find

$$(E_{n,0} - \frac{1}{2})B_0(x) = x\frac{dB_0^{(n)}}{dx}(x)(x) - \frac{1}{2}\frac{d^2 B_0^{(n)}}{dx^2}(x), \tag{4.88}$$

which is Hermite's equation with $E_{n,0} = n + 1/2$ and $B_0^{(n)}(x) = cH_n(x)$, where c is a constant, which we fix below.

For the higher order terms we first consider the left-hand-side of (4.87) (for $k + k' > 1$)

$$\begin{array}{ll} \left(\sum_{k=1}^{\infty} E_{n,k}\lambda^k\right)\left(\sum_{k=0}^{\infty} B_k^{(n)}(x)\right) & = \sum_{k=1,k'=0}^{\infty} E_{n,k} B_{k'}^{(n)}(x)\lambda^{k+k'} \\ & = \sum_{k''=1}^{\infty} \lambda^{k''}\left(\sum_{p=0}^{k''-1} E_{n,k''-p} B_p^{(n)}(x)\right), \end{array} \tag{4.89}$$

and move the $k + k' = 0$ term to the right-hand-side of (4.87). Relabeling the last term on the right-hand-side ($k \to k - 1$) of (4.87) we find that at $O(\lambda^k)$

$$\sum_{p=0}^{k-1} E_{n,k-p} B_p(x) = x\frac{dB_k^{(n)}}{dx}(x) - \frac{1}{2}\frac{d^2 B_k^{(n)}}{dx^2}(x) - x^3 B_{k-1}^{(n)}(x) - nB_k^{(n)}(x). \tag{4.90}$$

The final step is to replace the $B_k^{(n)}(x)$ by their polynomial coefficients, using the banded structure of the cubic perturbation to limit the number of terms:

$$B_k^{(n)}(x) = \sum_{j=0}^{n+3k} B_{k,j}^{(n)} x^j. \tag{4.91}$$

Using (4.91) we find

$$x\frac{dB_k^{(n)}}{dx}(x) = \sum_{j=0}^{n+3k} jB_{k,j}^{(n)} x^j, \tag{4.92}$$

$$\frac{d^2 B_k^{(n)}}{dx^2}(x) = \sum_{j=0}^{n+3k} j(j-1)B_{k,j}^{(n)} x^{j-2} = \sum_{j=0}^{n+3k-2} (j+1)(j+2)B_{k,j+2}^{(n)} x^j, \tag{4.93}$$

and

$$x^3 B_{k-1}^{(n)}(x) = \sum_{j=0}^{n+3k-3} B_{k-1,j}^{(n)} x^{j+3} = \sum_{j=3}^{n+3k} B_{k-1,j-3}^{(n)} x^j. \tag{4.94}$$

Inserting (4.91), (4.92), (4.93), (4.94) into (4.90), we find for $O(x^j)$

$$(j-n)B_{k,j}^{(n)} - \frac{1}{2}(j+1)(j+2)B_{k,j+2}^{(n)} - B_{k-1,j-3}^{(n)} = \sum_{p=0}^{k-1} E_{n,k-p} B_{p,j}^{(n)}. \tag{4.95}$$

Equation (4.95) serves as a recursion relation that will allow us to systematically construct the terms $B_{k,j}^{(n)}$. To do that, we first observe that there are a number of boundary conditions that must be met. The first obvious ones are that by construction $B_{k,j}^{(n)} = 0$ for the three cases $j > n+3k$, $k < 0$, and $j < 0$. Secondly, $B_{0,j}^{(n)}$ must be proportional to the coefficients of the Hermite polynomials. In particular, for n even we choose $B_{0,0}^{(n)} = 1$ and find

$$B_{0,k}^{(n)} = \left\{ \begin{array}{ll} \frac{(-1)^l 2^{2l}(n/2)!}{(n/2-l)!(2l)!} & k = 2l \\ 0 & k = 2l+1 \end{array} \right\}, \tag{4.96}$$

while for n odd we choose $B_{0,1}^{(n)} = 1$ and find

$$B_{0,k}^{(n)} = \left\{ \begin{array}{ll} 0 & k = 2l \\ \frac{(-1)^k 2^{2l+1}((n-1)/2)!}{((n-1)/2-l)!(2l+1)!} & k = 2l+1 \end{array} \right\}. \tag{4.97}$$

Now, we can actually choose $B_{k,0}^{(n)} = \delta_{k,0}$ for n even, which merely amounts to a particular choice of normalization. Similarly, we choose $B_{k,1}^{(n)} = \delta_{k,0}$ for n odd. Finally, we can simplify Eq. (4.95) for $B_{k,n+3k}^{(n)}$ using the boundary condition $B_{k,j>n+3k}^{(n)} = 0$:

$$3k B_{k,n+3k}^{(n)} - B_{k-1,n+3(k-1)}^{(n)} = 0, \tag{4.98}$$

with the solution

$$B_{k,n+3k}^{(n)} = \frac{1}{3^k k!} B_{0,n}^{(n)} \tag{4.99}$$

This completes the specification of the boundary conditions.

Before presenting the algorithm to solve the recursion relation, we must relate the energies to the coefficient matrix. Letting $j = 0$, $k > 0$, and using our boundary conditions, we find

$$E_{n,k} = \left\{ \begin{array}{ll} -B_{k,2}^{(n)} & n \text{ even} \\ -3B_{k,3}^{(n)} & n \text{ odd} \end{array} \right\}. \tag{4.100}$$

For n even, (4.95) becomes

$$(j-n)B_{k,j}^{(n)} - \frac{1}{2}(j+1)(j+2)B_{k,j+2}^{(n)} - B_{k-1,j-3}^{(n)} = -\sum_{p=0}^{k-1} B_{k-p,2}^{(n)} B_{p,j}^{(n)} \tag{4.101}$$

while for n odd (here and below) we must replace $B_{k,2}^{(n)} \to 3B_{k,3}^{(n)}$ in the sum on the right-hand-side. The recursion algorithm depends on whether j is greater or less than n. That is, for a given k and for $j > n$ we can iterate down from $j = n + 3k$ (which is fixed by the boundary condition) via

$$B_{k,j}^{(n)} = \frac{1}{j-n}\left(\frac{1}{2}(j+1)(j+2)B_{k,j+2}^{(n)} + B_{k-1,j-3}^{(n)} - \sum_{p=1}^{k-1} B_{k-p,2}^{(n)} B_{p,j}^{(n)} \right). \tag{4.102}$$

We have removed the $p = 0$ term in the sum in (4.95) due to the boundary condition $B_{0,j}^{(n)} = 0$ for $j > n$. Careful inspection of (4.102) shows that all terms on the right-hand-side are already known from previous steps. This iteration works until $j = n$ at which point we must include the $p = 0$ term. We now solve for $B_{k,2}^{(n)}$

$$B_{k,2}^{(n)} = \frac{1}{B_{0,n}^{(n)}}\left(\frac{1}{2}(j+1)(j+2)B_{k,j+2}^{(n)} + B_{k-1,j-3}^{(n)} - \sum_{p=1}^{k-1} B_{k-p,2}^{(n)} B_{p,j}^{(n)} \right). \tag{4.103}$$

Since $B_{k,2}^{(n)}$ is now known, we can iterate upwards

$$B_{k,j+2}^{(n)} = \frac{2}{(j+1)(j+2)}\left((j-n)B_{k,j}^{(n)} - B_{k-1,j-3}^{(n)} - \sum_{p=0}^{k-1} B_{k-p,2}^{(n)} B_{p,j}^{(n)} \right), \tag{4.104}$$

finally stopping at $j = n - 2$. In this way we have solved for $B_{k,j}^{(n)}$ for all j, and can proceed to order $k + 1$.

Practically speaking, this procedure is most easily coded for specific (generally low) values of n. We can use these specific values to construct the general form of $E_{n,k}$. Indeed we see that $E_{n,k}$ is a power series in n, with the maximum power $\sim (V_{n,n'})^k/(n^{k-1}) \sim n^{k/2+1}$. Thus, we can write

$$E_{n,k} = \sum_{\alpha=0}^{k/2+1} c_{k,\alpha}^{(n)} n^{\alpha}. \tag{4.105}$$

To find the coefficients $c_{k,\alpha}^{(n)}$ for a given k we evaluate $E_{n,k}$ for $0 \leq n \leq k/2+2$ and solve the above set of linear equations. Programming the above procedure in Mathematica is not terribly hard; an implementation is given in the Appendix.

The final results are for $k = 14$:

$$E_{n,0} = n + \frac{1}{2} \tag{4.106}$$

$$E_{n,2} = -\frac{1}{8}(11 + 30n + 30n^2), \tag{4.107}$$

$$E_{n,4} = -\frac{15}{32}(31 + 109n + 141n^2 + 94n^3), \tag{4.108}$$

$$E_{n,6} = -\frac{1}{128}(39709 + 162405n + 278160n^2 + 231510n^3 + 115755n^4), \tag{4.109}$$

$$\begin{aligned} E_{n,8} = -\tfrac{21}{2048} \quad & (916705 + 4244573n + 8374830n^2 \\ & +9387690n^3 + 5706705n^4 + 2282682n^5), \end{aligned} \tag{4.110}$$

$$\begin{aligned} E_{n,10} = -\tfrac{147}{8192} \quad & (20030557 + 101347305n + 228176070n^2 + 292090470n^3 \\ & +242127585n^4 + 115298820n^5 + 38432940n^6), \end{aligned} \tag{4.111}$$

$$\begin{aligned} E_{n,12} = -\tfrac{15}{65536} \quad & (71667471191 + 390365712807n + 956962033860n^2 \\ & +1405781660248n^3 + 1320554758215n^4 + 865910506692n^5 \\ & +337688603406n^6 + 96482458116n^7), \end{aligned} \tag{4.112}$$

$$E_{n,14} = -\frac{3}{262144} \quad (75633966807431 + 435563687342535n + 1153607094794760n^2 + 1838467262444400n^3 + 1990665987016770n^4 + 1469066290398630n^5 + 795267869208120n^6 + 261924947778780n^7 + 65481236944695n^8). \tag{4.113}$$

This procedure is much more efficient that the direct summation presented in the previous section. Note that the rapid growth of this series suggests that it is diverging. There exist methods such as Borel resummation that can resum the expansion [233, 234, 227]). The sum is indeed divergent and its divergence is due to the existence of a non-analytic imaginary part of the energy, which is the tunneling rate to be presented in the next section. Another method known as variational perturbation theory [235] also provides a better expansion than the above, and can also be applied to the imaginary parts. Finally, Alvarez [236] has presented a systematic WKB method that produces this series, and gives the connection between the convergence of subterms of this series with the classical normal form perturbation series for the cubic oscillator (note that there is an error in Alvarez's table: 4^N should be 4^{2N}).

4.4 WKB Tunneling Rate

The perturbation methods introduced above do not adequately handle the wavefunction outside of the potential well (see Fig. 4.1). Classically, a particle of energy E could be found in regions I or III, but is classically forbidden in region II. Thus, a classical particle placed in region I would stay there forever. A quantum particle, however, can tunnel through the classically forbidden region to emerge outside the

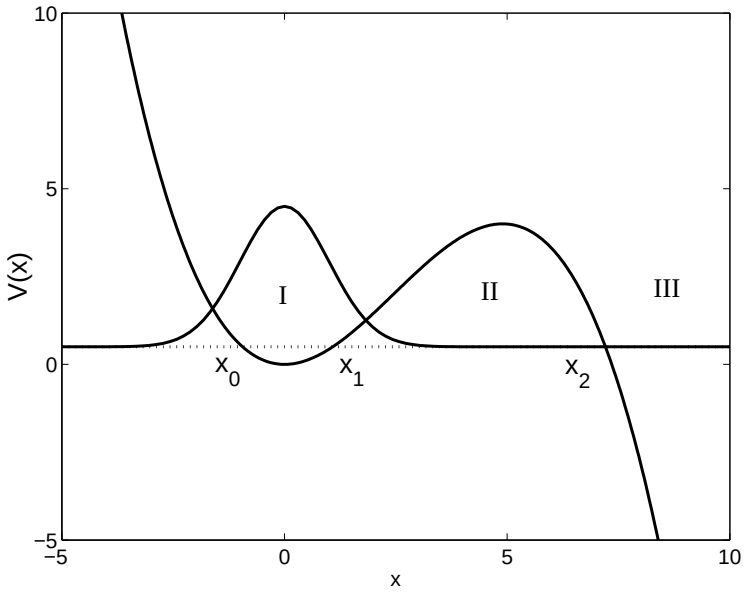

Figure 4.1: Cubic well. The metastable ground state wavefunction is shown, with classical turning points x_0, x_1, and x_2. The WKB wavefunction tunnels from region I through the classically forbidden region (region II) to yield an outgoing wave in region III.

well, and then escape to infinity. To calculate the rate of this process, we construct an outgoing WKB wavefunction which satisfies the Gamow-Siegert boundary condition. After matching this wavefunction in regions I, II, and III, we conclude this section by showing how the tunneling rate (or the imaginary part of the complex energy) can be found directly from this WKB wavefunction. We note that calculations similar to this have been sketched before [237, 238, 239], and aspects of the WKB matching of the harmonic oscillator are first found in [240].

4.4.1 General Potential

In this section we deal with the general Hamiltonian

$$H = \frac{1}{2m}p^2 + V(x), \tag{4.114}$$

with a potential minimum such that $V(x) \sim \frac{1}{2}m\omega^2 x^2$, such as that in Fig. 4.1. We apply our results to the cubic in the next section.

The standard WKB connection formulae [241] for the far turning point (x_2) states that a wavefunction in section II of the form

$$\Psi_{\rm II}(x) = \frac{A}{\sqrt{|v|}}\exp\left(-\frac{1}{\hbar}\int_x^{x_2}|p|dx'\right) + \frac{B}{\sqrt{|v|}}\exp\left(\frac{1}{\hbar}\int_x^{x_2}|p|dx'\right) \tag{4.115}$$

should match onto the exterior wavefunction in region III,

$$\begin{aligned}\Psi_{\rm III}(x) = &\frac{A+iB/2}{\sqrt{v}}\exp\left(\frac{i}{\hbar}\int_{x_2}^{x}pdx' - i\pi/4\right)\\ &+\frac{A-iB/2}{\sqrt{v}}\exp\left(-\frac{i}{\hbar}\int_{x_2}^{x}pdx' + i\pi/4\right)\end{aligned} \tag{4.116}$$

where

$$p(x) = mv(x) = \sqrt{2m(E-V(x))}. \tag{4.117}$$

If $A = iB/2$, this exterior wavefunction (4.116) will have the purely outgoing form

$$\Psi_{\rm III}(x) = \frac{B}{\sqrt{v}} \exp\left(\frac{i}{\hbar}\int_{x_2}^{x} p dx' + i\pi/4\right). \tag{4.118}$$

We can then rewrite (4.115) as

$$\begin{aligned}\Psi_{\rm II}(x) &= \frac{C}{\sqrt{|v|}} \exp\left(-\frac{1}{\hbar}\int_{x_1}^{x} |p| dx'\right) \\ &+\frac{i}{2}\frac{C}{\sqrt{|v|}} \exp\left(-\frac{2}{\hbar}\int_{x_1}^{x_2} |p| dx'\right) \exp\left(\frac{1}{\hbar}\int_{x_1}^{x} |p| dx'\right)\end{aligned} \tag{4.119}$$

and we can choose B and C to be real and related by

$$B = C \exp\left(-\frac{1}{\hbar}\int_{x_1}^{x_2} |p| dx'\right). \tag{4.120}$$

The wavefunction $\Psi_{\rm II}(x)$ in (4.119) has two parts. The first is a real exponentially decaying wavefunction. The second is a purely imaginary exponentially growing wavefunction. Its presence is necessary for the outgoing wave boundary condition. However, near the left turning point (x_1) it is exponentially suppressed and can be neglected. We therefore turn to the matching of the real part of $\Psi_{\rm II}(x)$ to region I.

In region I, we expect the wavefunction to be well approximated by a harmonic oscillator state

$$\Psi_{\rm I}(x) = (2^n n!)^{-1/2} \left(\frac{m\omega}{\hbar\pi}\right)^{1/4} H_n(\sqrt{m\omega/\hbar}x) \exp\left(-\frac{m\omega}{2\hbar}x^2\right). \tag{4.121}$$

with energy

$$E_n = \hbar\omega\left(n + \frac{1}{2}\right). \tag{4.122}$$

Note that we are neglecting any anharmonic effects, working to the zeroth order of perturbation theory in region I. Extending this wavefunction into region II, we use

the leading order behavior of the Hermite polynomials for large z, $H_n(z) \simeq (2z)^n$, to find

$$\Psi_{\rm I}(x) \sim 2^{n/2}(n!)^{-1/2}\pi^{-1/4}\left(\frac{m\omega}{\hbar}\right)^{n/2+1/4} x^n \exp\left(-\frac{m\omega}{2\hbar}x^2\right). \tag{4.123}$$

We now match $\Psi_{\rm I}(x)$ to $\Psi_{\rm II}(x)$ to determine the coefficient C. To do this we must evaluate the integral

$$S(x) = \int_{x_1}^{x} |p(x')|dx'. \tag{4.124}$$

We approximate the momentum by including only the quadratic term of the potential

$$|p(x)| \approx m\omega\sqrt{x^2 - x_1^2} \tag{4.125}$$

where the turning point is

$$x_1 = \sqrt{\frac{2E}{m\omega^2}} \approx \sqrt{\frac{\hbar}{m\omega}}(2n+1)^{1/2}. \tag{4.126}$$

Introducing the substitution $x = x_1 \cosh z$,

$$S(x) = m\omega x_1^2 \int_0^{z_1(x)} \sqrt{(\cosh^2 z - 1)}\sinh z dz \tag{4.127}$$

with

$$z_1(x) = \log\left(\frac{x}{x_1}(1 + \sqrt{1 - x^2/x_1^2})\right), \tag{4.128}$$

(note that $z_1(x) > 0$ and $x = x_1 \cosh z_1(x)$) we find that the transformed integral (4.127) can be done exactly to yield

$$S(x) = \frac{1}{2}m\omega x_1^2 \left(\sinh z_1(x)\cosh z_1(x) - z_1(x)\right). \tag{4.129}$$

We have thus found

$$S(x) = \frac{1}{2}m\omega x_1^2 \left(\frac{x^2}{x_1^2}\sqrt{1 - x_1^2/x^2} - \log\left(\frac{x}{x_1}(1 + \sqrt{1 - x_1^2/x^2})\right)\right), \tag{4.130}$$

which can be readily expanded in terms of x_1/x

$$S(x) \approx \frac{1}{2}m\omega\left(x^2 - \frac{1}{2}x_1^2 - x_1^2\log(2x/x_1)\right). \tag{4.131}$$

Note also that in the prefactor for $\Psi_{\rm II}(x)$ we can let $|v(x)| \approx \omega x$. Putting everything together, substituting (4.131) for S and (4.126) for the turning point x_1 in (4.115) we find

$$\Psi_{II}(x) \approx \frac{C}{\sqrt{\omega}}(2/x_1)^{n+1/2}e^{(2n+1)/4}x^n\exp\left(-\frac{m\omega}{2\hbar}x^2\right). \tag{4.132}$$

Comparing this with $\Psi_I(x)$ in (4.123) yields C

$$C = \frac{\omega^{1/2}(n+\frac{1}{2})^{(n+1/2)/2}}{(2\pi)^{1/4}(n!e^{n+1/2})^{1/2}}. \tag{4.133}$$

Now that we have determined C, we have fully specified the WKB solution. From this we can calculate the tunneling rate. Recall that a Gamow-Siegert wavefunction satisfies $H\Psi = E\Psi$ where E has both a real and imaginary part. In our case $E \approx \hbar\omega(n+1/2) - i\hbar\Gamma_n/2$. Under time evolution the state evolves very simply,

$$\Psi(x,t) = e^{-iHt/\hbar}\Psi(x) = e^{-i\omega t(n+1/2)}e^{-\Gamma_n t/2}\Psi(x), \tag{4.134}$$

and this probability density obeys the exponential decay law $\rho(x,t) = |\Psi(x,t)|^2 = e^{-\Gamma_n t}\rho(x,0)$ and thus

$$\frac{\partial\rho(x,t)}{\partial t} + \Gamma_n\rho(x,t) = 0. \tag{4.135}$$

From the Schrödinger equation, however, $\rho(x,t)$ satisfies the continuity equation

$$\frac{\partial\rho(x,t)}{\partial t} + \frac{\partial J(x,t)}{\partial x} = 0 \tag{4.136}$$

with $J(x,t)$ the probability current density

$$J(x,t) = \frac{\hbar}{2mi}\left(\Psi^*\frac{\partial\Psi}{\partial x} - \Psi\frac{\partial\Psi^*}{\partial x}\right). \tag{4.137}$$

Comparison of (4.136) with (4.135) shows

$$\Gamma_n \rho(x,t) = \frac{\partial J(x,t)}{\partial x}. \tag{4.138}$$

Integrating both sides of (4.138) from x_a (which we take to $-\infty$) to x_b (some point beyond x_2) at some fixed time yields

$$\Gamma_n = \frac{J(x_b) - J(x_a)}{\int_{x_a}^{x_b} \rho(x) dx} \tag{4.139}$$

This expression is a general definition of the tunneling rate for Gamow-Siegert states. Now, since $\Psi_{\rm I}(x)$ is normalized and dominates the denominator of our expression (for x_b not too large), we have

$$\int_{x_a}^{x_b} \rho(x) dx \approx \int_{-\infty}^{+\infty} \Psi_{\rm I}^2(x) dx = 1. \tag{4.140}$$

In addition, there is zero probablity current $J(x_a) = 0$ for $x_a \to -\infty$ since the imaginary part of $\Psi_{\rm I}(x)$ is exponentially suppressed. In the WKB approximation $\partial \Psi_{\rm III}(x)/\partial x \approx imv(x)\Psi_{\rm III}(x)/\hbar$, and thus

$$J(x_b) \approx \frac{\hbar}{2mi}\left(\frac{2im}{\hbar}B^2\right) = B^2 = C^2 \exp\left(-\frac{2}{\hbar}\int_{x_1}^{x_2} |p| dx\right). \tag{4.141}$$

Finally, substituting (4.133) for C, (4.141) for $J(x_b)$, and (4.140) in (4.139), we find the result

$$\Gamma_n = \frac{\omega}{n!\sqrt{2\pi}}\left(\frac{n+1/2}{e}\right)^{n+1/2} \exp\left(-\frac{2}{\hbar}\int_{x_1}^{x_2} |p| dx\right). \tag{4.142}$$

This expression is the WKB tunneling rate for the energy states of a metastable potential well with a barrier of arbitrary shape. Note that if we consider highly excited states and let $n \to \infty$, we can use Stirling's formula in the form

$$n! \to \sqrt{2\pi}\left(\frac{n+1/2}{e}\right)^{n+1/2} \tag{4.143}$$

for the factorial in (4.142) to recover Gamow's celebrated formula [171]

$$\Gamma = (\omega/2\pi)\exp\left(-\frac{2}{\hbar}\int_{x_1}^{x_2}|p|dx\right). \tag{4.144}$$

4.4.2 Cubic Potential

We now specialize our results to the cubic, and set $m = \hbar = \omega = 1$. First we present the expression for the turning points of the potential, that is, the roots of the cubic polynomial

$$\frac{1}{2}x^2 - \lambda x^3 - E = 0. \tag{4.145}$$

Using the standard expression for roots of a cubic (found in the Appendix) we find

$$\begin{array}{l} x_0 = \frac{1}{6\lambda}\left(1 + 2\cos(\theta + 2\pi/3)\right) \\ x_1 = \frac{1}{6\lambda}\left(1 + 2\cos(\theta + 4\pi/3)\right) \\ x_2 = \frac{1}{6\lambda}\left(1 + 2\cos(\theta)\right), \end{array} \tag{4.146}$$

where θ is defined by

$$\theta = \frac{1}{3}\arccos(1 - 108\lambda^2 E). \tag{4.147}$$

For small λ we can expand both (4.147)

$$\theta = (24E)^{1/2}\lambda + \frac{3}{8}(24E)^{3/2}\lambda^3 + O(\lambda^5) \tag{4.148}$$

and (4.146)

$$\begin{array}{l} x_0 = -(2E)^{1/2} + 2E\lambda - \frac{5}{2}(2E)^{3/2}\lambda^2 + 32E^2\lambda^3 + O(\lambda^4) \\ x_1 = +(2E)^{1/2} + 2E\lambda + \frac{5}{2}(2E)^{3/2}\lambda^2 + 32E^2\lambda^3 + O(\lambda^4) \\ x_2 = (2\lambda)^{-1} - 4E\lambda - 64E^2\lambda^3 + O(\lambda^5). \end{array} \tag{4.149}$$

The WKB integral is

$$\begin{array}{rl} S & = \int_{x_1}^{x_2} dx\sqrt{x^2 - 2\lambda x^3 - 2E} \\ & = (2\lambda)^{1/2}\int_{x_1}^{x_2} dx(x - x_0)^{1/2}(x - x_1)^{1/2}(x_2 - x)^{1/2}. \end{array} \tag{4.150}$$

Defining the variables

$$t = \frac{x - x_1}{x_2 - x_1} \tag{4.151}$$

and

$$z = \frac{x_2 - x_1}{x_1 - x_0} = \frac{1}{4(2E)^{1/2}\lambda} - \frac{1}{2} - \frac{17(2E)^{1/2}\lambda}{8} + O(\lambda^2), \tag{4.152}$$

and substituting (4.151) and (4.152) in (4.150), we find the result

$$S = (2\lambda)^{1/2}(x_2 - x_1)^2(x_1 - x_0)^{1/2} \int_0^1 dt\, t^{1/2}(1-t)^{1/2}(1+zt)^{1/2}. \tag{4.153}$$

The integral in S can be identified with the hypergeometric function ([210], Eq. 15.3.1)

$$F(a,b,c;-z) = \frac{\Gamma(c)}{\Gamma(b)\Gamma(c-b)} \int_0^1 dt\, t^{b-1}(1-t)^{c-b-1}(1+zt)^{-a} \tag{4.154}$$

if $a = -1/2$, $b = 3/2$, and $c = 3$, and the gamma functions are $\Gamma(3/2) = \sqrt{\pi}/2$, $\Gamma(3) = 2!$. Thus, we have

$$S = \frac{\pi}{8}(2\lambda)^{1/2}(x_2 - x_1)^2(x_1 - x_0)^{1/2} F(-1/2, 3/2, 3, -z). \tag{4.155}$$

This expression is exact. We use (4.149), (4.152), and the asymptotic form of the hypergeometric function for large z ([210] 15.3.14)

$$F(-1/2,3/2,3,-z) \simeq \frac{32}{15\pi} z^{1/2} \left(\begin{array}{l} 1 + \frac{5}{4}z^{-1} + \frac{75}{64}z^{-2} - \frac{15}{32}z^{-2}\log(16z) \\ +O(z^{-3}\log z) \end{array} \right), \tag{4.156}$$

to find (after some algebra)

$$S = \frac{1}{15\lambda^2} - \frac{1}{2}E + \frac{1}{2}E\log\left(\frac{E\lambda^2}{8}\right) + O(\lambda\log\lambda). \tag{4.157}$$

Substituting $E = (n + 1/2)$ and $\lambda^{-2} = 54N_s$ in (4.157) yields

$$S = \frac{18}{5}N_s - \frac{1}{2}(n+1/2) + \frac{1}{2}(n+1/2)\log\left(\frac{n+1/2}{432N_s}\right) + O(N_s^{-1/2}\log N_s). \tag{4.158}$$

Having calculated the WKB integral, we substitute (4.158) into our tunneling formula (4.142) to find

$$\Gamma_n = \frac{\omega}{\sqrt{2\pi}n!}(432N_s)^{n+1/2}\exp\left(-\frac{36}{5}N_s\right). \tag{4.159}$$

4.5 Instanton Calculation

In this section we derive the WKB result (4.159) using a path integral method, first applied by Coleman [242] to tunneling in quantum mechanics and quantum field theory. The term "instanton" was coined by t'Hooft, while Coleman named the relevant trajectory considered below the "bounce." These results are of importance because Caldeira and Leggett [243, 97] adapted these methods to calculate the effect of dissipation on tunneling. Schmid [244] proved the equivalence of their instanton calculation (under suitable conditions) to a multi-dimensional generalization of the WKB method. While we will not pursue further applications of either the instanton or multi-dimensional WKB methods in this thesis, we include this discussion both for completeness and as a guide to the literature.

The starting point of the instanton calculation is to consider the amplitude

$$D(x_f, x_i; T) = \langle x_f | e^{-TH/\hbar} | x_i \rangle. \tag{4.160}$$

This function is the time-evolution amplitude for a particle at point x_2 to reach x_1 after an *imaginary* time T; in statistical mechanics D is a thermal density matrix with $T/\hbar$ the *inverse* temperature. If H has a point spectrum, we can write

$$D(x_f, x_i; T) = \sum_n e^{-TE_n/\hbar} \Psi_n(x_f) \Psi_n^*(x_i). \tag{4.161}$$

In the "low-temperature limit" we take $T \to \infty$, where only the lowest energy level is dominant, and thus we have

$$D(x_f, x_i; T) \sim e^{-TE_0/\hbar} \Psi_0(x_f) \Psi_0^*(x_i) \tag{4.162}$$

Looking at evolution in imaginary time allows us to extract information about energy levels and wavefunctions.

For $H = p^2/2m + V$, the amplitude $D(x_f, x_i; T)$ can be given a path-integral representation [245]. We first discretize the time ($T = N\epsilon$), use the identity

$$e^{-TH/\hbar} = \prod_{k=1}^{N} e^{-\epsilon H/\hbar}, \tag{4.163}$$

split each exponential

$$e^{-\epsilon H/\hbar} \simeq e^{-\epsilon p^2/2m\hbar} e^{-\epsilon V(x)/\hbar} \tag{4.164}$$

and insert a complete set of states, one for each term in the product

$$e^{-\epsilon H/\hbar} \simeq \int \frac{dp_k dx_k}{2\pi\hbar} e^{-\epsilon p^2/2m} |p_k\rangle\langle p_k| e^{-\epsilon V(x)} |x_k\rangle\langle x_k|. \tag{4.165}$$

Expanding each term in (4.163) with (4.164) and (4.165), and using $\langle x|p\rangle = e^{ipx/\hbar}$, we find that

$$\begin{aligned} D(x_f, x_i; T) = &\left(\prod_{k=0}^{N-1} \int \frac{dp_k dx_k}{2\pi\hbar} \right) \delta(x_0 - x_i) \\ &\times \exp\left(-\frac{\epsilon}{\hbar} \sum_{n=0}^{N-1} \frac{p_n^2}{2m} + V(x_n) + i p_n \frac{x_{n+1} - x_n}{\epsilon} \right), \end{aligned} \tag{4.166}$$

where the initial δ-function fixes $x_0 = x_i$, and we have defined $x_N = x_f$.

The Gaussian momentum integrals in (4.166) can be done analytically to yield an integration over only the x variables

$$D(x_f, x_i; T) = \left(\frac{m}{2\pi\hbar\epsilon} \right)^{N/2} \left(\prod_{k=1}^{N-1} \int dx_k \right) e^{-S_N/\hbar} \tag{4.167}$$

where S is the discrete action

$$S_N = \epsilon \sum_{n=0}^{N-1} \frac{1}{2} m \epsilon^{-2} (x_{n+1} - x_n)^2 + V(x_n). \tag{4.168}$$

Incorporating the prefactor of (4.167) into the integration measure and taking the continuum limit $N \to \infty$, $\epsilon \to 0$, $N\epsilon = T$, we find

$$D(x_1, x_2; T) = \int \mathcal{D}x e^{-S[x(t)]/\hbar} \tag{4.169}$$

where S is called the Euclidean action

$$S[x(t)] = \int_{-T/2}^{T/2} dt \left(\frac{1}{2} m (dx/dt)^2 + V(x) \right), \tag{4.170}$$

and the functional integral runs over all paths such that $x(-T/2) = x_i$ and $x(T/2) = x_f$. In the following we set $x_i = x_f = 0$, which we assume is the minimum of $V(x)$.

Note that the integrand in this action can be identified with a Lagrangian $\mathcal{L} = T - U$, where the potential is $U = -V$. That is, the classical paths derived from this new Lagrangian run in an upside down potential. These paths are extremal paths of the action

$$\frac{\delta S}{\delta x} = -m \frac{d^2 x_{cl}}{dt^2} + V'(x_{cl}) = 0 \tag{4.171}$$

with $V'(x) = dV/dx$. Now, assuming we have found the path $x_{cl}(t)$ that solves this equation of motion, we can shift variables in the path integral (4.169) by $x(t) = x_{cl}(t) + y(t)$, where $y(-T/2) = y(T/2) = 0$. The Jacobian of this transformation is unity, and we find the result

$$D(0, 0; T) = e^{-S_0/\hbar} \int \mathcal{D}y e^{-\Delta S[y, x_{cl}]/\hbar}, \tag{4.172}$$

where $S_0 = S(x_{cl}(t))$ and

$$\Delta S[y, x_{cl}] = S[y] - S(x_{cl}) = \frac{\delta S}{\delta x}|_{x_{cl}} + \frac{1}{2!} y \frac{\delta^2 S}{\delta x^2}|_{x_{cl}} y + \cdots . \tag{4.173}$$

In (4.173) we have employed a type of Einstein summation convention: implied integrations over the unwritten time variables.

The first term of ΔS in (4.173) is zero since it is evaluated with the equation of motion (4.171), the second term is a Gaussian, and in the semi-classical approximation we drop the higher terms. Thus we have

$$\Delta S[y, x_{cl}] = \frac{1}{2}\int_{-T/2}^{T/2} dt\, y(t)\left(-m\frac{d^2}{dt^2} + V''(x_{cl}(t))\right) y(t). \tag{4.174}$$

The differential operator in ΔS can be diagonalized just as a one-dimensional Schrödinger equation, i.e. there exists $u_n(t)$ that satify the same boundary conditions as y and the eigenvalue equation

$$-\frac{d^2u_n}{dt^2}(t) + m^{-1}V''(x_{cl}(t))u_n(t) = \lambda_n u_n(t), \tag{4.175}$$

and satisfy the orthogonality relation

$$\int_{-T/2}^{T/2} dt\, u_n(t)u_m(t) = \delta_{n,m}. \tag{4.176}$$

For finite T the boundary conditions on $u_n(t)$ force the spectrum to be discrete, while for $T \to \infty$ (which is what we are interested in) there can be both discrete and continuous eigenvalues. Substituting $y(t) = m^{-1/2}\sum_n c_n u_n(t)$ into (4.174), and using (4.175) and (4.176) we diagonalize the action

$$\Delta S = \frac{1}{2}\sum_n \lambda_n c_n^2. \tag{4.177}$$

From the integration measure we extract a normalization factor $\mathcal{N}$ (to be determined shortly) and subsituting (4.177) in (4.172) we have

$$D(0,0;T) = e^{-S_0/\hbar}\mathcal{N}\prod_n\left(\int_{-\infty}^{\infty}(2\pi\hbar)^{-1/2}dc_n \exp[-\lambda_n c_n^2/2\hbar]\right). \tag{4.178}$$

Assuming that $\lambda_n > 0$, each Gaussian integral in (4.178) is well-behaved and and their integration leads to

$$D(0,0;T) = e^{-S_0/\hbar}\mathcal{N}\prod_n (\lambda_n)^{-1/2}\,. \tag{4.179}$$

We can formally write the product of eigenvalues in (4.179) as a "fluctuation determinant":

$$D(0,0;T) = e^{-S_0/\hbar}\mathcal{N}\det[-\partial_t^2 + m^{-1}V''(x_{cl}(t))]^{-1/2}. \tag{4.180}$$

This expression can be exactly computed for a harmonic oscillator [245, 246]

$$D_{HO}(0,0;T) = \Big(\frac{m\omega}{2\pi\hbar\sinh\omega T}\Big)^{1/2} = \sqrt{m\omega}\pi e^{-\omega T/2}(1-e^{-2\omega T})^{-1/2}. \tag{4.181}$$

In this case there are only the trivial paths $x_{cl}(t) = 0$ with $S_0 = 0$, and if we expand the square root the higher-order terms in $e^{-2\omega T}$ correctly include only the even quantum states of the oscillator (since $\Psi_n(0) = 0$ for n odd). Using (4.181) we can fix the normalization constant in (4.180) to the formal expression

$$\mathcal{N} = D_{HO}(0,0;T)\det[-\partial_t^2 + \omega^2]^{1/2}. \tag{4.182}$$

Recall that the determinant signifies a product of eigenvalues, as in (4.180). In summary, we have found that the semi-classical approximation to the path integral (4.172) is

$$D(0,0;T) = \Big(\frac{m\omega}{2\pi\hbar\sinh\omega T}\Big)^{1/2}\left(\frac{\det[-\partial_t^2+\omega^2]}{\det[-\partial_t^2 + m^{-1}V''(x_{cl}(t))]}\right)^{1/2}\exp(-S_0/\hbar). \tag{4.183}$$

If there are multiple paths which satisfy the classical equation of motion, we must add each to yield the total amplitude. In the limit $T \to \infty$ we should be able to find the energy of the ground state.

For our tunneling system, however, the ground state is only metastable. The path integral knows this as well. The relevant classical paths are not true minima of the action but only saddle points. In particular, our assumption that $\lambda_n > 0$ is false: for the paths considered here there is both one zero eigenvalue and a negative eigenvalue. This is quite general, for if a nontrivial classical solution $x_{cl}(t)$ exists, then by taking a time derivative of the equation of motion (4.171) we find the result

$$-\frac{d^3 x_{cl}}{dt^3} + m^{-1} V''(x_{cl}(t)) \frac{dx_{cl}}{dt} = 0. \tag{4.184}$$

Comparison with (4.175) shows that dx_{cl}/dt is an eigenfunction with eigenvalue zero. Furthermore, the trajectory begins at $x_i = 0$ at time $t = -T/2$, departs, turns around at some time t_0, and finally returns to $x_f = 0$ at $t = T/2$. Since this "bounce" trajectory turns around at t_0, its derivative dx_{cl}/dt has a node there, and cannot be the lowest eigenfunction. Therefore there is a groundstate with eigenvalue $\lambda_0 < 0$. Callan and Coleman studied this problem [247], and found a consistent prescription to handle these two eigenvalues. Their methods are in fact quite general.

The zero mode is a consequence of time-translation invariance. That is, in the limit $T \to \infty$, there is a continuous family of bounce solutions, parametrized by their centers $x_{cl}(t; t_0) = x_{cl}(t - t_0)$. The generator of this family is precisely the zero mode eigenvector, i.e.

$$x_{cl}(t; t_0 + dt_0) = x_{cl}(t; t_0) + dt_0 (S_0/m)^{1/2} u_1(t). \tag{4.185}$$

(The last factor is due to the normalization of u_1 in (4.176) and the fact that the bounce has $E = 0$). Each of these paths has equal action, thus there is a

zero eigenvalue associated with u_1. Furthermore, we see that $dc_1 = dt_0 S_0^{1/2}$, thus integration over c_1 is equivalent to an integration over the center of the bounce

$$\int \frac{dc_1}{(2\pi\hbar)^{1/2}} = \left(\frac{S_0}{2\pi\hbar}\right)^{1/2} \int dt_0 = \left(\frac{S_0}{2\pi\hbar}\right)^{1/2} T. \tag{4.186}$$

This shows that in (4.179) we should make the replacment $\lambda_1^{-1/2} \to (S_0/2\pi\hbar)^{1/2} T$.

The negative eigenvalue yields a Gaussian integral that, at face value, is obviously divergent

$$\int \frac{dc_0}{(2\pi\hbar)^{1/2}} \exp(+|\lambda_0| c_0^2/2\hbar). \tag{4.187}$$

However, one can define this integral by analytic continuation. This procedure, described in detail by Callan and Coleman [247], deforms the c_0 integration into the complex plane to pick up the steepest descent contour. This yields a purely imaginary part to the action. The particular direction in the complex plane determines the sign. Finally, the continuation only picks up half of the Gaussian integral, so there is a final factor of 1/2 that must be included. Note that by deforming c_0 into the complex plane one allows complex coordinate paths in the path integral. That these complex paths are related to complex scaling and the Gamow-Siegert boundary condition has been (implicity) proven by Schmid's demonstration [244] of the equivalence of the WKB and instanton calculations.

Altogether, if we define the zero bounce amplitude by the harmonic oscillator expression

$$D_0(0,0;T) = \left(\frac{m\omega}{2\pi\hbar \sinh \omega T}\right)^{1/2}, \tag{4.188}$$

and the quantity K by

$$K = (i/2)(S_0/2\pi\hbar)^{1/2} \left(\frac{\det[-\partial_t^2 + \omega^2]}{|\det'[-\partial_t^2 + m^{-1}V''(x_{cl}(t))]|}\right)^{1/2}, \tag{4.189}$$

where $|\det'|$ indicates that the absolute value of the determinant is taken, but with the zero eigenvalue removed, then we have the one bounce amplitude

$$D_1(0,0;T) = D_0(0,0;T)KT\exp(-S_0/\hbar). \tag{4.190}$$

Now, in addition to the zero and 1-bounce amplitudes, there are also n-bounce trajectories with action nS_0. It can be shown [248, 249] that the n-bounce trajectory yields the amplitude

$$D_n(0,0;T) = \frac{1}{n!}D_0(0,0;T)K^nT^n\exp(-nS_0/\hbar). \tag{4.191}$$

Finally, the complete path integral requires the summation over all n-bounce trajectories, thus the total amplitude is

$$D(0,0;T) = \sum_n D_n(0,0;T) = D_0(0,0;T)\exp\left(KTe^{-S_0/\hbar}\right). \tag{4.192}$$

In the large T limit we then identify the energy

$$E = \hbar\omega/2 - \hbar Ke^{-S_0/\hbar}, \tag{4.193}$$

where the first term comes from the 0-bounce (harmonic oscillator) amplitude (4.181). This gives the shift of the ground state energy due to the bounce. We see from (4.189) that this shift is imaginary, and can thus be identified with the tunneling rate as in the Gamow-Siegert WKB wavefunction. The tunneling rates of the excited states can also be found using path integral methods: the first excited state was calculated by Affleck and DeLuccia [250], and the higher states by Weiss and Heffner [251].

To calculate K, we must compute the ratio of two fluctuation determinants. This can be done in two ways. Coleman writes (in the Appendix to "Uses of Instantons", Chapter 7 in [248]) each determinant as a differential equation, whose solution requires only the properties of the bounce. He shows that if the classical solution has the asymptotic behavior (for $t \to \infty$)

$$x_{cl} \to (S_0/m\omega)^{1/2} A e^{-\omega t} \tag{4.194}$$

then the determinant ratio is

$$\left(\frac{\det[-\partial_t^2 + \omega^2]}{|\det'[-\partial_t^2 + m^{-1}V''(x_{cl}(t))]|} \right)^{1/2} = 2^{1/2}\omega A. \tag{4.195}$$

Another method is to find the spectrum of the fluctuation operators and perform the ratio of determinants directly. For the instantons encountered in the cubic and quadratic potentials this can be done exactly, and we calculate this below using an expression due to Kleinert. This result is, of course, in complete agreement with Coleman's work. Again, we must first construct the bounce. For simplicity we set $m = \omega = \hbar = 1$ in the following, reintroducing the appropriate units at the end.

The physical potential and the upside-down potential are shown in Fig. 4.2. The classical paths in the upside-down cubic (which is, of course, still a cubic) are found from the equations of motion

$$\frac{d^2x}{dt^2} - x + 3\lambda x^2 = 0, \tag{4.196}$$

which has the conserved energy

$$E = \frac{1}{2}\left(\frac{dx}{dt}\right)^2 - \frac{1}{2}x^2 + \lambda x^3. \tag{4.197}$$

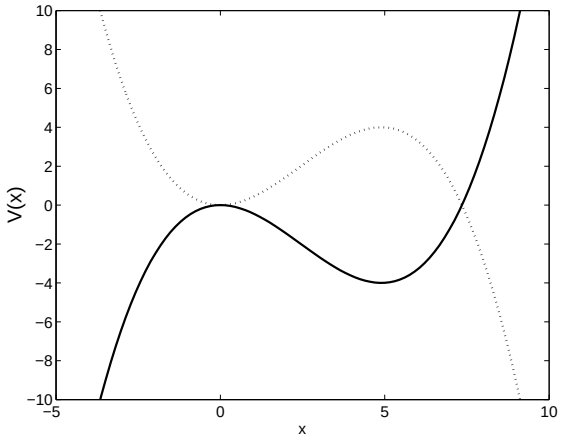

Figure 4.2: Cubic well potential $V(x)$ (dotted line), and the upside-down cubic potential $U(x) = -V(x)$ (solid line). The cubic parameter $\lambda = (54N_s)^{-1/2}$ is chosen such that $N_s = 4$.

Inverting (4.197) we can solve for the time t (taking the negative square root)

$$t = -\int_{x_2}^{x} \frac{ds}{2E + s^2 - 2\lambda s^3}. \tag{4.198}$$

Using (4.146) and (4.147) with $E \to -E$ for the roots $x_0 < x_1 < x_2$ of the cubic we have

$$t = -(2\lambda)^{-1/2} \int_{x_2}^{x} ds(s - x_0)^{-1/2}(s - x_1)^{-1/2}(x_2 - s)^{-1/2}. \tag{4.199}$$

Making the change of variable

$$s = x_2 - (x_2 - x_1)z^2 \tag{4.200}$$

in (4.199) we find

$$\alpha t = \int_0^{z_f(x)} dz(1 - z^2)^{-1/2}(1 - k^2 z^2)^{-1/2} = F(\phi, k) \tag{4.201}$$

where $F(\phi, k)$ is the incomplete elliptic integral,

$$\alpha^2 = \frac{1}{2}\lambda(x_2 - x_0), \tag{4.202}$$

$$z_f(x) = \sin\phi = \left(\frac{x_2 - x}{x_2 - x_1}\right)^{1/2}, \tag{4.203}$$

and

$$k^2 = \frac{x_2 - x_1}{x_2 - x_0}. \tag{4.204}$$

Inverting the elliptic integral (4.201) yields x in terms of the elliptic function $\mathrm{sn}(\alpha t, k) = \sin\phi$:

$$x(t) = x_2 + (x_1 - x_2)\mathrm{sn}^2(\alpha t, k). \tag{4.205}$$

(Note that Mathematica uses the convention $\mathrm{sn}(u, k) = \mathrm{JacobiSN}[u, k^2]$). This is, of course, a periodic function, where the period τ can be written as

$$\tau = \frac{2}{\alpha}F(\pi/2, k) = \frac{\pi}{\alpha}F(1/2, 1/2, 1, k^2) \tag{4.206}$$

where the first F (with two arguments) is the elliptic integral, the second (with four arguments) the hypergeometric function. The bounce is the solution to the classical equations which starts at $x = 0$ in the infinite past, falls off of the potential maximum and performs one oscillation (to the right in Fig. 4.2), to return to $x = 0$ in the infinite future. This infinite period solution corresponds to $E = 0$ and can be found by noting that in this case $x_0 = x_1 = 0$, $x_2 = (2\lambda)^{-1}$. The solution parameters become $\alpha = 1/2$ and $k = 1$, in which case the elliptic function takes the special form $\mathrm{sn}(u, 1) = \tanh(u)$. Thus, the bounce is

$$x(t) = \frac{1}{2\lambda}(1 - \tanh^2(t/2)) = \frac{1}{2\lambda}\frac{1}{\cosh^2(t/2)}. \tag{4.207}$$

This solution is plotted in Fig. 4.3.

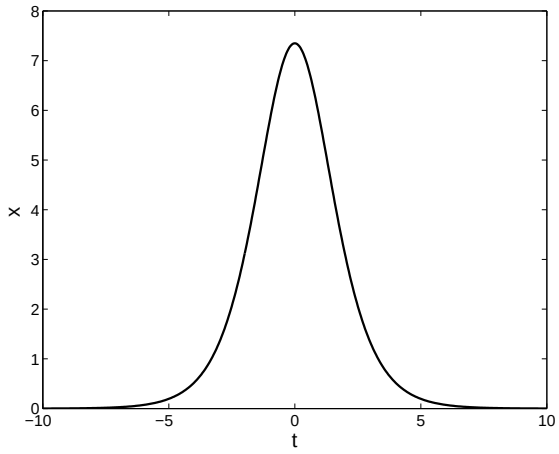

Figure 4.3: The bounce trajectory for the cubic well, with $\omega = 1$ and $N_s = (54\lambda^2)^{-1} = 4$.

Using Coleman's method [248], we have $S_0 = 2/15\lambda^2$, and $A = (30)^{1/2}$. Substituting these into (4.195) we find

$$\left(\frac{\det[-\partial_t^2 + \omega^2]}{|\det'[-\partial_t^2 + m^{-1}V''(x_{cl}(t))]|}\right)^{1/2} = 2^{1/2}\omega A = (60)^{1/2}. \tag{4.208}$$

Then, using this and $N_s = (54\lambda)^{-2}$ in (4.189) we find the result

$$K = (i/2)(2\pi)^{-1/2}(60)^{1/2}(36N_s/5)^{1/2} = (i/2)(2\pi)^{-1/2}(432N_s)^{1/2}. \tag{4.209}$$

Altogether, we have for the tunneling rate

$$\Gamma = 2|K|e^{-S_0} = \frac{1}{\sqrt{2\pi}}(432N_s)^{1/2}e^{-36N_s/5} \tag{4.210}$$

which, with $\omega = 1$ agrees with the WKB result Eq. (4.159) for the ground state.

Kleinert's method [246] considers the fluctuation operator eigenvalue equation

$$-\frac{d^2u_n}{dt^2}(t) + \left(1 - \frac{3}{\cosh^2(t/2)}\right)u_n(t) = \lambda_n u_n(t). \tag{4.211}$$

This equation is equivalent to the Schrödinger equation in the Rosen-Morse potential, which in this case is just $\tilde{V}(t) = 1 - 6\lambda x_{cl}(t)$. Closed form solutions for the eigenfunctions can be written in terms of hypergeometric functions. We follow Kleinert's presentation, which actually covers the more general potential

$$\tilde{V}(t) = 1 - \frac{m^2 s(s+1)}{\cosh^2(mt)} \tag{4.212}$$

(see [246], chapter 17), and thus we have $m = 1/2$, $s = 3$ (note that here m is a parameter, not the mass—the convention is Kleinert's). We find that there are three bound states whose eigenvalues are

$$\lambda_n = 1 - \frac{1}{4}(3-n)^2 \tag{4.213}$$

with $n = 0, 1, 2$. The first bound state has energy $\lambda_0 = -5/4$, with eigenfunction

$$u_0(t) = \frac{5^{1/2}}{4}\frac{1}{\cosh^3(t/2)}. \tag{4.214}$$

The second bound state is the zero-mode with $\lambda_1 = 0$ and

$$u_1(t) = \frac{15^{1/2}}{4}\frac{\sinh(t/2)}{\cosh^3(t/2)}, \tag{4.215}$$

and the last bound state has $\lambda_2 = 3/4$ with

$$u_2(t) = \frac{3^{1/2}}{2^{5/2}}\frac{1}{\cosh^3(t/2)}(4\sinh^2(t/2) - 1). \tag{4.216}$$

The remaining states are in the continuum. By forming an appropriate density of states, Kleinert finds that for s an integer the ratio of determinants for the continuum is

$$\left(\frac{\det[-\partial_t^2 + \omega^2]}{\det[-\partial_t^2 + V''(x_{cl}(t))]}\right)^{1/2}|_{continuum} = \omega^s \prod_{n=1}^{s}(1 + mn\omega^{-1}) \tag{4.217}$$

([246], Eq. 17.127). Letting $m = 1/2$, $s = 3$ and $z = 4$, and including the bound state eigenvalues $\lambda_0 = -5/4$ and $\lambda_2 = 3/4$ we find

$$\left(\frac{\det[-\partial_t^2 + \omega^2]}{|\det'[-\partial_t^2 + V''(x_{cl}(t))]|}\right)^{1/2} = \frac{15}{2}\left(\frac{16}{15}\right)^{1/2} = (60)^{1/2}, \tag{4.218}$$

in complete agreement with (4.208).

Thus, the instanton calculation for the ground state tunneling rate is

$$\Gamma = \frac{\omega}{\sqrt{2\pi}}(432N_s)^{1/2}e^{-36N_s/5} \tag{4.219}$$

where $N_s = \Delta U/\hbar\omega$, in complete agreement with that found using the WKB method.

4.6 Numerical Comparisons

The analytical approximations presented above can be directly compared with the results of numerical calculations using the complex scaling method, implemented as described in the previous Chapter but using the matrix elements of the cubic. Note that complex scaling was first applied to the cubic in [239], and more recently by [233, 252, 235]. We first consider the analytic energy levels and tunneling rates derived in the previous section. We then compare the eigenvalues of the complex scaled cubic potential with that of the washboard.

4.6.1 Comparison with Analytical Results

Figure 4.4 shows the first four levels of the cubic potential for the range $N_s = 6 \rightarrow 1$ computed numerically using complex scaling. The solid lines are the real parts of

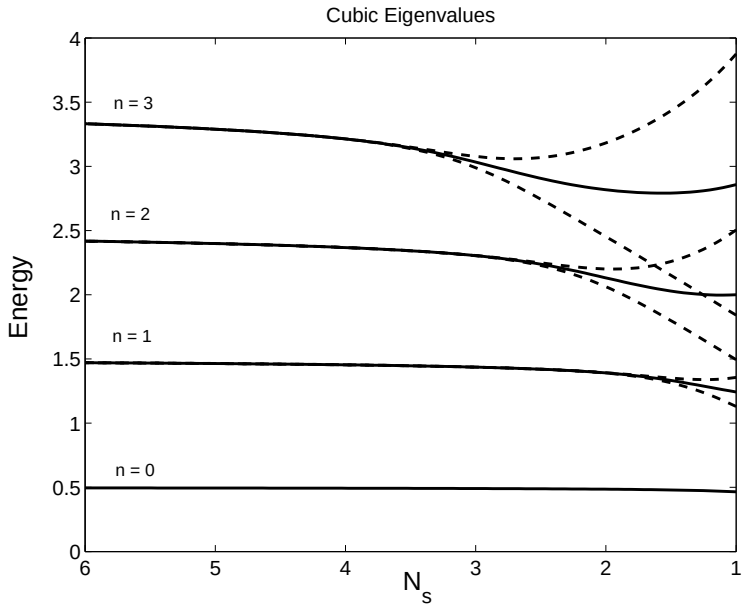

Figure 4.4: Resonances of the cubic well versus the number of levels N_s. The real parts of the resonance eigenvalues E_n with $n = 0, 1, 2, 3$ are shown. The dotted lines below and above each eigenvalue are $\mathrm{Re}(E_n) \pm \mathrm{Im}(E_n)$ used to represent the width of level n. (Note the reversed scale for N_s)

the resonance eigenvalues $E_{n,R} = \mathrm{Re}(E_n)$. The dashed lines are $E_{n,R} + \Gamma_n/2$ and $E_{n,R} - \Gamma_n/2$, where $\Gamma_n = -2\mathrm{Im}(E_n)$. As expected we see that for decreasing N_s the energy levels shift from their harmonic values $E_n = (n + 1/2)$, and broaden due to tunneling.

We now compare these eigenvalues with the perturbative expressions (4.106)-(4.110). In Figs. 4.5-4.7 we show the error $|E_{n,R} - E_{n,pert}|$ for the $n = 0$, $n = 1$, and $n = 2$ energy levels, with the order of the perturbation theory sums ranging from $N_{max} = 0 \rightarrow 8$. We see that for $N_s > 2$ each sum becomes a progressively better approximation to the eigenvalue as N_{max} increases. Also, note that the error scales

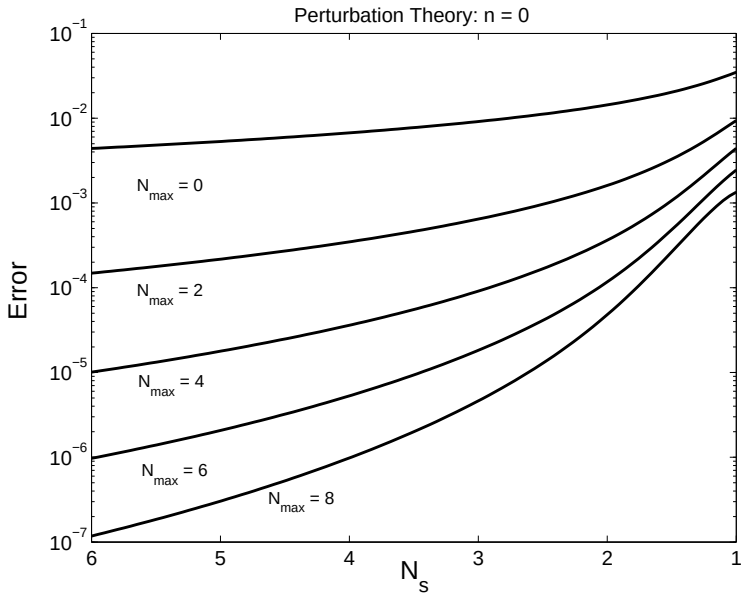

Figure 4.5: Error of cubic perturbation theory for state $n = 0$.

are different for each figure: the approximations are best for the ground state, and less so for each excited state.

For $N_s < 2$, however, perturbation theory begins to fail. The sharp cusps indicate when the perturbative and numerical values cross, and the error goes through zero. Finally, for small N_s, the results become *worse* as N_{max} increases (see especially Fig. 4.7). This is expected for an asymptotic series: after some number of terms the higher corrections begin to grow in magnitude, eventually diverging. This divergence occurs for any value of N_s, if N_{max} is allowed to be sufficiently large.

The corresponding tunneling rates from complex scaling and WKB are shown in Fig. 4.8. The agreement here is only of the right order of magnitude, thus we merely plot the tunneling rates. There have been two independent calculations that explore higher order corrections (in $1/N_s$) to the tunneling rate, the first by

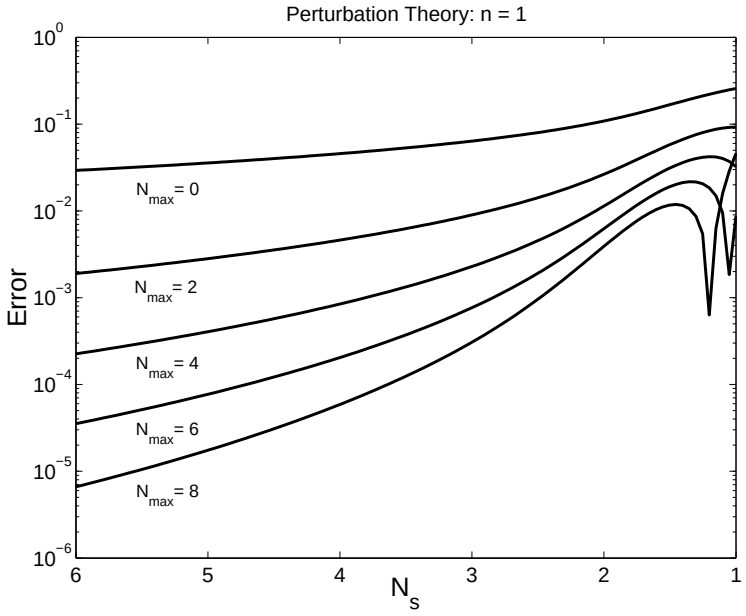

Figure 4.6: Error of cubic perturbation theory for state $n = 1$.

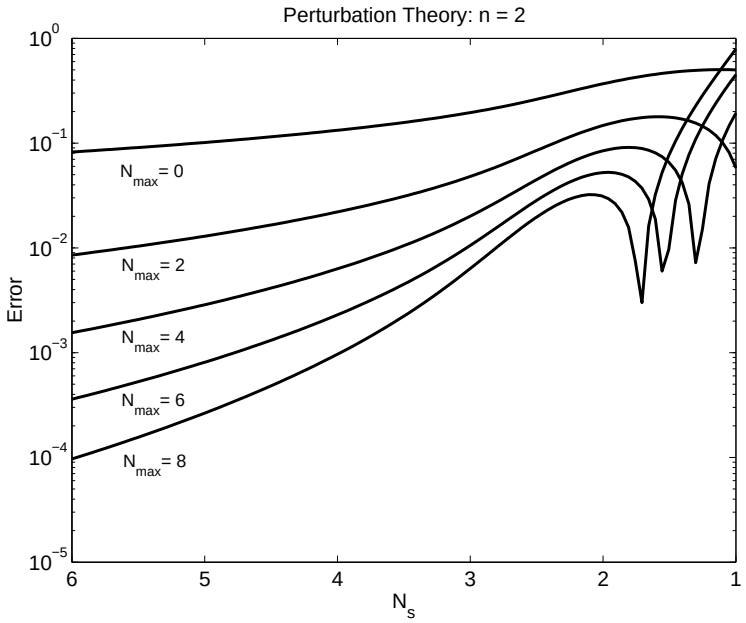

Figure 4.7: Error of cubic perturbation theory for state $n = 2$.

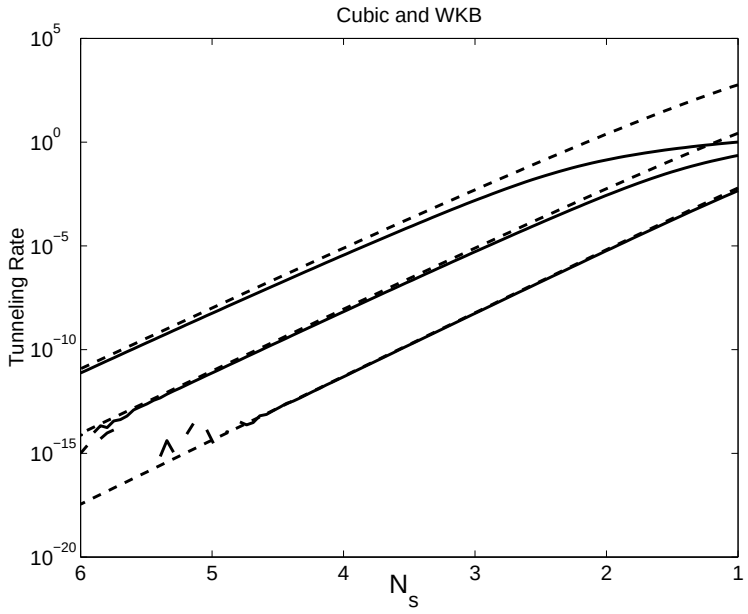

Figure 4.8: Tunneling rates of cubic oscillator for $n = 0, 1, 2$ as a function of N_s. The tunneling rate is given in units of ω_0. The solid lines are the complex scaling eigenvalues, the dashed lines are the lowest order WKB calculation.

Alvarez [233], the second by Kleinert and Mustapic [235]. In fact, there is some disagreement between the two calculations. We will not explore this here, but pause only to comment that Kleinert and Mustapic produced corrections up to order N_s^{-7}, and showed how a particular resummation method called variational perturbation theory can further improve their results, which they then compared with the complex scaling eigenvalues.

4.6.2 Comparison with Washboard

To compare the cubic approximation to results from the tilted washboard potential we consider the junction parameters of the previous chapter, namely $C = 6$ pF and

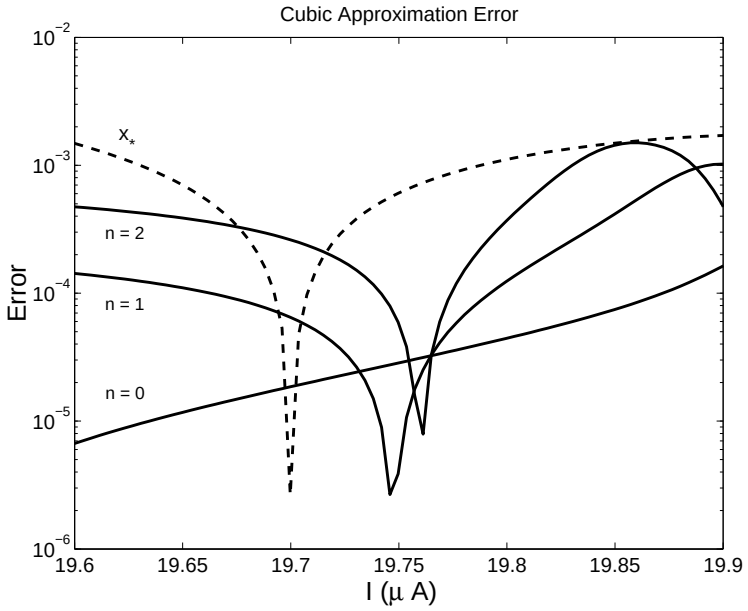

Figure 4.9: Error in the cubic approximation to the washboard using simple matching, real part. The solid lines are the absolute errors in the energy levels calculated using the simple matching of the barrier heights (see text). The dashed line is the error in variation of the potential minimum in the cubic approximation.

$I_c = 20\mu$A. The error in the real part of the scaled eigenvalues $E/\hbar\omega_0$ is shown in Fig. 4.9, where we have used the simple formula

$$N_s = \frac{2^{3/4}}{3}\left(\frac{E_J}{E_c}\right)^{1/2}(1-J_0)^{5/4} \tag{4.220}$$

and

$$\omega = \left(\frac{1-J}{1-J_0}\right)^{1/4} \tag{4.221}$$

to map the washboard onto the cubic, with $J_0 = 0.985$. Also plotted is the error in washboard minimum $\Delta x = |x_* - \alpha(\gamma_J - \gamma_0)|$ (the dashed lines). As before, the cusps occur when the errors momentarily go through zero. Note that an error in the washboard minimum leads to an error in the wavefunction of order $\sim 1 - e^{-\Delta x^2/2} \sim \Delta x^2$, and thus the actual error is of order 10^{-6}, while the error in the energy levels is of order 10^{-3}. This is the expected quantitative agreement of the simple cubic approximation.

There are ways to improve the accuracy of the cubic approximation. One method is to use the exact scaling of the frequencies, i.e. to use the more accurate formula

$$\omega = \left(\frac{1-J^2}{1-J_0^2}\right)^{1/4}. \tag{4.222}$$

Alternatively, one can merely set $J = J_0$ (such that $\omega = 1$) for the computation of the energy levels. Unfortunately, this makes the transformation to the cubic potential dependent on the bias current, which cannot be used for time-dependent calculations. The error in the energy levels using this procedure is shown as the solid lines in Fig. 4.10.

Another improvement is to use the exact expression for the dimensionless barrier height

$$N_s = 2^{-1/2} \left(\frac{E_J}{E_c} \right)^{1/2} \left((1 - J^2)^{1/4} - J(1 - J^2)^{-1/4} \arccos J \right) \tag{4.223}$$

and the standard relation $\lambda = (54 N_s)^{-1/2}$. The error is shown by the dashed lines in Fig. 4.10, which reveals a uniform level of error for each energy level. The improvement is more dramatic for the tunneling rates, whose *relative* error we plot in Fig. 4.11. Note that the initial fluctuations are due to the very small imaginary part of the eigenvalues ($\sim 10^{-14}$) which are near the level of round-off error in the numerical routines.

We have shown that the cubic approximation has, for parameters of interest for quantum computing, an accuracy of relative order $10^{-3} - 10^{-4}$. Errors in the tunneling rate are most sensitive, but can be minimized by matching the barrier heights of the cubic and the washboard. Errors in the energy levels are significantly less sensitive. Thus we conclude that the cubic approximation is more than adequate for energy level calculations. Finally, having examined the effect of the cubic approximation in the energy levels and states, we have justified its use to approximate the dynamics of the washboard.

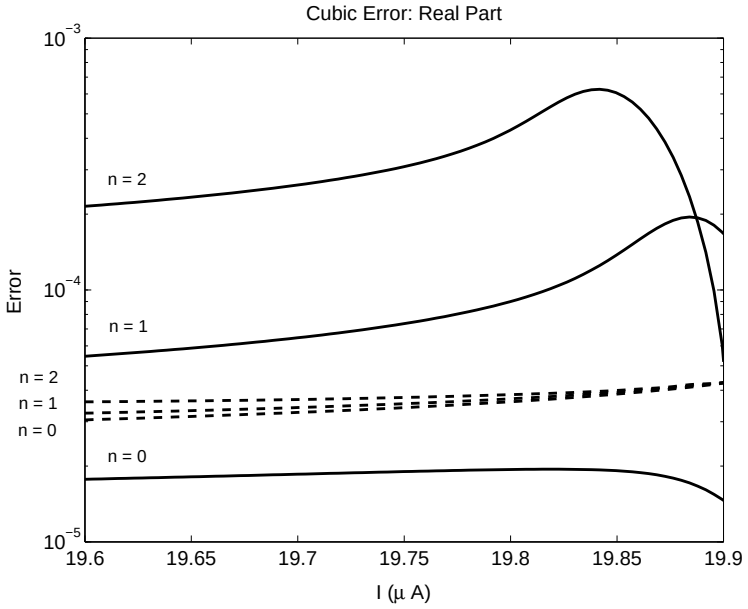

Figure 4.10: Error in the cubic approximation to the washboard using exact matching, real part. The solid lines are the absolute errors in the energy levels calculated using the exact matching of the barrier height (see text). The dashed lines are the errors when the washboard and cubic barriers are exactly equal.

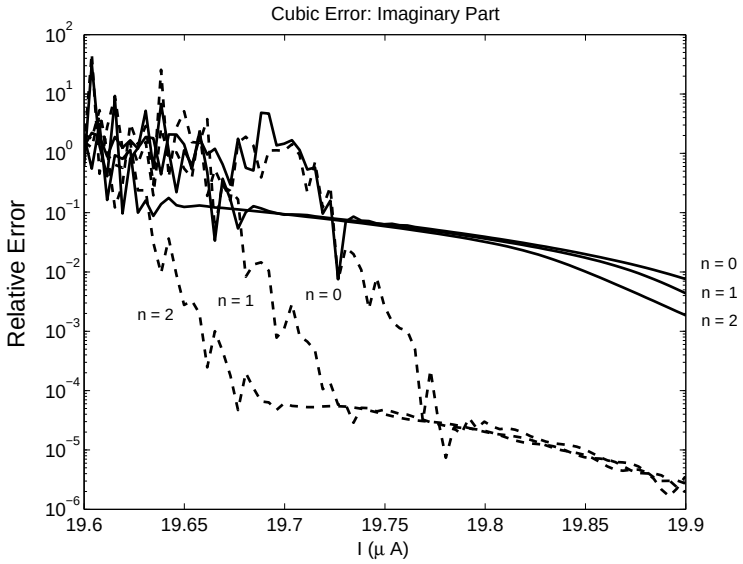

Figure 4.11: Error in the cubic approximation to the washboard, imaginary part. The solid lines are the relative errors in the tunneling rates calculated using simple matching (solid) and exact matching (dashed).

Chapter 5

Single Qubit Operations

If the current-biased Josephson junction can be used as a qubit, it must be controlled in some way. In particular, we must be able to apply a universal set of logic operations in order to run quantum algorithms on our device. As discussed in Chapter 1, the most convenient set of operations consists of single-qubit unitaries plus an entangling two-qubit gate. This Chapter focuses on single-qubit dynamics; the two-qubit problem is discussed in Chapter 2.

Our qubit is formed by the lowest two metastable energy states in one well of the tilted washboard potential. The first control method we consider is the application of a time-dependent perturbation that is resonant with the energy level spacing. If the system is initially in the lowest level, it will periodically oscillate from this lowest level to the next level and back. This phenomenon is called Rabi oscillation, and was first observed in NMR and atomic systems [253]. Observing

Rabi oscillations is traditionally one of the first indications of quantum coherence in simple quantum systems, and have recently been seen in current biased junctions by multiple groups [92, 93]. In principle, by using Rabi oscillations one can generate an arbitrary superposition of the two qubit states and thus implement single-qubit gates. For the Josephson junction phase qubit, however, the presence of additional levels and tunneling cannot be neglected. We study this problem in Section 2.

The energy levels of the phase qubit are not degenerate. Thus, even during idle periods there is dynamics—the first two levels will acquire a net phase difference of $(E_1 - E_0)t$. While this phase difference does not change the state probabilities, it does change the state amplitudes and plays an essential role in subsequent logic operations. This nondegeneracy problem can be solved in two ways. The first method is to use Rabi oscillations, by waiting for a delay time t_d, applying a π-pulse to achieve a NOT gate X (this will be defined below), waiting again for time t_d, and applying a final π-pulse. With this sequence of operations the phase acquired in the first half of the sequence is cancelled by the second half as can be seen from the identity $XZX = -Z$. This is a type of spin-echo technique and can be used for more general decoupling schemes [48, 49]. A second method is to engineer degenerate levels, e.g. by encoding a logical qubit in a degenerate subspace of a multi-qubit system.

In either case, it can be useful to dynamically control the energy levels. Since the phase qubit's energy levels are a function of the applied bias current, a pulse of the bias current will generate a shift of the energy levels. This bias ramp control technique will also be important for two-qubit operations, and arises in many related

schemes using current-biased junctions in the literature [254, 255, 256]. We study this problem in Section 3.

5.1 Rabi Oscillations

The model we consider is the cubic approximation of the previous chapter, and the application of a microwave drive at frequency $\omega/2\pi$. Thus we consider

$$H = \frac{1}{2}p^2 + \frac{1}{2}x^2 - \lambda x^3 + A(t)x\cos(\omega t + \phi). \tag{5.1}$$

We have allowed the amplitude of the drive to be time-dependent so that we can consider pulse shaping. The key parameters in this model are the nonlinearity λ, the drive frequency ω, the drive amplitude $A(t)$, and finally the phase of the drive ϕ.

We first explore a three-level approximation to H. We find that for small A we can control the first two levels. For larger A, there are significant off-resonant transitions to the third level. Three-level models have been studied in atomic physics for quite some time [257] and there have been recent studies of Rabi oscillations in phase qubits by multiple authors [258, 259, 260]. We provide a complete derivation that includes many of their results. We then proceed beyond the three-level approximation to study the full dynamics of H using split-operator techniques. This includes the simulation of tunneling at a fundamental level, without using *ad hoc* models. Finally, we use our accurate methods to study the effects of pulse-shaping on Rabi oscillations.

5.1.1 Three-Level Rotating Wave Approximation

Truncating our model Hamiltonian (5.1) to the first three levels, and ignoring the effects of tunneling, we have (with $\phi = 0$)

$$H_3 = \begin{pmatrix} E_0 & 0 & 0 \\ 0 & E_1 & 0 \\ 0 & 0 & E_2 \end{pmatrix} + A\cos\omega t \begin{pmatrix} x_{00} & x_{01} & x_{02} \\ x_{01} & x_{00} & x_{12} \\ x_{02} & x_{12} & x_{00} \end{pmatrix}. \tag{5.2}$$

The matrix elements have been calculated in Chapter 4, from which we recall

$$\begin{array}{ll} x_{00} & = 3\lambda/2, \\ x_{01} = x_{10} & = 2^{-1/2}(1 + 11\lambda^2/4), \\ x_{02} = x_{20} & = 2^{-1/2}\lambda, \\ x_{11} & = 9\lambda/2, \\ x_{12} = x_{21} & = 1 + 11\lambda^2/2, \\ x_{22} & = 15\lambda/2. \end{array} \tag{5.3}$$

From the Hamiltonian we define the transition frequencies

$$\begin{array}{ll} \omega_{01} & = E_1 - E_0, \\ \omega_{12} & = E_2 - E_1. \end{array} \tag{5.4}$$

Rabi oscillations occur when the drive is such that $\omega \approx \omega_{01}$; to describe this in detail we explore the time-dependent dynamics given by H_3. The goal of this section is to find the time-evolution operator using the rotating wave approximation.

The time-evolution operator satisfies (with $\hbar = 1$)

$$idU/dt = H(t)U(t), \tag{5.5}$$

$U(0) = I$. The formal solution is

$$U(t) = T\exp\left(-i\int_0^t H(s)ds\right) \tag{5.6}$$

where T denotes the time ordering symbol. For our problem, we define an interaction picture by

$$\bar{U}(t) = e^{iH_0 t}U(t), \tag{5.7}$$

where H_0 is time-independent. By direct substitution of (5.7) in (5.5), we find that $\bar{U}(t)$ satisfies

$$id\bar{U}/dt = \bar{H}(t)\bar{U}(t) \tag{5.8}$$

with

$$\bar{H}(t) = e^{iH_0 t}H(t)e^{-iH_0 t} - H_0. \tag{5.9}$$

Choosing H_0 to be

$$H_0 = \begin{pmatrix} 0 & 0 & 0 \\ 0 & \omega & 0 \\ 0 & 0 & 2\omega \end{pmatrix}. \tag{5.10}$$

we find from (5.9) and (5.2)

$$\bar{H}(t) = \bar{H}_0 + \bar{H}_1(t) \tag{5.11}$$

where $\bar{H}_0$ is the time-independent rotating wave Hamiltonian

$$\bar{H}_0 = \begin{pmatrix} E_0 & 0 & 0 \\ 0 & E_1 - \omega & 0 \\ 0 & 0 & E_2 - 2\omega \end{pmatrix} + \frac{A}{2}\begin{pmatrix} 0 & x_{01} & 0 \\ x_{01} & 0 & x_{12} \\ 0 & x_{12} & 0 \end{pmatrix}, \tag{5.12}$$

and $\bar{H}_1(t)$ has the time-dependent corrections

$$\bar{H}_1(t) = \frac{A}{2}\begin{pmatrix} 2x_{00}\cos\omega t & x_{01}e^{-i2\omega t} & 2x_{02}e^{-i2\omega t}\cos\omega t \\ x_{01}e^{i2\omega t} & 2x_{11}\cos\omega t & x_{12}e^{-i2\omega t} \\ 2x_{02}e^{i2\omega t}\cos\omega t & x_{12}e^{i2\omega t} & 2x_{22}\cos\omega t \end{pmatrix}. \tag{5.13}$$

In the rotating wave approximation, we ignore $\bar{H}_1(t)$, the assumption being that the high-frequency components will average out. This approximation should hold for weak fields; for strong fields there are significant corrections to the rotating wave approximation. These include the Bloch-Siegert shift, which can be included perturbatively using Floquet theory [134]. The rotating wave approximation has the advantange that it yields an analytic approximation to the propagator.

The approximate form for the time-evolution operator is

$$U(t) = e^{-iH_0 t} e^{-i\bar{H}_0 t}. \tag{5.14}$$

Note that H_0 is diagonal in our basis; to study Rabi oscillations we need only look at $\bar{H}_0$ and its eigenstates. If we define K by $\bar{H}_0 = E_0 I + (Ax_{01}/2)K$, we see that the eigenstates of $\bar{H}_0$ are also the eigenstates of

$$K = \begin{pmatrix} 0 & 1 & 0 \\ 1 & w & y \\ 0 & y & -z \end{pmatrix} \tag{5.15}$$

with $y = x_{12}/x_{01}$,

$$w = 2\left(\frac{\omega_{01} - \omega}{Ax_{01}}\right), \tag{5.16}$$

and

$$z = 2\left(\frac{2\omega - \omega_{02}}{Ax_{01}}\right). \tag{5.17}$$

The secular equation for K is

$$k^3 + (z - w)k^2 - (wz + 1 + y^2)k - z = 0. \tag{5.18}$$

Using the standard expression for the roots of a cubic, found in the Appendix, we find that K has the eigenvalues

$$k_n = \frac{1}{3}(w - z) + 2p^{1/2}\cos\left(\theta + \frac{2n\pi}{3}\right) \tag{5.19}$$

$(n = 0, 1, 2)$ with

$$p = \frac{1}{9}\left((z - w)^2 + 3(wz + y^2 + 1)\right), \tag{5.20}$$

$$q = \frac{1}{27}\left(2(z - w)^3 + 9(z - w)(wz + y^2 + 1) - 27z\right), \tag{5.21}$$

and

$$\cos 3\theta = -\frac{q}{2p^{3/2}}. \tag{5.22}$$

The eigenvectors are found by substitution to be

$$v_n = N_n \begin{pmatrix} y \\ k_n y \\ (k_n^2 - wk_n - 1) \end{pmatrix}, \tag{5.23}$$

with

$$N_n = \left((k_n^2 - wk_n - 1)^2 + y^2(k_n^2 + 1)\right)^{-1/2}. \tag{5.24}$$

This completely determines the rotating wave propagator through the relation

$$e^{-i\bar{H}_0 t} = \sum_{n=0}^{2} e^{-\bar{E}_n t} |v_n\rangle\langle v_n|, \tag{5.25}$$

where the eigenvalues $\bar{E}_n$ are

$$\bar{E}_n = E_0 + \frac{1}{2} A x_{01} k_n. \tag{5.26}$$

To show how Rabi oscillations emerge in this exact rotating wave solution, we consider the evolution of a state starting as $|0\rangle$. We define the amplitudes $a_n(t)$ by

$$e^{-i\bar{H}_0 t}|0\rangle = \sum_{n=0}^{2} a_n(t)|n\rangle. \tag{5.27}$$

These amplitudes have the explicit form

$$a_n(t) = \langle n|e^{-i\hbar H_0 t}|0\rangle = \sum_{m=0}^{2} e^{-i\bar{E}_m t}\langle n|v_m\rangle\langle v_m|0\rangle. \tag{5.28}$$

These amplitudes yield the solution, and the time-dependence yields the characteristic Rabi oscillations. Note that for any probability $p_n(t) = |a_n(t)|^2$, there are in general three characteristic frequencies: $\bar{E}_0 - \bar{E}_1$, $\bar{E}_0 - \bar{E}_2$, and $\bar{E}_1 - \bar{E}_2$. For our problem, however, we will find that there is one dominant frequency to the dynamics, the Rabi frequency: $\Omega_R = \bar{E}_0 - \bar{E}_2$.

Two-Level Oscillations

The formal solution can be greatly simplified in the limit that z is large—this condition corresponds to either strong anharmonicity or weak fields. We also use the approximation $y = x_{12}/x_{01} \approx \sqrt{2}$. The expressions that follow are simply the power series expansions in z^{-1} of the exact solutions above. We first consider the non-resonant case, when w is nonzero, and rederive the two-state Rabi oscillations. Working to lowest order in z^{-1}, we expand (5.22)

$$\theta = \frac{1}{3}\pi - \sqrt{3}(1 + w^2/4)^{1/2} z^{-1}, \tag{5.29}$$

thus

$$\begin{array}{ll} \cos\theta & = 1/2 + (3/2)(1 + w^2/4)^{1/2} z^{-1}, \\ \cos(\theta + 2\pi/3) & = -1, \\ \cos(\theta + 4\pi/3) & = 1/2 - (3/2)(1 + w^2/4)^{1/2} z^{-1}, \end{array} \tag{5.30}$$

and

$$\begin{array}{ll} k_0 & = w/2 + (1 + w^2/4)^{1/2}, \\ k_1 & = -z + w, \\ k_2 & = w/2 - (1 + w^2/4)^{1/2}. \end{array} \tag{5.31}$$

Using (5.31) to find the eigenvectors in (5.23), we find that $|v_1\rangle = |2\rangle$ has totally decoupled from states $|0\rangle$ and $|1\rangle$. The remaining eigenvectors are

$$\begin{array}{l} |v_0\rangle = \cos\eta|0\rangle + \sin\eta|1\rangle, \\ |v_2\rangle = \sin\eta|0\rangle - \cos\eta|1\rangle, \end{array} \tag{5.32}$$

where we have defined

$$\tan\eta = w/2 + (1 + w^2/4)^{1/2}. \tag{5.33}$$

Finally, using the eigenvectors (5.32) we can solve (5.28) for the amplitudes

$$\begin{array}{ll} a_0(t) & = e^{-i\phi}\left(\cos(\Omega_R t/2) - i\cos(2\eta)\sin(\Omega_R t/2)\right), \\ a_1(t) & = e^{-i\phi}\left(-i\sin(2\eta)\sin(\Omega_R t/2)\right), \\ a_2(t) & = 0, \end{array} \tag{5.34}$$

where the Rabi frequency is

$$\Omega_R = \bar{E}_0 - \bar{E}_2 = \left(\Omega_0^2 + (\omega_{01} - \omega)^2\right)^{1/2}, \tag{5.35}$$

the "bare" Rabi frequency is $\Omega_0 = Ax_{01}$, and the overall phase is $\phi = (\bar{E}_0 + \bar{E}_2)t/2$. Using the definition of η in (5.33) we find that the probability for the system to be in state $|1\rangle$ is

$$p_1(t) = |a_1(t)|^2 = \frac{\Omega_0^2}{\Omega_R^2} \sin^2(\Omega_R t/2). \tag{5.36}$$

If we drive at $\omega = \omega_{01}$, then $\Omega_R = \Omega_0$, $\eta = \pi/4$, and at the time $\tau = \pi/\Omega_0$ we have $p_1(\tau) = 1$. As a quantum logic operation, this π-pulse yields the X or NOT gate, which has the matrix form

$$X = \begin{pmatrix} 0 & 1 \\ 1 & 0 \end{pmatrix}. \tag{5.37}$$

Other single-qubit gates can be constructed by using other pulse times or non-resonant driving; appropriate combinations of these simple operations can yield an arbitrary single-qubit gate.

Three-Level Oscillations

The previous section effectively ignored any coupling to state $|2\rangle$. This holds only for vanishing z^{-1}, which for resonant driving at $\omega = \omega_{01}$ implies a very small Rabi frequency since from (5.28)

$$z^{-1} = \frac{1}{2}\left(\frac{\Omega_0}{\omega_{01} - \omega_{12}}\right) = \frac{Ax_{01}}{2(\omega_{01} - \omega_{12})}. \tag{5.38}$$

To achieve larger Rabi frequencies we must consider finite z^{-1}. We now explore the general analytic solution to evaluate this effect. We consider the resonant case ($w = 0$) including higher order terms in z^{-1}.

Solving (5.22) for θ we now find

$$\theta = \frac{1}{3}\pi - \sqrt{3}z^{-1} + \frac{9\sqrt{3}}{2}z^{-3} + O(z^{-5}). \tag{5.39}$$

We then have

$$\begin{array}{ll} \cos(\theta) & = 1/2 + (3/2)z^{-1} - (3/4)z^{-2}, \\ \cos(\theta + 2\pi/3) & = -1 + (3/2)z^{-2}, \\ \cos(\theta + 4\pi/3) & = 1/2 - (3/2)z^{-1} - (3/4)z^{-2}, \end{array} \tag{5.40}$$

and the eigenvalues

$$\begin{array}{ll} k_0 & = 1 + z^{-1} - (1/2)z^{-2}, \\ k_1 & = -z - 2z^{-1}, \\ k_2 & = -1 + z^{-1} + (1/2)z^{-2}. \end{array} \tag{5.41}$$

Substituting (5.41) in (5.23) the approximate eigenvectors are given by

$$v_0 = \frac{1}{\sqrt{2}}\begin{pmatrix} 1 \\ 1 \\ 0 \end{pmatrix} + \frac{z^{-1}}{2\sqrt{2}}\begin{pmatrix} -1 \\ 1 \\ 2\sqrt{2} \end{pmatrix} - \frac{z^{-2}}{8\sqrt{2}}\begin{pmatrix} 1 \\ 9 \\ 4\sqrt{2} \end{pmatrix}, \tag{5.42}$$

$$v_1 = \begin{pmatrix} 0 \\ 0 \\ 1 \end{pmatrix} - \sqrt{2}z^{-1}\begin{pmatrix} 0 \\ 1 \\ 0 \end{pmatrix} + z^{-2}\begin{pmatrix} \sqrt{2} \\ 0 \\ -1 \end{pmatrix}, \tag{5.43}$$

$$v_2 = \frac{1}{\sqrt{2}}\begin{pmatrix} 1 \\ -1 \\ 0 \end{pmatrix} + \frac{z^{-1}}{2\sqrt{2}}\begin{pmatrix} 1 \\ 1 \\ -2\sqrt{2} \end{pmatrix} - \frac{z^{-2}}{8\sqrt{2}}\begin{pmatrix} 1 \\ -9 \\ 4\sqrt{2} \end{pmatrix}. \tag{5.44}$$

Using (5.41) for the eigenvalues and (5.42)-(5.44) for the eigenvectors of $\bar{H}_0$ in (5.28), we calculate the matrix elements

$$\begin{array}{ll} a_0(t) & = e^{-i\phi}\left(\cos(\Omega_R t/2) + iz^{-1}\sin(\Omega_R t/2)\right), \\ a_1(t) & = e^{-i\phi}\left(-i(1 - (3/2)z^{-2})\sin(\Omega_R t/2)\right), \\ a_2(t) & = e^{-i\phi}\left(-i\sqrt{2}z^{-1}\sin(\Omega_R t/2)\right). \end{array} \tag{5.45}$$

In this expression, we have a modified Rabi frequency

$$\Omega_R = (\bar{E}_0 - \bar{E}_2) = \Omega_0(1 - (1/2)z^{-2}), \tag{5.46}$$

and the overall phase is $\phi = (\bar{E}_0 + \bar{E}_2)t/2$. The corresponding probabilities $p_n(t) = |a_n(t)|^2$ are

$$\begin{array}{ll} p_0(t) & \approx \cos^2(\Omega_R t/2) + z^{-2}\sin^2(\Omega_R t/2), \\ p_1(t) & \approx (1 - 3z^{-2})\sin^2(\Omega_R t/2), \\ p_2(t) & \approx 2z^{-2}\sin^2(\Omega_R t/2). \end{array} \tag{5.47}$$

The next higher order corrections are of order z^{-3}; additional frequencies will also appear at the next order.

From our approximate results we make the following observations. First, we see from (5.46) that we have a new Rabi frequency

$$\Omega_R = \Omega_0 \left(1 - \frac{1}{8}\frac{\Omega_0^2}{(\omega_{01} - \omega_{12})^2}\right). \tag{5.48}$$

For weak driving, the Rabi frequency varies linearly with the the driving amplitude, but is shifted ($\Omega_R < \Omega_0$) for larger power ($P \sim A^2$). Second, we see from (5.47) that at the lowest order that $p_2(t)$ oscillates with the *same* frequency as $p_1(t)$. For a π-pulse of $\tau = \pi/\Omega_R$ this introduces the population

$$p_2(\tau) = 2z^{-2} = \frac{1}{2}\frac{\Omega_0^2}{(\omega_{01} - \omega_{12})^2} = \frac{\pi^2}{4}\frac{1}{(\omega_{01} - \omega_{12})^2\tau^2}. \tag{5.49}$$

This excited state population is an intrinsic error in the logic gate. To limit this error, we must use longer pulse times or a more clever manipulation of the states. We can examine the constraints on the pulse time by using the perturbation theory from Chapter 4. There we found

$$E_0 = \omega_0 \left(\frac{1}{2} - \frac{11}{8}\lambda^2 - \frac{465}{32}\lambda^4 - \frac{39709}{128}\lambda^6\right), \tag{5.50}$$

$$E_1 = \omega_0 \left(\frac{3}{2} - \frac{71}{8}\lambda^2 - \frac{5625}{32}\lambda^4 - \frac{827539}{128}\lambda^6\right), \tag{5.51}$$

and

$$E_2 = \omega_0 \left(\frac{5}{2} - \frac{191}{8}\lambda^2 - \frac{23475}{32}\lambda^4 - \frac{5181319}{128}\lambda^6\right), \tag{5.52}$$

where $\lambda^2 = (54N_s)^{-1}$. We find

$$\omega_{01} - \omega_{12} = \omega_0 \frac{5}{36} N_s^{-1} \left(1 + \frac{47}{48}N_s^{-1} + \frac{118865}{93312}N_s^{-2}\right). \tag{5.53}$$

Altogether, we use (5.53) in (5.49), letting $p_2(\tau) = p_E$, and solve for τ:

$$\tau \sim \frac{18\sqrt{2}\pi}{5\omega_0} N_s p_E^{-1/2} \left(1 + \frac{47}{48} N_s^{-1} + \frac{118865}{93312} N_s^{-2}\right)^{-1}. \tag{5.54}$$

This expression shows that if the system is nearly harmonic (large N_s) or if we want accurate operations (small error p_E) we will need longer gate times if a single frequency is applied. For example, if we choose junction parameters such that $\omega_0/2\pi = 6$ GHz and $N_s = 4$, for an error probability of $p_E = 10^{-4}$ we find $\tau \sim 130$ ns; for $p_E = 10^{-3}$ we have $\tau \sim 40$ ns.

These limits only apply to "hard" pulses, where A is constant for the entire pulse. If one uses pulse shaping techniques much shorter gate times can be achieved. There will still be transient probability in state $|2\rangle$, but it can be driven to zero at the end of the pulse. This can be understood by the form of the rotating wave Hamiltonian $\bar{H}_0$. By turning the amplitude A on and off adiabatically with respect to $\omega_{01} - \omega_{12}$, the system will remain in the subspace spanned by the instantaneous eigenstates $|v_0\rangle$ and $|v_2\rangle$. For $A = 0$ this subspace is identical to that spanned by $|0\rangle$ and $|1\rangle$. Thus an appropriate pulse shape can drive an arbitrary qubit transformation with negligible final amplitude in state $|2\rangle$. We explore this using the full Hamiltonian in the next section.

There are other methods to drive accurate qubit transformations. The first proposed method [261] is to alternate the principal microwave drive with pulses at the frequency ω_{12}, chosen to cancel the transient population. While it succeeds at undoing the unwanted evolution, it comes at the cost of a drive at a second frequency whose phase relation to the first pulse is significant. This may not be a fundamental

objection: controlling the phase relations between microwave pulses may also be necessary for multi-qubit dynamics. Alternatively, the same effect can be achieved by using an appropriately timed sequence of pulses at the same frequency [258]. Another possibility is the use of pulses with arbitrary spectral components, perhaps found through optimal control theory [262].

Finally, we note that we have been studying an instance of the general question of controllability of quantum systems [263, 264]. For the three-level approximate Hamiltonian it can be proven that the system is controllable, i.e. an arbitrary unitary operation can be exactly synthesized by some control sequence. The proof, however, does not bound either the duration or the complexity of the required control pulse. Furthermore, this proof does not apply to the full Hamiltonian since the system is not finite-dimensional and the true spectrum is continuous. In practice, one would like to explore simple, experimentally relevant pulse shapes, while including all terms in the ideal Hamiltonian. We consider this in the next section, using more general split-operator methods to simulate the dynamics.

5.1.2 Numerical Simulation of Pulse Shaping

The approximations introduced in the previous section ignore many features of our true system. First, they assume a finite-dimensional Hilbert space, truncating the number of energy levels at the outset. As shown in the previous Chapters, since the system has a continuous spectrum, the metastable energy levels are a nontrivial *result* of the Schrödinger equation, not an assumption. Any simulation method

should incorporate this—specifically tunneling—at a fundamental level. Second, the rotating wave approximation ignores any nonresonant effects. These can be appreciable for large driving. and if the anharmonicity is small.

These deficiencies can be corrected by using direct numerical integration of the time-dependent Schrödinger equation through split-operator techniques. In this section we evaluate the three-level approximations using these more powerful methods. We then show how pulse shaping can improve the performance of logic operations on phase qubits.

Simulation of Tunneling

The use of split-operator techniques for simulation of gates is precisely the same technique described in Chapter 1. The time evolution operator is split and sequenced to yield a fully unitary small-time propagator, each term of which can be evaluated efficiently in position and momentum space. The transformation between bases is accomplished through the Fast-Fourier Transform. For tunneling however, there are three modifications that must be made.

First, an outgoing wavepacket will eventually hit the boundary of any finite lattice. Since the use of the FFT is equivalent to periodic boundary conditions, this outgoing wave will wrap around the lattice. This error can be avoided by introducing an absorbing boundary near the lattice edge [265]. A typical situation is illustrated in Fig. 5.1. By incorporating an absorbing boundary into the evolution, the decaying wavefunction is effectively exponentially damped before it hits the edge of the lattice. We do this by using the potential $V_A(x)$ shown in the figure (formed by hyperbolic

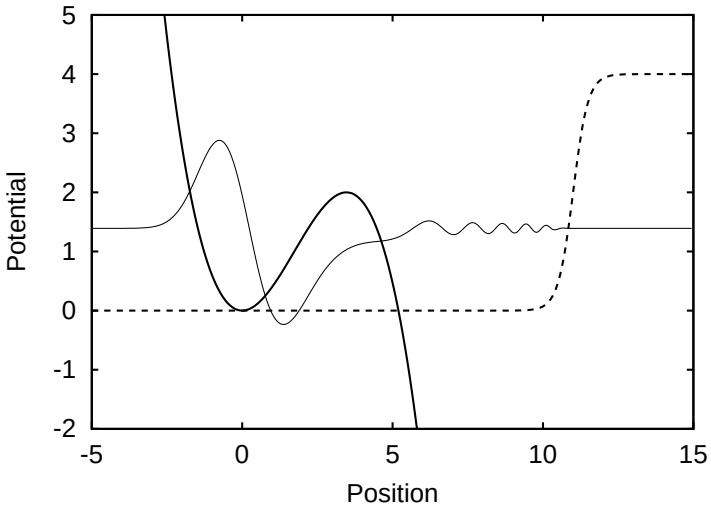

Figure 5.1: Cubic potential $V(x)$ (solid) with absorbing boundary $V_A(x)$ (dashed). The actual absorbing boundary used in the simulations is fifty times larger. The real part of the $n = 2$ resonance state wavefunction for $N_s = 2$ at $t = 100$ is shown as the thin solid line. The dynamics of the wavepacket beyond the boundary is exponentially damped.

tangents), and applying the operator $\exp(-\Delta t V_A(x))$ after each propagation step Δt.

The FFT also uses periodic boundary conditions in momentum space. This means that a wavepacket that is sufficiently accelerated will eventually have momenta large enough to wrap around the momentum lattice. In position space, this transforms a right-going wave into a left-going wave. The high momentum components of the wavepacket effectively "see" the discrete lattice in position space, and are perfectly reflected by it. One can eliminate this by using a momentum space absorber, or by placing the real-space absorber such that the relevant dynamics of the wavefunction have wavelengths significantly larger that the position lattice spacing. This is the situation shown in Fig. 5.1, where the boundary has quickly eliminated the outgoing wave.

Finally, experience has shown that fourth order integrators such as the Forest-Ruth integrator [57] (1.130) yield significantly more accurate tunneling rates than second order integrators. Note, however, that we have chosen to implement the absorbing boundary outside of the unitary integration scheme, assuming that there is no great advantange in doing so. For higher order schemes with negative timesteps there are certainly reasons not to do so, since $\exp(+\Delta t V_A(x))$ yields exponential amplification.

We can study the decay of a wavefunction, such as that shown in Fig. 5.1, by looking at either the survival amplitude

$$A(t) = \langle \Psi | e^{-iHt} | \Psi \rangle \tag{5.55}$$

or the non-decay probability

$$P(t) = \int_R dx |\Psi(x,t)|^2, \tag{5.56}$$

where the integral over the bound region of the potential. Note that for initially localized states, the two are not independent. To see this, we define $\hat{P}_R$ to be the projection operator onto region R, that is

$$\hat{P}_R = \int_R dx |x\rangle\langle x|. \tag{5.57}$$

For normalized initial states localized in region R we have $\hat{P}_R|\Psi\rangle = |\Psi\rangle$, in which case $P(0) = 1$. Defining the un-normalized state $|\Phi(t)\rangle = \hat{P}_R e^{-iHt}|\Psi\rangle$, we have $P(t) = \langle\Phi(t)|\Phi(t)\rangle$ and $A(t) = \langle\Psi|\Phi(t)\rangle$. Finally, we can use the Schwarz inequality to derive the relation

$$|A(t)|^2 = |\langle\Psi|\Phi(t)\rangle|^2 \leq \langle\Psi|\Psi\rangle\langle\Phi(t)|\Phi(t)\rangle = P(t). \tag{5.58}$$

We first study the survival amplitude. Note that if the state were truly a normalizable eigenstate with complex eigenvalue $E = E_0 - i\Gamma/2$, then we should have

$$A(t) = e^{-\Gamma t/2}\left(\cos(E_0 t) - i\sin(E_0 t)\right). \tag{5.59}$$

We test this expectation in Fig. 5.2, where we use our simulation method to compute $A(t)$ for the state shown in Fig. 5.1. The excellent agreement shows that the state is indeed metastable. In this case, we have used complex scaling to compute both the complex eigenvalue and the initial state. The basis set calculation generates an approximation to the scaled Gamow-Siegert state as a function of $\tilde{x}$:

$$\Psi_{GS,N}(\tilde{x}e^{i\theta}) = \sum_{n=1}^{N} c_n \phi_n(\tilde{x}), \tag{5.60}$$

where c_n are the calculated expansion coefficents and ϕ_n the basis functions. To approximate $\Psi_{GS}(x)$ we must evaluate the basis functions at $\tilde{x} = xe^{-i\theta}$:

$$\Psi_{GS,N}(x) = \sum_{n=1}^{N} c_n \phi_n(xe^{-i\theta}). \tag{5.61}$$

For a finite basis this "back-rotation" can generate subtle errors in the wavefunction that depend on the form of the basis functions; the sum may in fact fail to converge, i.e. $\Psi_{GS,N\to\infty}(x) \neq \Psi_{GS}(x)$ [266]. Recall, however, that the true Gamow-Siegert state is not normalizable; any normalizable initial state will have time evolution that deviates from exponential decay—no choice is unique. Our initial state is the approximate $\Psi_{GS,N}(x)$ normalized to unity on the lattice. The justification for this choice is precisely Fig. 5.2.

The non-decay probability $P(t)$ is shown in Fig. 5.3. The relative error in the tunneling rates for these states is generally near 10^{-4} using a fourth order integrator with timestep $\tau = 0.05$; the energy can be found more accurately. Note, however, that there is some dependence of the tunneling rate on the absorbing boundary.

Simulation of Rabi Oscillations

Having demonstrated the split-operator method for free evolution, we now introduce the microwave drive, with A constant and the phase $\phi = -\pi/2$, so that $\cos(\phi) = 0$. The characteristic Rabi oscillations are readily found. We show a typical example in Fig. 5.4. To suppress tunneling effects on this timescale we have chosen $N_s = 4$, in which case the resonant frequency is $\omega_{01} = E_1 - E_0 \approx 0.961$. In the figure we set $A = 0.005$, and see that the $|0\rangle$ and $|1\rangle$ states oscillate like a two-level system, but

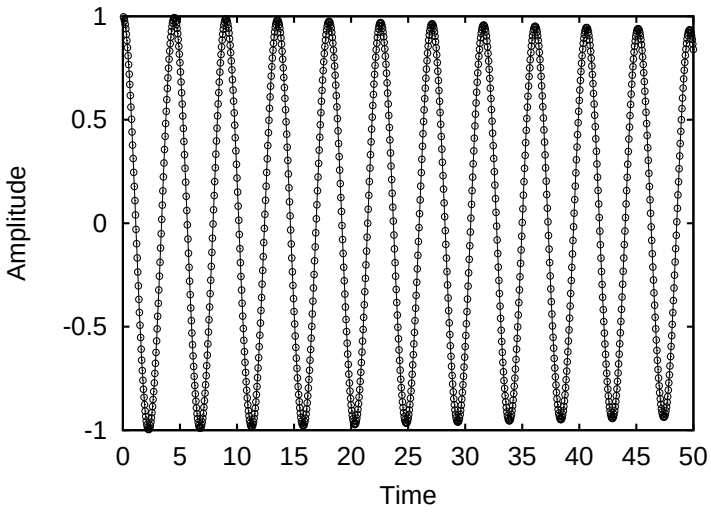

Figure 5.2: Real part of the survival amplitude $A(t)$ for the $n = 2$ resonance state wavefunction for $N_s = 2$. The dots indicate the split-operator evaluation, the line the expected $A(t) = e^{-\Gamma t/2}\cos(E_0 t)$, with $E_0 = 2.13157$ and $\Gamma = 0.13854$. No difference is discernable on this plot.

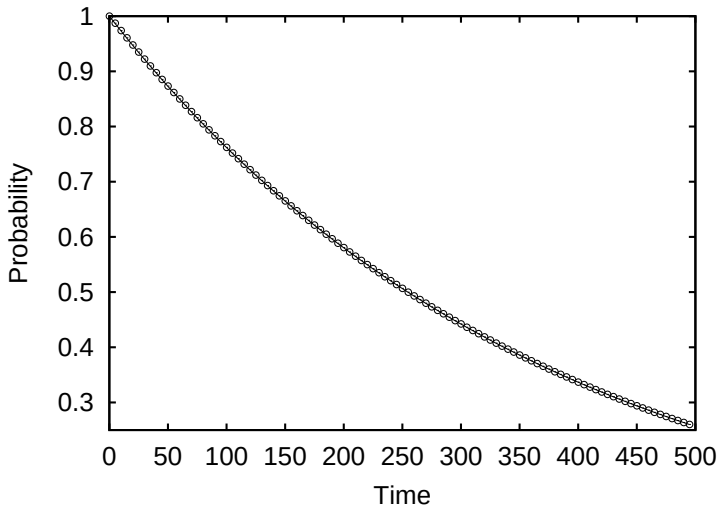

Figure 5.3: The non-decay probability $P(t)$ for the $n = 2$ resonance state wavefunction for $N_s = 2$. The dots indicate the split-operator evaluation, the line the expected exponential decay $P(t) = e^{-\Gamma t}$. No difference is discernable on this plot.

also shown is the probability to be in state $|2\rangle$. This follows the general expression of (5.47): $p_2(t) = 2z^{-2}\sin^2(\Omega t/2)$, but also includes the much higher frequency oscillations we had neglected.

Repeating these calculations for multiple drive amplitudes, we find the characteristic linear dependence of the Rabi frequency with amplitude $\Omega = Ax_{x01}$ (seen Fig. 5.5). Corrections to Ω such as (5.48) do not appear on this figure. However, deviations from two-state oscillations are still apparent. In Fig. 5.6 we show the probabilty $p_2(t_0)$, where $t_0 = \pi/\Omega_R$. The growing oscillations in p_2 are likely due to the importance of multiple frequencies at large power, evident in Fig. 5.4; the general trend, however, is well captured by our three-level analysis.

By repeating these calculations at fixed amplitude but at different frequencies,

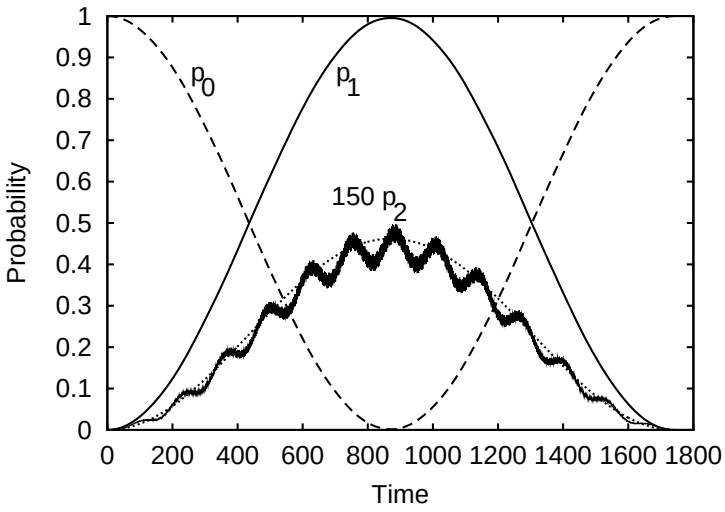

Figure 5.4: Rabi oscillation in the cubic potential with $N_s = 4$. The initial state is the metastable ground state, and the drive is resonant at $E_1 - E_0 \approx 0.961$ with amplitude $A = 0.005$. The state probabilities $p_0(t)$ (dashed curve) and $p_1(t)$ (solid curve) are shown. Also shown is $p_2(t)$ (multiplied by 150, thick solid curve) and the analytic approximation $2z^{-2}\sin^2(\Omega t/2)$ (dotted curve).

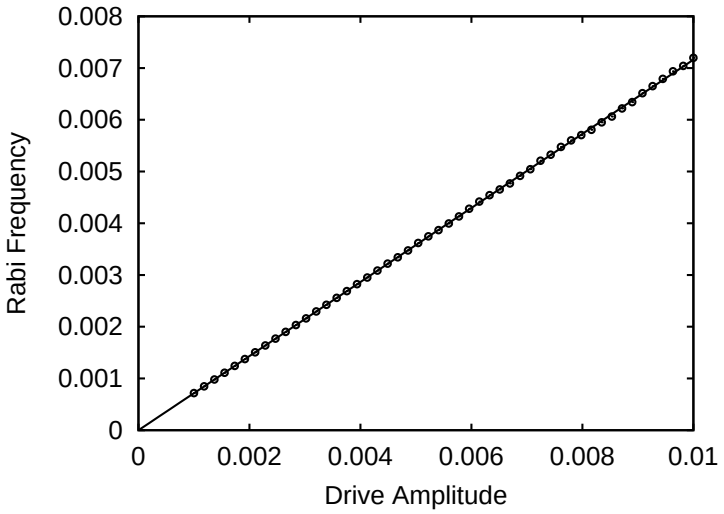

Figure 5.5: Rabi frequency as function of drive amplitude, in the cubic potential with $N_s = 4$. The initial state is the metastable ground state, and the drive is resonant at $E_1 - E_0 \approx 0.961$. The solid curve is the expected result $\Omega = Ax_{01}$, while the dots are the result of split-operator calculations.

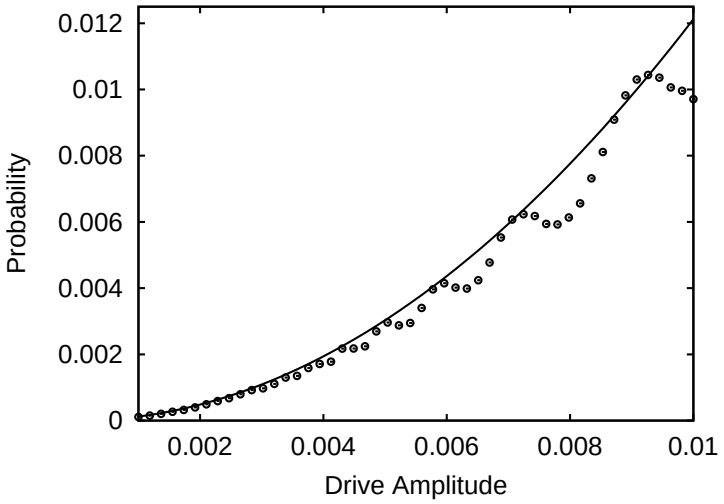

Figure 5.6: State 2 probability $p_2(t_0)$ as function of drive amplitude, in the cubic potential with $N_s = 4$, $t_0 = \pi/\Omega_R$. The initial state is the metastable ground state, and the drive is resonant at $E_1 - E_0 \approx 0.961$. The solid curve is the expected result $(2z^{-2})$ while the dots are the result of split-operator calculations.

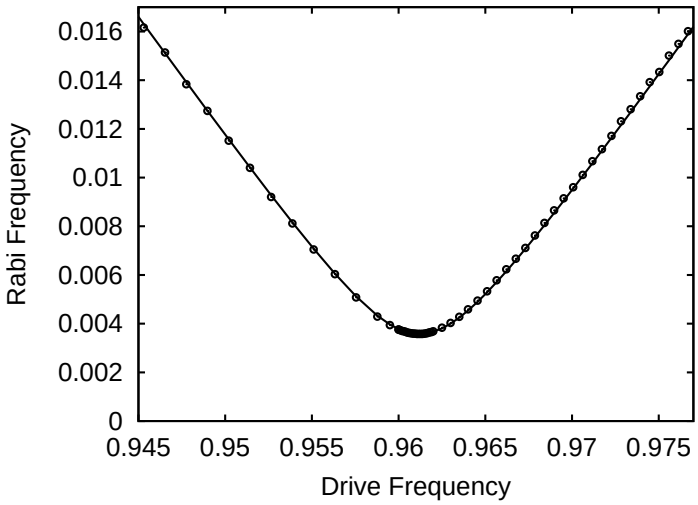

Figure 5.7: Rabi frequency Ω_R as function of drive frequency ω, in the cubic potential with $N_s = 4$. The initial state is the metastable ground state, and the drive has amplitude $A = 0.005$. The solid curve is the expected result $\Omega_R = (\Omega_0^2 + (\omega - \omega_{01})^2)^{1/2}$, while the dots are the result of split-operator calculations. The minimum Rabi frequency occurs when $\omega = \omega_{01}$, near 0.961.

we explore the non-resonant dynamics. In Fig. 5.7 we see the Rabi frequency, and in Fig. 5.8 we see the maximum probability of state $|1\rangle$. Both are well described by the two-state model described in Section 2.1.1.

Simulation of Pulse Shaping

The above calculations have used a drive of constant amplitude, which are called hard pulses in the NMR literature. More accurate logic operations are possible by pulse-shaping, i.e. allowing the amplitude A to be a function of time. We use

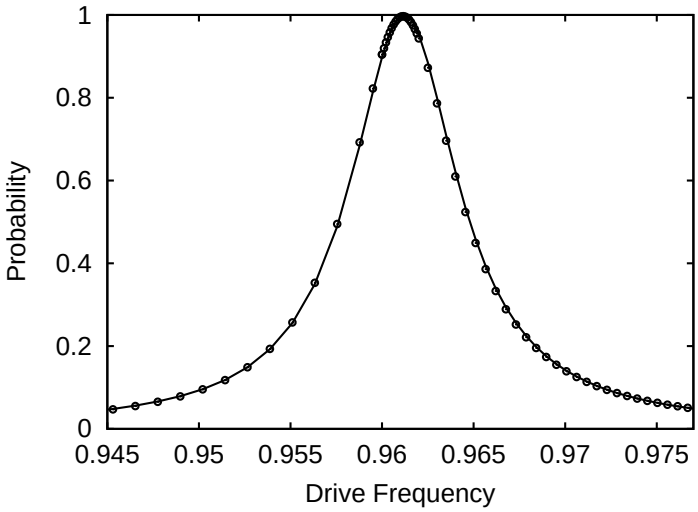

Figure 5.8: State 1 probability $p_1(t_0)$ as function of drive frequency ω, in the cubic potential with $N_s = 4$. The initial state is the metastable ground state, and the drive has amplitude $A = 0.005$. The time $t_0 = \pi/\Omega$ is when $p_1(t)$ achieves its first maximum. The solid curve is the expected result $p_1 = \Omega_0^2/\Omega_R^2$, while the dots are the result of split-operator calculations.

split-operator methods to study the simple Gaussian pulse shape

$$A(t) = \left\{ \begin{array}{ll} 0 & t < 0 \\ A_0 \exp\left(-2\alpha^2 (t - t_p/2)^2 / t_p^2\right) & 0 < t < t_p \\ 0 & t_p < t \end{array} \right\}, \tag{5.62}$$

where the constant A_0 takes the form

$$A_0 = \frac{\theta}{x_{01}\sqrt{2\pi}\mathrm{erf}(\alpha/\sqrt{2})} \frac{2\alpha}{t_p}, \tag{5.63}$$

θ is the desired rotation angle (for a π-pulse $\theta = \pi$), and the error function is defined by

$$\mathrm{erf}(x) = \frac{2}{\sqrt{\pi}} \int_0^x dw e^{-w^2}. \tag{5.64}$$

This type of pulse (among others) is considered in [258, 259] and an example of such a pulse is shown in Fig. 5.9. We use a fixed $\alpha = 3$ and vary the pulse length t_p in our subsequent simulations.

We simulate this type of pulse in Fig. 5.10. Note that while there is a transient population in state $|2\rangle$, it nearly vanishes at the end of the pulse, with a final value of $p_2(t_p) = 7.6 \times 10^{-5}$, nearly two orders of magnitude less than the corresponding probability for the hard pulse shown in Fig. 5.4 ($p_2 \sim 10^{-3}$). Notice also the intriguing asymmetric shape; there is a delay of the transfer of amplitude into state $|2\rangle$. Finally, we must confess that the effect of the pulse is not a perfect π-pulse: we find $p_1(t_p) = 0.995$. Nevertheless, it is clear that pulse-shaping can offer great advantages.

Repeating these calculations for multiple pulse times t_p, we show the pulse error $p_E = 1 - p_0(t_p) - p_1(t_p)$ in Fig. 5.11. For the hard pulses, we define $t_p = \pi/\Omega_0$. It can be clearly seen that the Gaussian pulse rapidly outperforms the hard pulse.

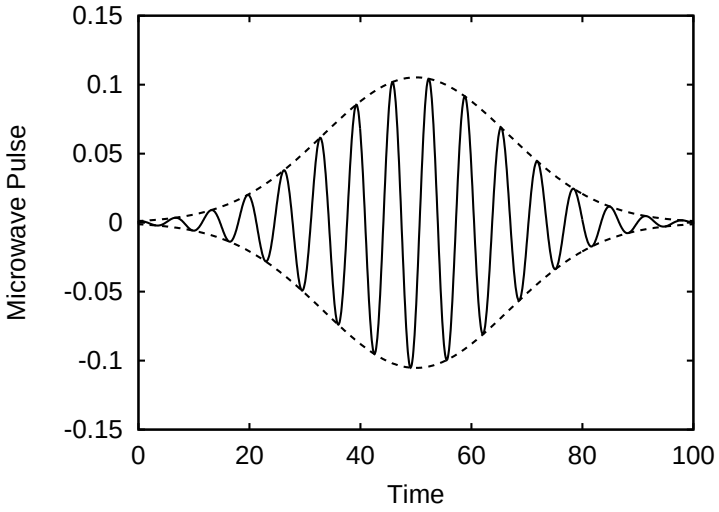

Figure 5.9: Gaussian pulse shape for a resonant π-pulse in cubic potential with $N_s = 4$. The solid curve is the product $A(t)\cos(\omega t)$, with $\omega = E_1 - E_0 \approx 0.961$, and $A(t)$ is given in the text, with parameters $\alpha = 3$ and $t_p = 100$ The dashed curves indicate the Gaussian envelope $\pm A(t)$.

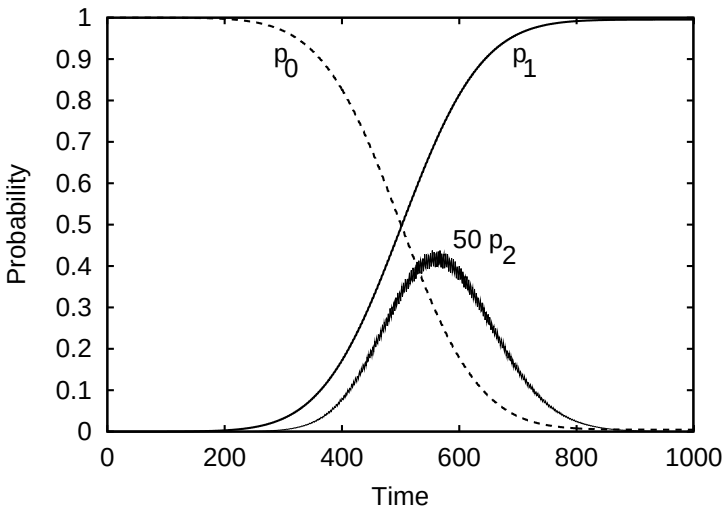

Figure 5.10: Resonant Gaussian π-pulse in cubic potential with $N_s = 4$. The initial state is the metastable ground state, and the drive is resonant at $E_1 - E_0 \approx 0.961$, the pulse length is $t_p = 1000$. The state probabilities $p_0(t)$ (solid curve) and $p_1(t)$ (dashed curve) are shown. Also shown is $p_2(t)$ (multiplied by 50, thin solid curve).

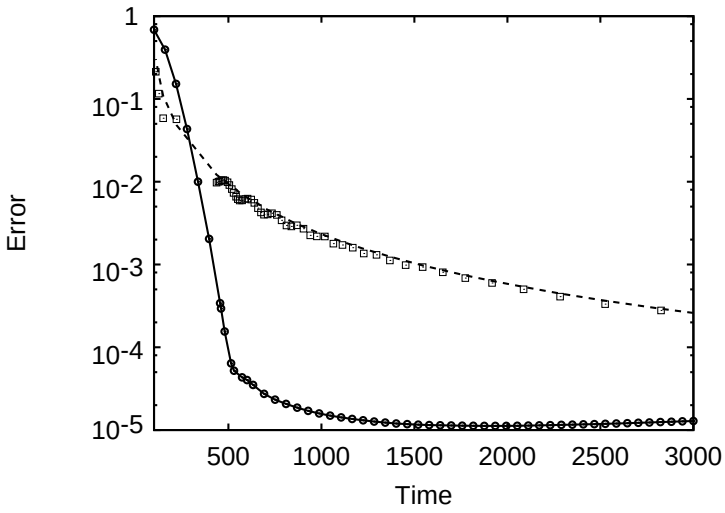

Figure 5.11: Pulse error $p_E = 1 - p_0(t_p) - p_1(t_p)$ for hard pulses (squares) and Gaussian pulses (dots) as function of pulse length t_p. The dashed curve is the theoretical estimate $p_E = 2z^{-2}$, while the solid curve is drawn to guide the eye.

There is an error floor, and in fact the Gaussian pulse error begins to increase for large t_p. This floor is directly due to tunneling of the wavefunction, whereas the dashed curve shows that the error of hard pulses is due to the non-adiabatic population of state $|v_1\rangle \sim |2\rangle$. Finally we note that for a junction with plasma frequency $\omega_0/2\pi = 6$GHz a π-pulse with $p_E \sim 10^{-4}$ can be achived with $t_p \sim 500/\omega_0 \sim 13$ns, about ten times faster than the corresponding hard pulse.

5.2 Bias Current Ramp

The second control technique we consider is bias current ramping. In a quantum computer, we might want to have two operation points. The first would be the idle

position, to store the qubit. This could be with a small bias current such that there is a large barrier height with a large N_s. In this case the state has little chance to tunnel. The second operation point would be for Rabi oscillations, which would require a smaller N_s for fast logic gates. The ramp from one point to the other is studied in this section.

We recall that the cubic approximation to the washboard is given by

$$H = \frac{1}{2}p^2 + \frac{1}{2}\omega^2(x - x_*)^2 - \lambda(x - x_*)^3 \tag{5.65}$$

where we have used energy units of $\hbar\omega_0$, the nonlinearity is

$$\lambda = \frac{1}{\sqrt{54N_s}}, \tag{5.66}$$

the frequency is

$$\omega^2 = \left(\frac{1 - J}{1 - J_0}\right)^{1/2}, \tag{5.67}$$

and the position of the minimum is

$$x_* = (3N_s/2)^{1/2}(1 - \omega^2). \tag{5.68}$$

Variations of the bias current J about J_0 will yield variations in both the frequency and the minimum of the potential. The frequency variation will yield a dynamical phase shift to the energy levels, and a small variation in the wavefunctions. The variation of the potential minimum, however, yields a large variation in the wavefunctions.

Instead of looking directly at the bias current (which will depend on the particular junction parameters), we consider instead variations of the frequency by

defining a detuning parameter

$$\epsilon(t) = \omega^2(t) - 1 \tag{5.69}$$

in terms of which the bias current is

$$J = 1 - (1 - J_0)(1 + \epsilon)^2. \tag{5.70}$$

A slightly more accurate mapping of the cubic to the washboard uses the alternative mapping

$$J = \left(1 - (1 - J_0^2)(1 + \epsilon)^2\right)^{1/2}. \tag{5.71}$$

In either case, increasing ϵ decreases the bias current, and for small variations they are linearly related. The particular bias current ramps we consider are shown in Fig. 5.12.

These ramps have the following functional forms:

$$\epsilon_L(t) = \left\{ \begin{array}{ll} \epsilon_0 & t < t_0 \\ \epsilon_0 + (t - t_0)(\epsilon_1 - \epsilon_0)/(t_1 - t_0) & t_0 < t < t_1 \\ \epsilon_1 & t_1 < t \end{array} \right\}, \tag{5.72}$$

$$\epsilon_C(t) = \left\{ \begin{array}{ll} \epsilon_0 & t < t_0 \\ (\epsilon_0 + \epsilon_1)/2 - (\epsilon_1 - \epsilon_0)\cos\left(\pi(t - t_0)/(t_1 - t_0)\right)/2 & t_0 < t < t_1 \\ \epsilon_1 & t_1 < t \end{array} \right\}, \tag{5.73}$$

and

$$\epsilon_G(t) = \frac{1}{2}(\epsilon_0 + \epsilon_1) + \frac{1}{2}(\epsilon_1 - \epsilon_0)\mathrm{erf}\left(\alpha(t - t_0/2 - t_1/2)/(t_1 - t_0)\right), \tag{5.74}$$

where α is a scaling parameter and $\mathrm{erf}(x)$ is the error function

$$\mathrm{erf}(x) = \frac{2}{\sqrt{\pi}} \int_0^x dw\, e^{-w^2}. \tag{5.75}$$

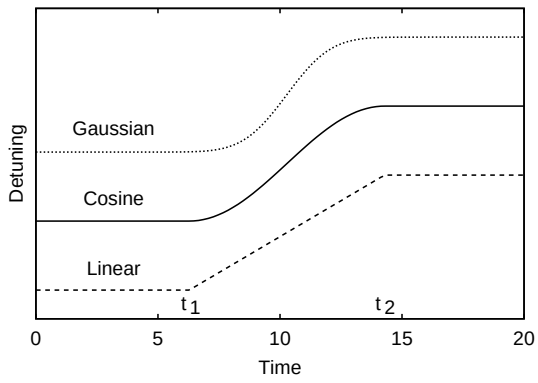

Figure 5.12: Ramp functions for the detuning $\epsilon(t)$. Each curve is offset for clarity. The first is linear ramping $\epsilon_L(t)$ (dashed curve), the second is a cosine ramp $\epsilon_C(t)$ (solid curve), and the third is an integrated Gaussian ramp $\epsilon_G(t)$ (dotted curve). The ramp time is $T = t_2 - t_1$.

.

We use $\alpha = 4$ in the following.

When the bias is ramped, the curvature and minimum of the cubic potential shift. This is illustrated in Fig. 5.13. Our goal is to transfer the ground state of the initial potential to the ground state of the final potential. If we ramp too quickly, the error which results is surprisingly large. We study this error in the following sections.

5.2.1 Harmonic Approximation I

We can gain significant insight into this problem by looking at the harmonic approximation. In fact, in this section we make the further approximation that the frequency remains fixed. The results of this approximation turn out to be quite

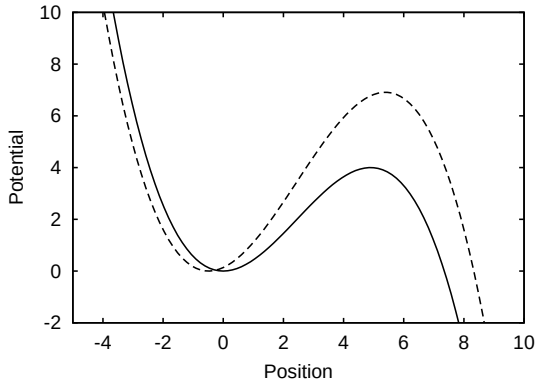

Figure 5.13: Potential energy functions for the cubic. The solid curve is the potential energy for $\epsilon = 0$, $N_s = 4$. The dashed curve is potential energy for $\epsilon = 0.2$.

reasonable, since the effects of the displacement of the minimum are far greater than those of the frequency shift. We consider the full harmonic approximation in a subsequent section.

The problem we solve is that of a harmonic oscillator with moving minimum

$$H(t) = \frac{1}{2}p^2 + \frac{1}{2}(x - x_c(t))^2 \tag{5.76}$$

where $x_c(t) = -(3N_s/2)^{1/2}\epsilon(t)$ and the pulses are those considered above, with $t_0 = 0$, $t_1 = T$, $\epsilon_0 = 0$, $\epsilon_1 = \Delta\epsilon$. We can simplify the Hamiltonian by using the displacement operator

$$D(\nu) = e^{\nu a^\dagger - \nu^* a} = e^{\nu a^\dagger} e^{-\nu^* a} e^{-|\nu|^2/2} \tag{5.77}$$

where $a = 2^{-1/2}(x + ip)$ is the annihilation operator, and the second expression follows from $[a, a^\dagger] = 1$ and application of the Baker-Campbell-Haussdorf formula. Using $D(\nu)$ we have

$$H(t) = a^\dagger a + \frac{1}{2} - \gamma(t)(a + a^\dagger) + \gamma(t)^2 = D(\gamma(t))H(0)D^\dagger(\gamma(t)) \tag{5.78}$$

where $\gamma(t) = 2^{-1/2}x_c(t) = -(3N_s/4)^{1/2}\epsilon(t)$, $\gamma(T) = \gamma_1 = -(3N_s/4)^{1/2}\Delta\epsilon$.

We wish to compute the final state fidelity

$$F(T) = |\langle 0|D^\dagger(\gamma_1)U(T)|0\rangle|^2 \tag{5.79}$$

where $U(T)$ is the time-evolution operator, $|0\rangle$ is the ground state of $H(0)$ and $D(\gamma_1)|0\rangle$ is the ground state of $H(T)$. Note that if we use a sudden pulse from $x_c = 0$ to $x_c = -(3N_s/2)^{1/2}\Delta\epsilon$ with $T = 0$, there is no evolution ($U(T) = I$) and we find

$$F(0) = |\langle 0|D^\dagger(\gamma_1)|0\rangle|^2 = e^{-|\gamma_1|^2}. \tag{5.80}$$

Thus, the larger the displacement, the smaller the overlap of the initial and final states. We calculate $F(T)$ for each of our pulse shapes.

To calculate $U(T)|0\rangle$ we adopt a simple argument. The results are, of course, in complete agreement with an exact analysis of the propagator; aspects of this will appear in the following sections. We first note that the coherent states

$$|\alpha\rangle = D(\alpha)|0\rangle \tag{5.81}$$

are eigenstates of the annihilation operator

$$a|\alpha\rangle = \alpha|\alpha\rangle, \tag{5.82}$$

and the ground state is a coherent state with $\alpha = 0$. Now, we can exactly solve for the time-evolved annihilation operator

$$a_H(t) = U^\dagger(t)aU(t) \tag{5.83}$$

which satisfies the Heisenberg equation of motion

$$\frac{da_H}{dt}(t) = i[H_H(t), a_H(t)] = -i\left(a_H(t) - \gamma(t)\right), \tag{5.84}$$

where $H_H(t) = U^\dagger(t)H(t)U(t)$. We can solve (5.84) immediately to find

$$a_H(t) = e^{-it}a + \nu(t) \tag{5.85}$$

where we have used the initial condition $a_H(0) = a$ and

$$\nu(t) = ie^{-it}\int_0^t ds\gamma(s)e^{is}. \tag{5.86}$$

This implies that $U(t)|0\rangle$ is eigenstate of a with eigenvalue $\nu(t)$, since

$$aU(t)|0\rangle = U(t)U^\dagger(t)aU(t)|0\rangle = U(t)(e^{-it}a + \nu(t))|0\rangle = \nu(t)U(t)|0\rangle. \tag{5.87}$$

We conclude that

$$U(T)|0\rangle = e^{i\Theta}D(\nu(T))|0\rangle \tag{5.88}$$

where Θ is an irrelevant but easily calculable phase. Finally, using the identity

$$D(\nu)D(\mu) = D(\nu+\mu)\exp\left(\frac{1}{2}(\mu^*\nu - \mu\nu^*)\right) \tag{5.89}$$

we calculate the fidelity

$$F_0(T) = |\langle 0|D^\dagger(\gamma_1)D(\nu(T))|0\rangle|^2 = \exp\left(-|\gamma_1 - \nu(T)|^2\right). \tag{5.90}$$

We recall that the ramp parameters are $t_0 = 0$, $t_1 = T$, $\epsilon_0 = 0$, and $\epsilon_1 = \Delta\epsilon$. Using these for each of our pulse shapes, we must calculate the integrals:

$$\nu(T) = -ie^{-iT}(3N_s/4)^{1/2}\int_0^T ds\epsilon(s)e^{is}. \tag{5.91}$$

For the linear pulse (5.72) we find

$$\nu_L(T) = -(3N_s/4)^{1/2}\Delta\epsilon\left(1 + \frac{i}{T}(1 - e^{-iT})\right), \tag{5.92}$$

in which case

$$F_L(T) = \exp\left(-3N_s\Delta\epsilon^2 T^{-2}\sin^2(T/2)\right). \tag{5.93}$$

Note that the fidelity decreases for large $\Delta\epsilon$ and short T, but is exactly 1 whenever the time satisfies $T = 2n\pi$. These occur when the wavepacket performs a perfectly timed bounce in the moving potential.

The cosine ramp (5.73) can also be integrated

$$\nu_C(T) = -(3N_s/4)^{1/2}\Delta\epsilon\left(1 + e^{-iT/2}\cos(T/2)\frac{\pi^2}{T^2 - \pi^2}\right) \tag{5.94}$$

and the corresponding fidelity is

$$F_C(T) = \exp\left(-\frac{3}{4}N_s\Delta\epsilon^2\frac{\pi^4}{(T^2 - \pi^2)^2}\cos^2(T/2)\right). \tag{5.95}$$

Observe that the exponent in (5.95) is oscillatory. There are times such that the wavepacket performs a perfect bounce: if $T = \pi + 2n\pi$ we have $F_C = 1$.

Finally, for the Gaussian ramp (5.74) we have

$$\nu_G(T) = -\frac{1}{2}(3N_s/4)^{1/2}\Delta\epsilon\left(1 - e^{-iT} + e^{-iT}i\int_0^T ds e^{is}\mathrm{erf}(\alpha(s/T - 1/2)\right). \tag{5.96}$$

Defining $z = \alpha(s/T - 1/2)$ we find for the integral

$$I = \int_0^T ds e^{is}\mathrm{erf}(\alpha(s/T - 1/2)) = \alpha^{-1}Te^{iT/2}\int_{-\alpha/2}^{\alpha/2} dz e^{iTz/\alpha}\mathrm{erf}(z) \tag{5.97}$$

Integrating by parts and using $\mathrm{erf}(-x) = -\mathrm{erf}(x)$ we have

$$I = i^{-1}e^{iT/2}\left(\mathrm{erf}(\alpha/2)(e^{iT/2} + e^{-iT/2}) - 2\pi^{-1/2}\int_{-\alpha/2}^{\alpha/2} dz e^{iTz/\alpha - z^2}\right). \tag{5.98}$$

At this point we assume that we can make the approximations $\mathrm{erf}(\alpha) = 1$ and replace the limits on the final integration by $\pm\infty$; even for moderate α this incurs little error. Doing so, and performing the Gaussian integral in (5.98), we find

$$I \approx i^{-1} e^{iT/2} \left(e^{iT/2} + e^{-iT/2} - 2e^{-\alpha^{-2}T^2/4} \right). \tag{5.99}$$

From (5.99) and (5.96) we find

$$\nu_G(T) = -(3N_s/4)^{1/2} \Delta\epsilon \left(1 - e^{-iT/2} e^{-\alpha^{-2}T^2/4} \right). \tag{5.100}$$

The fidelity is then

$$F_G(T) = \exp\left(-\frac{3}{4} N_s \Delta\epsilon^2 e^{-\alpha^{-2}T^2/2} \right). \tag{5.101}$$

Note that our assumption of large α ignores some small oscillatory component of the exponent.

Taking the time average of each exponent, and the limit $T \gg \pi$, we now summarize the three ramp fidelities in the averaged harmonic approximation. For the linear ramp (5.93), cosine (5.95) and Gaussian ramp fidelities (5.101) (with $\alpha = 4$) we have

$$\begin{aligned} F_L(T) &\simeq \exp\left(-(3/2) N_s \Delta\epsilon^2 T^{-2}\right), \\ F_C(T) &\simeq \exp\left(-(3/8) N_s \Delta\epsilon^2 \pi^4 T^{-4}\right), \\ F_G(T) &\simeq \exp\left(-(3/4) N_s \Delta\epsilon^2 e^{-T^2/32}\right). \end{aligned} \tag{5.102}$$

Clearly, for a given $\Delta\epsilon$ the scaling properties of each with the ramp time T gets progressively better. The linear ramp is only piecewise continuous and performs the worst. Both the cosine ramp and its derivative are continuous, and it fares somewhat better. The Gaussian ramp is smooth, yielding the best fidelity of all. We now compare these with true numerical results using split operator-methods.

5.2.2 Numerical Calculations

As with Rabi oscillations, it is straightforward to use split-operator methods to simulate the dynamics of the bias current ramp. We consider the ramping of the metastable state from $\epsilon_0 = 0.2$ at time $t_0 = 0$ to $\epsilon_1 = 0$ at time $t_1 = T$ ($\Delta\epsilon = -0.2$) where $N_s = 4$. For each ramp we calculate the final state fidelity

$$F_n(T) = |\langle\bar{\Psi}_n|U(T)|\Psi_n\rangle|^2, \tag{5.103}$$

with $n = 0, 1$, where $|\Psi_n\rangle$ is the n-th metastable state for $\epsilon_0 = 0.2$ and $|\bar{\Psi}_n\rangle$ is the n-th metastable state for $\epsilon_1 = 0$.

The results for the linear ramp are shown in Fig. 5.14, where we plot the error $E(T) = 1 - F_n(T)$. There are instants when the error in the ground state becomes very small. These times correspond to the perfect bouncing wavepacket dynamics discussed above. Note that there are similar features for the excited state error, but they occur at different times—in the harmonic approximation these times would be the same for all of the energy states. Note also that the excited state error is generally greater than the ground state error. Finally we observe that the averaged harmonic approximation of (5.102) provides an excellent guide to the overall behavior.

The results for the cosine ramp are shown in Fig. 5.15. Notice that the error decreases more rapidly than for the linear ramp (the vertical scales are slightly different) and there are again certain ramp times when the error is very small. The general behavior is again well described by the averaged harmonic approximation.

Last, we look at the Gaussian ramp in Fig. 5.16, seeing very rapid error decrease with ramp time. Here there is excellent agreement between the averaged

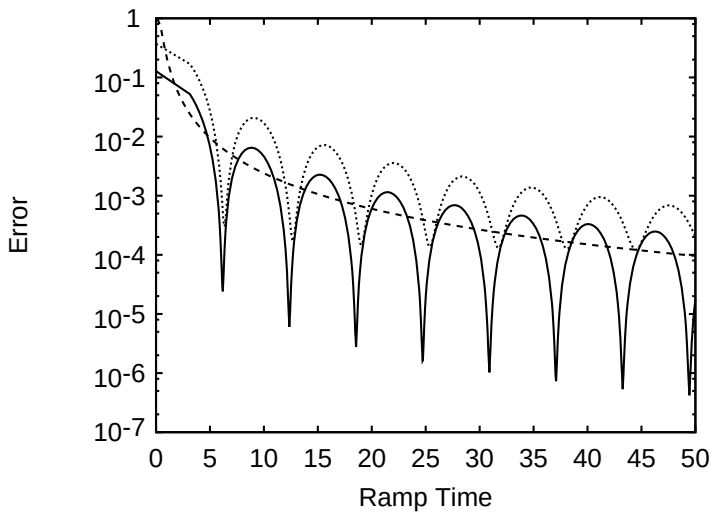

Figure 5.14: Final state fidelity error $E(T) = 1 - F(T)$ for the linear ramp as a function of the ramp time T. The bias ramp has $\epsilon_0 = -0.2$, $\epsilon_1 = 0$, $t_0 = 0$ and $t_1 = T$. The solid curve is the error in the ground state. The dotted curve is the error in the first excited state. The dashed curve is the averaged harmonic approximation.

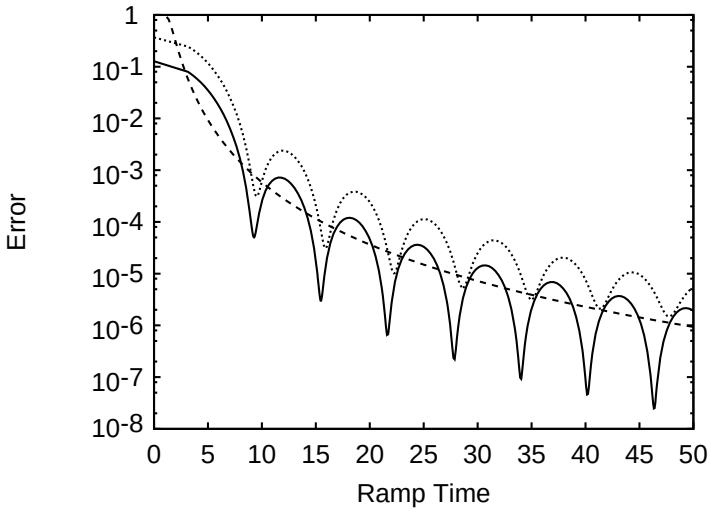

Figure 5.15: Final state fidelity error $E(T) = 1 - F(T)$ for the cosine ramp as a function of the ramp time T. The bias ramp has $\epsilon_0 = -0.2$, $\epsilon_1 = 0$, $t_0 = 0$ and $t_1 = T$. The solid curve is the error in the ground state. The dotted curve is the error in the first excited state. The dashed curve is the averaged harmonic approximation.

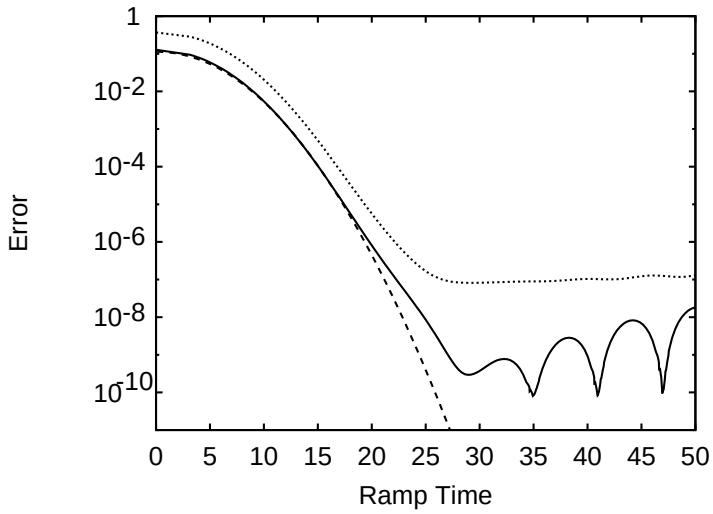

Figure 5.16: Final state fidelity error $E(T) = 1 - F(T)$ for the Gaussian ramp as a function of the ramp time T. The bias ramp has $\epsilon_0 = -0.2$, $\epsilon_1 = 0$, $t_0 = 0$ and $t_1 = T$. The solid curve is the error in the ground state. The dotted curve is the error in the first excited state. The dashed curve is the averaged harmonic approximation.

harmonic approximation and the ground state error, until the error falls below 10^{-6}. The oscillations in the ground state error are likely due to the oscillatory terms we neglected in the harmonic approximation. Finally, we see that there is an error floor to the first excited state, and for longer ramp times the error begins to grow, again due to quantum tunneling.

Thus, we have shown that the error of the bias current ramp, accurately simulated through split-operator methods, can be well understood using the averaged harmonic approxation. This approximation has ignored the variation of the frequency. The following section, using the exact harmonic propagator, shows that its

neglect is essentially harmless.

5.2.3 Harmonic Approximation II

We consider the harmonic approximation to the current-biased Josephson junction case where both the minimum and the frequency of the oscillator have time-dependence:

$$H = \frac{p^2}{2m} + \frac{1}{2}m\omega(t)^2(x - x_c(t))^2. \tag{5.104}$$

We first wish to expand our Hamiltonian in terms of creation and annihilation operators, but do not want the operators a and $a^\dagger$ to have any explicit time dependence. Thus, we consider a reference frequency ω_0 and let

$$x = \frac{x_0}{\sqrt{2}}(a + a^\dagger), \tag{5.105}$$

$$p = \frac{\hbar}{i\sqrt{2}x_0}(a - a^\dagger), \tag{5.106}$$

with

$$x_0 = \sqrt{\frac{\hbar}{m\omega_0}}. \tag{5.107}$$

We also define the dimensionless functions

$$\epsilon(t) = \frac{\omega(t)^2 - \omega_0^2}{\omega_0^2} \tag{5.108}$$

and

$$\gamma(t) = \frac{x_c(t)}{\sqrt{2}x_0} = -\left(\frac{3N_s}{4}\right)^{1/2}\epsilon(t). \tag{5.109}$$

With these definitions, the harmonic Hamiltonian is

$$H = f(t)A + f^*(t)A^\dagger + h(t)B + d(t)a + d^*(t)a^\dagger + g(t), \tag{5.110}$$

with $A = a^2/2$, $B = a^\dagger a + 1/2$, and the coefficients

$$\begin{array}{rl} f(t) = f^*(t) & = \hbar\omega_0\epsilon(t)/2, \\ h(t) & = \hbar\omega_0(1+\epsilon(t)/2), \\ d(t) = d^*(t) & = -\hbar\omega_0(1+\epsilon(t))\gamma(t), \\ g(t) & = \hbar\omega_0(1+\epsilon(t))\gamma(t)^2. \end{array} \tag{5.111}$$

In the Appendix we derive the general propagator for a Hamiltonian of the form (5.110), and find that the propagator is

$$U = e^{-i\Theta}S(r,\phi)R(\theta)D(\nu), \tag{5.112}$$

where the squeezing operator S, rotation operator R and displacement operator D are defined by

$$\begin{array}{ll} S(r,\phi) & = \exp(r(a^2e^{-i2\phi} - a^{\dagger 2}e^{i2\phi})/2), \\ R(\theta) & = \exp(-i\theta(a^\dagger a + 1/2)), \\ D(\nu) & = \exp(\nu a^\dagger - \nu^* a). \end{array} \tag{5.113}$$

The parameters r, θ, and ϕ are given by the auxiliary variables α and β:

$$\begin{array}{ll} \cosh r & = |\alpha| \\ e^{i\theta} & = \alpha^*|\alpha|^{-1} \\ e^{2i\phi} & = -\alpha\beta^*|\alpha|^{-1}|\beta|^{-1}. \end{array} \tag{5.114}$$

The variables α, β, and ν must satisfy the differential equations

$$\hbar\dot{\alpha} = -i(f^*\beta + h\alpha), \tag{5.115}$$

$$\hbar\dot{\beta} = i(f\alpha + h\beta), \tag{5.116}$$

$$\hbar\dot{\nu} = -i(\beta^* d + \alpha^* d^*). \tag{5.117}$$

The expression for Θ will not be needed.

We now solve the full system of equations (5.115)-(5.117) for the propagator. In the linear ramp considered here, we can do these analytically in terms of Airy functions. The equations to be solved are

$$\begin{array}{rlll} \dot{\alpha} & = -i\hbar^{-1}(f^*\beta + h\alpha) & = -i\omega_0(\epsilon\beta/2 + (1+\epsilon/2)\alpha), \\ \dot{\beta} & = i\hbar^{-1}(f\alpha + h\beta) & = i\omega_0(\epsilon\alpha/2 + (1+\epsilon/2)\beta). \end{array} \tag{5.118}$$

By forming the combinations $\alpha_+ = \alpha + \beta$ and $\alpha_- = \alpha - \beta$, (5.118) becomes

$$\begin{array}{ll} \dot{\alpha}_+ & = -i\omega_0\alpha_- \\ \dot{\alpha}_- & = -i\omega_0(1+\epsilon)\alpha_+ \end{array} \tag{5.119}$$

and taking an extra time derivative of $\dot{\alpha}_+$ we find

$$\ddot{\alpha}_+ + \omega_0^2(1+\epsilon)\alpha_+ = 0. \tag{5.120}$$

The initial conditions $\alpha(0) = 1$, $\beta(0) = 0$ imply $\alpha_+(0) = 1$, $\dot{\alpha}_+(0) = -i\omega_0$. Now, if we specialize to the linear ramp with $\epsilon_0 = 0$, $t_0 = 0$, and $t_1 = T$, then for $0 < t < T$ we find that the detuning is

$$\epsilon(t) = \Delta\epsilon t/T. \tag{5.121}$$

Substituting (5.121) into (5.120) shows that α_+ satisfies a variation of the Airy equation,

$$\ddot{\alpha}_+ + \omega_0^2(1 + \Delta\epsilon t/T)\alpha_+ = 0. \tag{5.122}$$

If we define the auxiliary variable

$$z(t) = \left(\frac{\Delta\epsilon}{\omega_0 T}\right)^{1/3}(\omega_0 t + \omega_0 T/\Delta\epsilon) \tag{5.123}$$

then the general solution of (5.122) is

$$\alpha_+(t) = c_1\mathrm{Ai}(-z(t)) + c_2\mathrm{Bi}(-z(t)). \tag{5.124}$$

From (5.124) α_- is

$$\alpha_-(t) = -i\left(\frac{\Delta\epsilon}{\omega_0 T}\right)^{1/3}(c_1\mathrm{Ai}'(-z(t)) + c_2\mathrm{Bi}'(-z(t))). \tag{5.125}$$

To satisfy the initial conditions we must have

$$\begin{pmatrix} \mathrm{Ai}(-z_0) & \mathrm{Bi}(-z_0) \\ \mathrm{Ai}'(-z_0) & \mathrm{Bi}'(-z_0) \end{pmatrix}\begin{pmatrix} c_1 \\ c_2 \end{pmatrix} = \begin{pmatrix} 1 \\ iz_0^{1/2} \end{pmatrix} \tag{5.126}$$

where $z_0 = z(0) = (\omega_0 T/\Delta\epsilon)^{2/3}$. Inverting (5.126) yields

$$\begin{array}{ll} c_1 & = \pi(\mathrm{Bi}'(-z(0)) - iz_0\mathrm{Bi}(-z(0))), \\ c_2 & = \pi(-\mathrm{Ai}'(-z(0)) + iz_0\mathrm{Ai}(-z(0)). \end{array} \tag{5.127}$$

This completely specifies α_+ and α_- through (5.124) and (5.125), and thus α and β.

Turning to (5.117) for ν, we see that since $d = d^*$

$$\hbar\dot{\nu} = -i(\beta^* d + \alpha^* d) = -id\alpha_+^*. \tag{5.128}$$

Using (5.111) for d and its time-dependence with ϵ we find

$$\dot{\nu} = -i\omega_0 \left(\frac{3N_s}{4}\right)^{1/2} \left(\frac{\Delta\epsilon t}{T}\right) \left(1 + \frac{\Delta\epsilon t}{T}\right) \alpha_+^*. \tag{5.129}$$

We can rewrite (5.129) using z from (5.123)

$$\dot{\nu} = -i\omega_0 \left(\frac{3N_s}{4}\right)^{1/2} \left((z/z_0)^2 - z/z_0\right) \alpha_+^*. \tag{5.130}$$

Integrating ν we find

$$\nu(T) = \left(\frac{3N_s}{4}\right)^{1/2} \left(-\Delta\epsilon\alpha_-^*(T) - iz_0^{-3/2}(\alpha_+^*(T) - 1)\right). \tag{5.131}$$

Our final task is to compute the fidelity

$$F = |\langle\bar{\Psi}_0|U(T)|\Psi_0\rangle|^2, \tag{5.132}$$

where $|\Psi_0\rangle = |0\rangle$ is the ground state of the initial Hamiltonian $H(0)$ and $|\bar{\Psi}_0\rangle$ is the ground state of the final Hamiltonian $H(T)$. Using properties of the squeezing and displacement operators (given in the Appendix) we can write

$$H(T) = (1 + \epsilon_1)^{1/2} S(r_1, 0) D(\nu_1) H(0) D^\dagger(\nu_1) S^\dagger(r_1, 0), \tag{5.133}$$

where

$$\begin{aligned} r_1 &= \operatorname{arccosh}\left((1+\Delta\epsilon/2)(1+\Delta\epsilon)^{-1/2}\right) \\ \nu_1 &= -(3N_s/4)^{1/2}\Delta\epsilon(1+\Delta\epsilon)^{1/2}e^{-r_0}. \end{aligned} \tag{5.134}$$

The relation between the initial and final ground states is

$$|\bar{\Psi}_0\rangle = S(r_1,0)D(\nu_1)|\Psi_0\rangle. \tag{5.135}$$

Thus, the fidelity is, using our propagator $U(T)$

$$F = |\langle 0|D^\dagger(\nu_1)S^\dagger(r_1,0)S(r,\phi)R(\theta)D(\nu)|0\rangle|^2. \tag{5.136}$$

This can be simplified by using $R(\theta)D(\nu)R^\dagger(\theta) = D(\nu')$, $\nu' = \nu e^{-i\theta}$ and $R(\theta)|0\rangle = e^{-i\theta/2}|0\rangle$:

$$F = |\langle 0|D^\dagger(\nu_1)S^\dagger(r_1,0)S(r,\phi)D(\nu')|0\rangle|^2. \tag{5.137}$$

The full expression for this matrix element, derived in [267] (Eq. (3.25), with $\mu = \cosh r$ and $\nu = \sinh r e^{2i\phi}$), is

$$\begin{aligned} \langle 0|D^\dagger(\beta_2)S^\dagger(r_2,\phi_2)S(r_1,\phi_1)D(\beta_1)|0\rangle = N^{1/2}\exp\left(-\frac{1}{2}|\beta_1|^2 - \frac{1}{2}|\beta_2|^2\right) \\ \times \exp\left(N\beta_2^*\beta_1 - NK\beta_2^{*2} + NK^*\beta_1^2\right), \end{aligned} \tag{5.138}$$

where

$$N = \left(\cosh r_1 \cosh r_2 - \sinh r_1 \sinh r_2 e^{i2(\phi_1-\phi_2)}\right)^{-1} \tag{5.139}$$

and

$$K = \frac{1}{2}\left(\sinh r_1 \cosh r_2 e^{i2\phi_1} - \cosh r_1 \sinh r_2 e^{i2\phi_2}\right). \tag{5.140}$$

In Fig. 5.17 we plot the error $E(T) = 1 - F(T)$ for the linear ramp with $\epsilon_0 = 0$, $\epsilon_1 = 0.2$, $t_0 = 0$ and $t_1 = T$, and $N_s = 4$. This situation is essentially the reverse

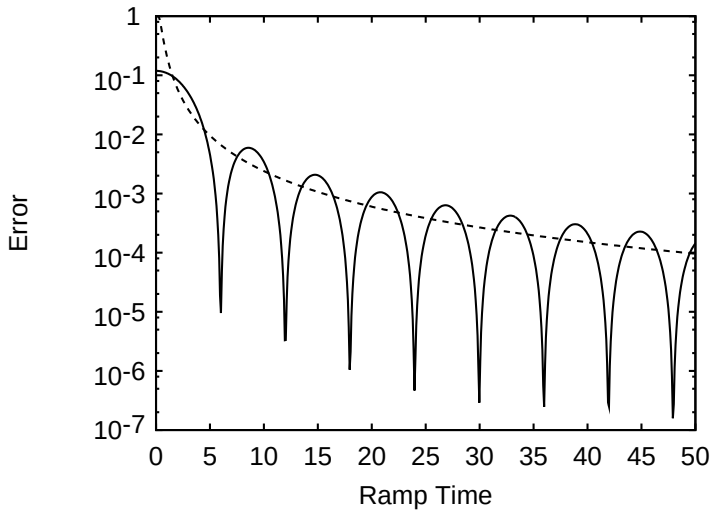

Figure 5.17: Final state fidelity error $E(T) = 1 - F(T)$ for the linear ramp as a function of the ramp time T. The solid curve is the error in the ground state calculated using the harmonic propagator, including the shift in frequency and potential minimum. The dashed curve is the averaged harmonic approximation, which only includes the shift in the potential minimum.

of that considered before, but now including the frequency shift. Also shown is the averaged harmonic approximation we derived previously, with $\Delta\epsilon = \epsilon_1 - \epsilon_0 = 0.2$. From this plot we conclude that it is the movement of the minimum, not the effect of the frequency shift, which is the dominant feature in the fidelity. The oscillations in $E(T)$, however, are now due to Airy instead of trigonometric functions.

Chapter 6

Two Qubit Operations

In Chapter 5 we showed how a single qubit can be constructed from a current-biased Josephson junction, and how microwave pulses and bias current ramps can be used to control the system. In this Chapter, we examine a simple capacitive coupling scheme, and show that bias current pulses can produce two types of two-qubit quantum logic operations, a controlled-phase gate and a swap gate.

As discussed in Chapter 1, by combining single-qubit and two-qubit operations an arbitrary n-qubit unitary operation can be performed. The controlled dynamics discussed here are therefore one of the most important issues for quantum computation using phase qubits. The central results on gates were first published in [37]. An analysis of the physical coupling scheme and its spectroscopic features was first reported in [268], while the first experimental realization was tested in [269]. More details on the experiments can be found in the Ph.D. theses of A. J. Berkley [270]

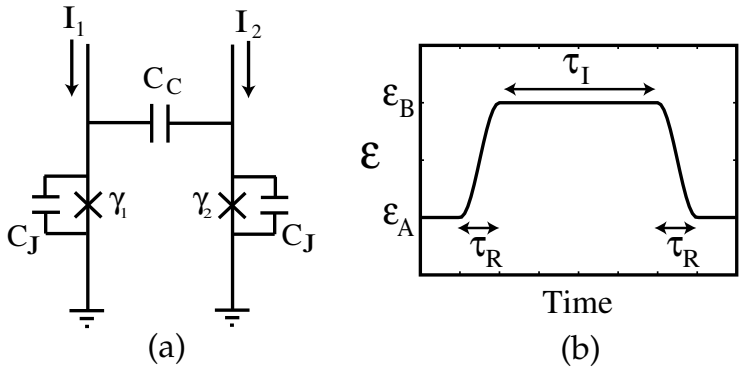

Figure 6.1: (a) Circuit diagram for capacitively coupled Josephson junctions; (b) Time-dependent ramp of bias current ramp, specified through the detuning ϵ.

and H. Xu [11].

There have been several important prior studies of the capacitive coupling of superconducting qubits. The capacitive coupling of two charge qubits was considered in [271, 272], and has been experimentally realized in two important time-domain experiments [90, 91]. The coupling of charge qubits to an LC oscillator or current-biased Josephson junction for quantum information processing has also been considered [273, 274, 275, 276]. The use of a current-biased junction to distribute entanglement has also been proposed [254]. We note that the fundamental physics of the MIT three-junction qubit [277, 278] also includes capacitive coupling, although without current bias. There have also been classical studies of capacitively coupled Josephson junctions [279, 280].

In Section 2 we consider the physical circuit shown in Fig. 6.1(a). We derive the Hamiltonian and perform an analysis of the relevant energy levels and entanglement. In Section 3 we use this analysis to show how two fundamental logic gates can be

constructed by using the bias current ramp illustrated in Fig. 6.1(b). We control the dynamics by using the detuning parameter ϵ as in Chapter 5. Key to the construction is the use of quantum interference between the two-qubit state $|11\rangle$ and an auxiliary level. This takes the form of a simple two-state oscillation, such that the population of our two-qubit state is

$$p_{11}(t) = |\langle 11|e^{-iHt}|11\rangle|^2 = a + b\cos^2(\Omega t). \tag{6.1}$$

The quantity Ω is given by a difference in energy levels, and a and b are related to the eigenstates and satisfy $a+b=1$. By allowing this interaction to occur for a time $\tau_I = k\pi/\Omega$, we achieve $p_{11}(\tau_I) = 1$. This allows the system to momentarily leave and return to the two-qubit subspace, and enables useful quantum logic operations in the presence of auxiliary levels.

These methods are in fact quite general, and have been proposed for quantum information processing in ion traps [281, 282], neutral atoms in optical lattices [283], and in fixed interaction architectures [284, 285], where the respective auxiliary levels are the center of mass motion in the ion trap, weakly bound states of two atoms, and barrier qubits used to mediate interactions. Such schemes are clearly advantageous for multi-qubit dynamics; we will study one such instance in the next Chapter. Finally, in Section 4, we explore the dynamical optimization of these operations.

6.1 Capacitively coupled phase qubits

6.1.1 Hamiltonian

As described in Chapter 2, the dynamics of an ideal current-biased Josephson junction [100] is determined by the gauge-invariant phase difference γ between the junction electrodes. The supercurrent through the junction and the voltage drop across the junction are given by the Josephson relations $I = I_c \sin\gamma$ and $V = (\Phi_0/2\pi)\dot{\gamma}$. Here I_c is the critical current of the junction, and $\Phi_0 = h/2e$ is the flux quantum. The Hamiltonian for this system can be written as

$$H = \frac{1}{2C_J}\left(\frac{2\pi}{\Phi_0}\right)^2 p_\gamma^2 - \left(\frac{I_c\Phi_0}{2\pi}\right)(\cos\gamma + J\gamma), \tag{6.2}$$

where $p_\gamma = (\Phi_0/2\pi)Q_J$, the momentum canonically conjugate to γ, is proportional to the charge $Q_J = C_J V$ on the junction, C_J is the intrinsic junction capacitance, and $J = I/I_c$ is the normalized bias current. For $J < 1$, there exist local minima of the "washboard" potential, about which the phase can oscillate with the characteristic plasma frequency $\omega_p(J) = (2\pi I_c/\Phi_0 C_J)^{1/2}(1-J^2)^{1/4}$.

The circuit diagram for two capacitively coupled junctions is shown in Fig. 6.1. The two junctions have the characteristic capacitances C_1 and C_2, with critical currents I_{c1} and I_{c2}; the applied bias currents are I_1 and I_2, while the coupling capacitance is C_{12}. The equations of motion for this coupled system can be directly by extending the equations of motion for two uncoupled current biased junctions. This is done by adding and subtracting a current $\dot{Q}$ to each bias line, to represent

the charging of the coupling capacitor. Thus we have

$$\begin{aligned} C_1\left(\frac{\Phi_0}{2\pi}\right)\ddot{\gamma}_1 + I_{c1}\sin\gamma_1 = &\quad I_1 - \dot{Q}, \\ C_2\left(\frac{\Phi_0}{2\pi}\right)\ddot{\gamma}_2 + I_{c2}\sin\gamma_2 = &\quad I_2 + \dot{Q}. \end{aligned} \tag{6.3}$$

To close this system of equations, we relate the charge Q to the two phase variables via

$$Q = C_{12}(V_1 - V_2) = C_{12}\left(\frac{\Phi_0}{2\pi}\right)(\dot{\gamma}_1 - \dot{\gamma}_2). \tag{6.4}$$

The equations of motion (6.3) with (6.4) follow from the Lagrangian

$$\mathcal{L} = \frac{1}{2}\left(\frac{\Phi_0}{2\pi}\right)^2 \sum_{jk} \dot{\gamma}_j A_{jk} \dot{\gamma}_k - \sum_j U_j(\gamma_j), \tag{6.5}$$

where the potential is the sum of the washboard potentials for each junction

$$U_j(\gamma) = -\left(\frac{\Phi_0}{2\pi}\right)(I_{cj}\cos\gamma + I_j\gamma), \tag{6.6}$$

and the capacitance matrix is defined by

$$A = \begin{pmatrix} C_1 + C_{12} & -C_{12} \\ -C_{12} & C_2 + C_{12} \end{pmatrix}. \tag{6.7}$$

Physically, the kinetic energy terms represent the charging of the various capacitors. That is, if we let $\mathcal{L} = T - U$ and use the Josephson voltage relations, we find

$$T = \frac{1}{2}C_1V_1^2 + \frac{1}{2}C_2V_2^2 + \frac{1}{2}C_{12}(V_1 - V_2)^2 \tag{6.8}$$

which is precisely the electrostatic energy stored by the three capacitors.

Constructing the canonical momenta and Hamiltonian in the usual way, we find

$$p_j = \frac{\partial\mathcal{L}}{\partial\dot{\gamma}_j} = \left(\frac{\Phi_0}{2\pi}\right)^2 \sum_k A_{jk}\dot{\gamma}_k, \tag{6.9}$$

and

$$H = \sum_j p_j \dot{\gamma}_j - \mathcal{L} = \frac{1}{2}\left(\frac{2\pi}{\Phi_0}\right)^2 \sum_{ij} p_i (A^{-1})_{ij} p_j + \sum_i U_i(\gamma_i), \tag{6.10}$$

where A^{-1} is the inverse of the capacitance matrix A. It has the explicit form

$$A^{-1} = \frac{1}{(C_1 + C_{12})(C_2 + C_{12}) - C_{12}^2} \begin{pmatrix} C_2 + C_{12} & C_{12} \\ C_{12} & C_1 + C_{12} \end{pmatrix}. \tag{6.11}$$

In fact, the Hamiltonian in (6.10) can be trivially extended to an array of capacitively coupled junctions given a suitable definition of the capacitance matrix.

The capacitance matrix simplifies if both junctions have equal capacitance. In this case, we let $C_1 = C_2 = C_J$, $C_{12} = C$ and define the coupling parameter ζ

$$\zeta = \frac{C}{C_J + C}. \tag{6.12}$$

For this case, the two-junction capacitance matrix Eq. (6.7) takes the form

$$A_2 = C_J(1-\zeta)^{-1} \begin{pmatrix} 1 & -\zeta \\ -\zeta & 1 \end{pmatrix} \tag{6.13}$$

with the inverse

$$A_2^{-1} = C_J^{-1}(1+\zeta)^{-1} \begin{pmatrix} 1 & \zeta \\ \zeta & 1 \end{pmatrix}. \tag{6.14}$$

Using (6.14) in (6.10) yields the result

$$H = \frac{1}{2C_J(1+\zeta)}\left(\frac{2\pi}{\Phi_0}\right)^2 (p_1^2 + p_2^2 + 2\zeta p_1 p_2) - \left(\frac{\Phi_0}{2\pi}\right)(I_{c1}\cos\gamma_1 + I_1\gamma_1 + I_{c2}\cos\gamma_2 + I_2\gamma_2). \tag{6.15}$$

For multiple junctions, determining the capacitance matrices can become quite tedious. For example, with three identical junctions with $C_1 = C_2 = C_3 = C_J$ with coupling capacitances $C_{12} = C_{23} = C$ the capacitance matrix is

$$A_3 = C_J(1-\zeta)^{-1} \begin{pmatrix} 1 & -\zeta & 0 \\ -\zeta & 1+\zeta & -\zeta \\ 0 & -\zeta & 1 \end{pmatrix} \tag{6.16}$$

with inverse

$$A_3^{-1} = C_J^{-1}(1+2\zeta)^{-1} \begin{pmatrix} 1+\zeta-\zeta^2 & \zeta & \zeta^2 \\ \zeta & 1 & \zeta \\ \zeta^2 & \zeta & 1+\zeta-\zeta^2 \end{pmatrix}. \tag{6.17}$$

In general, if we let $A = C_J(1-\zeta)^{-1}(I+\zeta B)$, then the inverse matrix has the expansion $A^{-1} = C_J^{-1}(1-\zeta)(I-\zeta B+\zeta^2 B^2+\dots)$. The coupling matrix B couples neighboring junctions, such that the nearest neighbor velocity coupling of strength ζ in A will lead to momentum coupling of strength ζ^k between junctions j and $j+k$. To reduce coupling to the next-nearest junctions, ζ needs to be small compared to 1.

As with a single tilted washboard potential, a cubic approximation to the Hamiltonian allows us to see the dominant physics without specific junction parameters. The relevant approximation to (6.15) is

$$\begin{aligned} H = \; & \tfrac{1}{2}(1+\zeta)^{-1}\left(p_1^2+p_2^2+2\zeta p_1 p_2\right) \\ & +\tfrac{1}{2}\omega_1^2(x_1-x_{c1})^2-\lambda_1(x_1-x_{c1})^3+\tfrac{1}{2}\omega_2^2(x_2-x_{c2})^2-\lambda_2(x_2-x_{c2})^3 \end{aligned} \tag{6.18}$$

where the energy scale is

$$\hbar\omega_0 = \sqrt{8E_cE_{J1}}(1-J_{0,1}^2)^{1/4} = \sqrt{8E_cE_{J2}}(1-J_{0,2}^2)^{1/4} \tag{6.19}$$

with $J_{0,1}$ the reference bias current for junction 1, and $J_{0,2}$ the reference bias current for junction 2. At this reference bias, the number of states in the uncoupled metastable wells can be different

$$\begin{aligned} N_{s1} &= 2^{-1/2}\left(E_{J1}/E_c\right)^{1/2}\left((1-J_{0,1}^2)^{1/4}-J_{0,1}(1-J_{0,1}^2)^{-1/4}\arccos J_{0,1}\right) \\ N_{s2} &= 2^{-1/2}\left(E_{J2}/E_c\right)^{1/2}\left((1-J_{0,2}^2)^{1/4}-J_{0,2}(1-J_{0,2}^2)^{-1/4}\arccos J_{0,2}\right) \end{aligned} \tag{6.20}$$

and the remaining parameters in the cubic are

$$\begin{array}{ll} \omega_1 & = (1-J_1^2)^{1/4}(1-J_{0,1}^2)^{-1/4} \\ \omega_2 & = (1-J_2^2)^{1/4}(1-J_{0,2}^2)^{-1/4} \\ \lambda_1 & = (54N_{s1})^{-1/2} \\ \lambda_2 & = (54N_{s2})^{-1/2} \\ x_{c1} & = (3N_{s1}/2)^{1/2}(1-\omega_1^2) \\ x_{c2} & = (3N_{s2}/2)^{1/2}(1-\omega_2^2). \end{array} \tag{6.21}$$

In the following, we consider the simple case $E_{J1} = E_{J2}$, in which case $J_{0,1} = J_{0,2} = J_0$ and $N_{s1} = N_{s2}$.

6.1.2 Energy Levels and Entanglement

The complex scaling method used to find the resonances for the one-dimensional washboard is equally applicable to the two-dimensional Hamiltonians (6.15) or (6.18). As in Chapter 5 we consider the variation of the bias currents such that the frequencies are given by a detuning parameter ϵ:

$$\begin{array}{ll} \omega_1^2 & = 1+\epsilon, \\ \omega_2^2 & = 1-\epsilon, \end{array} \tag{6.22}$$

which implies the following variation of the bias currents

$$\begin{array}{ll} J_1^2 & = 1-(1-J_0^2)(1+\epsilon)^2 \\ J_2^2 & = 1-(1-J_0^2)(1-\epsilon)^2. \end{array} \tag{6.23}$$

The slightly less accurate mapping with $J_1^2 \to J_1$, $J_2^2 \to J_2$ and $J_0^2 \to J_0$ was quoted in [37]; for typical phase qubits the difference is small, and in no way affects our argument.

Since the washboard minimum varies with the detuning, we explicitly keep track of this by labeling the eigenstates $|n;\epsilon)$, where $n = 0, 1, \cdots$ represents the energy level with eigenvalue $E_n(\epsilon)$. The round brackets are used to distinguish

these coupled states from the uncoupled energy levels, which are the product states $|jk;\epsilon\rangle = |j;\epsilon\rangle \otimes |k;-\epsilon\rangle$, where $|j;\epsilon\rangle$ are energy states of an isolated junction with normalized bias current J_1 and $|k;-\epsilon\rangle$ are those for bias current J_2. When needed, we denote the corresponding uncoupled energy levels by $\bar{E}_{jk}(\epsilon)$.

There are two relevant regimes for the energy levels, the harmonic case when N_s is large, and the anharmonic case with N_s is small (~ 3). Recall from (6.20) that this is determined by the value of J_0. About this bias, we can bring the two junctions into resonance by setting $\epsilon \sim 0$. For certain values of the bias the effect of the coupling is maximal. This is revealed by avoided level crossings of the energy levels and in the entanglement of the wavefunctions. We explore these effects for the harmonic and anharmonic cases in this Section.

The energy levels of the first five excited states for the harmonic case $N_s = 20$ are shown in Fig. 6.2, with coupling $\zeta = 0.01$. We see avoided crossings with energy splitting given by $\Delta E \sim \zeta$. The entanglement of the corresponding states are shown in Fig. 6.3. As discussed in Chapter 1, the entropy of entanglement is given in ebits [27]: a state with one ebit entanglement is a maximally entangled two-qubit state. The ground state is not shown, but is nearly independent of ϵ in both energy ($E_0(\epsilon) \sim 0.992$) and entanglement ($\mathcal{E}_0(\epsilon) \sim 10^{-4}$). We observe that the avoided level crossings for the various energy levels all occur near $\epsilon = 0$. The entanglement of the first two states $\mathcal{E}_1(\epsilon) \simeq \mathcal{E}_2(\epsilon)$ goes from zero to a maximal two-qubit value $\mathcal{E} = 1$ as ϵ passes through zero (in Fig. 6.3(a)). As seen in Fig. 6.3(b)-(d), and as will be explained shortly, this measure of the entanglement can be greater than unity.

The energy and entanglement for $N_s = 20$ can be understood by looking at

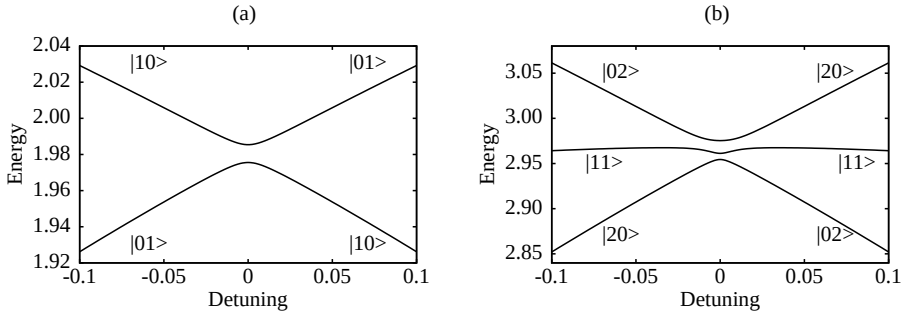

Figure 6.2: Energy Levels versus detuning ϵ for $N_s = 20$. (a) The energy levels $E_1(\epsilon)$ and $E_2(\epsilon)$, with an avoided crossing at $\epsilon = 0$. (b) The energy levels $E_3(\epsilon)$, $E_4(\epsilon)$, and $E_5(\epsilon)$, with a three-state avoided crossing at $\epsilon = 0$. The ground state $E_0(\epsilon) \sim 0.992$ has little variation with ϵ.

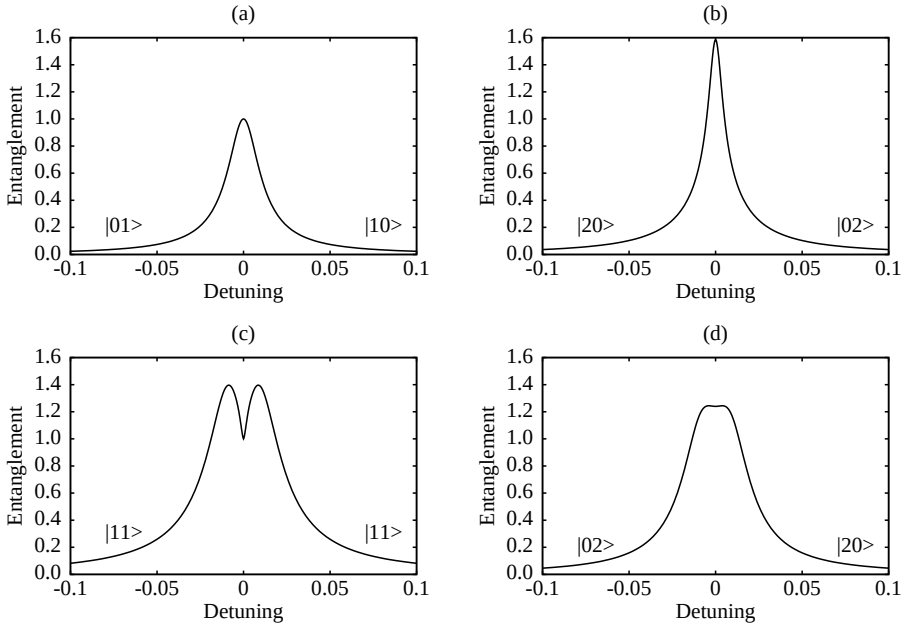

Figure 6.3: Entanglement versus detuning ϵ for $N_s = 20$. The entanglement of the energy states: (a) $\mathcal{E}_1(\epsilon)$, (b) $\mathcal{E}_3(\epsilon)$, (c) $\mathcal{E}_4(\epsilon)$, and (d) $\mathcal{E}_5(\epsilon)$. Not shown are $\mathcal{E}_0(\epsilon) \sim 10^{-4}$ and $\mathcal{E}_2(\epsilon) \simeq \mathcal{E}_1(\epsilon)$.

the harmonic approximation to the Hamiltonian, i.e. the limit $\lambda_1, \lambda_2 \to 0$. In this case, we can exactly diagonalize the Hamiltonian using the normal modes of the system, which are

$$\begin{array}{ll} x_+ & = 2^{-1/2}(\cos\phi - s\sin\phi)x_1 + 2^{-1/2}(\cos\phi + s\sin\phi)x_2, \\ x_- & = 2^{-1/2}(-s\cos\phi - \sin\phi)x_1 + 2^{-1/2}(s\cos\phi - s\sin\phi)x_2, \end{array} \tag{6.24}$$

with $s = (1+\zeta)^{1/2}(1-\zeta)^{-1/2}$ and

$$\tan\phi = \frac{\zeta - \sqrt{\zeta^2 + \epsilon^2(1-\zeta^2)}}{\epsilon\sqrt{1-\zeta^2}}. \tag{6.25}$$

The Hamiltonian becomes

$$H = \frac{1}{2}\omega_+(p_+^2 + x_+^2) + \frac{1}{2}\omega_-(p_-^2 + x_-^2), \tag{6.26}$$

with

$$\omega_\pm^2 = (1+\zeta)^{-1}[1 \pm \sqrt{\zeta^2 + \epsilon^2(1-\zeta^2)}]. \tag{6.27}$$

For $\epsilon = 0$, we find from (6.25) $\phi = 0$, while (6.27) yields $\omega_+^2 = 1$, $\omega_-^2 = (1-\zeta)/(1+\zeta)$. The normal modes (6.24) become

$$x_\pm \simeq 2^{-1/2}(\pm x_1 + x_2) + O(\zeta). \tag{6.28}$$

Using the creation operators for each mode

$$a_\pm^\dagger = 2^{-1/2}(\pm a_1^\dagger + a_2^\dagger), \tag{6.29}$$

we find the eigenstates and energy levels are

$$\begin{array}{ll} |\Psi_{n_+,m_-}\rangle & = (n!m!)^{-1/2} {a_+^\dagger}^n {a_-^\dagger}^m |00\rangle, \\ E_{n_+,m_-} & = \omega_+(n_+ + 1/2) + \omega_-(n_- + 1/2). \end{array} \tag{6.30}$$

The first few states $|n,0)$ are, for small ζ

$$\begin{array}{lll} |0,0) & = |\Psi_{0_+,0_-}\rangle = & |00,0\rangle, \\ |1,0) & = |\Psi_{0_+,1_-}\rangle = & 2^{-1/2}(|01,0\rangle - |10,0\rangle), \\ |2,0) & = |\Psi_{1_+,0_-}\rangle = & 2^{-1/2}(|01,0\rangle + |10,0\rangle), \\ |3,0) & = |\Psi_{0_+,2_-}\rangle = & 2^{-1}(|02,0\rangle + |20,0\rangle - 2^{1/2}|11,0\rangle), \\ |4,0) & = |\Psi_{1_+,1_-}\rangle = & 2^{-1}(|02,0\rangle - |20,0\rangle), \\ |5,0) & = |\Psi_{2_+,0_-}\rangle = & 2^{-1}(|02,0\rangle + |20,0\rangle + 2^{1/2}|11,0\rangle). \end{array} \tag{6.31}$$

All of these states are in Schmidt form, so we can easily calculate their entanglement using (1.41): $\mathcal{E}_0 = 0$, $\mathcal{E}_1 = \mathcal{E}_2 = 1$, $\mathcal{E}_3 = \mathcal{E}_5 = 3/2$, and $\mathcal{E}_4 = 1$. Entanglement greater than one occurs when there are more than two terms in the Schmidt decomposition, as in the states $|3,0)$ and $|5,0)$. While there are significant deviations from these results in Fig. 6.3, the general picture is clear: the coupling of the normal modes leads to highly entangled eigenstates at $\epsilon \sim 0$.

However, for $|\epsilon| > 0.1$, the energy states are essentially unentangled and well approximated by the product states, which we have used to label the corresponding energy levels in Fig. 6.2 and Fig. 6.3. Thus for $\epsilon_A = -0.1$ we find that the eigenstates satisfy the relations $|1;\epsilon_A) \cong |10;\epsilon_A\rangle$, $|2;\epsilon_A) \cong |01;\epsilon_A\rangle$, and $|4;\epsilon_A) \cong |11;\epsilon_A\rangle$. The ground state $|0;\epsilon) \cong |00;\epsilon\rangle$, not shown, remains essentially unentangled for all ϵ. These four states will be our two-qubit basis. In addition, there are the auxiliary states $|3;\epsilon_A) \cong |20;\epsilon_A\rangle$ and $|5;\epsilon_A) \cong |02;\epsilon_A\rangle$. These auxiliary states will be important for our logic gates.

The energy levels in the anharmonic case with $N_s = 3$ are shown in Fig. 6.4, with the entanglement shown in Fig. 6.5. We see that for the first two energy levels the avoided level crossing and entanglement are quite similar to the harmonic case, and the energy splitting is $E_2(0) - E_1(0) \simeq \zeta$. The higher energy levels, however, are significantly different. We now see two avoided level crossings that occur for

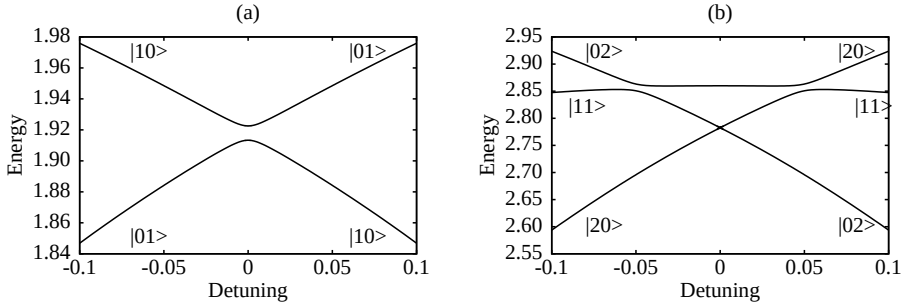

Figure 6.4: Energy Levels versus detuning ϵ for $N_s = 3$. (a) The energy levels $E_1(\epsilon)$ and $E_2(\epsilon)$, with an avoided crossing at $\epsilon = 0$. (b) The energy levels $E_3(\epsilon), E_4(\epsilon)$, and $E_5(\epsilon)$, with two-state avoided crossings of 4 and 5 at $\epsilon = \pm 0.05$, and 3 and 4 at $\epsilon = 0$. The ground state $E_0(\epsilon) \sim 0.976$ has little variation with ϵ.

$\epsilon_\pm \sim \pm 0.05$. These are due to the anharmonic energy levels of each junction. The entanglement of each of the higher energy levels exhibits clear signatures at these detunings as well. Each splitting is characteristic of a two-state system, and the relevant states at these positions are approximately

$$\begin{array}{ll} |4, \epsilon_-) & = 2^{-1/2}(|02, \epsilon_-\rangle - |11, \epsilon_-\rangle) \\ |5, \epsilon_-) & = 2^{-1/2}(|02, \epsilon_-\rangle + |11, \epsilon_-\rangle) \end{array} \tag{6.32}$$

and

$$\begin{array}{ll} |4, \epsilon_+) & = 2^{-1/2}(|20, \epsilon_+\rangle - |11, \epsilon_+\rangle) \\ |5, \epsilon_+) & = 2^{-1/2}(|20, \epsilon_+\rangle + |11, \epsilon_+\rangle) \end{array} \tag{6.33}$$

with $E_5(\epsilon_\pm) - E_4(\epsilon_\pm) \simeq 2^{1/2}\zeta$.

The remaining avoided level crossing at $\epsilon = 0$ is very small (of order ζ^2) and is not visible on this figure. It is accompanied by a very sharp variation of the entanglement in states 3 and 4. To understand this, we consider a simplified

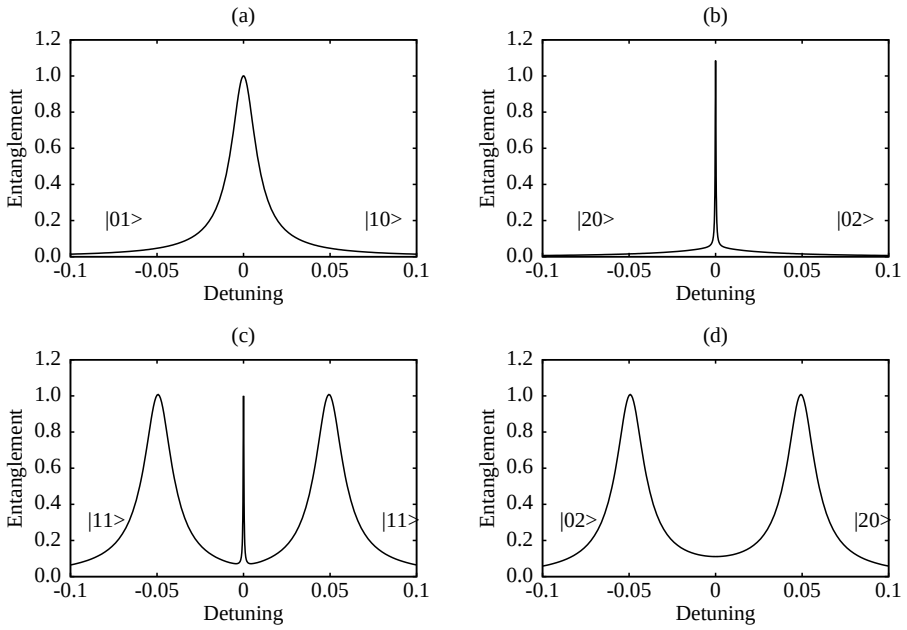

Figure 6.5: Entanglement versus detuning ϵ for $N_s = 3$. The entanglement of the energy states: (a) $\mathcal{E}_1(\epsilon)$, (b) $\mathcal{E}_3(\epsilon)$, (c) $\mathcal{E}_4(\epsilon)$, and (d) $\mathcal{E}_5(\epsilon)$. Not shown are $\mathcal{E}_0(\epsilon) \sim 10^{-4}$ and $\mathcal{E}_2(\epsilon) \simeq \mathcal{E}_1(\epsilon)$.

three-state model for the states $|02,0\rangle, |20,0\rangle$ and $|11,0\rangle$:

$$H_3 = \begin{pmatrix} \bar{E}_{02} & 0 & 2^{-1/2}\zeta \\ 0 & \bar{E}_{20} & 2^{-1/2}\zeta \\ 2^{-1/2}\zeta & 2^{-1/2}\zeta & \bar{E}_{11} \end{pmatrix}. \tag{6.34}$$

where we have use the harmonic oscillator matrix element $\langle 02|p_1 p_2|11\rangle = 2^{-1/2}$. At $\epsilon = 0$, we have $\bar{E}_{20} = \bar{E}_{02}$, and we can write $H_3 = \bar{E}_{02} I + 2^{-1/2}\zeta K$, with

$$K = \begin{pmatrix} 0 & 0 & 1 \\ 0 & 0 & 1 \\ 1 & 1 & z \end{pmatrix} \tag{6.35}$$

and

$$z = 2^{1/2}\left(\frac{\bar{E}_{11} - \bar{E}_{02}}{\zeta}\right). \tag{6.36}$$

The eigenvalues of K can be directly computed:

$$\begin{aligned} k_0 &= (z - \sqrt{z^2+8})/2, \\ k_1 &= 0, \\ k_2 &= (z + \sqrt{z^2+8})/2, \end{aligned} \tag{6.37}$$

and the eigenvectors are the energy states

$$\begin{aligned} |3,0) &= 2^{-1/2}\cos\theta(|02,0\rangle + |20,0\rangle) - \sin\theta|11,0\rangle, \\ |4,0) &= 2^{-1/2}(|02,0\rangle - |20,0\rangle), \\ |5,0) &= 2^{-1/2}\sin\theta(|02,0\rangle + |20,0\rangle) + \cos\theta|11,0\rangle, \end{aligned} \tag{6.38}$$

with

$$\tan\theta = \frac{1}{2\sqrt{2}}\left(\sqrt{z^2+8} - z\right). \tag{6.39}$$

The character of the eigenstates is controlled by z. For general θ the two-qubit state $|11,0\rangle$ is always coupled to the auxiliary levels. Using the sixth order perturbation theory from Chapter 4 for $\bar{E}_{02}$ and $\bar{E}_{11}$, we can show

$$z = \frac{5\sqrt{2}}{36}(N_s\zeta)^{-1}\left(1 + \frac{47}{48}N_s^{-1} + \frac{118865}{93312}N_s^{-2}\right). \tag{6.40}$$

If we take the harmonic limit $N_s \to \infty$ or the strong coupling limit, then $z \to 0$ and $\theta = \pi/4$, and the eigenstates reduce to the harmonic oscillator approximations given

above. In the weak coupling limit or the limit of very small N_s, we have $z \to \infty$ and $\theta = \pi/2$, and only in this case does $|11, 0\rangle$ decouple from the other states. For $\zeta = 0.01$ and $N_s = 3$, we find $\theta \sim 0.14$ (in radians); for $N_s = 5$ we have $\theta \sim 0.26$. This implies that if we were to assume no coupling to the auxiliary levels, this would introduce an error of order 10^{-2} to 10^{-1} which would be considerable. A method that uses this coupling to construct a quantum logic gate is introduced in the next section.

6.2 Quantum Logic Gates

To construct useful quantum logic operations we must choose some natural encoding of the quantum information, and a ramp sequence for the bias currents. Since the eigenstates are essentially unentangled for $|\epsilon| \geq 0.1$, we can can use the states at $\epsilon_A = -0.1$ as our two-qubit basis. While there is residual entanglement at this operation point, it can be reduced by using either a larger $|\epsilon_A|$ or by multi-junction encoding schemes. These procedures are easy to implement (in principle), and have been generally studied as a "dressed qubit" formalism [286].

To implement quantum logic gates, we vary ϵ with time as shown in Fig. 6.1(b). The idea is to ramp the bias currents, moving the system smoothly (with ramp time τ_R) from ϵ_A, where the eigenstates are essentially unentangled, to ϵ_B, where the eigenstates are maximally entangled. Entangling evolution is then allowed to occur for an interaction time τ_I, after which the system is ramped back to ϵ_A. The natural choices for ϵ_B are either $\epsilon_B = \epsilon_-$ or $\epsilon_B = 0$. The first choice can be made to generate

a controlled phase gate, while the second can be used to implement a swap between states $|01, \epsilon_A\rangle$ and $|10, \epsilon_A\rangle$. We study these in detail in the sections below.

6.2.1 Controlled Phase Gate

We first consider the case $\epsilon_B = \epsilon_-$. As shown in Fig. 6.4 the dominant feature in the energy levels and the eigenstates at $\epsilon = \epsilon_-$ is the avoided level crossing between states 4 and 5; the other relevant two-qubit states can be taken as $|0, \epsilon_-) \simeq |00, \epsilon_-\rangle$, $|1, \epsilon_-) \simeq |10, \epsilon_-\rangle$, and $|2, \epsilon_-) \simeq |01, \epsilon_-\rangle$. The remaining two-qubit state, however is a superposition of the energy states (6.32)

$$|11, \epsilon_-\rangle = 2^{-1/2}[|5, \epsilon_-) - |4, \epsilon_-)]. \tag{6.41}$$

If we prepare this state and evolve it in time, it will perform a simple two-state oscillation

$$\begin{array}{rl} e^{-iH(\epsilon_-)t}|11, \epsilon_-\rangle & = 2^{-1/2}[e^{-iE_5(\epsilon_-)t}|5, \epsilon_-) - e^{-iE_4(\epsilon_-)t}|4, \epsilon_-)] \\ & = e^{-i\phi_{11}}[\cos(\Omega t)|11, \epsilon_-\rangle - i\sin(\Omega t)|02, \epsilon_-\rangle], \end{array} \tag{6.42}$$

with

$$\begin{array}{ll} \phi_{11} & = (E_5(\epsilon_-) + E_4(\epsilon_-))t/2, \\ \Omega & = (E_5(\epsilon_-) - E_4(\epsilon_-))/2. \end{array} \tag{6.43}$$

Now, for this evolution to be a two-qubit gate, we must minimize the amplitude in $|02, \epsilon_-\rangle$. This can be done by using the interaction time

$$\tau_I = \frac{\pi k}{\Omega} = \frac{2\pi k}{E_5(\epsilon_-) - E_4(\epsilon_-)}, \tag{6.44}$$

where k is an integer. The choice $k = 1$ is particularly interesting, for it yields

$$e^{-iH(\epsilon_-)\tau_I}|11, \epsilon_-\rangle = (-1) \times e^{-i\phi_{11}}|11, \epsilon_-\rangle. \tag{6.45}$$

The phase factor ϕ_{11} is approximately the phase advance of state $|11,\epsilon_-\rangle$ if there were no interaction between the qubits; the interaction has produced the overall factor of -1. It is this controlled phase that can be used for quantum logic.

In the complete two-qubit basis $\{|00\rangle,|01\rangle,|10\rangle,|11\rangle\}$ the evolution operator is

$$e^{-iH(\epsilon_-)\tau_I} = \begin{pmatrix} e^{-i\phi_{00}} & 0 & 0 & 0 \\ 0 & e^{-i\phi_{01}} & 0 & 0 \\ 0 & 0 & e^{-i\phi_{10}} & 0 \\ 0 & 0 & 0 & -e^{-i\phi_{11}} \end{pmatrix}, \tag{6.46}$$

where the phases are

$$\begin{array}{ll} \phi_{00} & = E_0(\epsilon_-)\tau_I \simeq \bar{E}_{00}(\epsilon_-)\tau_I \\ \phi_{01} & = E_2(\epsilon_-)\tau_I \simeq \bar{E}_{01}(\epsilon_-)\tau_I \\ \phi_{10} & = E_1(\epsilon_-)\tau_I \simeq \bar{E}_{10}(\epsilon_-)\tau_I \\ \phi_{11} & = (E_4(\epsilon_-) + E_5(\epsilon_-))\tau_I/2 \simeq \bar{E}_{11}(\epsilon_-)\tau_I \end{array} \tag{6.47}$$

The two-qubit gate is composed of an essential two-qubit interaction, and remaining single-qubit gates. These are particularly simple, being the z-rotations

$$R_z(\alpha) = e^{-i\alpha Z/2} = \begin{pmatrix} e^{-i\alpha/2} & 0 \\ 0 & e^{i\alpha/2} \end{pmatrix}. \tag{6.48}$$

Taking the tensor product of two of these single-qubit gates and an overall phase we have

$$e^{i\alpha_1} R_z(\alpha_2) \otimes R_z(\alpha_3) = e^{i\alpha_1} \begin{pmatrix} e^{-i(\alpha_2+\alpha_3)/2} & 0 & 0 & 0 \\ 0 & e^{-i(\alpha_2-\alpha_3)/2} & 0 & 0 \\ 0 & 0 & e^{i(\alpha_2-\alpha_3)/2} & 0 \\ 0 & 0 & 0 & e^{i(\alpha_2+\alpha_3)/2} \end{pmatrix}. \tag{6.49}$$

Multiplying our evolution operator (6.46) by (6.49)

$$U_1 = e^{i\alpha_1} \left(R_z(\alpha_2) \otimes R_z(\alpha_3)\right) e^{-iH(\epsilon_-)\tau_I}, \tag{6.50}$$

and setting

$$\begin{array}{ll} \alpha_1 & = (\phi_{01} + \phi_{10})/2 \\ \alpha_2 & = (\phi_{10} - \phi_{00}) \\ \alpha_3 & = (\phi_{01} - \phi_{00}) \end{array} \tag{6.51}$$

we find the result

$$U_1(\phi) = \begin{pmatrix} 1 & 0 & 0 & 0 \\ 0 & 1 & 0 & 0 \\ 0 & 0 & 1 & 0 \\ 0 & 0 & 0 & e^{-i\phi} \end{pmatrix}, \tag{6.52}$$

with the controlled phase

$$\begin{aligned} \phi &= \pm\pi + \phi_{11} - \phi_{01} - \phi_{10} + \phi_{00} \\ &= (E_5(\epsilon_-) + E_0(\epsilon_-) - E_1(\epsilon_-) - E_2(\epsilon_-))\tau_I \\ &= (E_4(\epsilon_-) + E_0(\epsilon_-) - E_1(\epsilon_-) - E_2(\epsilon_-))\tau_I. \end{aligned} \tag{6.53}$$

Here we have used $+\pi$ in the second line and $-\pi$ in the third. While a general controlled phase is sufficient for universal quantum computation, in our case we expect $\phi \sim \pm\pi$, which yields the controlled-Z gate $U_1(\pi) = U_{\rm CZ}$ [7]. The single-qubit gates in (6.49) can be implemented by small bias ramps or short delays (< 1ns). In principle, by combining the the phase gate with the single-qubit Rabi oscillations of the Chapter 5 we have all the ingredients for quantum logic algorithms.

This discussion has assume we can prepare the superposition states instantaneously. In fact, we must ramp from ϵ_A to $\epsilon_B = \epsilon_-$ in a finite ramp time τ_R. To include this ramp and simulate the full dynamics, we have numerically computed the eigenfunctions through complex scaling, and evolved each of the corresponding eigenfunctions using the ramp function. We choose $\zeta = 0.01$, $N_s = 4$, and for the ramp we use $\epsilon_A = -0.1$, $\epsilon_B = -0.036$, $\tau_R = 20\pi$ and $\tau_I = 434$. To summarize our results, we consider the state populations (transition probabilities) defined by

$$p_{n;m} = |(n;\epsilon_A|U(t)|m;\epsilon_A)|^2 \tag{6.54}$$

where $U(t)$ is the full time-evolution operator. The results are displayed in Fig. 6.6. In Fig. 6.6(a), we show the populations $p_{0;0}(t)$, $p_{1;1}(t)$ and $p_{2;2}(t)$ as a function of time, each evolved using split-operator methods. Also shown is the ramp func-

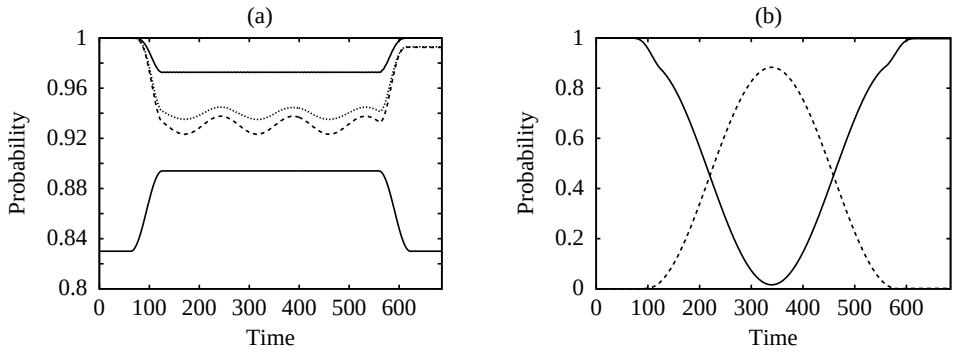

Figure 6.6: Phase Gate with $N_s = 4$, $\zeta = 0.01$, $\epsilon_A = -0.036$, $\epsilon_B = 0$, $\tau_R = 20\pi$, and $\tau_I = 434$. (a) The state populations $p_{0;0}(t)$ (upper solid), $p_{1;1}(t)$ (dashed), $p_{2;2}(t)$ (dotted). Also shown is the displaced ramp function $\epsilon(t) + 0.93$ (lower solid). (b) The state populations $p_{4;4}(t)$ (solid) and $p_{5;4}(t)$ (dashed).

tion which implements a cosine ramp from ϵ_A to ϵ_B and back. This ramp has the functional form

$$\epsilon_C(t) = \left\{ \begin{array}{ll} \epsilon_A & t < t_0 \\ (\epsilon_A + \epsilon_B)/2 - (\epsilon_B - \epsilon_A)\cos\left(\pi(t - t_0)/(t_1 - t_0)\right)/2 & t_0 < t < t_1 \\ \epsilon_B & t_1 < t < t_2 \\ (\epsilon_A + \epsilon_B)/2 - (\epsilon_B - \epsilon_A)\cos\left(\pi(t - t_2)/(t_3 - t_2)\right)/2 & t_2 < t < t_3 \\ \epsilon_A & t_3 < t \end{array} \right\}, \tag{6.55}$$

where $\tau_R = t_1 - t_0 = t_3 - t_2$ and $\tau_I = t_2 - t_1$.

From Fig. 6.6 we observe some oscillations in the $|1, \epsilon_A)$ and $|2, \epsilon_B)$ states, which can be accounted for in logic design. In Fig. 6.6(b), the populations of states $|4, \epsilon_A)$ and $|5, \epsilon_A)$ are shown, when the initial condition is $|4, \epsilon_A)$. The two-state oscillation seems imperfect, since $p_{5;4}(t) < 0.9$ for the entire evolution. This is due to the displacement of the eigenstates, which leads to a reduction in the wavefunction overlap, i.e. $|\langle 02, \epsilon_B | 02, \epsilon_A \rangle| < 1$. The wavefunctions corresponding to this evolution are shown in Fig. 6.7.

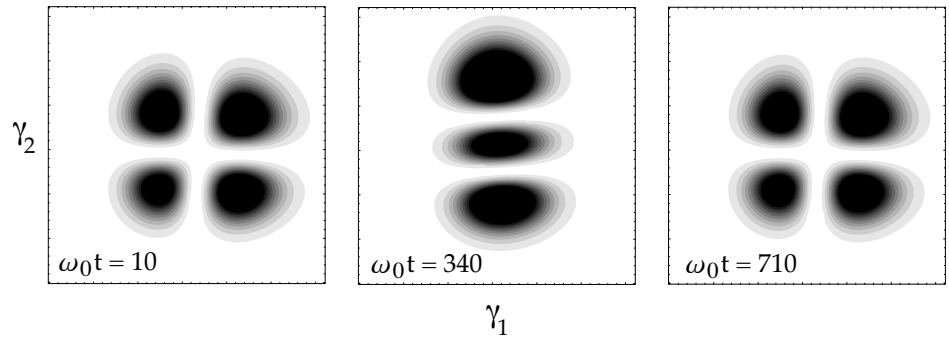

Figure 6.7: Wave function (modulus squared) evolving from $|4, \epsilon_A) \simeq |11, \epsilon_A\rangle$ to $|02, \epsilon_B\rangle$ and back.

6.2.2 Swap Gate

The swap gate involves ramping the system to $\epsilon_B = 0$ instead of $\epsilon_B = \epsilon_-$. When ramping the system to $\epsilon_B = 0$, we encounter two simultaneous evolutions. The first is two-state dynamics of $|11, 0\rangle$ with the auxiliary state $2^{-1/2}(|02, 0\rangle + |20, 0\rangle)$, the second is the swapping of state $|01, 0\rangle$ with $|10, 0\rangle$. The first evolution is handled as with the phase gate, while for the second we allow an arbitrary swap of the states. We recall that the full swap gate is

$$U_{\text{SWAP}} = \begin{pmatrix} 1 & 0 & 0 & 0 \\ 0 & 0 & 1 & 0 \\ 0 & 1 & 0 & 0 \\ 0 & 0 & 0 & 1 \end{pmatrix}. \tag{6.56}$$

A gate very similar to U_{SWAP} will be constructed in this section.

Note that U_{SWAP} is a particularly useful interaction, as it allows information to be passed through the quantum computer without moving the physical qubits. That is, suppose we have prepared the superposition state $a|0\rangle + b|1\rangle$ in qubit 1,

and qubit 2 is in state $|0\rangle$. Applying the swap gate we find

$$U_{\rm SWAP}(a|0\rangle + b|1\rangle)|0\rangle = |0\rangle(a|0\rangle + b|1\rangle). \tag{6.57}$$

The information in qubit 1 is now in qubit 2. Unfortunately, when swapping information over large distances any errors in the swap gates will inevitably build up. More sophisticated information transfer techniques must then be considered. One method is to simply have a dedicated set of "bus" qubits, used only to propagate information, and equiped with an error correction mechanism. Another method is to use a sequence of two-qubit measurements to prepare entanglement between distant qubits [287]. This entanglement can then be purified [288] and used to teleport states across the computer [26]. For small computers, however, the use of swap gates will probably be more practical.

We first consider the evolution of the state $|11,0\rangle$, which is the superposition of the fifth and third energy eigenstates (6.38)

$$|11,0\rangle = \cos\theta|5,0) - \sin\theta|3,0) \tag{6.58}$$

with θ defined in (6.39). If this state is prepared and subsequently evolved with $\epsilon = 0$ held fixed, we have

$$\begin{aligned} e^{-iH(0)t}|11;0\rangle &= \cos\theta e^{-iE_5(0)t}|5;0) - \sin\theta e^{-iE_3(0)t}|3;0) \\ &= e^{-i\phi_{11}}[\cos(\Omega t) - i\cos(2\theta)\sin(\Omega t)]|11;0\rangle \\ &\quad -ie^{-i\phi_{11}}\sin(2\theta)\sin(\Omega t)2^{-1/2}(|02;0\rangle + |20;0\rangle), \end{aligned} \tag{6.59}$$

where

$$\begin{aligned} \phi_{11} &= (E_5(0) + E_3(0))t/2, \\ \Omega &= (E_5(0) - E_3(0))/2. \end{aligned} \tag{6.60}$$

As with the phase gate, we can minimize the auxiliary state amplitude by choosing

an appropriate interaction time

$$\tau_I = \frac{\pi k}{\Omega} = \frac{2\pi k}{E_5(0) - E_3(0)}, \tag{6.61}$$

with k an integer.

Along with this dynamics is the swap of states $|01;0\rangle$ and $|10;0\rangle$. Using their decomposition in (6.31)

$$\begin{array}{ll} |01;0\rangle & = 2^{-1/2}(|1;0\rangle + |2;0\rangle), \\ |10;0\rangle & = 2^{-1/2}(|2;0\rangle - |1;0\rangle), \end{array} \tag{6.62}$$

we find

$$\begin{array}{ll} e^{-iH(0)\tau_I}|01;0\rangle & = e^{-i\phi_{01}}(\cos\theta_1|01;0\rangle - i\sin\theta_1|10;0\rangle), \\ e^{-iH(0)\tau_I}|10;0\rangle & = e^{-i\phi_{10}}(\cos\theta_1|10;0\rangle - i\sin\theta_1|01;0\rangle), \end{array} \tag{6.63}$$

with

$$\begin{array}{ll} \phi_{01} & = \phi_{10} = (E_1(0) + E_2(0))\tau_I/2, \\ \theta_1 & = (E_2(0) - E_1(0))\tau_I/2. \end{array} \tag{6.64}$$

Altogether, with the ground state phase $\phi_{00} = E_0(0)\tau_I$, we find the following for the two-qubit evolution operator

$$e^{-iH(0)\tau_I} = \begin{pmatrix} e^{-i\phi_{00}} & 0 & 0 & 0 \\ 0 & e^{-i\phi_{01}}\cos\theta_1 & -ie^{-i\phi_{01}}\sin\theta_1 & 0 \\ 0 & -ie^{-i\phi_{10}}\sin\theta_1 & e^{-i\phi_{10}}\cos\theta_1 & 0 \\ 0 & 0 & 0 & (-1)^k e^{-i\phi_{11}} \end{pmatrix}. \tag{6.65}$$

This gate has both two-qubit and single-qubit components, which we can again separate using (6.49) by defining

$$U_2 = e^{i\alpha_1}\left(R_z(\alpha_2)\otimes R_z(\alpha_3)\right)e^{-iH(\epsilon_-)\tau_I}, \tag{6.66}$$

with

$$\begin{array}{ll} \alpha_1 & = (\phi_{01} + \phi_{10})/2, \\ \alpha_2 & = (\phi_{10} - \phi_{00}), \\ \alpha_3 & = (\phi_{01} - \phi_{00}). \end{array} \tag{6.67}$$

We find

$$U_2(\theta_1, \theta_2) = \begin{pmatrix} 1 & 0 & 0 & 0 \\ 0 & \cos\theta_1 & -i\sin\theta_1 & 0 \\ 0 & -i\sin\theta_1 & \cos\theta_1 & 0 \\ 0 & 0 & 0 & e^{-i\theta_2} \end{pmatrix} \tag{6.68}$$

where θ_2 is a remaining controlled phase,

$$\theta_2 = \pm k\pi + \phi_{11} - \phi_{01} - \phi_{10} + \phi_{00}. \tag{6.69}$$

For a general swap angle θ_1 and controlled phase θ_2 this gate is universal [18]. For $\theta_1 = \pi/4$ we can use this gate to dynamically prepare the maximally entangled states $2^{-1/2}(|01;0\rangle \pm i|10;0\rangle)$. By tuning the dynamics such that $\theta_1 = \pi/2$, we can construct a swap-like gate.

To perform such fine-tuning, we observe that the condition $\theta_1 = \pi/2$ actually places a condition on the energy levels

$$\theta_1 = \frac{\pi}{2} = \pi k \left(\frac{E_2(0) - E_1(0)}{E_5(0) - E_3(0)} \right). \tag{6.70}$$

Thus, only if the energy ratio R_E

$$R_E = \frac{E_5(0) - E_3(0)}{E_2(0) - E_1(0)} \tag{6.71}$$

is equal to an even integer ($R_E = 2k$) can the swap dynamics be synchronized with the two-state oscillations of $|11,0\rangle$. The only remaining freedom in the energy levels is through N_s. Therefore we plot R as a function of N_s in Fig. 6.8. As shown in the figure, we have $R_E = 4$ when $N_s = 5.1592$.

We simulate the full dynamics using split-operator methods and the numerically computed complex scaling eigenfunctions. We use $\zeta = 0.01$, $N_s = 5.1592$, $\epsilon_A = -0.1$, $\epsilon_B = 0$, $\tau_R = 20\pi$ and $\tau_I = 278$. The results are displayed in Fig. 6.9. In

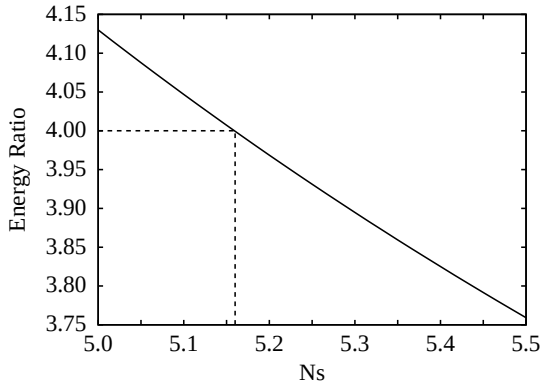

Figure 6.8: Energy ratio R as function of N_s. For $N_s = 5.1592$, we have $R_E = 4$.

Fig. 6.9(a), we show the time-dependence of the ground state population $p_{0;0}(t)$ of state $|0, \epsilon_A)$ and the cosine ramp from ϵ_A to ϵ_B and back. In Fig. 6.9(b) we show the population of $|1, \epsilon_A)$ and $|2, \epsilon_A)$ as a function of time, when the initial condition is $|1, \epsilon_A) \simeq |10, \epsilon_A)$. We observe a nearly complete swap to $|01, \epsilon_A)$. Similarly, we see in Fig. 6.9(c), the populations of $|1, \epsilon_A)$ and $|2, \epsilon_A)$ as a function of time when the initial condition is $|2, \epsilon_A) \simeq |01, \epsilon_A)$, and that no swap occurs in the other states.

Finally, the populations of states $|4, \epsilon_A)$ and $|5, \epsilon_A)$ are shown in Fig. 6.9(d), when the initial condition is $|4, \epsilon_A) \simeq |11, \epsilon_A)$. There are two oscillations since we have $k = 2$ for the full swap. The wave function for the swap of $|10; \epsilon_A)$ to $|01; \epsilon_A)$ is shown in Fig. 6.10.

6.2.3 Gate Fidelity

To evaluate the success of these two-qubit operations, we consider the following scenario. We are given a two-qubit gate V meant to approximate the ideal two-qubit gate W, and allow V to act on an input state $|\Psi\rangle$. We then perform a test to

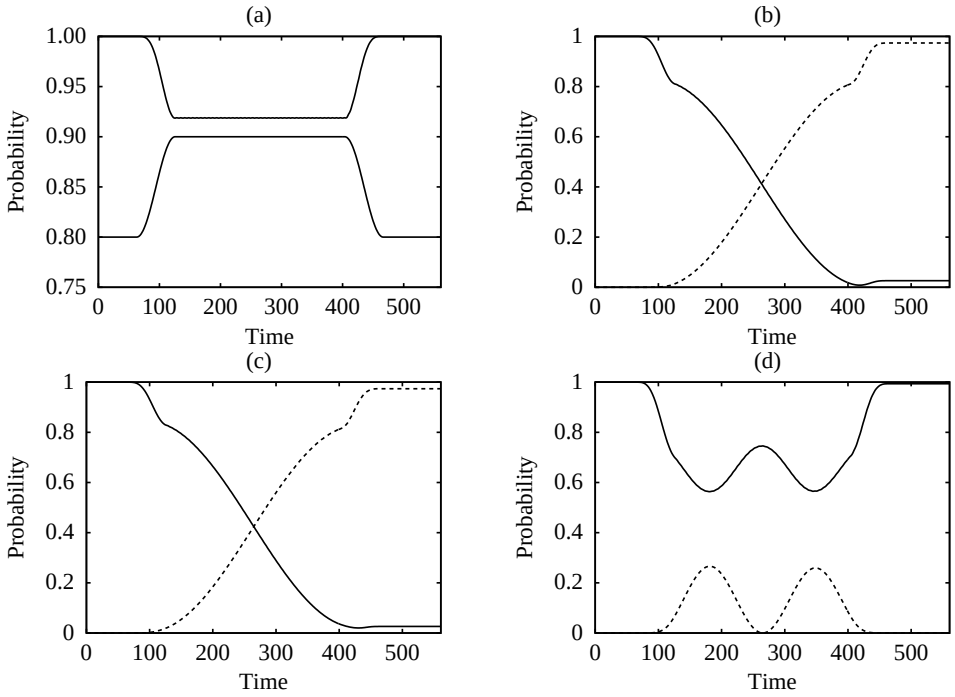

Figure 6.9: Swap Gate with $N_s = 5.1592$, $\zeta = 0.01$, $\epsilon_A = -0.1$, $\epsilon_B = 0$, $\tau_R = 20\pi$, and $\tau_I = 278$. (a) The state populations $p_{0;0}(t)$ (upper solid) and the displaced ramp function $\epsilon(t) + 0.9$ (lower solid). (b) The state populations $p_{1;1}(t)$ (solid) and $p_{2;1}(t)$ (dashed). (c) The state populations $p_{2;2}(t)$ (solid) and $p_{1;2}(t)$ (dashed). (d) The state populations $p_{4;4}(t)$ (solid) and $p_{5;4}(t)$ (dashed).

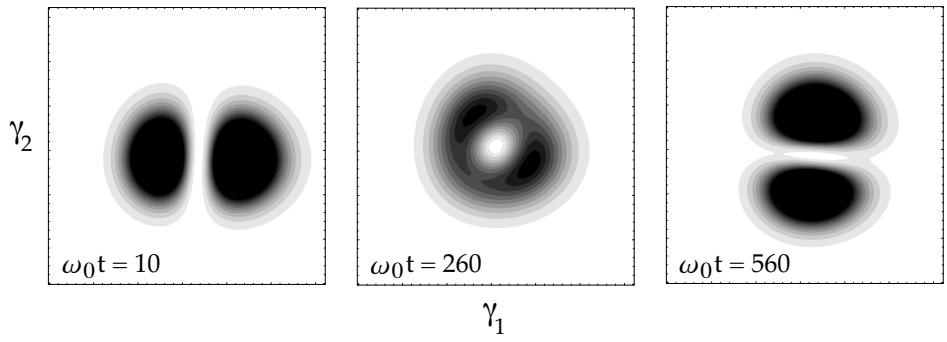

Figure 6.10: Wave function (modulus squared) evolving from $|1, \epsilon_A) \simeq |10, \epsilon_A\rangle$ to $|2, \epsilon_A) \simeq |01, \epsilon_A\rangle$.

determine if the final state $V|\Psi\rangle$ is the intended state $W|\Psi\rangle$. The probability that $V|\Psi\rangle$ passes the test is the fidelity

$$F_{\Psi}(V,W) = |\langle\Psi|W^{\dagger}V|\Psi\rangle|^2. \tag{6.72}$$

This fidelity depends on both the gates V and W and the input state $|\Psi\rangle$. We can remove this state dependence by averaging over a large number N of input states, which defines the average gate fidelity

$$\bar{F}(V,W) = \frac{1}{N}\sum_{k=1}^{N} |\langle\Psi_k|W^{\dagger}V|\Psi_k\rangle|^2. \tag{6.73}$$

This measure will accurately reflect the success of our quantum logic operations. A simple formula for this fidelity was found by Nielsen [289]. He showed that the average over the input states (using the Haar measure) can be expressed as a sum over a unitary operator basis. That is, choose a set of d^2 unitary operators U_j for the general d-dimensional Hilbert space, which are orthogonal in the sense

$$\mathrm{tr}(U_j^{\dagger}U_k) = d\delta_{jk} \tag{6.74}$$

Using such a basis the average gate fidelity can be written

$$\bar{F}(V,W) = \frac{\sum_j \mathrm{tr}\left(WU_j^{\dagger}W^{\dagger}VU_jV^{\dagger}\right) + d^2}{d^2(d+1)}. \tag{6.75}$$

For the two-qubit system $d = 4$ and the unitary operator basis set can be taken as

$$\begin{array}{cccc} \{I\otimes I, & I\otimes X, & I\otimes Y, & I\otimes Z, \\ X\otimes I, & X\otimes X, & X\otimes Y, & X\otimes Z, \\ Y\otimes I, & Y\otimes X, & Y\otimes Y, & Y\otimes Z, \\ Z\otimes I, & Z\otimes X, & Z\otimes Y, & Z\otimes Z\}, \end{array} \tag{6.76}$$

where I, X, Y, and Z are the Pauli operators

$$I = \begin{pmatrix} 1 & 0 \\ 0 & 1 \end{pmatrix}, \tag{6.77}$$

$$X = \begin{pmatrix} 0 & 1 \\ 1 & 0 \end{pmatrix}, \tag{6.78}$$

$$Y = \begin{pmatrix} 0 & -i \\ i & 0 \end{pmatrix}, \tag{6.79}$$

$$Z = \begin{pmatrix} 1 & 0 \\ 0 & -1 \end{pmatrix}. \tag{6.80}$$

The numerical calculations for our phase and swap gates necessarily include states outside of the two-qubit basis. We define the evolution matrix V by

$$V_{jk} = \langle \Psi_j | U | \Psi_k \rangle \tag{6.81}$$

where U is the time-evolution operator

$$U(t,0) = T \exp\left(-i \int_0^t ds H(s)/\hbar \right), \tag{6.82}$$

and the indices in (6.81) refer to the four two-qubit states, e.g. $|00\rangle$, $|01\rangle$, $|10\rangle$, and $|11\rangle$. Since the system may evolve outside of the two-qubit basis, the matrix V is not necessarily unitary. The leakage probability L [290] quantifies this non-unitarity:

$$L = \max_{\Psi} (1 - \langle \Psi | V^\dagger V | \Psi \rangle). \tag{6.83}$$

We observe that L is the maximum eigenvalue of $I - V^\dagger V$.

Before calculating the gate fidelity, we remove the single-qubit phases with (6.49), and set $W = U_1(\pi)$ for the phase gate, and $W = U_2(\pi/2, \pi/4)$ for the swap gate. Using the basis (6.76) in (6.75) we calculate the average gate fidelity $\bar{F}$ and the leakage L in Table 6.1. Also shown is the total gate time $\tau_G = \tau_I + 2\tau_R$ in dimensionless units (ω_0^{-1}), and in physical units with $\omega_0/2\pi = 6$ GHz. Note that gate times are of order 10 ns, which is similar to what we found for the single-qubit π-pulse using the Gaussian pulse shape in Chapter 5. Remarkably, this indicates

Table 6.1: Fidelity Measures of Phase and Swap Gates

Gate	F	L	τ_G	$t_G = \tau_G/\omega_0$
U_1	0.996	0.003	560	14.9 ns
U_2	0.972	0.006	404	10.7 ns

that even for the weak coupling considered here ($\zeta = 0.01$), the two-qubit coupled logic gates are as fast if not faster than the single qubit operations.

6.3 Optimized Results

The ramps used to generate the above results have not been optimized to produce the best fidelity, minimal leakage, or speed. To optimize the above quantum logic gates, we first identify the relevant errors. We recall that there is residual entanglement in the eigenstates. We have in fact ignored this by using as the two-qubit basis the eigenstates at $\epsilon_A = -0.1$. These errors will only be important during measurement since the dynamical evolution can be considered with respect to any basis. As previously mentioned, the "dressed qubit" protocols of [286] can correct for these errors.

The most important remaining errors are the leakage from the two-qubit basis to the auxiliary levels. Although the general ramp sequence cannot be adjusted, our schematic interference method can still be optimized by adjusting the ramp profile. Another source of error is that the higher energy levels have higher tunneling rates. For the phase gate, we can estimate the error due to tunneling by $p_T \sim \Gamma_2 \tau_G/2$. Since the gate time is of order $2^{1/2}\pi\zeta^{-1}$, and $\Gamma_2 = 2^{-3/2}\pi^{-1/2}(432N_s)^{5/2}e^{-36N_s/5}$, we

have

$$p_T \sim \frac{\sqrt{\pi}}{4}\zeta^{-1}(432N_s)^{5/2}e^{-36N_s/5}. \tag{6.84}$$

With $N_s = 4$ and $\zeta = 0.01$ we find $p_T \sim 10^{-3}$; for $N_s = 5$ we find $p_T \sim 10^{-6}$. By choosing a large enough N_s the error due to tunneling can be made sufficiently small for quantum error correction [291].

6.3.1 Phase Gate Optimization

To explore these optimizations we first consider the phase gate with $N_s = 5$. We look at the final state probability $p_F = p_{4;4}(\tau_F)$ in state $|4;\epsilon_A) \simeq |11;\epsilon_A\rangle$. We evolve this state using the split-operator methods and a linear ramp for various ramp and interaction times τ_R and τ_I. The linear ramp has the functional form

$$\epsilon_C(t) = \left\{ \begin{array}{ll} \epsilon_A & t < t_0 \\ \epsilon_A + (\epsilon_B - \epsilon_A)(t-t_0)/(t_1-t_0) & t_0 < t < t_1 \\ \epsilon_B & t_1 < t < t_2 \\ \epsilon_B + (\epsilon_A - \epsilon_B)(t-t_2)/(t_3-t_2) & t_2 < t < t_3 \\ \epsilon_A & t_3 < t \end{array} \right\}, \tag{6.85}$$

where $\tau_R = t_1 - t_0 = t_3 - t_2$ and $\tau_I = t_2 - t_1$.

The results are shown in the contour plot of Fig. 6.11. The dark regions indicate large p_F, while the light regions have small p_F. We see that the ramp and interaction times are correlated. This is expected, since a longer ramp allows the two-state dynamics to begin before the ramp has completed, in which case a smaller interaction time is necessary. The optimized total gate time $\tau_I + 2\tau_R$ remains nearly constant. We find that the maximum state probability for the linear ramp is $p_{F,max} = 0.9995$.

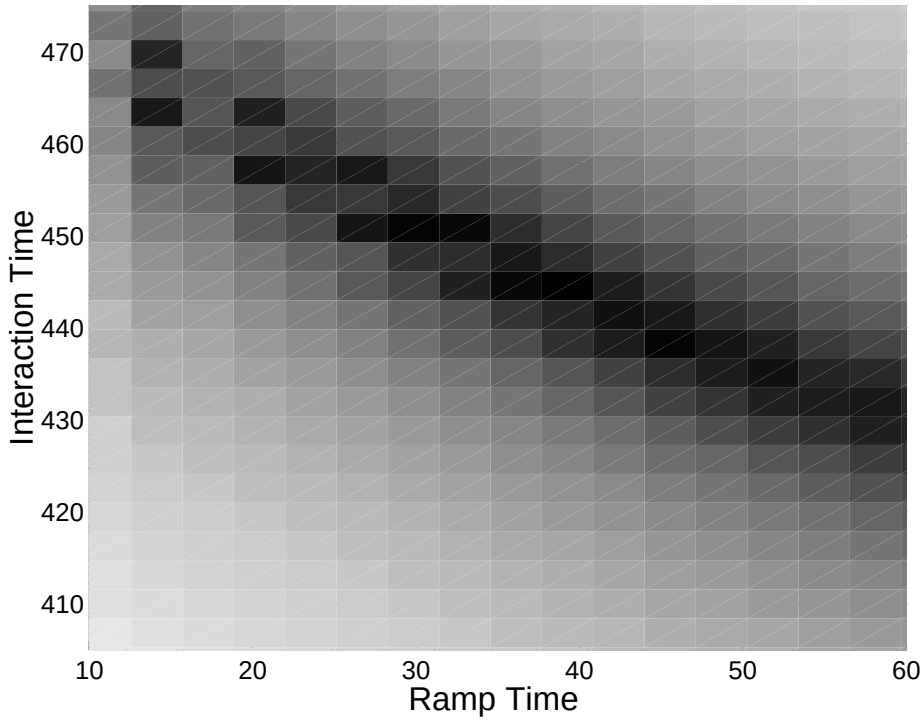

Figure 6.11: Phase gate optimization with linear ramp and $\zeta = 0.01$ and $N_s = 5$. The final state probability p_F is shown in the contour plot, with dark indicating large p_F (near unity). The maximum $p_F = 0.9995$ is found for a ramp time $\tau_R = 12\pi$ and an interaction time $\tau_I = 141\pi$.

Results for cosine and Gaussian ramps are shown in Figs. 6.12 and 6.13, respectively. The cosine ramp has been introduced before (6.55), while the Gaussian ramp has the functional form

$$\epsilon_G(t) = \epsilon_A + \frac{1}{2}(\epsilon_B - \epsilon_A)\left(\mathrm{erf}(\alpha(t-t_1)/\tau_R) + \mathrm{erf}(\alpha(t_2-t)/\tau_R)\right), \tag{6.86}$$

where $t_2 - t_1 = \tau_I + \tau_R$, and we have used $\alpha = 4$. These ramps perform slightly better than the linear ramp, each having a maximal probability $p_{F,max} = 0.9999$. A plot of the final probability with fixed interaction time $\tau_I = 142\pi$ for the cosine ramp is shown in Fig. 6.14. Observe that using the optimal ramp time will make the gate relatively insensitive to errors in the ramp time.

6.3.2 Swap Gate Optimization

A similar analysis applies to the swap gate. Note however, that there are two time scales, one for the swap of $|01;0\rangle$ and $|10;0\rangle$, and one for the evolution of $|11;0\rangle$ with the auxiliary states. While we heuristically argued that these time scales will synchronize for $N_s \simeq 5.16$, our numerical results show that for real ramp profiles this condition fails. Therefore, we focus on the swap operation alone.

Using the Gaussian ramp we evolve the state $|1;\epsilon_A) \simeq |10;\epsilon_A\rangle$, and consider the final swap probability p_S to be in state $|2;\epsilon_A) \simeq |01;\epsilon_A\rangle$, for various ramp and interaction times τ_R and τ_I. The results are shown, with $N_s = 5$, in the contour plot of Fig. 6.15. The dark regions indicate large p_S, while the light regions have small p_S. Surprisingly, there is a much more asymmetric shape than the phase gate. This is clearly seen in Fig. 6.16, where the final probability is shown with $\tau_I = 99\pi$. For

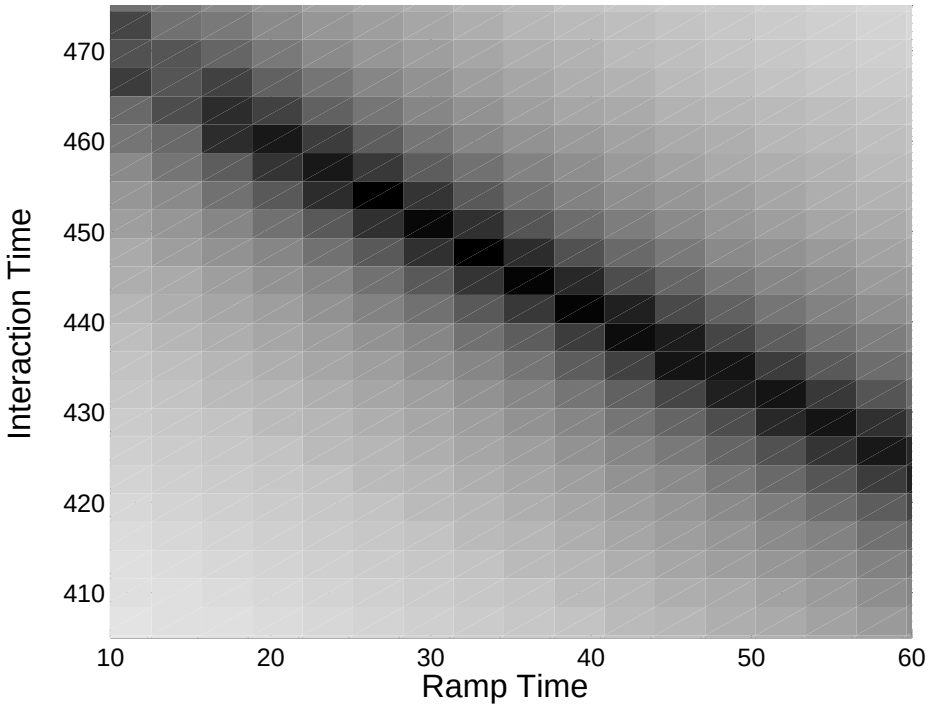

Figure 6.12: Phase gate optimization with cosine ramp and $\zeta = 0.01$ and $N_s = 5$. The final state probability p_F is shown in the contour plot, with dark indicating large p_F (near unity). The maximum $p_F = 0.9999$ is found for a ramp time $\tau_R = 10\pi$ and an interaction time $\tau_I = 142\pi$.

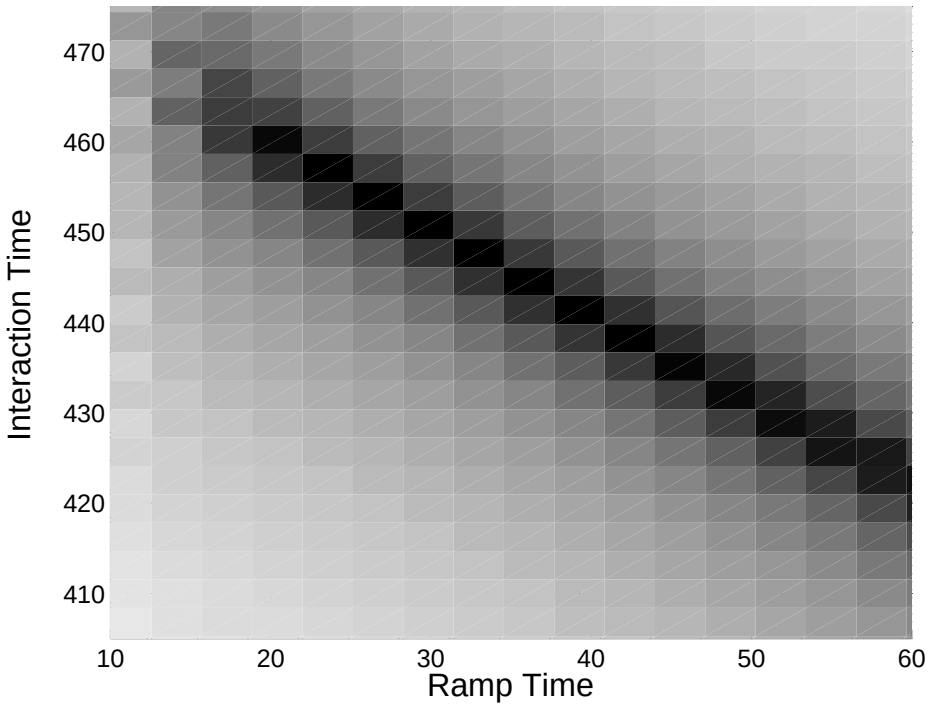

Figure 6.13: Phase gate optimization with Gaussian ramp and $\zeta = 0.01$ and $N_s = 5$. The final state probability p_F is shown in the contour plot, with dark indicating large p_F (near unity). The maximum $p_F = 0.9999$ is found for a ramp time $\tau_R = 11\pi$ and an interaction time $\tau_I = 141\pi$.

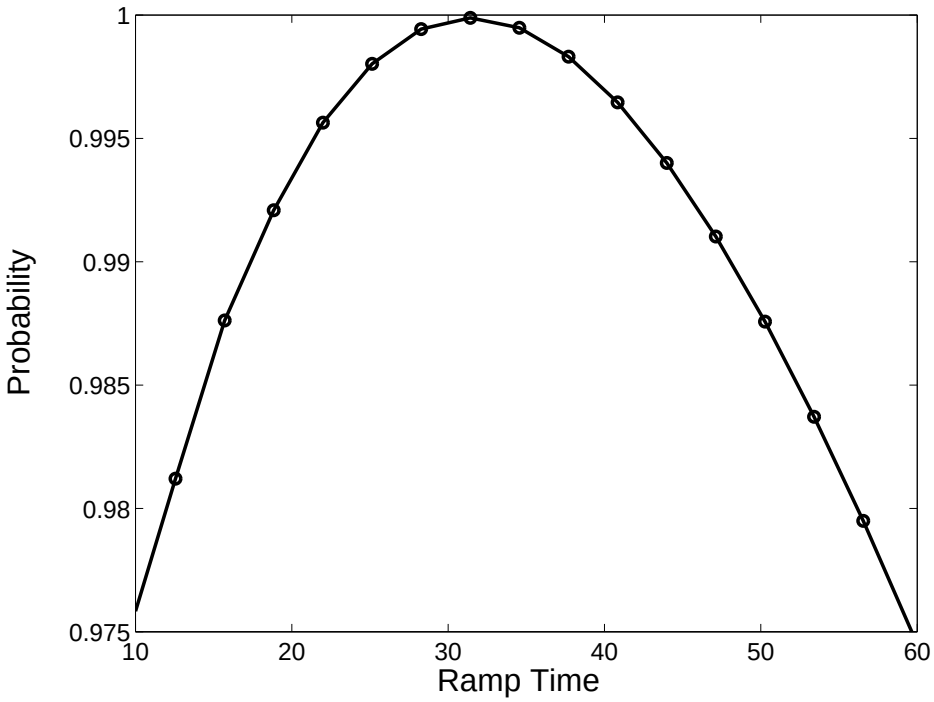

Figure 6.14: Phase gate optimization with cosine ramp and $\zeta = 0.01$, $N_s = 5$, and $\tau_I = 142\pi$. The final state probability p_F is shown; the maximum $p_F = 0.9999$ occurs for the ramp time $\tau_R = 10\pi$.

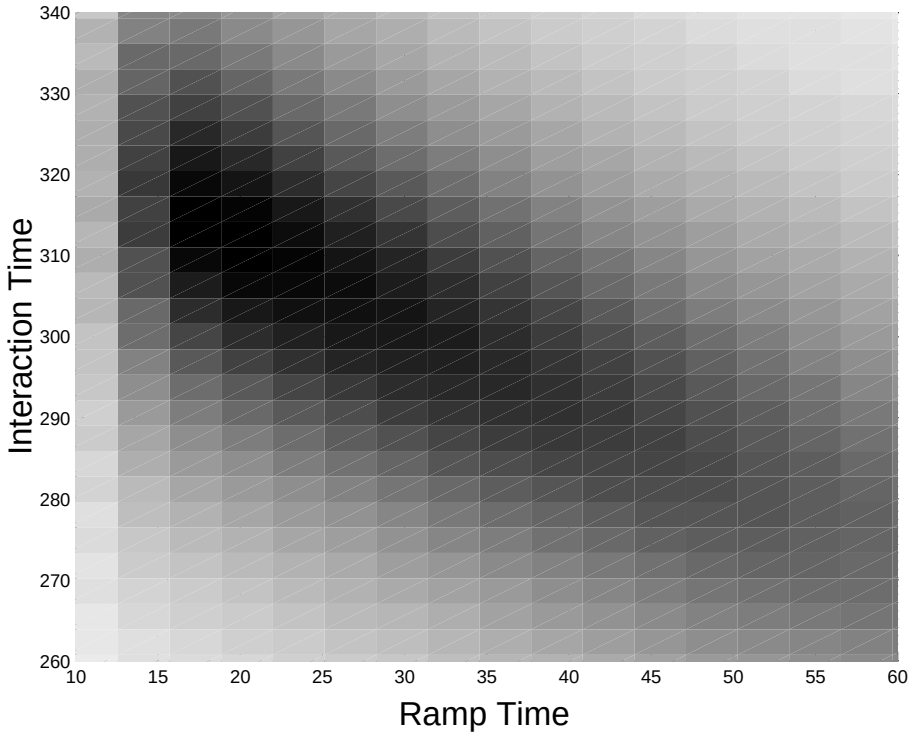

Figure 6.15: Swap gate optimization with Gaussian ramp and $\zeta = 0.01$ and $N_s = 5$. The final swap probability p_S is shown in the contour plot, with dark indicating large p_S (near unity). The maximum $p_S = 0.992$ is found for a ramp time $\tau_R = 6\pi$ and an interaction time $\tau_I = 99\pi$.

these parameters the maximal swap probability is $p_{S,max} = 0.992$.

There does not seem to be a simple explanation for the differences between Fig. 6.16 and Fig. 6.14. Nevertheless, we see that we can enhance the accuracy of both the phase and swap gates by increasing N_s and optimizing the ramp profile. Further gains in accuracy should be possible by decreasing the coupling strength [255], but at the cost of longer gate times. Finally, by combining microwave-pulse Rabi oscillations with the bias current ramps used here we may be able to further

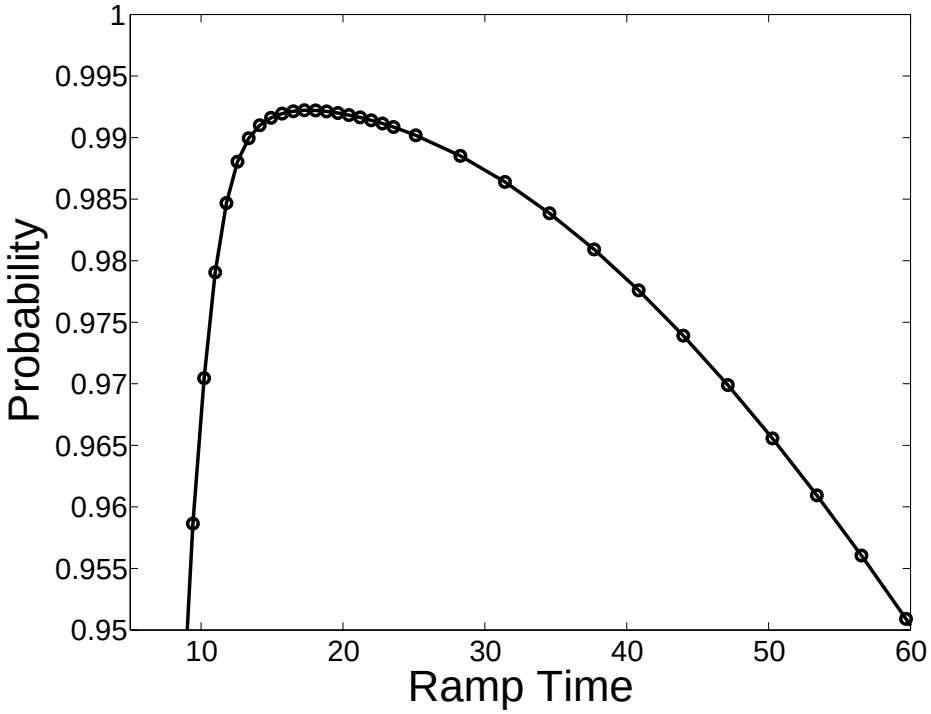

Figure 6.16: Swap gate optimization with Gaussian ramp and $\zeta = 0.01$, $N_s = 5$, and $\tau_I = 99\pi$. The final swap probability p_S is shown; the maximum $p_S = 0.992$ occurs for the ramp time $\tau_R = 6\pi$.

increase the gate fidelities.

Chapter 7

Resonant Coupling of Phase Qubits

The quantum logic gates presented in Chapter 6 use a fixed capacitive interaction between the qubits. As a consequence, the qubits must have either widely separated energy levels or small coupling to remain decoupled during idle periods in the computer. It is therefore desirable to consider coupling schemes that can switch the coupling of distant qubits on and off. More sophisticated coupling schemes would also make it easier to scale up from one or two qubits to the large number of qubits ultimately required for key applications such as factorization [4], quantum simulation [40], and database search [292]. Finally, the next key experimental challenge for the scaling of superconducting qubits is to produce the multiparticle entangled states needed for error correction [293] and teleportation [26], preferably in a device that controllably couples distant qubits.

A number of coupling schemes have been considered for superconducting qubits.

One important class is that based on inductor-capacitor (LC) oscillators. The first such proposal [294] used the ground state dynamics of the oscillator to mediate interactions between charge qubits; this design was refined in [295]. This second-order interaction only produces virtual excitations of the LC degree of freedom. The direct excitation of the oscillator was first discussed in [6], and yields an architecture that is very similar to the ion-trap quantum computer [282], where the oscillator is the center of mass mode of the linear ion chain. The qubit's quantum state can be transferred to the oscillator, which then interacts with other qubits, and is finally transferred back. This type of resonant coupling method for superconducting qubits has now been considered for coupling charge qubits [276] and flux qubits [296] with an LC oscillator, charge qubits coupled by a current-biased junction [254], and phase qubits coupled by nanomechanical [255] oscillators. For superconducting phase qubits, the relevant dynamical operations are precisely those considered previously in Chapter 6 [37].

A new approach to the scaling of superconducting qubits [297] utilizes an analogy to the strong-coupling regime of atomic cavity-QED experiments [298]. This analogy was recently realized in an elegant experiment [299], in which a single Cooper-pair box qubit (the atom) was capacitively coupled to a superconducting transmission line (the cavity). The sub-μm sized charge qubit was first characterized by measurements of the resonator in the dispersive regime. This was followed by the observation of the resonant vacuum Rabi splitting, a spectroscopic indication of entanglement between the charge qubit and a single photon in the resonator. In a related experiment, the coherent dynamics of a flux qubit coupled to an associated

SQUID detector has been observed [300].

In this Chapter, we present the theory for experimental results that extend this new field of superconducting cavity-QED to three macroscopic qubits—two Josephson junctions and a resonator, the analog of two atoms and a cavity. Figure 1 shows a circuit schematic of our system, which consists of two large ($10\mu\text{m} \times 10\mu\text{m}$) Josephson-junction phase qubits connected together by a series inductor-capacitor (LC) resonator. This system is distinct from atomic cavity-QED systems in that our "atoms" are distinguishable and independently tunable. This experiment is the first to demonstrate the method of resonant coupling.

In Section 2, we analyze the circuit in Fig. 1 and its Hamiltonian. In Section 3, we describe the spectroscopic measurements used to study the coupling of each junction to the LC oscillator, and the coupling of *all three* degrees of freedom together. The spectroscopic evidence is found to be in clear agreement with the quantum mechanical model. These measurements were performed by Huizhong Xu [11], and have been reported in [301]. We performed the theoretical calculations using the complex scaling methods described in Chapter 3. In Section 4, we derive the harmonic approximation used to understand the quantum states. In Section 5, we show how this resonant coupling reduces to capacitive coupling for certain junction frequencies. This important result explains how our original "two-qubit" spectroscopic measurements [269] can be reconciled with our new, more complete, model of the circuit that has three degrees of freedom.

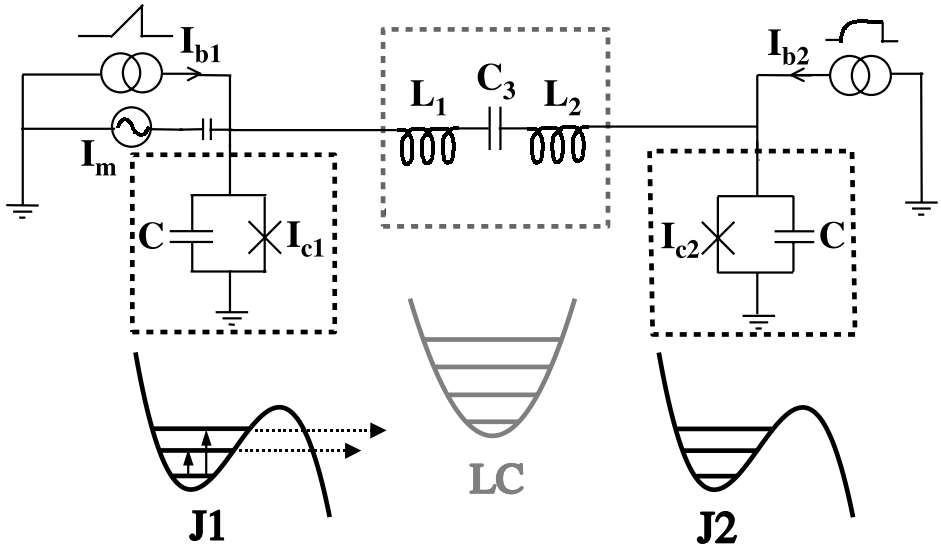

Figure 7.1: Schematic of a macroscopic superconducting three-body system which consists of two Josephson junctions and an LC resonator. The two junctions J1 and J2 (in the left and right dashed boxes) have anharmonic potentials with unequal energy level spacings (shown below). The horizontal arrows represent quantum tunneling and the vertical arrows denote microwave-induced transitions. The LC oscillator (in the center dashed box) has a harmonic well with equal energy level spacings.

7.1 Hamiltonian

The three degrees of freedom for the circuit in Fig. 7.1 are the macroscopic quantum variables γ_1 and γ_2 (the gauge-invariant phase differences across junctions J1 and J2, respectively), and $\gamma_3 = 2\pi LI/\Phi_0$ corresponding to the current I flowing through the total inductance $L = L_1 + L_2$. Each degree of freedom corresponds to distinct coherent motions of billions of electron pairs, and is therefore macroscopic both in size and number [79].

The equations of motion for this system can be found directly by applying Kirchoff's circuit laws. First, we demand the conservation of current at each node:

$$\begin{array}{ll} I_{b1} & = I_{c1}\sin\gamma_1 + C_1\dot{V}_1 + I, \\ I_{b2} & = I_{c2}\sin\gamma_2 + C_2\dot{V}_2 - I, \\ I & = C_3\dot{V}_3, \end{array} \tag{7.1}$$

where we have used Josephson's current law in the first two lines. Second, we apply the voltage loop equation

$$V_3 = V_1 - V_2 - L\dot{I}. \tag{7.2}$$

In the above, I_{b1} and I_{b2} are the bias currents, I_{c1} and I_{c2} the critical currents of the junctions, with capacitances C_1 and C_2 and voltages V_1 and V_2. The coupling mode has capacitance C_3 and total inductance $L = L_1 + L_2$, with the voltage across the capacitor V_3 and current I. Finally, we have the Josephson voltage relations

$$\begin{array}{ll} V_1 = & (\Phi_0/2\pi)\dot{\gamma}_1, \\ V_2 = & (\Phi_0/2\pi)\dot{\gamma}_2. \end{array} \tag{7.3}$$

Equations (7.1)-(7.3) determine the dynamics of the system.

When constructing the Hamiltonian, we have the freedom to choose either the voltage V_3 or the current I as the "coordinate" of the LC-resonator. The resulting

Hamiltonians may look different, but are simply related by a canonical transformation. We present both derivations, first taking the voltage V_3 as the coordinate to construct Hamiltonian H_1. We then use the coordinate $\gamma_3 = 2\pi LI/\Phi_0$ to construct H_2, and finally show their equivalence. This freedom of representation is well known, and leads to some subtlety when one attempts to introduce dissipation [302].

Combining (7.1)-(7.3) we have the system of second order equations

$$\begin{array}{ll} C_1(\Phi_0/2\pi)\ddot{\gamma}_1 + C_3\dot{V}_3 + I_{c1}\sin\gamma_1 - I_{b1} &= 0, \\ C_2(\Phi_0/2\pi)\ddot{\gamma}_2 - C_3\dot{V}_3 + I_{c2}\sin\gamma_2 - I_{b2} &= 0, \\ LC_3\ddot{V}_3 + V_3 - (\Phi_0/2\pi)(\ddot{\gamma}_1 - \ddot{\gamma}_2) &= 0. \end{array} \tag{7.4}$$

These equations can be derived from the following Lagrangian

$$\begin{array}{ll} \mathcal{L}_1 = & \frac{1}{2}(\Phi_0/2\pi)^2(C_1\dot{\gamma}_1^2 + C_2\dot{\gamma}_2^2) + \frac{1}{2}LC_3^2\dot{V}_3^2 \\ & + C_3V_3(\Phi_0/2\pi)(\dot{\gamma}_1 - \dot{\gamma}_2) - \frac{1}{2}C_cV_c^2 - U_1(\gamma_1) - U_2(\gamma_2) \end{array} \tag{7.5}$$

where

$$\begin{array}{ll} U_1(\gamma_1) &= -(\Phi_0/2\pi)(I_{c1}\cos\gamma_1 + I_{b1}\gamma_1), \\ U_2(\gamma_2) &= -(\Phi_0/2\pi)(I_{c2}\cos\gamma_2 + I_{b2}\gamma_2). \end{array} \tag{7.6}$$

We proceed to construct the Hamiltonian, first defining the canonical momenta

$$\begin{array}{lll} p_1 &= \partial\mathcal{L}_1/\partial\dot{\gamma}_1 &= (\Phi_0/2\pi)^2C_1\dot{\gamma}_1 + (\Phi_0/2\pi)C_3V_3, \\ p_2 &= \partial\mathcal{L}_1/\partial\dot{\gamma}_2 &= (\Phi_0/2\pi)^2C_2\dot{\gamma}_2 - (\Phi_0/2\pi)C_3V_3, \\ \bar{p}_3 &= \partial\mathcal{L}_1/\partial\dot{V}_3 &= LC_3^2\dot{V}_3. \end{array} \tag{7.7}$$

We have used the symbol $\bar{p}_3$ instead of p_3 for future convenience. Inverting (7.7), we find the velocities as functions of the coordinates and momenta

$$\begin{array}{ll} \dot{\gamma}_1 &= (\Phi_0/2\pi)^{-2}C_1^{-1}(p_1 - (\Phi_0/2\pi)C_3V_3), \\ \dot{\gamma}_2 &= (\Phi_0/2\pi)^{-2}C_2^{-1}(p_2 + (\Phi_0/2\pi)C_3V_3), \\ \dot{V}_3 &= L^{-1}C_3^{-2}\bar{p}_3. \end{array} \tag{7.8}$$

The Hamiltonian is defined by

$$H_1 = p_1\dot{\gamma}_1 + p_2\dot{\gamma}_2 + \bar{p}_3\dot{V}_3 - \mathcal{L}_1. \tag{7.9}$$

Substituting (7.8) and (7.5) into (7.9), we find

$$\begin{array}{ll} H_1 = & \frac{1}{2}C_1^{-1}(\Phi_0/2\pi)^{-2}(p_1 - (\Phi_0/2\pi)C_3V_3)^2 \\ & + \frac{1}{2}C_2^{-1}(\Phi_0/2\pi)^{-2}(p_2 + (\Phi_0/2\pi)C_3V_3)^2 \\ & + \frac{1}{2}L^{-1}C_3^{-2}\bar{p}_3^2 + \frac{1}{2}C_3V_3^2 + U_1(\gamma_1) + U_2(\gamma_2). \end{array} \tag{7.10}$$

To recover the physical interpretation of this Hamiltonian as a conserved energy of the system, we rewrite H_1 in terms of the voltages and currents. Using (7.7), (7.3) and (7.1) in (7.10), we find

$$E = \frac{1}{2}C_1V_1^2 + \frac{1}{2}C_2V_2^2 + \frac{1}{2}C_3V_3^2 + \frac{1}{2}LI^2 + U_1(\gamma_1) + U_2(\gamma_2). \tag{7.11}$$

This shows how the electrostatic energy is stored in each capacitor, and the magnetic field energy in each inductor (including the Josephson junctions acting as nonlinear inductors).

Our second derivation uses the coordinate $\gamma_3 = 2\pi LI/\Phi_0$, in terms of which the equations of motion (7.1)-(7.3) can be written

$$\begin{array}{ll} C_1(\Phi_0/2\pi)\ddot{\gamma}_1 - C_3(\Phi_0/2\pi)(\ddot{\gamma}_3 + \ddot{\gamma}_2 - \ddot{\gamma}_1) + I_{c1}\sin\gamma_1 - I_1 &= 0, \\ C_2(\Phi_0/2\pi)\ddot{\gamma}_2 + C_3(\Phi_0/2\pi)(\ddot{\gamma}_3 + \ddot{\gamma}_2 - \ddot{\gamma}_1) + I_{c2}\sin\gamma_2 - I_2 &= 0, \\ C_3(\Phi_0/2\pi)(\ddot{\gamma}_3 + \ddot{\gamma}_2 - \ddot{\gamma}_1) + (\Phi_0/2\pi)L^{-1}\gamma_3 &= 0. \end{array} \tag{7.12}$$

These equations of motion follow from the Lagrangian

$$\begin{array}{ll} \mathcal{L}_2 = & \frac{1}{2}(\Phi_0/2\pi)^2(C_1\dot{\gamma}_1^2 + C_2\dot{\gamma}_2^2) + \frac{1}{2}(\Phi_0/2\pi)^2C_3(\dot{\gamma}_3 + \dot{\gamma}_2 - \dot{\gamma}_1)^2 \\ & -\frac{1}{2}(\Phi_0/2\pi)^2L^{-1}\gamma_3^2 - U_1(\gamma_1) - U_2(\gamma_2) \end{array} \tag{7.13}$$

where U_1 and U_2 are again given by (7.6). Forming the canonical momenta of $\mathcal{L}_2$, we find

$$\begin{array}{lll} p_1 &= \partial\mathcal{L}_2/\partial\dot{\gamma}_1 &= C_1(\Phi_0/2\pi)^2\dot{\gamma}_1 - C_3(\Phi_0/2\pi)^2(\dot{\gamma}_3 + \dot{\gamma}_2 - \dot{\gamma}_1), \\ p_2 &= \partial\mathcal{L}_2/\partial\dot{\gamma}_2 &= C_2(\Phi_0/2\pi)^2\dot{\gamma}_2 + C_3(\Phi_0/2\pi)^2(\dot{\gamma}_3 + \dot{\gamma}_2 - \dot{\gamma}_1), \\ p_3 &= \partial\mathcal{L}_2/\partial\dot{\gamma}_3 &= C_3(\Phi_0/2\pi)^2(\dot{\gamma}_3 + \dot{\gamma}_2 - \dot{\gamma}_1). \end{array} \tag{7.14}$$

Observe that while these momenta seem quite different, by (7.2) the momenta p_1 and p_2 of (7.14) and (7.7) are in fact numerically the same. The momenta p_3 and $\bar{p}_3$, however, are not (hence the choice of notation). In general, the momenta are only defined dynamically by the corresponding Lagrangian or Hamiltonian. Inverting (7.14) we find

$$\begin{array}{ll} \dot{\gamma}_1 &= C_1^{-1}(\Phi_0/2\pi)^{-2}(p_1 + p_3), \\ \dot{\gamma}_2 &= C_2^{-1}(\Phi_0/2\pi)^{-2}(p_2 - p_3), \\ \dot{\gamma}_3 &= (\Phi_0/2\pi)^{-2}(C_1^{-1}p_1 - C_2^{-1}p_2 + (C_3^{-1} + C_2^{-1} + C_1^{-1})p_3). \end{array} \tag{7.15}$$

Using (7.13) and (7.15) and the definition

$$H_2 = p_1\dot{\gamma_1} + p_2\dot{\gamma_2} + p_3\dot{\gamma_3} - \mathcal{L}_2 \tag{7.16}$$

we find the result

$$\begin{array}{rl} H_2 = & \frac{1}{2}C_1^{-1}(\Phi_0/2\pi)^{-2}(p_1+p_3)^2 + \frac{1}{2}C_2^{-1}(\Phi_0/2\pi)^{-2}(p_2-p_3)^2 \\ & +\frac{1}{2}C_3^{-1}(\Phi_0/2\pi)^{-2}p_3^2 + \frac{1}{2}(\Phi_0/2\pi)^2L^{-1}\gamma_3^2 + U_1(\gamma_1) + U_2(\gamma_2). \end{array} \tag{7.17}$$

How are the two Hamiltonians (7.10) and (7.17) related? They differ only in their treatment of the third degree of freedom: $(V_3, \bar{p}_3)$ or (γ_3, p_3). In fact, the two sets of coordinates are related by the simple canonical transformation

$$\begin{array}{ll} \gamma_3 & = C_3^{-1}(\Phi_0/2\pi)^{-1}\bar{p}_3 \\ p_3 & = -(\Phi_0/2\pi)C_3V_3. \end{array} \tag{7.18}$$

Performing the transformation (7.18) in (7.17) yields (7.10), as expected.

In the following, we consider $C_1 = C_2 = C$, and rewrite (7.17) in the form:

$$\begin{aligned} H = & \overbrace{\frac{p_1^2}{2m} - \frac{\Phi_0}{2\pi}(I_{c1}\cos\gamma_1 + I_{b1}\gamma_1)}^{H_{\mathrm{J1}}} + \overbrace{\frac{p_2^2}{2m} - \frac{\Phi_0}{2\pi}(I_{c2}\cos\gamma_2 + I_{b2}\gamma_2)}^{H_{\mathrm{J2}}} \\ & + \underbrace{\frac{p_3^2}{2m_3} + \frac{1}{2}m_3\omega_3^2\gamma_3^2}_{H_{\mathrm{LC}}} + \underbrace{\xi\frac{p_1p_3}{\sqrt{mm_3}} - \xi\frac{p_2p_3}{\sqrt{mm_3}}}_{H_{coupling}} \end{aligned} \tag{7.19}$$

where p_i $(i = 1, 2, 3)$ are the canonical momenta of the three degrees of freedom with corresponding effective masses of $m_1 = m_2 = m = C(\Phi_0/2\pi)^2$ and $m_3 = (\Phi_0/2\pi)^2C_3C/(C + 2C_3)$. The quantity $\Phi_0 = h/2e$ is the flux quantum, C is the junction capacitance for J1 and J2, C_3 is the capacitance of the LC resonator, I_{c1} and I_{c2} are the junctions' critical currents, I_{b1} and I_{b2} are two steady bias currents, $\omega_3 = 1/\sqrt{LC_3C/(C + 2C_3)}$ is the angular frequency of the LC resonator, and $\xi = \sqrt{C_3/(C + 2C_3)}$ is a dimensionless coupling coefficient.

The first term in H, H_{J1}, is the Hamiltonian for J1 alone. It has dynamics analogous to that of a particle moving in a tilted washboard potential (see Fig. 7.1). Metastable energy states [85, 146] are present in the well and can be observed if the qubit is well isolated. The potential and the level spacings can be controlled by the bias current I_{b1}. The metastable states have zero dc voltage, but can tunnel [81] to continuum states that exhibit a finite dc voltage across the junction. We can probe the states by applying a microwave current I_m that can drive transitions from the ground state to the excited states. These excited states have much higher tunneling rates and thus are easily detected.

The second term, H_{J2}, describes J2, which has dynamics similar to J1 but is independently controlled by its bias current I_{b2}. H_{LC} describes the harmonic oscillator dynamics of the LC resonator (see Fig. 7.1). Finally, $H_{coupling}$ represents the capacitive coupling of each junction to the resonator. Note that the momenta p_i are proportional to the charges stored on each capacitor in the circuit [268], and thus the coupling is electrostatic.

7.2 Experiment

The Josephson junctions used in the experiment are thin-film 10μm $\times$ 10μm Nb /AlOx/ Nb junctions made by Hypres, Inc. on a 5mm $\times$ 5mm silicon chip. The critical currents of the junctions are $\sim 120\mu$A in zero magnetic field, but can be adjusted by applying an external magnetic field. The coupling inductor is a 780μm $\times$ 90μm thin-film niobium loop connecting the two junctions, and the coupling capacitance

consists of two capacitors in series, each formed by $60\mu\text{m} \times 60\mu\text{m}$ parallel niobium films separated by a 200 nm layer of SiO_2. With this geometry we estimate the inductance $L \approx 1.5$ nH and the capacitance $C_3 \approx 0.37$ pF; with $C \approx 4.8$ pF these values give $\omega_3/2\pi \approx 7$ GHz. The chip is mounted inside a Cu box that is attached to the mixing chamber of a dilution refrigerator with a base temperature of about 25 mK. More details on the experimental technique can be found in the Ph.D. of H. Xu [11]. We note that this same chip was previously examined [269] at junction frequencies near 5 GHz, less than $\omega_3/2\pi$ (with $I_{c1} \sim I_{c2} \sim 15\mu$A), where the effect of the LC resonator reduced to purely capacitive coupling. For the higher frequencies considered here ($6 - 10$ GHz with $I_{c1} \sim I_{c2} \sim 22\mu$A), however, its effect should be described by the Hamiltonian in (7.19).

Figure 7.2 shows the spectrum of the system when the bias current I_{b1} for junction J1 is ramped and that for junction J2 is held at $I_{b2} = 0$. The circles denote measured resonance peak positions when microwaves are continuously applied to induce transitions from the ground state to excited states. The dashed lines are from quantum mechanical calculations using the Hamiltonian in (7.19) with the parameters in Fig. 7.1 (obtained by fitting) and $I_{b2} = 0$. The zero-biased junction J2 is effectively decoupled from the rest of the system since it has a much larger energy scale (~ 19 GHz) than both junction J1 and the LC resonator (~ 7 GHz). Therefore, we observe a spectrum essentially due to junction J1 and the LC resonator only. The avoided crossing between the first and second excited states occurs at $I_{b1} \approx 21.12\mu$A. As shown in the next section, states of the form $(|001\rangle \pm |100\rangle)/\sqrt{2}$ are predicted here, where the first, second, and third positions in the ket denote

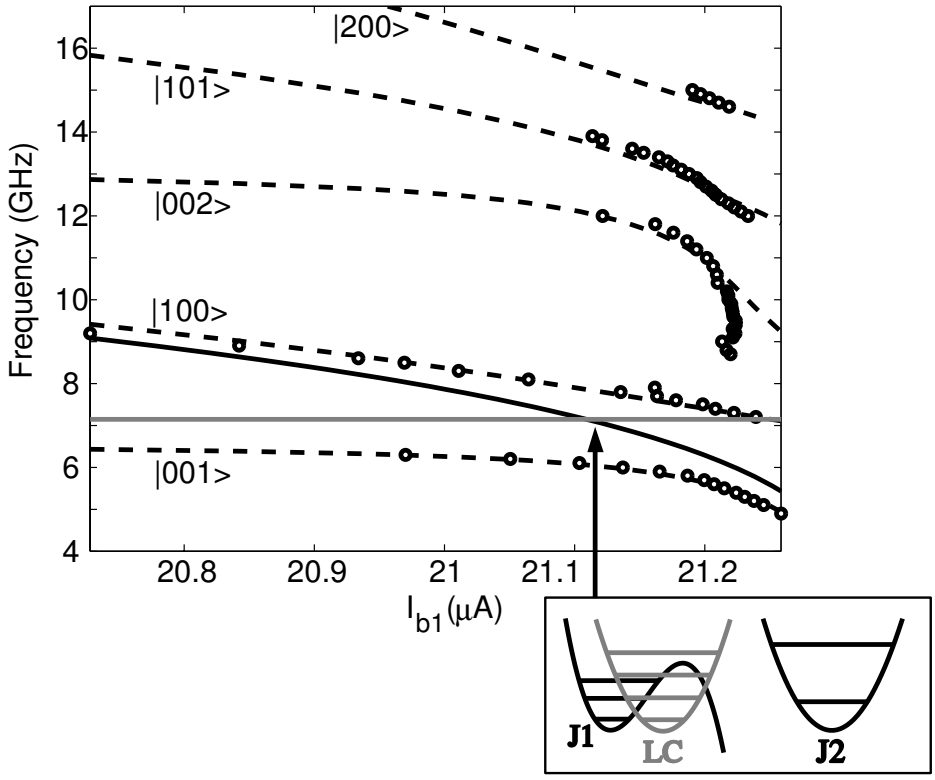

Figure 7.2: Spectrum of the system when the bias current I_{b1} for junction J1 is ramped and $I_{b2} = 0$ for junction J2. Circles are measured microwave resonance positions, dashed black lines are from quantum mechanical calculations using (7.19) with parameters given in Table 7.1 and $I_{b2} = 0$. The solid curves denote uncoupled $|0\rangle$ to $|1\rangle$ level spacings for J1 (black) and the resonator (gray), while that for J2 ($\sim$ 19 GHz) is not shown in the plot. At the degeneracy point $I_{b1} \approx 21.12\mu$A (shown in the lower box), the first two excited states are $(|001\rangle \pm |100\rangle)/\sqrt{2}$, where the state notation is $|$J1, J2, LC$\rangle$. The deviation of the fit for the third excited state is probably due to its large tunnelling rates at high bias currents.

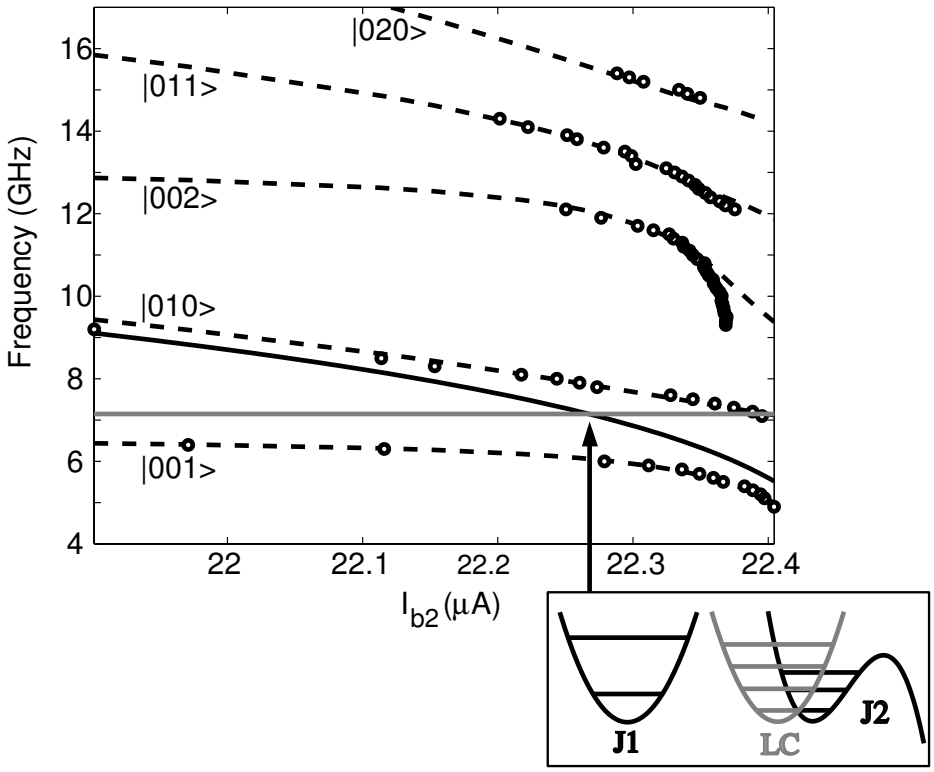

Figure 7.3: Spectrum of the system when the bias current I_{b2} for junction J2 is ramped and $I_{b1} = 0$ for junction J1. Circles are measured microwave resonance positions, dashed black lines are from quantum mechanical calculations using (7.19) with parameters given in Table 7.1 and $I_{b1} = 0$. The solid curves denote uncoupled $|0\rangle$ to $|1\rangle$ level spacings for J2 (black) and the resonator (gray), while that for J1 ($\sim$ 19 GHz) is not shown in the plot. At the degeneracy point $I_{b2} = 22.27\mu$A (shown in the lower box) the first two excited states are $(|001\rangle \pm |010\rangle)/\sqrt{2}$, where the state notation is $|$J1, J2, LC$\rangle$. The deviation of the fit for the third excited state is probably due to its large tunnelling rates at high bias currents.

Table 7.1: Fitting Parameters from Spectroscopic Data

C (pF)	C_3 (pF)	I_{c1} (μA)	I_{c2} (μA)	L (nH)
4.85 ± 0.05	0.33 ± 0.01	21.388 ± 0.003	22.536 ± 0.003	1.70 ± 0.05

the states of J1, J2, and the LC oscillator, respectively. The next three excited states at the degeneracy point are $(|002\rangle + |200\rangle - \sqrt{2}|101\rangle)/2$, $(|002\rangle - |200\rangle)/\sqrt{2}$, and $(|002\rangle + |200\rangle + \sqrt{2}|101\rangle)/2$. We note these states are entangled only between junction J1 and the LC resonator, since junction J2 is frozen in its ground state.

Figure 7.3 shows the measured spectrum for the case of $I_{b1} = 0$ while ramping the bias current for J2. Similarly, comparison with theory reveals the states here describe entanglement between junction J2 and the LC resonator. We find good agreement between data and theoretical calculations using the same parameters as listed in Fig. 7.1 and $I_{b1} = 0$.

The observation of higher order transitions in Figs. 7.2 and 7.3, such as transitions from $|000\rangle$ to states involving $|002\rangle$ (analogous to a two-photon state in cavity-QED) provides strong evidence for the quantum nature of the system. Coupling the LC oscillator to the anharmonic junctions has introduced nonlinearity that allows us to distinguish these quantum transitions from the resonances of a classical harmonic oscillator. We also note that a single set of five parameters, shown in Table 7.1, has been used to fit the ten curves in Figs. 7.2-7.3. The good agreement between data and theory obtained here cannot be achieved by any classical model that includes only three degrees of freedom. Thus by tuning one junction into resonance with the LC resonator, we have observed evidence of entanglement between a single junction

qubit and an LC resonator, analogous to the recent coherent coupling of a single Cooper-pair box to a superconducting transmission line [299].

We next show spectroscopic evidence for entangled states between *two* junction qubits and an LC resonator. Figure 7.4 shows the measured spectrum when J2 is biased at a constant current and the bias current for J1 is ramped. Using the previously determined parameters, we compute the energy levels by adjusting the only remaining parameter $I_{b2} = 22.330\mu$A. That is, all six curves shown in Fig. 7.4 have been fit using just one parameter. The measured I_{b2} is 22.110μA; the discrepancy between this and the fitted value appears to come from the calibration of the current ramp which has overestimated the critical current of junction J2 by 1%. This error is in addition to any systematic error in the assumption $C_1 = C_2 = C$. Nevertheless, Fig. 7.4 shows excellent agreement between theory and experiment and we conclude that the multi-level spectroscopic measurements are clearly well explained by the quantum mechanics of the Hamiltonian given in (7.19).

The lowest three excited states of (7.19) are formed from the subspace spanned by $|100\rangle$, $|010\rangle$ and $|001\rangle$. In our case, $\hbar\omega_2 \approx \hbar\omega_3$, where $\hbar\omega_2$ is the $|0\rangle$ to $|1\rangle$ level spacing for J2. Therefore, for J1 at low bias we expect the first two excited states to be $(|010\rangle \pm |001\rangle)/\sqrt{2}$ with a splitting of $\xi\hbar\omega_3$ (see Fig. 7.4 for $I_{b1} < 21\mu$A). We also note the presence of a triple degeneracy point at $I_{b1} \approx 21.15\mu$A, where the first three excited states make their closest approach. At this bias, the predicted states are $(|100\rangle - |010\rangle - \sqrt{2}|001\rangle)/2$, $(|100\rangle + |010\rangle)/\sqrt{2}$, and $(|100\rangle - |010\rangle + \sqrt{2}|001\rangle)/2$, with corresponding energies of $\hbar\omega_3(1 - \xi/\sqrt{2})$, $\hbar\omega_3$ and $\hbar\omega_3(1 + \xi/\sqrt{2})$. The first and third excited states are entangled states involving the two junctions and the

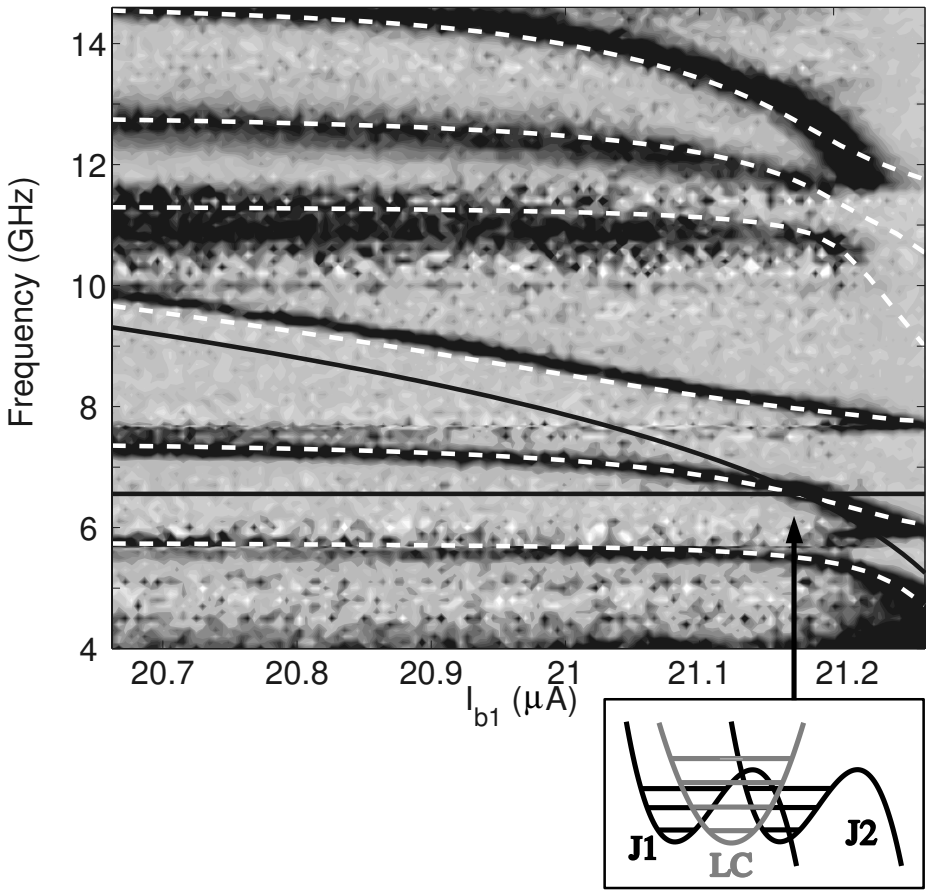

Figure 7.4: Enhancement in escape rate when the bias current I_{b1} for junction J1 is ramped and junction J2 is biased at a constant current of $I_{b2} = 22.330\mu$A. Black corresponds to highest enhancement and light gray to zero enhancement. The white dashed lines are from quantum mechanical calculations using (7.19) with parameters given in Fig. 1 and $I_{b2} = 22.330\mu$A. The solid black lines indicate the uncoupled $|0\rangle$ to $|1\rangle$ level spacings for J1 (curved) and J2 (horizontal), while that for the LC resonator (≈ 7.1 GHz) is not shown in the plot. At the triple degeneracy point $I_{b1} \approx 21.15\mu$A (shown in the lower box), the three lowest excited states are $(|100\rangle - |010\rangle - \sqrt{2}|001\rangle)/2$, $(|100\rangle + |010\rangle)/\sqrt{2}$, and $(|100\rangle - |010\rangle + \sqrt{2}|001\rangle)/2$. The higher energy states are superpositions of the multiply excited states $|200\rangle$, $|020\rangle$, $|002\rangle$, $|110\rangle$, $|101\rangle$ and $|011\rangle$.

LC resonator, while the second excited state corresponds to an in-phase oscillation of the two junctions that does not couple to the resonator. The higher levels shown in Fig. 3 also agree well with our calculations, and correspond to entangled states with multiple excitations in all three degrees of freedom.

7.3 Harmonic Approximation

As previously noted, the Hamiltonian (7.19) describes three coupled degrees of freedom. We wish to show how, in certain regimes, the dynamics can be reduced to two degrees of freedom. We accomplish this in the next section. As a first step we approximate the dynamics by only the harmonic terms in the Hamiltonian. We can then diagonalize this Hamiltonian into its normal modes.

The harmonic oscillator approximation follows by expanding the washboards of $H_{\rm J1}$ and $H_{\rm J2}$ in (7.19) about their minima, keeping only the quadratic terms. We also perform a scaling transformation

$$\begin{aligned} x_1 &= m^{1/2}\omega_1(\gamma_1 - \arcsin(I_1/I_{c1})), \\ p_1 &= m^{-1/2}\omega_1^{-1}p_{1;\rm old}, \\ x_2 &= m^{1/2}\omega_2(\gamma_2 - \arcsin(I_2/I_{c2})), \\ p_2 &= m^{-1/2}\omega_2^{-1}p_{2;\rm old}, \\ x_3 &= m_3^{1/2}\omega_3\gamma_3, \\ p_3 &= m_3^{-1/2}\omega_3^{-1}p_{3;\rm old}, \end{aligned} \tag{7.20}$$

with

$$\begin{aligned} \omega_1 &= \left(\frac{2\pi I_{c1}}{\Phi_0 C}\right)^{1/2}\left(1-\frac{I_1^2}{I_{c1}^2}\right)^{1/4}, \\ \omega_2 &= \left(\frac{2\pi I_{c2}}{\Phi_0 C}\right)^{1/2}\left(1-\frac{I_2^2}{I_{c2}^2}\right)^{1/4}. \end{aligned} \tag{7.21}$$

Substituting (7.20) and (7.21) in (7.19), we find

$$H = \frac{1}{2}\omega_1^2 p_1^2 + \frac{1}{2}x_1^2 + \frac{1}{2}p_2^2 + \frac{1}{2}x_2^2 + \frac{1}{2}\omega_3^2 p_3^2 + \frac{1}{2}x_3^2 + \xi\omega_1\omega_3 p_1 p_3 - \xi\omega_2\omega_3 p_2 p_3. \quad (7.22)$$

Note that we can rewrite (7.22) in matrix notation

$$H = \frac{1}{2}p^T M^{-1} p + \frac{1}{2}x^T K x, \quad (7.23)$$

where

$$M^{-1} = \begin{pmatrix} \omega_1^2 & 0 & \xi\omega_1\omega_3 \\ 0 & \omega_2^2 & -\xi\omega_2\omega_3 \\ \xi\omega_1\omega_3 & -\xi\omega_2\omega_3 & \omega_3^2 \end{pmatrix} \quad (7.24)$$

and

$$K = \begin{pmatrix} 1 & 0 & 0 \\ 0 & 1 & 0 \\ 0 & 0 & 1 \end{pmatrix}. \quad (7.25)$$

For a Hamiltonian of the form (7.23), the normal mode coordinates can be conveniently defined by

$$\begin{aligned} \bar{x} &= OM^{1/2}x, \\ \bar{p} &= OM^{-1/2}p, \end{aligned} \quad (7.26)$$

where O is an orthogonal matrix. In this case the Hamiltonian is transformed to

$$H = \frac{1}{2}\bar{p}^T\bar{p} + \frac{1}{2}\bar{x}^T\Omega^2\bar{x} \quad (7.27)$$

with

$$\Omega^2 = OM^{-1/2}KM^{-1/2}O^T. \quad (7.28)$$

Thus, if we choose the orthogonal matrix O to diagonalize $M^{-1/2}KM^{-1/2}$, then H will be in diagonal form. The normal mode frequencies are given by the square-roots of the eigenvalues of Ω^2. In our particular case above, $K = I$ (the identity), and thus $\Omega^2 = OM^{-1}O^T$. The eigenvalues of Ω^2 are simply the eigenvalues of M^{-1}.

Finding the eigenvalues of a three-by-three matrix can be performed analytically, but here we focus on the specific case when $\omega_1 = \omega_2 = \omega_0$. In this case the inverse mass matrix is

$$M^{-1} = \begin{pmatrix} \omega_0^2 & 0 & \xi\omega_0\omega_3 \\ 0 & \omega_0^2 & -\xi\omega_0\omega_3 \\ \xi\omega_0\omega_3 & -\xi\omega_0\omega_3 & \omega_3^2 \end{pmatrix}. \tag{7.29}$$

This can be simplified by first making the transformation $\bar{p} = O_1 p$, with

$$O_1 = \begin{pmatrix} 1/\sqrt{2} & 1/\sqrt{2} & 0 \\ -1\sqrt{2} & 1/\sqrt{2} & 0 \\ 0 & 0 & 1 \end{pmatrix}, \tag{7.30}$$

such that

$$\bar{M}^{-1} = O_1 M^{-1} O_1^T = \begin{pmatrix} \omega_0^2 & 0 & 0 \\ 0 & \omega_0^2 & -\sqrt{2}\xi\omega_0\omega_3 \\ 0 & -\sqrt{2}\xi\omega_0\omega_3 & \omega_3^2 \end{pmatrix}. \tag{7.31}$$

The remaining sub-matrix can be diagonalized exactly, with frequencies

$$\omega_\pm^2 = \frac{1}{2}\left(\omega_0^2 + \omega_3^2 \pm [(\omega_0^2 - \omega_3^2)^2 + 8\xi^2\omega_0^2\omega_3^2]^{1/2}\right). \tag{7.32}$$

The full normal modes are given by

$$\begin{aligned} \bar{p}_0 &= 2^{-1/2}p_1 + 2^{-1/2}p_2, \\ \bar{p}_+ &= -2^{-1/2}\cos\theta p_1 + 2^{-1/2}\cos\theta p_2 - \sin\theta p_3, \\ \bar{p}_- &= -2^{-1/2}\sin\theta p_1 + 2^{-1/2}\sin\theta p_2 + \cos\theta p_3, \end{aligned} \tag{7.33}$$

with frequencies ω_0, ω_+ and ω_-, respectively, and

$$\tan\theta = \frac{\omega_+^2 - \omega_0^2}{\sqrt{2}\xi\omega_0\omega_3}. \tag{7.34}$$

If $\omega_3 = \omega_0$, we have

$$\omega_+^2 = \omega_0^2(1 + \sqrt{2}\xi), \tag{7.35}$$

$$\omega_-^2 = \omega_0^2(1 - \sqrt{2}\xi), \tag{7.36}$$

and $\theta = \pi/4$. Thus the modes are

$$\begin{array}{ll} \bar{p}_0 & = 2^{-1/2}p_1 + 2^{-1/2}p_2, \\ \bar{p}_+ & = -2^{-1}p_1 + 2^{-1}p_2 - 2^{-1/2}p_3, \\ \bar{p}_- & = -2^{-1}p_1 + 2^{-1}p_2 + 2^{-1/2}p_3. \end{array} \tag{7.37}$$

Using the creation operators

$$\begin{array}{ll} \bar{a}_0^\dagger & = 2^{-1/2}a_1^\dagger + 2^{-1/2}a_2^\dagger, \\ \bar{a}_+^\dagger & = -2^{-1}a_1^\dagger + 2^{-1}a_2^\dagger - 2^{-1/2}a_3^\dagger, \\ \bar{a}_-^\dagger & = -2^{-1}a_1^\dagger + 2^{-1}a_2^\dagger + 2^{-1/2}a_3^\dagger, \end{array} \tag{7.38}$$

and the definition

$$|\Psi_{j,k,l}\rangle = (j!k!l!)^{-1/2}{a_+^\dagger}^j {a_0^\dagger}^k {a_-^\dagger}^l |000\rangle, \tag{7.39}$$

we construct the first few quantum states:

$$\begin{array}{lll} |1) = |\Psi_{0,0,1}\rangle & = -2^{-1}|100\rangle + 2^{-1}|010\rangle + 2^{-1/2}|001\rangle, \\ |2) = |\Psi_{0,1,0}\rangle & = 2^{-1/2}|100\rangle + 2^{-1/2}|010\rangle, \\ |3) = |\Psi_{1,0,0}\rangle & = -2^{-1}|100\rangle + 2^{-1}|010\rangle - 2^{-1/2}|001\rangle. \end{array} \tag{7.40}$$

These approximately correspond to the three lowest states probed in Fig. 7.4 at the point of the avoided triple crossing.

7.4 Effective Coupling in the Two Junction Model

If the loop inductance L is set to zero, then the Hamiltonian (7.19) should reduce to the capacitive-coupling Hamiltonian

$$H = \frac{1}{2m}(1+\zeta)^{-1}(p_1^2 + p_2^2 + 2\zeta p_1 p_2) - \frac{\Phi_0}{2\pi}(I_{c1}\cos\gamma_1 + I_1\gamma_1 + I_{c2}\cos\gamma_2 + I_2\gamma_2). \tag{7.41}$$

In this section we show how this arises, using three methods. Each is a type of perturbation theory in the limit $\omega_3 \gg \omega_1, \omega_2$.

First, if we perform the harmonic approximation to (7.41) as in the previous section, we find

$$H_2 = \frac{1}{2}p^T M_2^{-1} p + \frac{1}{2}x^T K_2 x \tag{7.42}$$

where now there are only two degrees of freedom and M_2 and K_2 are

$$M_2^{-1} = (1+\zeta)^{-1} \begin{pmatrix} \omega_1^2 & \zeta\omega_1\omega_2 \\ \zeta\omega_1\omega_2 & \omega_2^2 \end{pmatrix} \tag{7.43}$$

and

$$K_2 = \begin{pmatrix} 1 & 0 \\ 0 & 1 \end{pmatrix}. \tag{7.44}$$

The eigenfrequencies are

$$\omega_{2,\pm}^2 = \frac{1}{2}(1+\zeta)^{-1}(\omega_1^2 + \omega_2^2 \pm [(\omega_1-\omega_2)^2 + 4\zeta^2\omega_1\omega_2]^{1/2}). \tag{7.45}$$

In particular, if $\omega_1 = \omega_2 = \omega_0$, then we find

$$\begin{aligned} \omega_{2,+}^2 &= \omega_0^2, \\ \omega_{2,-}^2 &= \omega_0^2(1-\zeta)(1+\zeta)^{-1}. \end{aligned} \tag{7.46}$$

We wish to compare these frequencies to those found from the three degree of freedom analysis presented above, for $\omega_1 = \omega_2 = \omega_0$ and $\omega_3 \gg \omega_0$. This comparison will give us an approximate frequency dependent coupling to incorporate into a two-mode model. Comparison of the two models shows that we should equate $\omega_{2,-}^2$ of (7.46) with ω_-^2 of (7.32). Expanding (7.32) to lowest order in ξ we find

$$\omega_-^2 = \omega_0^2 \left(1 - \frac{2\xi^2}{1-\omega_0^2/\omega_3^2}\right), \tag{7.47}$$

and setting this equal to $\omega_{2,-}^2$ of (7.46) yields:

$$\frac{1-\zeta(\omega_0)}{1+\zeta(\omega_0)} = 1 - \frac{2\xi^2}{1-\omega_0^2 E_z^{-2}}. \tag{7.48}$$

Solving (7.48) for ζ we find

$$\zeta(\omega_0) = \frac{\xi^2}{(1-\xi^2)-\omega_0^2/\omega_3^2}. \tag{7.49}$$

We see that the effect of the LC mode, through ω_3, is to provide an effective frequency dependent coupling between the two junctions. We also see that $\zeta(\omega_0) > \zeta(0)$. Thus, measurements made at junction plasma frequencies approaching the resonance frequency of the LC mode will see a larger effective coupling than measurements made at zero frequency.

We can rederive (7.49) directly from the equations of motion, by using the Fourier transforms of x_1,x_2, and x_3, denoted by $\tilde{x}_1$, $\tilde{x}_2$, and $\tilde{x}_3$. First we consider the equations of motion of H_2 in (7.42):

$$\begin{aligned} \ddot{x}_1 &= -(1+\zeta)^{-1}\omega_1^2 x_1 - \zeta(1+\zeta)^{-1}\omega_1\omega_2 x_2, \\ \ddot{x}_2 &= -(1+\zeta)^{-1}\omega_2^2 x_2 - \zeta(1+\zeta)^{-1}\omega_1\omega_2 x_1, \end{aligned} \tag{7.50}$$

or the Fourier space version

$$\begin{aligned} ((1+\zeta)^{-1}\omega_1^2 - \omega^2)\tilde{x}_1 &= -\zeta(1+\zeta)^{-1}\omega_1\omega_2\tilde{x}_2, \\ ((1+\zeta)^{-1}\omega_2^2 - \omega^2)\tilde{x}_2 &= -\zeta(1+\zeta)^{-1}\omega_1\omega_2\tilde{x}_1. \end{aligned} \tag{7.51}$$

By comparison, for the three-mode model of (7.21) we find

$$\begin{aligned} \ddot{x}_1 &= -\omega_1^2 x_1 - \xi\omega_1\omega_3 x_3, \\ \ddot{x}_2 &= -\omega_2^2 x_2 + \xi\omega_2\omega_3 x_3, \\ \ddot{x}_3 &= -\omega_3^2 x_3 - \xi\omega_1\omega_3 x_1 + \xi\omega_2\omega_3 x_3. \end{aligned} \tag{7.52}$$

In Fourier space, we can rewrite (7.52) as

$$\begin{aligned} (\omega_1^2 - \omega^2)\tilde{x}_1 &= -\xi\omega_1\omega_3\tilde{x}_3, \\ (\omega_2^2 - \omega^2)\tilde{x}_2 &= \xi\omega_2\omega_3\tilde{x}_3, \\ (\omega_3^2 - \omega^2)\tilde{x}_3 &= -\xi\omega_1\omega_3\tilde{x}_1 - \xi\omega_2\omega_3\tilde{x}_2. \end{aligned} \tag{7.53}$$

From (7.53) we can write $\tilde{x}_3$ in terms of $\tilde{x}_1$ and $\tilde{x}_2$:

$$\tilde{x}_3 = \frac{\xi\omega_3}{\omega_3^2 - \omega^2}(-\omega_1\tilde{x}_1 + \omega_2\tilde{x}_2). \tag{7.54}$$

Substituting (7.54) back into (7.53) we find

$$\begin{aligned} \left(\omega_1^2 - \frac{\xi^2\omega_1^2}{1-\omega^2/\omega_3^2} - \omega^2\right)\tilde{x}_1 &= -\frac{\xi^2\omega_1\omega_2}{1-\omega^2/\omega_3^2}\tilde{x}_2, \\ \left(\omega_2^2 - \frac{\xi^2\omega_2^2}{1-\omega^2/\omega_3^2} - \omega^2\right)\tilde{x}_2 &= -\frac{\xi^2\omega_1\omega_2}{1-\omega^2/\omega_3^2}\tilde{x}_1. \end{aligned} \tag{7.55}$$

Comparing (7.55) to our two-mode model (7.51) we find

$$\frac{1}{1+\zeta(\omega)} = 1 - \frac{\xi^2}{1-\omega^2/\omega_3^2}, \tag{7.56}$$

which leads to the same final frequency dependent coupling as (7.49)

$$\zeta(\omega) = \frac{\xi^2}{(1-\xi^2)-\omega^2/\omega_3^2}. \tag{7.57}$$

A final derivation uses the electrical engineering notion of impedance. Recall that the impedance of a capacitor is $Z_C(\omega) = (i\omega C)^{-1}$ and that of an inductor is $Z_L(\omega) = i\omega L$. We can now define the impedance of the series LC line to be a frequency-dependent effective capacitance:

$$Z_{LC}(\omega) = (i\omega C_3)^{-1} + i\omega L = (i\omega C_{\text{eff}}(\omega))^{-1} \tag{7.58}$$

Solving (7.58) for $C_{\text{eff}}(\omega)$ we find the result

$$C_{\text{eff}}(\omega) = \frac{C_3}{1-\omega^2 L C_3}. \tag{7.59}$$

Treating this as the coupling capacitance we have

$$\zeta(\omega) = \frac{C_{\text{eff}}(\omega)}{C + C_{\text{eff}}(\omega)} = \frac{C_3/C}{1-\omega^2 L C_3 + C_3/C}. \tag{7.60}$$

Recalling that $\xi^2 = C_3/(C+2C_3)$ and $\omega_3^2 = (C+2C_3)/(LCC_3)$, we note that (7.60) is equal to

$$\zeta(\omega) = \frac{\xi^2}{(1-\xi^2)-\omega^2/\omega_3^2}. \tag{7.61}$$

This analysis explains how the same chip can exhibit both resonant and capacitive coupling. The observed avoided crossings in Fig. 7.4 at the triple degeneracy

point $I_{b1} \approx 21.15\mu$A exhibit strong coupling with a dimensionless coupling coefficient of $\xi/\sqrt{2} = \sqrt{C_3/(2C + 4C_3)} \approx 0.18$ because $\omega_1 \approx \omega_2 \approx \omega_3$. However, if the LC frequency ω_3 is much greater than either junction frequency, the LC mode can be set to its ground state. Our analysis of this regime shows that the LC mediated interaction arises as a second order perturbation, and can be modeled by a frequency dependent capacitive coupling. This agrees with the previous measurements [269], which with $\omega/2\pi \approx 5$ GHz and $\omega_3/2\pi \approx 7$ GHz found $\zeta \approx 0.13$, very close to the expected value of $\zeta(\omega) = 0.14$ found from (7.49).

The effective coupling increases from ξ^2 to ξ when the junctions are in resonance with the LC mode. Thus if ξ^2 were 0.01, then ξ would be 0.1 thereby boosting the coupling strength on resonance by one order of magnitude. Furthermore the off-resonance coupling is proportional to ξ^4 when the junction frequencies are detuned from each other and ω_3 is much greater than either junction frequency, hence allowing the dynamic decoupling of each degree of freedom.

We note that the two junction qubits here are separated by almost 1 mm, yet a strong coupling strength between the two can be achieved by tuning them into resonance with a resonator. Based on this resonant coupling method, logic gates can be constructed, similar to those designed [37] for capacitive coupling, but with a larger ratio of coupling to decoupling. While the experimentally observed spectroscopic coherence time [146] for the present device is too short ($\sim$ 2 ns) for logic gates, it should be possible to increase the coherence time using improved qubit isolation, such as an inductive broadband impedance transforming scheme [93].

Chapter 8

Conclusion

In this dissertation we have explored the fundamental physics and dynamical operation of a quantum computer using current-biased Josephson junctions or "phase qubits".

The first part of this thesis reviewed the fundamental physics of the current-biased Josephson junction. In Chapter 2 we showed how the phase difference of a Josephson junction becomes a quantum variable, obeying a one-dimensional Schrödinger equation. In Chapters 3 and 4 the relevant quantum mechanical features of the current-biased junction were derived. This resulted in a set of quasi-stable resonance states, with the energy levels and tunneling rates controlled by the bias current. The lowest two states can be used as a phase qubit.

The second part of this thesis developed the theory of quantum computation using phase qubits. In Chapter 5, we showed how simple experimental modulations

of the bias current produce unitary transformations of the quantum states that can be used for single-qubit operations. In Chapter 6 we considered the capacitive coupling of phase qubits, and how coupled two-qubit operations could be performed. In Chapter 7 we studied a resonant coupling scheme using three degrees of freedom. In particular we showed theoretical calculations for the quantum mechanical energy levels and compared the spectra to those observed in the laboratory.

In this Chapter we conclude by looking at what remains to be demonstrated for quantum computation with phase qubits. DiVincenzo has framed five fundamental requirements for a physical implementation of a quantum computer. A quantum computer must have (i) qubits that can be (ii) initialized to some known state. The computer must have (iii) qubits with long decoherence times, (iv) a universal set of logic gates, and (v) a qubit-specific measurement capability. The results of this thesis have shown that requirement (iv) can be met in a Josephson junction phase qubit implementation. Moreover, requirements (i), (ii), and (v) have been demonstrated experimentally. Requirement (iii) is the most challenging, and has not been addressed in this thesis. Thus, we comment on the important topics of decoherence, scaling, and quantum error correction, and how our work can be extended.

8.1 Decoherence

The calculations performed in the previous Chapters have assumed ideal dynamics governed by the appropriate Schrödinger equation. In a real device, there is an

inevitable coupling to the environment which induces decoherence (decay of superposition states) and dissipation (loss of energy associated with decay to the ground state). These effects must be treated by a more general method, such as path-integral influence-functional techniques [140, 303] or Bloch-Redfield equations [304].

We have chosen not to model these effects for three reasons. First, at this stage of theoretical analysis, while some sources of decoherence have been identified [146, 305, 306], each depends on the particular design of the junction and its control circuit. As the development of isolation schemes progresses, careful modeling will be necessary for each circuit, especially as we approach truly coherent quantum information devices, or find that such development cannot proceed. Currently, there is no known fundamental limit to the coherence times of superconducting qubits with sufficient isolation, thus we have chosen to look at the system Hamiltonian without the enviroment. Second, prior to our work [37], it was not known if quantum logic operations existed for coupled phase qubits. The work presented here was a necessary first step, before a detailed study of decoherence in single or coupled qubits. Finally, most decoherence modeling is ultimately phenomenological, and introduces significant approximations to both the environment and the system. For quantum computation, however, we wish to treat the system dynamics as accurately as possible. One option, outside the scope of this thesis, is the stochastic Schrödinger equation method using split-operator techniques with quantum trajectories [307].

8.2 Scaling

The general issue of scaling is how one can proceed from a small number of qubits—such as the systems of one, two and three degrees of freedom we have studied in Chapters 5, 6, and 7—to the many qubits needed for truly interesting applications of quantum computation. This issue is in fact related to all aspects of quantum computation—state preparation, control, and measurement. It is unknown at this point whether truly scalable architectures for quantum computation can be realized in the laboratory.

The clear analysis of Blume-Kohout, Caves, and Deutsch [308] emphasizes that the fundamental issue is how the resource requirements of the system grow as the number of elements increases. These resources include energy, the complexity of control fields, and the precision of state measurements. The most abstract resource, and in their argument the most important, is Hilbert space dimension.

For concrete analysis, we imagine a set of N phase qubits, weakly coupled such that we can ignore the interaction energy. Assuming that no auxiliary states are used, the maximal energy N-qubit state occurs when each junction is in state $n = 1$, i.e.

$$|\Psi\rangle = \underbrace{|1\rangle \otimes |1\rangle \otimes \cdots |1\rangle}_{N\text{times}}, \tag{8.1}$$

with total energy (above the ground state) $E_N \simeq N\hbar\omega_{01}$. Note that by encoding the information in a set of qubits described by a tensor product of individual states, the energy resource is *linear* in the number of qubits. Since each qubit can be in

either state $|0\rangle$ or $|1\rangle$, the Hilbert space dimension D_N satisfies

$$D_N \geq 2^N. \tag{8.2}$$

This dimension has the expected *exponential* dependence on the number of elements. Finally, to control each qubit using the operations developed in Chapters 5 and 6, we merely need to tune each bias current, a *linear* number of control fields. For a linear array of qubits, any two can be brought into interaction by a number of swap gates which scales linearly in the number of qubits. These characteristic dependences indicate that, at this level of analysis, phase qubits are scalable: they produce a Hilbert space dimension exponential in N using a linear number of resources.

A more careful analysis shows that (8.2) is too conservative. As shown in Chapter 3, each phase qubit has in fact a continuum of energy states. In the approximation that the resonances are discrete, they have energy differences which decrease for increasing quantum number. This is demonstrated by the perturbation theory in Chapter 4. Thus, if we actually count the number of levels less than E_N, we will find a much larger number. We can numerically calculate the number of levels for any given set of single-junction energy levels by using recursion relations [309]. For simplicity, however, we can use the harmonic oscillator approximation which should again underestimate the number of levels. For N harmonic oscillators the number of states with energy less than $M\hbar\omega$ is [310]

$$S_{M,N} = \frac{(N+M)!}{N!M!}. \tag{8.3}$$

Thus, we find

$$D_N = S_{N,N} = \frac{(2N)!}{(N!)^2} \simeq 4^N, \tag{8.4}$$

the last equation following from Stirling's approximation. Thus, for N phase qubits the number of states D_N is much greater than the simple bound (8.2).

We see that the existence of extra levels in the phase qubit is an issue not only for the single and two-qubit operations but also for the general N-qubit system. However, if we restrict our operations to those developed in Chapters 5 and 6, the relevant energy levels can still be controlled scalably, i.e. using a linear number of controls.

However, we have unrealistically assumed weak coupling for both the energy levels and state measurement. In general, the measurement of one qubit will subsequently disturb other qubits, even beyond the "standard" quantum state projection. This can occur because of current fluctuations through the coupling capacitors, quasi-particle production, and other interactions [11]. A careful design should remove qubits from interaction before measurements occur. One possible design is shown in Fig. 8.1. Each "information qubit" is coupled to a "measurement qubit"; the information qubits are also coupled to each other through a "coupling qubit." If the coupling and information qubits are set to a significantly high energy, one expects that the measurement will not disturb their quantum states appreciably. Since this requires about $3N$ junctions to store N actual qubits, this design is—at first glance—scalable. However, this type of design has yet to studied theoretically or experimentally in any detail.

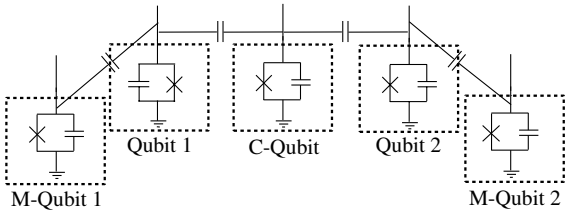

Figure 8.1: Schematic multi-qubit device. The information qubits are labelled Qubit 1 and Qubit 2, and each have a M(easurement)-qubit, M-Qubit 1 and M-Qubit 2. They are coupled through another C(oupling) qubit.

8.3 Quantum Error Correction

The quantum logic operations developed in Chapters 5 and 6 have an intrinsic error probability of order 10^{-4}. For a small quantum algorithm this level of error is probably acceptable, but for large-scale computation one would like to correct it before it grows. This can be done using the methods of quantum error correction, first discovered by Shor [293] and Steane [311].

In error correction, one uses multiple qubits for redundancy in the qubit encoding to protect against errors. In the simplest scheme one can use a replacement rule such as

$$|0\rangle \rightarrow |000\rangle, |1\rangle \rightarrow |111\rangle. \tag{8.5}$$

If a bit-flip error occurs on the first qubit (i.e. $|0\rangle \rightarrow |1\rangle$ with some probability p_E), its value can still be determined from the other qubits, and a correction made. This correction removes all single bit-flip errors, leaving an error term proportional to p_E^2 if the errors are independent.

By more ingenious encoding techniques [7], this simple example can be ex-

tended to *all* types of errors on a single qubit, such as phase-flips (i.e. $|1\rangle \rightarrow -|1\rangle$). The fundamental error correction step should transform the error probability by

$$p_{E,C} \simeq K p_E^2. \tag{8.6}$$

K is some constant that depends on the number of possible two-qubit errors that remain after the error correction step; $p_0 = 1/K$ is called the threshold probability. If $p_E < p_0$, the transformed error probability $p_{E,C}$ has decreased, and further encoding (called *concatenation*) will continue to decrease the error probability. This threshold probability p_0 is hard to calculate, requiring many assumptions about the quantum computer, but is now believed to be on the order of 10^{-4}, or perhaps as high as 10^{-2} for certain error models [312]. It is significant to note that the single and two-qubit operations constructed in Chapters 5 and 6 have errors just within the 10^{-4} error threshold.

Finally, we note that the fundamental techniques of error correction involve standard quantum logic gates, as well as measurement and feedback. These last two operations remain to be studied in phase qubits (and many other types of qubits), in both theory and experiment.

8.4 The Superposition Principle, Entanglement, and Beyond

The results of this thesis—mostly technical results on one possible design for a quantum computer—have been motivated by another goal. The two-qubit logic

gates developed in this thesis can be used in experiments to test the time-evolution of entangled states such as those described in Chapter 7. If these states display the appropriate dynamics, this implies that we can create and verify superposition states such as the Bell state

$$2^{-1/2}\left(|00\rangle + |11\rangle\right) \tag{8.7}$$

or the Greenberger-Horne-Zeilinger (GHZ) state [313]

$$2^{-1/2}\left(|000\rangle + |111\rangle\right). \tag{8.8}$$

These states are entangled, and have properties not shared by classical systems [314]. For the current-biased Josephson junction, these are entangled states of *macroscopic* variables—solid-state examples of Schrödinger's cat. If future experimenters successfully demonstrate their predicted properties, they will have shown that Nature obeys the superposition principle at the macroscopic level,a question posed by Leggett more than 20 years ago [79, 80].

If our world is truly quantum, at all scales of size and complexity, then surely we can dream of what lies beyond?

Appendix A

Mathematical Appendix

A.1 Properties of the Airy Functions

The Airy functions Ai and Bi are the two independent solutions to the differential equation

$$\frac{d^2w(x)}{dx^2} - xw(x) = 0. \tag{A.1}$$

Many properties of these functions can be found in [210]. These functions have the following integral representations

$$\mathrm{Ai}(x) = \frac{1}{\pi}\int_0^\infty \cos(t^3/3 + xt)dt, \tag{A.2}$$

$$\mathrm{Bi}(x) = \frac{1}{\pi}\int_0^\infty \left(\sin(t^3/3 + xt) + \exp(-t^3/3 + xt)\right) dt. \tag{A.3}$$

The Wronskian of Ai and Bi is constant and given by

$$W[\mathrm{Ai},\mathrm{Bi}](x) = \mathrm{Ai}(x)\mathrm{Bi}'(x) - \mathrm{Ai}'(x)\mathrm{Bi}(x) = \pi^{-1}. \tag{A.4}$$

It is convenient to define two auxiliary functions Gi and Hi such that $\mathrm{Bi}(x) = \mathrm{Gi}(x) + \mathrm{Hi}(x)$, with the integral representations

$$\mathrm{Gi}(x) = \frac{1}{\pi}\int_0^\infty \sin(t^3/3 + xt)dt, \tag{A.5}$$

$$\mathrm{Hi}(x) = \frac{1}{\pi}\int_0^\infty \exp(-t^3/3 + xt)dt. \tag{A.6}$$

These functions $-\mathrm{Gi}(x)$ and $\mathrm{Hi}(x)$ are known as *Scorer* functions, and satisfy the inhomogenous differential equation

$$\frac{d^2w(x)}{dx^2} - xw(x) = \pi^{-1}. \tag{A.7}$$

The functions Ai, Gi, and Hi have the following asymptotic forms:

$$\mathrm{Ai}(x) \to \left\{ \begin{array}{cc} \frac{1}{2}\pi^{-1/2}x^{-1/4}\exp(-\frac{2}{3}x^{3/2}) & x \to +\infty \\ \pi^{-1/2}|x|^{-1/4}\cos(\frac{2}{3}|x|^{3/2} - \pi/4) & x \to -\infty \end{array} \right\}, \tag{A.8}$$

$$\mathrm{Gi}(x) \to \left\{ \begin{array}{cc} \pi^{-1}x^{-1} & x \to +\infty \\ -\pi^{-1/2}|x|^{-1/4}\sin(\frac{2}{3}|x|^{3/2} - \pi/4) & x \to -\infty \end{array} \right\}, \tag{A.9}$$

$$\mathrm{Hi}(x) \to \left\{ \begin{array}{cc} \pi^{-1/2}x^{-1/4}\exp(+\frac{2}{3}x^{3/2}) & x \to +\infty \\ -\pi^{-1}x^{-1} & x \to -\infty \end{array} \right\}. \tag{A.10}$$

From the asymptotic form (A.8), we find that the zeros of the Airy function, the quantities $-a_n$ with $a_n > 0$ such that $\mathrm{Ai}(-a_n) = 0$, satisfy the approximate relation

$$\frac{2}{3}a_n^{3/2} - \pi/4 \simeq (n - 1/2)\pi, \tag{A.11}$$

or

$$a_n \simeq \left[\frac{3\pi(n - 1/4)}{2}\right]^{2/3}, \tag{A.12}$$

where we have chosen the range of n to be the positive integers $1, 2, \cdots$.

Starting from the fundamental differential equation, many definite integrals can be calculated solely in terms of Ai and Bi and their derivatives. The strategy to determine these integrals is to insert unity in the form $1 = d(x)/dx$, integrate by parts, and use the fundamental differential equation in the form $xw(x) = w''(x)$, with w any linear combination of Ai and Bi. The simplest example is

$$\begin{aligned} \int_a^b w(x)^2 dx &= \int_a^b w(x)^2 (d(x)/dx) dx \\ &= xw(x)^2|_a^b - 2\int_a^b xw(x)w'(x)dx \\ &= xw(x)^2|_a^b - 2\int_a^b w''(x)w'(x)dx \\ &= xw(x)^2|_a^b - \int_a^b d(w'(x)^2)/dxdx \\ &= (xw(x)^2 - w'(x)^2)|_a^b. \end{aligned} \tag{A.13}$$

A more complicated example is an integral of the form

$$f(y; a, b) = \int_a^b w_1(x) w_2(x + y) dx, \tag{A.14}$$

with $w_{1,2}(x) = a_{1,2}\mathrm{Ai}(x) + b_{1,2}\mathrm{Bi}(x)$. Using a similar strategy to that shown above, we compute

$$\begin{aligned} f(y; a, b) &= \int_a^b w_1(x) w_2(x + y) d(x + y)/dxdx \\ &= (x + y) w_1(x) w_2(x + y)|_a^b \\ &\quad - \int_a^b (w_1'(x)(x + y) w_2(x + y) + (x + y) w_1(x) w_2'(x + y)) dx \\ &= w_1(x) w_2''(x + y)|_a^b \\ &\quad - \int_a^b (w_1'(x) w_2''(x + y) + w_1''(x) w_2'(x + y)) - y \int_a^b w_1(x) w_2'(x + y) \\ &= w_1(x) w_2''(x + y)|_a^b \\ &\quad - \int_a^b d(w_1'(x) w_2'(x + y))/dxdx - yd/dy \int_a^b w_1(x) w_2(x + y) \\ &= (w_1(x) w_2''(x + y) - w_1'(x) w_2'(x + y))|_a^b - y df(y; a, b)/dy \end{aligned} \tag{A.15}$$

Rearranging (A.15) we see that

$$d(yf(y; a, b))/dy = (w_1(x) w_2''(x + y) - w_1'(x) w_2'(x + y))|_a^b. \tag{A.16}$$

If we now integrate (A.16) with respect to y, (the integration constant can be set

to zero) we find

$$\int_a^b w_1(x)w_2(x+y)dx = \frac{(w_1(x)w_2'(x+y) - w_1'(x)w_2(x+y))|_a^b}{y}. \tag{A.17}$$

This expression was found by Gordon [315]. Taking the limit of $y \to 0$ and noting that the Wronskian of w_1 and w_2 is constant, (A.17) becomes a generalized version of (A.13),

$$\int_a^b w_1(x)w_2(x)dx = [w_1(x)w_2''(x) - w_1'(x)w_2'(x)]|_a^b, \tag{A.18}$$

an equation (along with many others) found by Albright [316].

Applying this procedure to Scorer functions, however, introduces extra terms because of the inhomogenous differential equation (A.7). We find

$$\int_a^b \mathrm{Hi}(x)\mathrm{Hi}(x+y)dx = \frac{(\mathrm{Hi}(x)\mathrm{Hi}'(x+y) - \mathrm{Hi}'(x)\mathrm{Hi}(x+y))|_a^b}{y} + \frac{1}{\pi}\int_0^y \mathrm{Hi}(x+y')|_a^b dy', \tag{A.19}$$

$$\int_a^b \mathrm{Gi}(x)\mathrm{Gi}(x+y)dx = \frac{(\mathrm{Gi}(x)\mathrm{Gi}'(x+y) - \mathrm{Gi}'(x)\mathrm{Gi}(x+y))|_a^b}{y} - \frac{1}{\pi}\int_0^y \mathrm{Gi}(x+y')|_a^b dy', \tag{A.20}$$

$$\int_a^b \mathrm{Gi}(x)\mathrm{Hi}(x+y)dx = \frac{(\mathrm{Gi}(x)\mathrm{Hi}'(x+y) - \mathrm{Gi}'(x)\mathrm{Hi}(x+y))|_a^b}{y} - \frac{1}{\pi}\int_0^y \mathrm{Hi}(x+y')|_a^b dy', \tag{A.21}$$

$$\int_a^b \mathrm{Hi}(x)\mathrm{Gi}(x+y)dx = \frac{(\mathrm{Hi}(x)\mathrm{Gi}'(x+y) - \mathrm{Hi}'(x)\mathrm{Gi}(x+y))|_a^b}{y} + \frac{1}{\pi}\int_0^y \mathrm{Gi}(x+y')|_a^b dy'. \tag{A.22}$$

A particular class of integrals which requires special treatment is that with a or b set to $\pm\infty$. In these cases, use of the integral representations is often necessary. For example, consider

$$\begin{aligned} I_G(y,z) &= \int_{-\infty}^{+\infty} \mathrm{Gi}(x+y)\mathrm{Gi}(x+z)dx \\ &= \tfrac{1}{\pi^2}\int_0^{+\infty} dt \int_0^{+\infty} dt' \int_{-\infty}^{+\infty} dx \sin(t^3/3+(x+y)t)\sin(t'^3/3+(x+z)t'). \end{aligned} \tag{A.23}$$

If we expand the sines in the integrand can as complex exponentials

$$\begin{aligned} \sin(t^3/3+(x+y)t)\times\sin(t'^3/3+(x+z)t') = \\ -\exp(i(t^3/3+t'^3/3+yt+zt'+x(t+t'))/4 \\ +\exp(i(t^3/3-t'^3/3+yt-zt'+x(t-t'))/4 \\ +\exp(i(t'^3/3-t^3/3+zt'-yt+x(t'-t))/4 \\ -\exp(-i(t^3/3+t'^3/3+yt+zt'+x(t+t'))/4, \end{aligned} \tag{A.24}$$

the integrations over x can now be performed in terms of the δ-function

$$\delta(k) = \frac{1}{2\pi}\int_{-\infty}^{+\infty} dx e^{ikx}, \tag{A.25}$$

with the result

$$I_G(y,z) = -\frac{1}{2\pi}\int_0^{+\infty} dt \int_0^{+\infty} dt'[2i\sin(t(y-z))\delta(t+t') - 2\cos(t(y-z))\delta(t-t')]. \tag{A.26}$$

Since the first δ-function is nonzero only on the limits of the integration [at $(t,t') = (0,0)$], only the second term in (A.26) contributes, leading to

$$I_G(y,z) = \frac{1}{\pi}\int_0^{+\infty} dt\cos(t(y-z)) = \frac{1}{2\pi}\int_{-\infty}^{\infty} e^{it(y-z)}dt = \delta(y-z). \tag{A.27}$$

Thus

$$\int_{-\infty}^{\infty} \mathrm{Gi}(-(x+E))\mathrm{Gi}(-(x+E'))dx = \delta(E-E'). \tag{A.28}$$

More easily, one can show

$$\begin{aligned} I_A(y,z) &= \textstyle\int_{-\infty}^{+\infty} \mathrm{Ai}(x+y)\mathrm{Ai}(x+z)dx \\ &= \frac{1}{\pi^2}\textstyle\int_{-\infty}^{+\infty} dx \int_0^{+\infty} dt \int_0^{+\infty} dt' \cos(t^3/3 + (x+y)t)\cos(t'^3/3 + (x+z)t') \\ &= \frac{1}{4\pi^2}\textstyle\int_{-\infty}^{+\infty} dx \int_{-\infty}^{+\infty} dt \int_{-\infty}^{+\infty} dt' \exp(i(t^3/3 + yt + t'^3/3 + zt' + x(t+t')) \\ &= \frac{1}{2\pi}\textstyle\int_{-\infty}^{+\infty} dt \int_{-\infty}^{+\infty} dt' \delta(t+t') \exp(i(t^3/3 + yt + t'^3/3 + zt') \\ &= \frac{1}{2\pi}\textstyle\int_{-\infty}^{+\infty} \exp(it(y-z)) \\ &= \delta(y-z). \end{aligned} \tag{A.29}$$

The final integral to consider is

$$\begin{aligned} I_{AG}(y,z) &= \textstyle\int_{-\infty}^{+\infty} \mathrm{Ai}(x+y)\mathrm{Gi}(x+z)dx \\ &= \pi^{-2}\textstyle\int_{-\infty}^{+\infty} dx \int_0^{+\infty} dt \int_0^{+\infty} dt' \cos(t^3/3 + (x+y)t)\sin(t'^3/3 + (x+z)t'). \end{aligned} \tag{A.30}$$

Expanding the product of cosine and sine as above we find

$$\begin{aligned} \cos(t^3/3 + (x+y)t) \times \sin(t'^3/3 + (x+z)t') = \\ (4i)^{-1}[\exp(i(t^3/3 + t'^3/3 + yt + zt' + x(t+t')) \\ - \exp(i(t^3/3 - t'^3/3 + yt - zt' + x(t-t')) \\ + \exp(i(t'^3/3 - t^3/3 + zt' - yt + x(t'-t)) \\ - \exp(-i(t^3/3 + t'^3/3 + yt + zt' + x(t+t'))], \end{aligned} \tag{A.31}$$

and performing the x-integral in (A.30) yields

$$\begin{aligned} I_{AG}(y,z) &= \pi^{-1} int_0^{+\infty} dt \textstyle\int_0^{+\infty} dt' [\delta(t+t')\sin(t(y-z) - \delta(t-t')\sin(t(y-z))] \\ &= -\pi^{-1}\textstyle\int_0^{+\infty} \sin(t(y-z)) \\ &= -\pi^{-1}(y-z)^{-1}. \end{aligned} \tag{A.32}$$

Using the above results, the following relevant integrals are readily computed:

$$\int_{-\infty}^{0} \mathrm{Ai}(-(x+E))\mathrm{Ai}(-(x+E'))dx = -\frac{\mathrm{Ai}(-E)\mathrm{Ai}'(-E') - \mathrm{Ai}'(-E)\mathrm{Ai}(-E')}{E-E'}, \tag{A.33}$$

$$\int_{0}^{+\infty} \mathrm{Ai}(-(x+E))\mathrm{Ai}(-(x+E'))dx = \frac{\mathrm{Ai}(-E)\mathrm{Ai}'(-E') - \mathrm{Ai}'(-E)\mathrm{Ai}(-E')}{E-E'} + \delta(E-E'), \tag{A.34}$$

$$\int_{0}^{+\infty} \mathrm{Bi}(-(x+E))\mathrm{Bi}(-(x+E'))dx = \frac{\mathrm{Bi}(-E)\mathrm{Bi}'(-E') - \mathrm{Bi}'(-E)\mathrm{Bi}(-E')}{E-E'} + \delta(E-E'), \tag{A.35}$$

$$\int_{0}^{+\infty} \mathrm{Ai}(-(x+E))\mathrm{Bi}(-(x+E'))dx = \frac{\mathrm{Ai}(-E)\mathrm{Bi}'(-E') - \mathrm{Ai}'(-E)\mathrm{Bi}(-E')}{E-E'} + \frac{1}{\pi(E-E')}, \tag{A.36}$$

$$\int_{0}^{+\infty} \mathrm{Bi}(-(x+E))\mathrm{Ai}(-(x+E'))dx = \frac{\mathrm{Bi}(-E)\mathrm{Ai}'(-E') - \mathrm{Bi}'(-E)\mathrm{Ai}(-E')}{E-E'} + \frac{1}{\pi(E-E')}. \tag{A.37}$$

The most difficult integral is (A.35), which we sketch here:

$$\begin{aligned} I_{BB}(E,E') &= \int_0^{+\infty} \mathrm{Bi}(-(x+E))\mathrm{Bi}(-(x+E'))dx \\ &= \int_{-\infty}^{+\infty} \mathrm{Gi}(-(x+E))\mathrm{Gi}(-(x+E'))dx \\ &\quad - \int_{-\infty}^{0} \mathrm{Gi}(-(x+E))\mathrm{Gi}(-(x+E'))dx \\ &\quad + \int_0^{+\infty} \mathrm{Gi}(-(x+E))\mathrm{Hi}(-(x+E'))dx \\ &\quad + \int_0^{+\infty} \mathrm{Hi}(-(x+E))\mathrm{Gi}(-(x+E'))dx \\ &\quad + \int_0^{+\infty} \mathrm{Hi}(-(x+E))\mathrm{Hi}(-(x+E'))dx. \end{aligned} \tag{A.38}$$

Using (A.28) and (A.19)-(A.22) and noting that terms at infinity are zero according to the the asymptotic forms (A.8)-(A.10), we find the result

$$\begin{aligned}
&I_{BB}(E,E') = \delta(E-E') \\
&+(E-E')^{-1}[\mathrm{Gi}(-E)\mathrm{Gi}'(-E') - \mathrm{Gi}'(-E)\mathrm{Gi}(-E') - \pi^{-1}\textstyle\int_{-E}^{-E'}\mathrm{Gi}(s)ds] \\
&+(E-E')^{-1}[\mathrm{Gi}(-E)\mathrm{Hi}'(-E') - \mathrm{Gi}'(-E)\mathrm{Hi}(-E') - \pi^{-1}\textstyle\int_{-E}^{-E'}\mathrm{Hi}(s)ds] \\
&+(E-E')^{-1}[\mathrm{Hi}(-E)\mathrm{Gi}'(-E') - \mathrm{Hi}'(-E)\mathrm{Gi}(-E') + \pi^{-1}\textstyle\int_{-E}^{-E'}\mathrm{Gi}(s)ds] \\
&+(E-E')^{-1}[\mathrm{Hi}(-E)\mathrm{Hi}'(-E') - \mathrm{Hi}'(-E)\mathrm{Hi}(-E') + \pi^{-1}\textstyle\int_{-E}^{-E'}\mathrm{Hi}(s)ds].
\end{aligned} \tag{A.39}$$

The integrals over Gi and Hi thankfully cancel in pairs, leaving the promised form

$$I_{BB}(E,E') = \delta(E-E') + \frac{\mathrm{Bi}(-E)\mathrm{Bi}'(-E') - \mathrm{Bi}'(-E)\mathrm{Bi}(-E')}{E-E'}. \tag{A.40}$$

A.2 Matrix Elements of the Washboard

A.2.1 Square Well Basis

The square well basis consists of the eigenfunctions of the free-particle Hamiltonian

$$H = \frac{p^2}{2m} \tag{A.41}$$

subject to the boundary condition that $\Psi_n(x=-L/2) = \Psi_n(x=+L/2) = 0$. These states can be written as

$$\Psi_n(x) = \sqrt{2/L}\sin(n\pi(x/L+1/2)). \tag{A.42}$$

Now, we wish to compute the square-well matrix elements

$$\langle n|x^k|m\rangle = \int_{-L/2}^{+L/2} dx \Psi_n(x) x^k \Psi_m(x), \tag{A.43}$$

$$\langle n|p^k|m\rangle = \int_{-L/2}^{+L/2} dx \Psi_n(x) (-i\hbar d/dx)^k \Psi_m(x), \tag{A.44}$$

$$\langle n|\sin(zx)|m\rangle = \int_{-L/2}^{+L/2} dx \Psi_n(x)\sin(zx)\Psi_m(x), \tag{A.45}$$

$$\langle n|\cos(zx)|m\rangle = \int_{-L/2}^{+L/2} dx \Psi_n(x)\cos(zx)\Psi_m(x). \tag{A.46}$$

These integrals are all essentially elementary; we list the relevant results, omitting the tedious algebra

$$\langle n|p^2|m\rangle = \frac{\hbar^2 n^2\pi^2}{L^2}\delta_{n,m}, \tag{A.47}$$

$$\langle n|x|m\rangle = \begin{pmatrix} 0 & n=m \\ 4nm(-1+(-1)^{m+n})L\pi^{-2}(n^2-m^2)^{-2} & n\neq m \end{pmatrix}, \tag{A.48}$$

$$\langle n|x^2|m\rangle = \begin{pmatrix} \frac{1}{12}L^2(1-\frac{6}{n^2\pi^2}) & n=m \\ 4nm(1+(-1)^{m+n})L^2\pi^{-2}(n^2-m^2)^{-2} & n\neq m \end{pmatrix}, \tag{A.49}$$

$$\langle n|x^3|m\rangle = \begin{pmatrix} 0 & n=m \\ 3nm(-1+(-1)^{m+n})L^3(\pi^2(n^2-m^2)^2 & \\ -16(n^2+m^2))\pi^{-4}(n^2-m^2)^{-4} & n\neq m \end{pmatrix}, \tag{A.50}$$

$$\langle n|\cos(zx)|m\rangle = -\frac{4mn(1+(-1)^{m+n})zL\sin(zL/2)}{(n^2-m^2)^2\pi^4+(zL)^4-2(n^2+m^2)\pi^2(zL)^2}, \tag{A.51}$$

$$\langle n|\sin(zx)|m\rangle = -\frac{4mn(1-(-1)^{m+n})zL\cos(zL/2)}{(n^2-m^2)^2\pi^4+(zL)^4-2(n^2+m^2)\pi^2(zL)^2}. \tag{A.52}$$

A.2.2 Harmonic Oscillator Basis

The harmonic oscillator Hamiltonian

$$H = \frac{p^2}{2m} + \frac{1}{2}m\omega_0^2 x^2 \tag{A.53}$$

has wavefunctions

$$\Psi_n(x) = c_n H_n(x/x_0)\exp\left(-\frac{x^2}{2x_0^2}\right), \tag{A.54}$$

where $H_n(x)$ is the n-th Hermite polynomial and we have defined

$$x_0 = \sqrt{\frac{\hbar}{m\omega_0}} \tag{A.55}$$

and

$$c_n = (\pi x_0^2)^{-1/4}(2^n n!)^{-1/2}. \tag{A.56}$$

These wavefunctions satisfy the differential equation

$$-\frac{\hbar^2}{2m}\frac{d^2\Psi_n(x)}{dx^2} + \frac{1}{2}m\omega_0^2 x^2 \Psi_n(x) = \hbar\omega_0 \left(n + \frac{1}{2}\right) \Psi_n(x) \tag{A.57}$$

The Hermite polynomials are most easily defined by their generating function

$$e^{-x^2+2tx} = \sum_{n=0}^{\infty} \frac{t^n}{n!} H_n(x). \tag{A.58}$$

Now, one would like to compute the following matrix elements:

$$\langle n|x^k|m\rangle = \int_{-\infty}^{+\infty} dx \Psi_n(x) x^k \Psi_m(x), \tag{A.59}$$

$$\langle n|p^k|m\rangle = \int_{-\infty}^{+\infty} dx \Psi_n(x) (-i\hbar d/dx)^k \Psi_m(x), \tag{A.60}$$

$$\langle n|\sin(zx)|m\rangle = \int_{-\infty}^{+\infty} dx \Psi_n(x) \sin(zx) \Psi_m(x), \tag{A.61}$$

$$\langle n|\cos(zx)|m\rangle = \int_{-\infty}^{+\infty} dx \Psi_n(x) \cos(zx) \Psi_m(x). \tag{A.62}$$

To evaluate these integrals we use the following algebraic approach. We define the ladder operators a and $a^\dagger$,

$$\begin{array}{ll} a & = 2^{-1/2}(x/x_0 + ip/p_0), \\ a^\dagger & = 2^{-1/2}(x/x_0 - ip/p_0), \end{array} \tag{A.63}$$

where $p_0 = \hbar/x_0$. These operators have the commutation relation

$$[a, a^\dagger] = 1 \tag{A.64}$$

and they simplify the Hamiltonian to the following form:

$$H = \hbar\omega_0(a^\dagger a + 1/2). \tag{A.65}$$

On the eigenstates of H they act as

$$\begin{array}{ll} a|n\rangle & = \sqrt{n}|n-1\rangle, \\ a^\dagger|n\rangle & = \sqrt{n+1}|n+1\rangle, \end{array} \tag{A.66}$$

and

$$a^\dagger a|n\rangle = n|n\rangle. \tag{A.67}$$

Reversing and iterating (A.66) we find that the eigenstates can be written as

$$|n\rangle = \frac{{a^\dagger}^n}{\sqrt{n!}}|0\rangle. \tag{A.68}$$

Using these creation and annihilation operators, we first expand our operators x, x^2, x^3 and p, p^2 in terms of a and $a^\dagger$:

$$\begin{array}{ll} x & = 2^{-1/2}x_0(a + a^\dagger), \\ x^2 & = 2^{-1}x_0^2(a^2 + aa^\dagger + a^\dagger a + {a^\dagger}^2), \\ x^3 & = 2^{-3/2}x_0^3(a^3 + a^2a^\dagger + aa^\dagger a + aa^{\dagger 2} + a^\dagger aa^\dagger + {a^\dagger}^2 a + {a^\dagger}^3), \\ p & = -i2^{-1/2}p_0(a - a^\dagger), \\ p^2 & = -2^{-1}p_0^2(a^2 - aa^\dagger - a^\dagger a + {a^\dagger}^2). \end{array} \tag{A.69}$$

Using (A.66), (A.69) and the orthogonality relation $\langle n|m\rangle = \delta_{n,m}$, we find

$$\langle n|x|m\rangle = 2^{-1/2}x_0(\sqrt{m}\delta_{n,m-1} + \sqrt{m+1}\delta_{n,m+1}), \tag{A.70}$$

$$\begin{array}{rl} \langle n|x^2|m\rangle = & 2^{-1}x_0^2(\sqrt{m(m-1)}\delta_{n,m-2} + (2m+1)\delta_{n,m} \\ & +\sqrt{(m+1)(m+2)}\delta_{n,m+2}), \end{array} \tag{A.71}$$

$$\begin{array}{rl} \langle n|x^3|m\rangle = & 2^{-3/2}x_0^3(\sqrt{m(m-1)(m-2)}\delta_{n,m-3} + 3\sqrt{m^3}\delta_{n,m-1} \\ & +3\sqrt{(m+1)^3}\delta_{n,m+1} + \sqrt{(m+1)(m+2)(m+3)}\delta_{n,m+3}), \end{array} \tag{A.72}$$

$$\langle n|p|m\rangle = -i2^{-1/2}p_0(\sqrt{m}\delta_{n,m-1} - \sqrt{m+1}\delta_{n,m+1}), \tag{A.73}$$

$$\begin{array}{rl} \langle n|p^2|m\rangle = & 2^{-1}p_0^2(-\sqrt{m(m-1)}\delta_{n,m-2} + (2m+1)\delta_{n,m} \\ & -\sqrt{(m+1)(m+2)}\delta_{n,m+2}). \end{array} \tag{A.74}$$

Slightly more complicated is the evaluation of the $\sin(zx)$ and $\cos(zx)$ matrix elements. We first consider the more fundamental matrix element

$$u_{nm}(z) = \langle n|e^{izx}|m\rangle, \tag{A.75}$$

in terms of which we have

$$\begin{array}{ll} \langle n|\cos(zx)|m\rangle & = \frac{1}{2}(u_{nm}(z)+u_{nm}(-z)) \\ \langle n|\sin(zx)|m\rangle & = \frac{1}{2i}(u_{nm}(z)-u_{nm}(-z)) \end{array} \tag{A.76}$$

Using (A.68) and letting $\bar{z} = zx_0/\sqrt{2}$, we find that

$$u_{n,m}(z) = \frac{1}{\sqrt{n!m!}}\langle 0|a^n e^{i\bar{z}(a+a^\dagger)}{a^\dagger}^m|0\rangle. \tag{A.77}$$

We can now use the Zassenhaus formula

$$e^{A+B} = e^A e^B e^{-[A,B]/2} e^C \tag{A.78}$$

with C given by higher-order multiple commutators of A and B. If $[A,[A,B]] = [B,[A,B]] = 0$, then $C = 0$. In our case, since $[a,a^\dagger] = 1$ we have $[a,[a,a^\dagger]] = [a^\dagger,[a,a^\dagger]] = 0$. Thus we can simplify

$$e^{i\bar{z}(a+a^\dagger)} = e^{i\bar{z}a} e^{i\bar{z}a^\dagger} e^{\bar{z}^2/2}. \tag{A.79}$$

Substituting (A.79) into (A.77) we have

$$u_{n,m}(z) = \frac{e^{\bar{z}^2/2}}{\sqrt{n!m!}}\langle 0|a^n e^{i\bar{z}a}{a^\dagger}^m e^{i\bar{z}a^\dagger}|0\rangle, \tag{A.80}$$

which we rewrite as

$$u_{n,m}(z) = \frac{e^{\bar{z}^2/2}}{\sqrt{n!m!}}[\partial_v^n \partial_w^m \langle 0|e^{va}e^{wa^\dagger}|0\rangle]|_{v=w=i\bar{z}}. \tag{A.81}$$

The term in brackets in (A.81) can be explicitly evaluated by reversing the Zassenhaus formula (A.78), that is

$$e^{va}e^{wa^\dagger} = e^{vw/2}e^{va+wa^\dagger} = e^{vw}e^{wa^\dagger}e^{va}. \tag{A.82}$$

Using (A.82) in (A.81), and $a|0\rangle = 0$ and $\langle 0|a^\dagger = 0$ which follows from (A.66), we have

$$u_{n,m}(z) = \frac{e^{\bar{z}^2/2}}{\sqrt{n!m!}}[\partial_v^n \partial_w^m e^{vw}]|_{v=w=i\bar{z}}. \tag{A.83}$$

We can evaluate (A.83) directly for $n > m$, in which case we first perform the derivatives with respect to v:

$$u_{n,m}(z) = \frac{e^{\bar{z}^2/2}}{\sqrt{n!m!}}[\partial_w^m w^n e^{vw}]|_{v=w=i\bar{z}}. \tag{A.84}$$

Now, focusing on the term in brackets in (A.84), we use the Leibniz formula for the derivatives to find

$$\begin{array}{ll} \partial_w^m w^n e^{vw} & = \sum_{k=0}^m \frac{m!}{(k!)(m-k)!}(\partial_w^{m-k} w^n)(\partial_w^k e^{vw}) \\ & = \sum_{k=0}^m \frac{m!}{(k!)(m-k)!}\frac{n!}{(n-m+k)!} w^{n-m+k} v^k e^{vw}. \end{array} \tag{A.85}$$

Substituting (A.85) into (A.84), we find

$$u_{n,m}(z) = \frac{m! e^{-\bar{z}^2/2}}{\sqrt{n!m!}}(i\bar{z})^{n-m} \sum_{k=0}^m \frac{n!}{k!(m-k)!(n-m+k)!}(-1)^k (\bar{z}^2)^k. \tag{A.86}$$

Finally, this can be simplified by noting that the associated Laguerre polynomial is defined by ([210], Eq. 22.3.9)

$$L_m^r(x) = \sum_{k=0}^m \frac{(r+m)!}{k!(m-k)!(r+k)!}(-1)^k x^k. \tag{A.87}$$

Thus, for $n > m$, we have

$$u_{n,m}(z) = \langle n|e^{izx}|m\rangle = \sqrt{\frac{m!}{n!}}\left(\frac{izx_0}{\sqrt{2}}\right)^{n-m} e^{-z^2x_0^2/4} L_m^{n-m}(z^2x_0^2/2). \tag{A.88}$$

Our derivation can be repeated for $n < m$ and leads to essentially the same results (with n and m switched). Letting $n_+ = \max(n,m)$ and $n_- = \min(n,m)$, we find the result

$$\langle n|e^{izx}|m\rangle = \sqrt{\frac{n_-!}{n_+!}}\left(\frac{izx_0}{\sqrt{2}}\right)^{n_+-n_-} e^{-z^2x_0^2/4} L_{n_-}^{n_+-n_-}(z^2x_0^2/2). \tag{A.89}$$

A.3 Mathematica Perturbation Theory Code

```
Ex[n_,g_,No_]:=
Module[{nlevel,norder,Bmat,A1,A2,A3,A4,Ax,hitnlevel},nlevel=n;
   norder=No;
   neven = If[EvenQ[nlevel],1,0];
   Bmat = Table[0,{m,0,norder},{j,0,nlevel+3*m}];
   Do[Bmat = ReplacePart[Bmat, (-1)^((k-1+neven)/2)
                          2^(k-1+neven) ((nlevel-1+neven)/2)!
                          / (((nlevel-k)/2)! k!),{1,k+1}],
                             {k,1-neven,nlevel,2}];
   Do[Bmat = ReplacePart[Bmat, Bmat[[1]][[nlevel+1]]
                          3^{-k}/(k!),\{k+1,nlevel+3*k+1\}],
                             {k,1,norder}];
   Do[hitnlevel = 0;
      Do[j=nlevel+3*kx-jk;
         A1 = If[j>nlevel+3*kx-2,0,Bmat[[kx+1]][[j+2+1]]];
         A2 = If[j<3,0,Bmat[[kx-1+1]][[j-3+1]]];
         A4 = Sum[Bmat[[kx-p+1]][[3-neven+1]]
                   If[j>nlevel+3*p,0,Bmat[[p+1]][[j+1]]],
                   {p,1,kx-1}];
         A3 = A4 + Bmat[[kx+1]][[3-neven+1]]
                   If[j>nlevel,0,Bmat[[1]][[j+1]]];
```

```
        Ax = If[j==nlevel, ((nlevel+1)(nlevel+2)A1/2
                           + A2 - (3-2neven)A4)
                           / ((3-2 neven) Bmat[[1]][[nlevel+1]],
                           ((j+1)(j+2)A1/2 + A2
                            - (3-2neven)A3)/(j-nlevel)];
        jx = If[j==nlevel,3-neven,j];
        jx = If[(j<nlevel)&&(hitnlevel==1),nlevel-j+3-neven,jx];
        Ax = If[(j<nlevel)&&(hitnlevel==1),
                (2/(jx(jx-1)) ((jx-nlevel-2) Bmat[[kx+1]][[jx-2+1]]
                - If[jx<5,0,Bmat[[kx-1+1]][[jx-5+1]] + (3-2neven)
                    Sum[Bmat[[kx-p+1]][[3-neven+1]]
                       If[jx>nlevel+3*p+2,0,Bmat[[p+1]][[jx-2+1]]],
                        {p,0,kx-1}]), Ax];
        Bmat = ReplacePart[Bmat,Ax,{kx+1,jx+1}];
        hitnlevel = hitnlevel + If[j==nlevel,1,0];
        {jk,2,nlevel+3*kx-neven,2}],{kx,1,norder}];
   (nlevel+1/2)
    - Sum[(3-2neven)Bmat[[k+1]][[3-neven+1]] g^k,{k,1,norder}]];
}
```

A.4 Roots of a Cubic Polynomial

The roots of the general cubic polynomial

$$ax^3 + bx^2 + cx + d, \tag{A.90}$$

if real, can be written in terms of trigonometric functions. First define

$$p = \frac{b^2 - 3ac}{9a^2} \tag{A.91}$$

and

$$q = \frac{2b^3 - 9abc + 27a^2d}{27a^3}. \tag{A.92}$$

Then the roots will be real if $q^2 - 4p^3 \leq 0$; if this is the case we define θ by

$$\cos 3\theta = -\frac{q}{2p^{3/2}}. \tag{A.93}$$

The three roots are

$$x_n = -\frac{b}{3a} + 2p^{1/2} \cos\left(\theta + \frac{2n\pi}{3}\right) \tag{A.94}$$

with $n = 0, 1, 2$.

A.5 General Propagator for a Quadratic Hamiltonian

Here we construct the general propagator for an arbitrary time-dependent quadratic Hamiltonian

$$H = f(t)A + f^*(t)A^\dagger + h(t)B + d(t)a + d^*(t)a^\dagger + g(t), \tag{A.95}$$

where a and $a^\dagger$ are annihilation and creation operators, and

$$\begin{array}{ll} A = & \frac{1}{2}a^2, \\ A^\dagger = & \frac{1}{2}{a^\dagger}^2, \\ B = & a^\dagger a + \frac{1}{2}. \end{array} \tag{A.96}$$

Our derivation is essentially that due to [317]; an alternative derivation can be found in [267]. We first list the relevant commutators between these operators:

$$[a, a^\dagger] = 1, \tag{A.97}$$

$$[a, A] = 0, \tag{A.98}$$

$$[a, A^\dagger] = a^\dagger, \tag{A.99}$$

$$[a, B] = a, \tag{A.100}$$

$$[a^\dagger, A] = -a, \tag{A.101}$$

$$[a^\dagger, A^\dagger] = 0, \tag{A.102}$$

$$[a^\dagger, B] = -a^\dagger, \tag{A.103}$$

$$[A, A^\dagger] = B, \tag{A.104}$$

$$[A, B] = 2A, \tag{A.105}$$

$$[A^\dagger, B] = -2A^\dagger. \tag{A.106}$$

Anticipating our final result, we define the following unitary operators: the rotation operator $R(\theta)$:

$$R(\theta) = \exp(-i\theta B), \tag{A.107}$$

the squeezing operator $S(r, \phi)$:

$$S(r, \phi) = \exp(r(Ae^{-i2\phi} - A^\dagger e^{i2\phi})), \tag{A.108}$$

and finally the displacement operator $D(\nu)$:

$$D(\nu) = \exp(\nu a^\dagger - \nu^* a). \tag{A.109}$$

Properties of these operators, and their generalization to two coupled harmonic oscillators, are found in [318]. Using the commutation relations derived above, we can show that these operators have the following effect on a:

$$R(\theta) a R^\dagger(\theta) = e^{i\theta} a, \tag{A.110}$$

$$S(r,\phi) a S^\dagger(r,\phi) = a \cosh r + a^\dagger e^{2i\phi} \sinh r, \tag{A.111}$$

$$D(\nu) a D^\dagger(\nu) = a - \nu. \tag{A.112}$$

Finally we note that $S(r,\phi)$ can be decomposed as

$$S(r,\phi) = R(-\phi) S(r,0) R(\phi). \tag{A.113}$$

Now, our ansatz for the general propagator U is

$$U = e^{-i\Theta} S(r,\phi) R(\theta) D(\nu). \tag{A.114}$$

To verify this, we substitute into the Schrödinger equation for the propagator,

$$i\hbar \dot{U} = HU, \tag{A.115}$$

(where $\dot{U} = dU/dt$) and match terms. Now, using our factorization of U in (A.114) we find for $H = i\hbar \dot{U} U^\dagger$ the result

$$\begin{aligned} H = \; & \hbar \dot{\Theta} U + i\hbar \dot{S}(r,\phi) S^\dagger(r,\phi) \\ & + i\hbar S(r,\phi) \dot{R}(\theta) R^\dagger(\theta) S^\dagger(r,\phi) \\ & + i\hbar S(r,\phi) R(\theta) \dot{D}(\nu) D^\dagger(\nu) R^\dagger(\theta) S^\dagger(r,\phi). \end{aligned} \tag{A.116}$$

We proceed to simplify this expression. First, we look at $\dot{S}(r,\phi)$:

$$\begin{aligned}\dot{S}(r,\phi) &= \dot{R}(-\phi)S(r,0)R(\phi) + R(-\phi)\dot{S}(r,0)R(\phi) + R(-\phi)S(r,0)\dot{R}(\phi) \\ &= i\dot{\phi}BS(r,\phi) + R(-\phi)(\dot{r}(A-A^\dagger)R(\phi)S(r,\phi) \\ &\quad +R(-\phi)S(r,0)(-i\dot{\phi}B)S^\dagger(r,0)R(\phi)S(r,\phi).\end{aligned} \tag{A.117}$$

Thus, we find that

$$\dot{S}(r,\phi)S^\dagger(r,\phi) = i\dot{\phi}B + \dot{r}(Ae^{-i2\phi} - A^\dagger e^{i2\phi}) - i\dot{\phi}S(r,\phi)BS^\dagger(r,\phi). \tag{A.118}$$

The last term in (A.118) can be further simplified:

$$\begin{aligned}S(r,\phi)BS^\dagger(r,\phi) &= (a^\dagger\cosh r + ae^{-2i\phi}\sinh r)(a\cosh r + a^\dagger e^{2i\phi}\sinh r) + \tfrac{1}{2} \\ &= B(\cosh^2 r + \sinh^2 r) + 2\sinh r\cosh r(Ae^{-2i\phi} + A^\dagger e^{2i\phi}).\end{aligned} \tag{A.119}$$

So finally,

$$\begin{aligned}\dot{S}(r,\phi)S^\dagger(r,\phi) = \; & i\dot{\phi}(B(1-\cosh^2 r - \sinh^2 r) - 2\sinh r\cosh r(Ae^{-2i\phi} + A^\dagger e^{2i\phi})) \\ & +\dot{r}(Ae^{-2i\phi} - e^{2i\phi}A^\dagger).\end{aligned} \tag{A.120}$$

We now look at the second term of H in (A.116):

$$\begin{aligned}S(r,\phi)\dot{R}(\theta)R^\dagger(\theta)S^\dagger(r,\phi) &= -i\dot{\theta}S(r,\phi)BS^\dagger(r,\phi) \\ &= -i\dot{\theta}(B(\cosh^2 r + \sinh^2 r) \\ &\quad +2\sinh r\cosh r(Ae^{-2i\phi} + A^\dagger e^{2i\phi})).\end{aligned} \tag{A.121}$$

Finally, we look at the last term of (A.116). Using the Zassenhaus formula (A.78)

with $C = 0$,

$$e^{A+B} = e^A e^B e^{-[A,B]/2}, \tag{A.122}$$

we see that $D(\nu)$ can be factored

$$\begin{aligned}D(\nu) &= e^{\nu a^\dagger - \nu^* a} = e^{\nu a^\dagger}e^{-\nu^* a}e^{|\nu|^2[a^\dagger,a]/2} \\ &= e^{\nu a^\dagger}e^{-\nu^* a}e^{-|\nu|^2/2}.\end{aligned} \tag{A.123}$$

Taking the derivative of (A.123) we find

$$\dot{D}(\nu) = \dot{\nu}a^\dagger D - \dot{\nu}^* e^{\nu a^\dagger}ae^{-\nu a^\dagger}D - \frac{1}{2}|\dot{\nu}|^2 D. \tag{A.124}$$

Using the relation in (A.112), we find

$$\dot{D}(\nu)D^{\dagger}(\nu) = \dot{\nu}a^{\dagger} - \dot{\nu}^{*}a + \frac{1}{2}(\nu\dot{\nu}^{*} - \dot{\nu}\nu^{*}). \tag{A.125}$$

Then we find from (A.111):

$$R(\theta)\dot{D}(\nu)D^{\dagger}(\nu)R^{\dagger}(\theta) = \dot{\nu}e^{-i\theta}a^{\dagger} - \dot{\nu}^{*}e^{i\theta}a + \frac{1}{2}(\nu\dot{\nu}^{*} - \dot{\nu}\nu^{*}), \tag{A.126}$$

and finally

$$\begin{aligned} S(r,\phi)R(\theta)\dot{D}(\nu)D^{\dagger}(\nu)R^{\dagger}(\theta)S^{\dagger}(r,\phi) = \quad & \dot{\nu}e^{-i\theta}(a^{\dagger}\cosh r + ae^{-2i\phi}\sinh r) \\ & -\dot{\nu}^{*}e^{i\theta}(a\cosh r + a^{\dagger}e^{2i\phi}\sinh r) \\ & +\tfrac{1}{2}(\nu\dot{\nu}^{*} - \dot{\nu}\nu^{*}). \end{aligned} \tag{A.127}$$

We have now completed the calculation of all terms in $H = i\hbar\dot{U}U^{\dagger}$. Substituting (A.120), (A.121), and (A.127) into (A.116) and comparing with our model Hamiltonian (A.95), we see that r, ϕ, θ, ν, and Θ must satisfy the following differential equations:

$$f(t) = \hbar(\dot{\phi} + \dot{\theta})2\sinh r\cosh re^{-2i\phi} + i\hbar\dot{r}e^{-2i\phi}, \tag{A.128}$$

$$f^{*}(t) = \hbar(\dot{\phi} + \dot{\theta})2\sinh r\cosh re^{2i\phi} + i\hbar\dot{r}e^{2i\phi}, \tag{A.129}$$

$$h(t) = -\hbar\dot{\phi} + \hbar(\dot{\phi} + \dot{\theta})(\cosh^{2} r + \sinh^{2} r), \tag{A.130}$$

$$d(t) = i\hbar\dot{\nu}e^{-i(\theta+2\phi)}\sinh r - i\hbar\dot{\nu}^{*}e^{i\theta}\cosh r, \tag{A.131}$$

$$d^{*}(t) = i\hbar\dot{\nu}e^{-i\theta}\cosh r - i\hbar\dot{\nu}^{*}e^{i(\theta+2\phi)}\sinh r, \tag{A.132}$$

$$g(t) = \hbar\dot{\Theta} + \hbar\frac{i}{2}(\nu\dot{\nu}^{*} - \dot{\nu}\nu^{*}). \tag{A.133}$$

While the above equations are exact, they are not in the most convenient form. To simplify them we define the following auxiliary variables

$$\begin{aligned} \alpha &= e^{-i\theta}\cosh r, \\ \beta &= -e^{-i(\theta+2\phi)}\sinh r. \end{aligned} \tag{A.134}$$

These variables satisfy the following constraint $|\alpha|^2 - |\beta|^2 = 1$, and thus

$$\alpha\dot{\alpha}^* + \dot{\alpha}\alpha^* = \beta\dot{\beta}^* + \dot{\beta}\beta^*. \tag{A.135}$$

By direct substitution of (A.134) it can be verified that (A.128)-(A.131) can be written in terms of α and β:

$$f(t) = -i\hbar(\dot{\beta}\alpha^* - \beta\dot{\alpha}^*), \tag{A.136}$$

$$f^*(t) = i\hbar(\alpha\dot{\beta}^* - \dot{\alpha}\beta^*), \tag{A.137}$$

$$\begin{aligned} h(t) &= i\hbar(\dot{\alpha}\alpha^* - \beta\dot{\beta}^*) \\ &= i\hbar(\dot{\beta}\beta^* - \alpha\dot{\alpha}^*), \end{aligned} \tag{A.138}$$

$$d(t) = -i\hbar(\dot{\nu}\beta + \dot{\nu}^*\alpha^*), \tag{A.139}$$

$$d^*(t) = i\hbar(\dot{\nu}^*\beta^* + \dot{\nu}\alpha). \tag{A.140}$$

Equations (A.136)-(A.140) can in fact be inverted to yield

$$\hbar\dot{\alpha} = -i(f^*\beta + h\alpha), \tag{A.141}$$

$$\hbar\dot{\beta} = i(f\alpha + h\beta), \tag{A.142}$$

$$\hbar\dot{\nu} = -i(\beta^* d + \alpha^* d^*), \tag{A.143}$$

and their complex conjugates, and finally

$$\hbar\dot{\Theta} = g - \hbar\frac{i}{2}(\nu\dot{\nu}^* - \dot{\nu}\nu^*). \tag{A.144}$$

These equations must be supplemented by the initial condition that $U(0) = I$, where I is the identity operator. This is satisfied by putting $r(0) = 0$, $\phi(0) = 0$, $\theta(0) = 0$,

$\nu(0) = 0$, and $\Theta(0) = 0$, and thus $\alpha(0) = 1$, $\beta(0) = 0$. The solution of these (A.141)-(A.144) and the relations

$$\cosh r = |\alpha|, \tag{A.145}$$

$$e^{i\theta} = \frac{\alpha^*}{|\alpha|}, \tag{A.146}$$

$$e^{2i\phi} = -\frac{\alpha\beta^*}{|\alpha||\beta|}, \tag{A.147}$$

fully determine the propagator

$$U = e^{-i\Theta} S(r, \phi) R(\theta) D(\nu). \tag{A.148}$$

BIBLIOGRAPHY

[1] Feynman, R. P. *Int. J. Theor. Phys.* **21**, 467 (1982).

[2] Jozsa, R. In *The Geometric Universe,* Huggett, S. A., Mason, L. J., Tod, K. P., Tsou, S. T., and Woodhouse, N. M. J., editors (Oxford University Press, New York, 1998).

[3] Jozsa, R. and Linden, N. *Proc. R. Soc. Lond. A* **459**, 2011 (2003).

[4] Shor, P. W. In *Proc. 35th Annu. Symp. Foundations of Computer Science,* Goldwasser, S., editor, 124 (IEEE Computer Society Press, Los Alamitos, California, 1994).

[5] Ekert, A. and Jozsa, R. *Rev. Mod. Phys.* **68**, 733 (1996).

[6] Makhlin, Y., Schön, G., and Shnirman, A. *Rev. Mod. Phys.* **73**, 357 (2001).

[7] Nielsen, M. A. and Chuang, I. L. *Quantum Computation and Quantum Information.* Cambridge University Press, (2000).

[8] Galindo, A. and Martin-Delgado, M. A. *Rev. Mod. Phys.* **74**, 347 (2002).

[9] Ott, E. *Chaos in dynamical systems.* Cambridge University Press, New York, (1993).

[10] Magnus, W., Karrass, A., and Solitar, D. *Combinatorial group theory: presentations of groups in terms of generators and relations.* Dover, New York, (1976).

[11] Xu, H. *Quantum Phenomena in Josephson junction circuits and their use as qubits.* PhD thesis, University of Maryland, (2004).

[12] Feynman, R. P. *Found. Phys.* **16**, 507 (1986).

[13] Schumacher, B. *Phys. Rev. A* **51**, 2738 (1995).

[14] Deutsch, D. *Proc. R. Soc. London, Ser. A* **400**, 97 (1985).

[15] Deutsch, D. *Proc. R. Soc. London, Ser. A* **425**, 73 (1989).

[16] DiVincenzo, D. P. *Phys. Rev. A* **51**, 1015 (1995).

[17] Barenco, A. *Proc. R. Soc. Lond. A* **449**, 679 (1995).

[18] Lloyd, S. *Phys. Rev. Lett.* **75**, 346 (1995).

[19] Deutsch, D., Barenco, A., and Ekert, A. *Proc. R. Soc. Lond. A* **449**, 669 (1995).

[20] Barenco, A., Bennett, C. H., Cleve, R., DiVincenzo, D. P., Margolus, N., Shor, P., Sleator, T., Smolin, J. A., and Weinfurter, H. *Phys. Rev. A* **52**, 3457 (1995).

[21] Weaver, N. *J. Math. Phys.* **41**, 240 (2000).

[22] Kraus, B. and Cirac, J. I. *Phys. Rev. A* **63**, 062309 (2001).

[23] Khaneja, N., Brockett, R., and Glaser, S. J. *Phys. Rev. A* **63**, 032308 (2001).

[24] Makhlin, Y. *Quant. Inf. Proc.* **1**, 243 (2002).

[25] Zhang, J., Vala, J., Sastry, S., and Whaley, K. B. *Phys. Rev. A* **67**, 042313 (2003).

[26] Bennett, C. H., Brassard, G., Crépeau, C., Josza, R., Peres, A., and Wootters, W. K. *Phys. Rev. Lett.* **70**, 1895 (1993).

[27] Bennett, C. H., Bernstein, H. J., Popescu, S., and Schumacher, B. *Phys. Rev. A* **53**, 2046 (1996).

[28] Wootters, W. K. *Phys. Rev. Lett.* **80**, 2245 (1998).

[29] Bremner, M. J., Dawson, C. M., Dodd, J. L., Gilchrist, A., Harrow, A. W., Mortimer, D., Nielsen, M. A., and Osborne, T. J. *Phys. Rev. Lett.* **89**, 247902 (2002).

[30] Zhang, J., Vala, J., Sastry, S., and Whaley, K. B. *Phys. Rev. Lett.* **91**, 027903 (2003).

[31] Zhang, J., Vala, J., Sastry, S., and Whaley, K. B. *Phys. Rev. A* **69**, 042309 (2004).

[32] Vidal, G., Hammerer, K., and Cirac, J. I. *Phys. Rev. Lett.* **88**, 237902 (2002).

[33] Hammerer, K., Vidal, G., and Cirac, J. I. *Phys. Rev. A* **66**, 062321 (2002).

[34] Childs, A. M., Haselgrove, H. L., and Nielsen, M. A. *Phys. Rev. A* **68**, 052311 (2003).

[35] Haselgrove, H. L., Nielsen, M. A., and Osborne, T. J. *Phys. Rev. A* **68**, 042303 (2003).

[36] Vidal, G. and Dawson, C. M. *Phys. Rev. A* **69**, 010301 (2004).

[37] Strauch, F. W., Johnson, P. R., Dragt, A. J., Lobb, C. J., Anderson, J. R., and Wellstood, F. C. *Phys. Rev. Lett.* **91**, 167005 (2003).

[38] Vandersypen, L. M. and Chuang, I. L. quant-ph/0404064 (2004).

[39] Ramakrishna, V. and Rabitz, H. *Phys. Rev. A* **54**, 1715 (1996).

[40] Lloyd, S. *Science* **273**, 1073 (1996).

[41] Ekert, A. and Jozsa, R. *Phil. Trans. R. Soc. Lond. A* **356**, 1769 (1998).

[42] Wiesner, S. quant-ph/9603028 (1996).

[43] Zalka, C. *Proc. R. Soc. Lond. A* **454**, 313 (1998).

[44] Dodd, J. L., Nielsen, M. A., Bremner, M. J., and Thew, R. T. *Phys. Rev. A* **65**, 040301 (2002).

[45] Nielsen, M. A., Bremner, M. J., Dodd, J. L., Childs, A. M., and Dawson, C. M. *Phys. Rev. A* **66**, 022317 (2002).

[46] Nielsen, M. A., Dawson, C. M., Dodd, J. L., Gilchrist, A., Mortimer, D., Osborne, T. J., Bremner, M. J., Harrow, A. W., and Hines, A. *Phys. Rev. A* **67**, 052301 (2003).

[47] Bremner, M. J., Dodd, J. L., Nielsen, M. A., and Bacon, D. *Phys. Rev. A* **69**, 012313 (2004).

[48] Viola, L., Knill, E., and Lloyd, S. *Phys. Rev. Lett.* **82**, 2417 (1999).

[49] Viola, L., Lloyd, S., and Knill, E. *Phys. Rev. Lett.* **83**, 4888 (1999).

[50] Zanardi, P. *Phys. Lett. A* **258**, 77 (1999).

[51] Ruth, R. D. *IEEE Trans. Nucl. Sci.* **30**, 2669 (1983).

[52] Neri, F. *Lie Algebras and Canonical Integration.* University of Maryland preprint (1988).

[53] Koseleff, P. *Formal Calculus for Lie Methods in Hamiltonian Mechanics.* PhD thesis, Ecole Polytechnique, (1993).

[54] Yoshida, H. *Phys. Lett. A* **150**, 262 (1990).

[55] Suzuki, M. *Phys. Lett. A* **146**, 319 (1990).

[56] Creutz, M. and Gocksch, A. *Phys. Rev. Lett.* **63**, 9 (1989).

[57] Forest, E. and Ruth, R. D. *Physica D* **43**, 105 (1990).

[58] Sheng, Q. *IMA J. Num. Anal.* **9**, 199 (1989).

[59] Suzuki, M. *J. Math. Phys.* **32**, 400 (1991).

[60] Chin, S. A. *Phys. Rev. E* **69**, 046118 (2004).

[61] Suzuki, M. *Phys. Lett. A* **201**, 425 (1995).

[62] Chin, S. A. *Phys. Lett. A* **226**, 344 (1997).

[63] Chin, S. A. and Chen, C. R. *J. Chem. Phys.* **114**, 7338 (2001).

[64] Chin, S. A. and Kidwell, D. W. *Phys. Rev. E* **62**, 8746 (2000).

[65] Omelyan, I. P., Mryglod, I. M., and Folk, R. *Phys. Rev. E* **66**, 026701 (2002).

[66] Chin, S. A. physics/0312005 (2004).

[67] Feit, M. D., Fleck, Jr., J. A., and Steiger, A. *J. Comp. Phys.* **47**, 412 (1982).

[68] Takahashi, K. and Ikeda, K. *J. Chem. Phys.* **99**, 8680 (1993).

[69] Leforestier, C., Bisseling, R. H., Cerjan, C., Feit, M. D., Friesner, R., Guldberg, A., Hammerich, A., Jolicard, G., Karrlein, W., Meyer, H., Lipkin, N., Roncero, O., and Kosloff, R. *J. Comp. Phys.* **94**, 59 (1991).

[70] Chin, S. A. and Chen, C. R. *J. Chem. Phys.* **117**, 1409 (2002).

[71] Josephson, B. *Phys. Lett.* **1**, 251 (1962).

[72] Bardeen, J., Cooper, L. N., and Schrieffer, J. R. *Phys. Rev.* **108**, 1175 (1957).

[73] Bardeen, J. *Phys. Rev. Lett.* **6**, 57 (1961).

[74] Bardeen, J. *Phys. Rev. Lett.* **9**, 147 (1962).

[75] Packard, R. E. *Rev. Mod. Phys.* **70**, 641 (1998).

[76] Davis, J. C. and Packard, R. E. *Rev. Mod. Phys.* **74**, 741 (2002).

[77] Feynman, R. P., Leighton, R. B., and Sands, M. *Lectures on Physics.* Addison-Wesley, New York, (1965).

[78] Anderson, P. W. In *Lectures on The Many-Body Problem, Volume 2,* Caianiello, E. R., editor (Academic Press, New York, 1964).

[79] Leggett, A. J. *Prog. Theor. Phys. (Suppl.)* **69**, 80 (1980).

[80] Leggett, A. J. *J. Phys. Condens. Matter* **14**, R415 (2001).

[81] Voss, R. F. and Webb, R. A. *Phys. Rev. Lett.* **47**, 265 (1981).

[82] Washburn, S., Webb, R. A., Voss, R. F., and Faris, S. M. *Phys. Rev. Lett.* **54**, 2712 (1985).

[83] Schwartz, D. B., Sen, B., Archie, C. N., and Lukens, J. E. *Phys. Rev. Lett.* **55**, 1547 (1985).

[84] Devoret, M. H., Martinis, J. M., and Clarke, J. *Phys. Rev. Lett.* **55**, 1908 (1985).

[85] Martinis, J. M., Devoret, M. H., and Clarke, J. *Phys. Rev. Lett.* **55**, 1543 (1985).

[86] Martinis, J. M., Devoret, M. H., and Clarke, J. *Phys. Rev. B* **35**, 4682 (1987).

[87] Friedman, J. R., Patel, V., Chen, W., Tolpygo, S. K., and Lukens, J. E. *Nature* **406**, 43 (2000).

[88] van der Wal, C. H., ter Haar, A. C. J., Wilhelm, F. K., Schouten, R. N., Harmans, C. J. P. M., Orlando, T. P., Lloyd, S., and Mooij, J. E. *Science* **290**, 773 (2000).

[89] Nakamura, Y., Pashkin, Y. A., and Tsai, J. S. *Nature* **398**, 786 (1999).

[90] Pashkin, Y. A., Yamamoto, T., Astafiev, O., Nakamura, Y., Averin, D. V., and Tsai, J. S. *Nature* **421**, 823 (2003).

[91] Yamamoto, T., Pashkin, Y. A., Astafiev, O., Nakamura, Y., and Tsai, J. S. *Nature* **425**, 941 (2003).

[92] Yu, Y., Han, S., Chu, X., Chu, S.-I., and Wang, Z. *Science* **296**, 889 (2002).

[93] Martinis, J. M., Nam, S., Aumentado, J., and Urbina, C. *Phys. Rev. Lett.* **89**, 117901 (2002).

[94] Chiorescu, I., Nakamura, Y., Harmans, C. J. P. M., and Mooij, J. E. *Science* **299**, 1869 (2003).

[95] Carruthers, P. and Nieto, M. M. *Rev. Mod. Phys.* **40**, 411 (1968).

[96] Leggett, A. J. In *Percolation, Localization, and Superconductivity,* Goldman, A. M. and Wolf, S. A., editors, 1, (1983).

[97] Caldeira, A. O. and Leggett, A. J. *Ann. Phys.* **149**, 374 (1983).

[98] Leggett, A. J. In *Essays in Theoretical Physics in honour of Dirk ter Haar,* Parry, W. E., editor, 95 (Pergamon, New York, 1984).

[99] Leggett, A. J. In *Directions in Condensed Matter Physics,* Grinstein, G. and Mazenko, G., editors, 187, (1986).

[100] Leggett, A. J. In *Chance and Matter,* Souletie, J., Vannimenus, J., and Stora, R., editors, 395 (Elsevier, Amsterdam, 1987).

[101] Schön, G. and Zaikin, A. D. *Physics Reports* **198**, 237 (1990).

[102] Cooper, L. N. *Phys. Rev.* **104**, 1189 (1956).

[103] Anderson, P. *Phys. Rev.* **112**, 1900 (1958).

[104] Cohen, M. H., Falicov, L. M., and Phillips, J. C. *Phys. Rev. Lett.* **8**, 316 (1962).

[105] Prange, R. E. *Phys. Rev.* **131**, 1083 (1963).

[106] Ambegaokar, V. and Baratoff, A. *Phys. Rev. Lett.* **10**, 486 (1963).

[107] Wallace, P. and Stavn, M. *Can. J. Phys.* **43**, 411 (1964).

[108] Loss, D. and Mullen, K. *J. Phys. A: Math. Gen.* **25**, L235 (1992).

[109] Anderson, P. *Rev. Mod. Phys.* **38**, 298 (1966).

[110] Leggett, A. J. *Prog. Theor. Phys.* **36**, 901 (1966).

[111] Leggett, A. J. *Rev. Mod. Phys.* **73**, 307 (2001).

[112] Anglin, J. R., Drummond, P., and Smerzi, A. cond-mat/0206586 (2000).

[113] Anglin, J. R., Drummond, P., and Smerzi, A. *Phys. Rev. A* **64**, 063605 (2001).

[114] Paraoanu, G.-S., Kohler, S., Sols, F., and Leggett, A. J. *J. Phys. B* **34**, 4689 (2001).

[115] Ferrell, R. A. and Prange, R. E. *Phys. Rev. Lett.* **10**, 479 (1963).

[116] Rogovin, D., Nagel, J., and Scully, M. *Phys. Rev. B* **23**, 1156 (1981).

[117] Lee, P. A. and Scully, M. O. *Phys. Rev. B* **3**, 769 (1971).

[118] Rogovin, D., Scully, M., and DiRienzo, A. *Phys. Rev. B* **18**, 3231 (1978).

[119] Ferrell, R. A. *Phys. Rev. B* **25**, 496 (1982).

[120] DiRienzo, A. L. and Young, R. A. *Phys. Rev. B* **25**, 6684 (1982).

[121] Unnerstall, T. and Rieckers, A. *Phys. Rev. B* **39**(4), 2173 (1989).

[122] Stephen, M. J. *Phys. Rev. Lett.* **21**, 1629 (1968).

[123] Scully, M. O. and Lee, P. A. *Phys. Rev. Lett.* **22**, 23 (1969).

[124] McCumber, D. E. *Phys. Rev. Lett.* **23**, 1228 (1969).

[125] Unnerstall, T. and Rieckers, A. *Phys. Rev. B* **45**, 10115 (1992).

[126] DiRienzo, A. L. and Young, R. A. *Am. J. Phys.* **51**, 587 (1982).

[127] Shimshoni, E., Gefen, Y., and Fishman, S. *Phys. Rev. B* **40**, 2158 (1989).

[128] Shimshoni, E. and Ben-Jacob, E. *Phys. Rev. B* **43**, 2705 (1991).

[129] Ambegaokar, V., Eckern, U., and Schön, G. *Phys. Rev. Lett.* **48**, 1745 (1982).

[130] Ambegaokar, V. In *Percolation, Localization, and Superconductivity,* Goldman, A. M. and Wolf, S. A., editors. NATO ASI Series B, (1983).

[131] Eckern, U., Schön, G., and Ambegaokar, V. *Phys. Rev. B* **30**, 6419 (1984).

[132] Ben-Jacob, E. and Geven, Y. *Phys. Lett. A* **108**, 289 (1985).

[133] Krieger, J. B. and Iafrate, G. J. *Phys. Rev. B* **33**, 5494 (1986).

[134] Shirley, J. H. *Phys. Rev.* **138**, B979 (1965).

[135] Avron, J. E. and Nemirovsky, J. *Phys. Rev. Lett.* **68**, 2212 (1992).

[136] Mullen, K., Loss, D., and Stoof, H. T. C. *Phys. Rev. B* **47**, 2689 (1993).

[137] Rogovin, D. and Scully, M. *Phys. Rev. B* **21**, 3868 (1980).

[138] Rogovin, D. and Nagel, J. *Phys. Rev. B* **26**, 3698 (1989).

[139] Unnerstall, T. *J. of Stat. Phys.* **54**, 379 (1989).

[140] Caldeira, A. O. and Leggett, A. J. *Physica* **121A**, 587 (1983).

[141] Likharev, K. and Zorin, A. *J. Low Temp. Phys.* **59**, 347 (1985).

[142] Schön, G. and Zaikin, A. *Physica B* **152**, 203 (1988).

[143] Zwerger, W., Dorsey, A. T., and Fisher, M. P. A. *Phys. Rev. B* **34**, 6518 (1986).

[144] Loss, D. and Mullen, K. *Phys. Rev. A* **43**, 2129 (1991).

[145] Apenko, S. *Phys. Lett. A* **142**, 277 (1989).

[146] Berkley, A. J., Xu, H., Gubrud, M. A., Ramos, R. C., Anderson, J. R., Lobb, C. J., and Wellstood, F. C. *Phys. Rev. B.* **68**, 060502 (2003).

[147] Wannier, G. H. *Phys. Rev.* **117**, 432 (1960).

[148] Zak, J. *Phys. Rev. Lett.* **20**, 1477 (1968).

[149] Wannier, G. H. *Phys. Rev.* **181**, 1364 (1969).

[150] Zak, J. *Phys. Rev.* **181**, 1366 (1969).

[151] Nenciu, G. *Rev. Mod. Phys.* **63**, 91 (1991).

[152] Glück, M., Kolovsky, A. R., Korsch, H. J., and Moiseyev, N. *Eur. Phys. J. D* **4**, 239 (1998).

[153] Glück, M., Kolovsky, A., and Korsch, H. J. *J. Phys. A* **32**, L49 (1999).

[154] Glück, M., Kolovsky, A. R., and Korsch, H. J. *Phys. Rev. Lett.* **83**, 891 (1999).

[155] Glück, M., Kolovsky, A. R., and Korsch, H. J. *J. Opt. B* **2**, 694 (2000).

[156] Thommen, Q., Garreua, J. C., and Zehnle, V. *Phys. Rev. A* **65**, 053406 (2002).

[157] Thommen, Q., Garreau, J. C., and Zehnle, V. *Am. J. Phys.* **72**, 1017 (2004).

[158] Ben Dahan, M., Peik, E., Reichel, J., Castin, Y., and Salomon, C. *Phys. Rev. Lett.* **76**, 4508 (1996).

[159] Mendez, E. E., Agulló-Rueda, F., and Hong, J. M. *Phys. Rev. Lett.* **60**, 2426 (1988).

[160] Voisin, P., Bleuse, J., Bouche, C., Gaillard, S., Alibert, C., and Regreny, A. *Phys. Rev. Lett.* **61**, 1639 (1988).

[161] Wilkinson, S. R., Bharucha, C. F., Madison, K. W., Niu, Q., and Raizen, M. G. *Phys. Rev. Lett.* **76**, 4512 (1996).

[162] Wilkinson, S. R., Bharucha, C. F., Fischer, M. C., Madison, K. W., Morrow, P. R., Niu, Q., Sundaram, B., and Raizen, M. G. *Nature* **387**, 575 (1997).

[163] Bharucha, C. F., Madison, K. W., Morrow, P. R., Wilkinson, S. R., Sundaram, B., and Raizen, M. G. *Phys. Rev. A* **55**, R857 (1997).

[164] Fischer, M. C., Gutiérrez-Medina, B., and Raizen, M. G. *Phys. Rev. Lett.* **87**, 040402 (2001).

[165] Glück, M., Kolovsky, A. R., and Korsch, H. J. *Phys. Rep.* **366**, 103 (2002).

[166] Liu, W. M., Fan, W. B., Zheng, W. M., Liang, J. Q., and Chui, S. T. *Phys. Rev. Lett.* **88**, 170408 (2002).

[167] Schmidt, J. M., Cleland, A. N., and Clarke, J. *Phys. Rev. B* **43**, 229 (1991).

[168] Winter, R. G. *Phys. Rev.* **123**, 1503 (1961).

[169] Ludviksson, A. *J. Phys. A* **20**, 4733 (1987).

[170] Mandelshtam, V. A., Ravuri, T. R., and Taylor, H. S. *Phys. Rev. Lett.* **70**, 1932 (1993).

[171] Gamow, G. *Z. Phys.* **51**, 204 (1928).

[172] Siegert, A. J. F. *Phys. Rev.* **56**, 750 (1939).

[173] Bohm, A., Gadella, M., and Mainland, G. B. *Am. J. Phys.* **57**, 1103 (1989).

[174] Gurney, R. W. and Condon, E. U. *Phys. Rev.* **33**, 127 (1929).

[175] Merzbacher, E. *Phys. Today* **10**, 44 (2002).

[176] Larkin, A. I. and Ovchinnikov, Y. N. *Sov. Phys. JETP* **64**, 185 (1986).

[177] Chow, K. S., Browne, D. A., and Ambegaokar, V. *Phys. Rev. B* **37**, 1624 (1988).

[178] Kopietz, P. and Chakravarty, S. *Phys. Rev. B* **38**, 97 (1988).

[179] Newton, R. G. *Scattering Theory of Waves and Particles.* Dover, New York, (2002).

[180] Kruppa, A. T. and Arai, K. *Phys. Rev. A* **59**, 3556 (1999).

[181] Massmann, H. *Am. J. Phys.* **53**, 679 (1985).

[182] Wigner, E. P. *Phys. Rev.* **98**, 145 (1955).

[183] Khalfin, L. A. *Sov. Phys. JETP* **6**, 1053 (1958).

[184] Fonda, L., Ghirardi, G. C., and Rimini, A. *Rep. Prog. Phys.* **41**, 589 (1978).

[185] Dicus, D. A., Repko, W. W., Schwitters, R. F., and Tinsley, T. M. *Phys. Rev. A* **65**, 032116 (2002).

[186] van Dijk, W. and Nogami, Y. *Phys. Rev. Lett.* **83**, 2867 (1999).

[187] van Dijk, W. and Nogami, Y. *Phys. Rev. C* **65**, 024608 (2002).

[188] Garcai-Calderon, G., Mateos, J. L., and Moshinsky, M. *Phys. Rev. Lett.* **74**, 337 (1995).

[189] Cavalcanti, R. M. *Phys. Rev. Lett.* **80**, 4353 (1998).

[190] van Dijk, W. and Nogami, Y. *Phys. Rev. Lett.* **90**, 028901 (2003).

[191] de la Madrid, R. and Gadella, M. *Am. J. Phys.* **70**, 626 (2002).

[192] Bohm, A., Harshman, N. L., and Walther, H. *Phys. Rev. A* **66**, 012107 (2002).

[193] Misra, B. and Sudarshan, E. C. G. *J. Math. Phys.* **18**, 756 (1977).

[194] Kofman, A. G. and Kurizki, G. *Nature* **405**, 546 (2000).

[195] Barone, A., Kurizki, G., and Kofman, A. G. *Phys. Rev. Lett.* **92**, 200403 (2004).

[196] Lukes, T. and Somaratna, K. T. S. *J. Phys. C* **2**, 586 (1969).

[197] Whitcombe, A. R. *J. Phys. C* **4**, 1 (1971).

[198] Moyer, C. A. *J. Phys. C* **6**, 1461 (1973).

[199] Geltman, S. *J. Phys. B* **11**, 3323 (1978).

[200] Fernandez, F. M. and Castro, E. A. *Am. J. Phys.* **53**, 757 (1985).

[201] Elberfeld, W. and Kleber, M. *Z. Phys. B* **73**, 23 (1988).

[202] Glasser, M. L., Jaskolski, W., Garcia-Moliner, F., and Velasco, V. R. *Phys. Rev. B* **42**, 7630 (1990).

[203] Cavalcanti, R. M., Giacconi, P., and Soldati, R. *J. Phys. A* **36**, 12065 (2003).

[204] Alvarez, G. and Sundaram, B. *Phys. Rev. A* **68**, 013407 (2003).

[205] Cocke, S. and Reichl, L. E. *Phys. Rev. A* **52**, 4515 (1995).

[206] Nickel, J. C. and Reichl, L. E. *Phys. Rev. A* **58**, 4210 (1998).

[207] Emmanouilidou, A. and Reichl, L. E. *Phys. Rev. A* **62**, 022709 (2000).

[208] Korsch, H. J. and Mossmann, S. *J. Phys. A* **36**, 2139 (2003).

[209] Dunne, G. V. and Gauthier, C. S. *Phys. Rev. A* **69**, 053409 (2004).

[210] Abramowitz, M. and Stegun, I. *Handbook of Mathematical Functions.* Dover, (1965).

[211] Rabinovitch, A., Thieberger, R., and Friedman, M. *J. Phys. B* **18**, 393 (1985).

[212] Levine, R. D. *Quantum Mechanics of Molecular Rate Processes.* Clarendon Press, (1969).

[213] Bohm, D. *Quantum Theory.* Dover, New York, (1989).

[214] Herbst, I. W. *Commun. Math. Phys.* **75**, 197 (1980).

[215] Balslev, E. and Combes, J. M. *Commun. Math. Phys.* **22**, 280 (1971).

[216] Simon, B. *Ann. Math.* **97**, 247 (1973).

[217] Herbst, I. W. and Simon, B. *Phys. Rev. Lett.* **41**, 67 (1978).

[218] Moiseyev, N. *Phys. Rep.* **302**, 212 (1998).

[219] Nicolaides, C. A. and Themelis, S. I. *Phys. Rev. A* **45**, 349 (1992).

[220] Luc-Koenig, E. and Bachelier, A. *J. Phys. B* **13**, 1743 (1980).

[221] Luc-Koenig, E. and Bachelier, A. *J. Phys. B* **13**, 1769 (1980).

[222] Galindo, A. and Pascual, P. *Quantum Mechanics*. Springer-Verlag, (1991).

[223] Bender, C. M. and Turbiner, A. *Phys. Lett. A* **173**, 442 (1993).

[224] Caliceti, E. and Maioli, M. *Ann. de l'Institut Henri Poincare-A* **38**, 175 (1983).

[225] Caliceti, E., Graffi, S., and Maioli, M. *Commun. Math. Phys.* **75**, 51 (1980).

[226] Bender, C. M. and Boettcher, S. *Phys. Rev. Lett.* **80**, 5243 (1998).

[227] Bender, C. M. and Dunne, G. V. *J. Math. Phys.* **40**, 4616 (1999).

[228] Delabaere, E. and Pham, F. *Phys. Lett. A* **250**, 25 (1998).

[229] Delabaere, E. and Pham, F. *Phys. Lett. A* **250**, 29 (1998).

[230] Bender, C. M., Brody, D. C., and Jones, H. F. *Phys. Rev. Lett.* **89**, 270401 (2002).

[231] Bender, C. M. and Wu, T. T. *Phys. Rev.* **184**, 1231 (1969).

[232] Drummond, J. E. *J. Phys. A* **14**, 1651 (1981).

[233] Alvarez, G. *Phys. Rev. A* **37**, 4079 (1988).

[234] Caliceti, E. *J. Phys. A* **33**, 3753 (2000).

[235] Kleinert, H. and Mustapic, I. *Internat. J. Modern Phys. A* **11**, 4383 (1996).

[236] Alvarez, G. *J. Phys. A* **22**, 617 (1989).

[237] Waxman, D. and Leggett, A. J. *Phys. Rev. B* **32**, 4450 (1985).

[238] Shepard, H. K. *Phys. Rev. D* **27**, 1288 (1983).

[239] Yaris, R., Bendler, J., Lovett, R. A., Bender, C. M., and Fedders, P. A. *Phys. Rev. A* **18**, 1816 (1978).

[240] Furry, W. H. *Phys. Rev.* **71**, 360 (1947).

[241] Merzbacher, E. *Quantum Theory.* Wiley and Sons, (1970).

[242] Coleman, S. *Phys. Rev. D* **15**, 2929 (1977).

[243] Caldeira, A. O. and Leggett, A. J. *Phys. Rev. Lett.* **46**, 211 (1981).

[244] Schmid, A. *Ann. Phys.* **170**, 333 (1986).

[245] Feynman, R. P. and Hibbs, A. R. *Quantum mechanics and path integrals.* McGraw-Hill, (1965).

[246] Kleinert, H. *Path integrals in quantum mechanics, statistics and polymer physics.* World Scientific, (1995).

[247] Callan, C. G. and Coleman, S. *Phys. Rev. D* **16**, 1762 (1977).

[248] Coleman, S. *Aspects of Symmetry.* Cambridge University Press, (1985).

[249] Holstein, B. R. *Am. J. Phys.* **56**, 338 (1988).

[250] Affleck, I. K. and Luccia, F. D. *Phys. Rev. D* **20**, 3168 (1979).

[251] Weiss, U. and Haeffner, W. *Phys. Rev. D* **27**, 2916 (1983).

[252] Hontscha, W., Hänggi, P., and Pollak, E. *Phys. Rev. B* **41**, 2210 (1990).

[253] Allen, L. and Eberly, J. H. *Optical Resonance and Two-Level Atoms.* Dover, New York, (1987).

[254] Blais, A., Maassen van den Brink, A., and Zagoskin, A. M. *Phys. Rev. Lett.* **90**, 127901 (2003).

[255] Cleland, A. N. and Geller, M. R. *Phys. Rev. Lett.* **93**, 070501 (2004).

[256] Plourde, B. L. T., Zhang, J., Whaley, K. B., Wilhelm, F. K., Robertson, T. L., Hime, T., Linzen, S., Reichardt, P. A., Wu, C.-E., and Clarke, J. *Phys. Rev. B* **70**, 140501 (2004).

[257] Shore, B. W. *The Theory of Coherent Atomic Excitation.* Wiley and Sons, New York, (1990).

[258] Steffen, M., Martinis, J. M., and Chuang, I. L. *Phys. Rev. B* **89**, 224518 (2003).

[259] Amin, M. H. S. cond-mat/0407080 (2004).

[260] Meier, F. and Loss, D. cond-mat/0408594 (2004).

[261] Tian, L. and Lloyd, S. *Phys. Rev. A* **62**, 050301 (2000).

[262] Palao, J. P. and Kosloff, R. *Phys. Rev. Lett.* **89**, 188301 (2002).

[263] Peirce, A. P., Dahleh, M. A., and Rabitz, H. *Phys. Rev. A* **37**, 4950 (1988).

[264] Ramakrishna, V., Dahleh, M. V. S. M., Rabitz, H., and Peirce, A. *Phys. Rev. A* **51**, 960 (1995).

[265] Kosloff, R. and Kosloff, D. *J. Comput. Phys.* **63**, 363 (1986).

[266] Caoto, A., Gyarmati, B., Kruppa, T., Pal, K. F., and Moiseyev, N. *Phys. Rev. A* **41**, 3469 (1990).

[267] Yuen, H. P. *Phys. Rev. A* **13**, 2226 (1976).

[268] Johnson, P. R., Strauch, F. W., Dragt, A. J., Ramos, R. C., Lobb, C. J., Anderson, J. R., and Wellstood, F. C. *Phys. Rev. B* **67**, 020509 (2003).

[269] Berkley, A. J., Xu, H., Ramos, R. C., Gubrud, M. A., Strauch, F. W., Johnson, P. R., Anderson, J. R., Dragt, A. J., Lobb, C. J., and Wellstood, F. C. *Science* **300**, 1548 (2003).

[270] Berkley, A. J. *A Superconducting Quantum Bit.* PhD thesis, University of Maryland, (2003).

[271] Marquardt, F. and Bruder, C. *Phys. Rev. B* **63**, 054514 (2001).

[272] Plastina, F., Fazio, R., and Palma, G. M. *Phys. Rev. B* **64**, 113306 (2001).

[273] Buisson, O. and Hekking, F. W. J. cond-mat/0008275 (2000).

[274] Al-Saidi, W. A. and Stroud, D. *Phys. Rev. B* **65**, 014512 (2001).

[275] Hekking, F. W. J., Buisson, O., Balestro, F., and Vergniory, M. G. cond-mat/0201284 (2002).

[276] Plastina, F. and Falci, G. *Phys. Rev. B* **67**, 224514 (2003).

[277] Mooij, J. E., Orlando, T. P., Levitov, L., Tian, L., van der Wal, C. H., and Lloyd, S. *Science* **285**, 1036 (1999).

[278] Orlando, T. P., Mooij, J. E., Tian, L., van der Wal, C. H., Levitov, L. S., Lloyd, S., and Mazo, J. J. *Phys. Rev. B* **60**, 15398 (1999).

[279] Valkering, T. P., Hooijer, C. L. A., and Kroon, M. F. *Physica D* **135**, 137 (2000).

[280] Abdullaev, F. K., Abdumalikov,Jr., A.A., Buisson, O., and Tsoy, E. N. *Phys. Rev. B* **62**, 6766 (2000).

[281] Monroe, C., Meekhof, D. M., King, B. E., Itano, W. M., and Wineland, D. J. *Phys. Rev. Lett.* **75**, 4714 (1995).

[282] Cirac, J. I. and Zoller, P. *Phys. Rev. Lett.* **74**, 4091 (1995).

[283] Charron, E., Tiesinga, E., Mies, F., and Williams, C. *Phys. Rev. Lett.* **88**, 077901 (2002).

[284] Zhou, X., Zhou, Z.-W., Guo, G.-C., and Feldman, M. J. *Phys. Rev. Lett.* **89**, 197903 (2002).

[285] Benjamin, S. C. and Bose, S. *Phys. Rev. Lett.* **90**, 247901 (2003).

[286] Wu, L.-A. and Lidar, D. A. *Phys. Rev. Lett.* **91**, 097904 (2003).

[287] Brennen, G. K., Song, D., and Williams, C. J. *Phys. Rev. A* **67**, 050302 (2003).

[288] Bennett, C. H., Brassard, G., Popescu, S., Schumacher, B., Smolin, J. A., and Wootters, W. K. *Phys. Rev. Lett.* **76**, 722 (1996).

[289] Nielsen, M. A. *Phys. Lett. A* **303**, 249 (2002).

[290] Fazio, R., Palma, G. M., and Siewert, J. *Phys. Rev. Lett.* **83**, 5385 (1999).

[291] Preskill, J. In *Quantum information and computation,* Lo, H.-K., Spiller, T., and Popescu, S., editors (World Scientific, Singapore, 1998).

[292] Grover, L. K. *Phys. Rev. Lett.* **79**, 325 (1997).

[293] Shor, P. W. *Phys. Rev. A* **52**, 2493 (1995).

[294] Shnirman, A., Schön, G., and Hermon, Z. *Phys. Rev. Lett.* **79**, 2371 (1997).

[295] Makhlin, Y., Schön, G., and Shnirman, A. *Nature* **398**, 305 (1999).

[296] Smirnov, A. Y. and Zagoskin, A. M. cond-mat/0207214 (2002).

[297] Blais, A., Huang, R.-S., Wallraff, A., Girvin, S. M., and Schoelkopf, R. J. *Phys. Rev. A* **69**, 062320 (2004).

[298] Raimond, J. M., Brune, M., and Haroche, S. *Rev. Mod. Phys.* **73**, 565 (2001).

[299] Wallraff, A., Schuster, D. I., Blais, A., Frunzio, L., Huang, R.-S., Majer, J., Kumar, S., Girvin, S. M., and Schoelkopf, R. J. *Nature* **431**, 162 (2004).

[300] Chiorescu, I., Bertet, P., Semba, K., Nakamura, Y., Harmans, C. J. P. M., and Mooij, J. E. *Nature* **431**, 159 (2004).

[301] Xu, H., Strauch, F. W., Dutta, S. K., Johnson, P. R., Paik, H., Ramos, R. C., Anderson, J. R., Dragt, A. J., Lobb, C. J., and Wellstood, F. C. cond-mat/0409284 (2004).

[302] Leggett, A. J. *Phys. Rev. B* **30**, 1208 (1984).

[303] Leggett, A. J., Chakravarty S., Dorsey, A. T., Fisher, M. P. A., Garg, A., and Zwerger, W. *Rev. Mod. Phys.* **59**, 1 (1987).

[304] Burkard, G., Koch, R. H., and DiVincenzo, D. P. *Phys. Rev. B* **69**, 064503 (2004).

[305] Martinis, J. M., Nam, S., Aumentado, J., Lang, K. M., and Urbina, C. *Phys. Rev. B* **67**, 094510 (2003).

[306] Ioffe, L. B., Geshkenbein, V. B., Helm, C., and Blatter, G. *Phys. Rev. Lett.* **93**, 057001 (2004).

[307] Strunz, W. T., Diósi, L., Gisin, N., and Yu, T. *Phys. Rev. Lett.* **83**, 4909 (1999).

[308] Blume-Kohout, R., Caves, C. M., and Deutsch, I. H. *Found. Phys.* **32**, 1641 (2002).

[309] Van Isacker, P. *Phys. Rev. Lett.* **89**, 262502 (2002).

[310] Planck, M. *Verh. Dtsch. Phys. Ges. Berlin* **2**, 237 (1900).

[311] Steane, A. M. *Phys. Rev. Lett.* **77**, 793 (1996).

[312] Knill, E. quant-ph/0410199 (2004).

[313] Greenberger, D. M., Horne, M. A., , Shimony, A., and Zeilinger, A. *Am. J. Phys.* **58**, 1131 (1990).

[314] Mermin, N. D. *Rev. Mod. Phys.* **65**, 803 (1993).

[315] Gordon, R. G. *J. Chem. Phys.* **51**, 14 (1969).

[316] Albright, J. R. and Gavathas, E. P. *J. Phys. A* **19**, 2663 (1986).

[317] Hu, B. L. and Matacz, A. *Phys. Rev. D* **49**, 6612 (1994).

[318] Schumaker, B. L. and Caves, C. M. *Phys. Rev. A* **31**, 3093 (1985).